Elastomer-Based Elastocaloric Cooling

Zur Erlangung des akademischen Grades einer

Doktorin der Ingenieurwissenschaften (Dr.-Ing.)

von der KIT-Fakultät für Maschinenbau
des Karlsruher Instituts für Technologie (KIT)

angenommene

Dissertation

von

M.Sc. Carina Stephanie Ludwig

Tag der mündlichen Prüfung: 19. Dezember 2025
Erster Gutachter: Prof. Dr. Manfred Kohl
Zweiter Gutachter: Prof. Dr. Jürgen Rühe

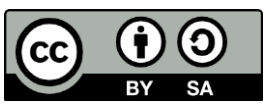

Abstract

Cooling technologies are omnipresent in modern society and play an indispensable role in everyday life. The ongoing growth of industry and population inevitably results in higher energy demand in this technology sector. Conventional vapor-compression technology is associated with high electricity consumption and relies on volatile gaseous refrigerants with a substantial global warming potential (GWP). Elastocaloric solid-state cooling, which relies on temperature changes induced by mechanical loading, has emerged as a promising environmentally friendly alternative to vapor-compression technology. The elastocaloric effect, and the associated reversible temperature in elastomers, is based on the strain-induced crystallization (SIC) and the entropy elasticity (EE). Elastomer materials, like natural rubber (NR) are inexpensive and exhibit distinct temperature changes upon mechanical load cycling. Moreover, the SIC is also responsible for the fatigue resistance of NR under dynamic loading. To enable rapid heat transfer, foil refrigerants are of special interest due to their high surface-to-volume ratio. In literature, only a limited number of studies have concentrated on the development of rubber-based elastocaloric devices. This work focuses on material characterization and the engineering of miniature-scale elastocaloric cooling devices using NR foils and solid-to-solid heat transfer.

Foil refrigerants of 9 × 26.5 mm^2 lateral size are investigated, which are laser-cut from sheets with thicknesses ranging from 60 to 900 µm. Sheet materials such as commercially available NR, NR latex, and NR produced with different crosslinking methods are employed. The elastocaloric effect is evaluated under uniaxial tensile loading, while an infrared (IR) camera captures the emitted radiation, which correlates with the material's surface temperature. The reversible temperature change exhibits a strong dependence on the strain, strain rate, and pre-strain. For a NR foil with a thickness of 290 µm and the maximum engineering strain of 700 % an adiabatic temperature change ΔT_{ad} of approximately 20.3 K is induced. This corresponds to a temperature change of +10.0 K upon loading and of -10.3 K upon unloading. The required strain rate to achieve quasi-adiabatic loading conditions increases with decreasing foil thickness. For the foils with a thickness of 290 µm, an engineering strain rate of 9.3 s^{-1} is required. Among all examined foils, the engineering stress-strain curves exhibit a hysteresis loop, with maximum engineering stress levels of several MPa. The work input corresponds to the area enclosed by the hysteresis loop and increases with the maximum engineering strain and strain rate. In contrast, it decreases with shorter hold times under constant load and for the operation with pre-strain. An engineering pre-strain of 300 % is identified as optimum due to its increased material coefficient of performance COP_{mat} of around 6 and remaining ΔT_{ad} of 12.4 K. In addition, the foil thickness decreases while the surface area enlarges, thereby increasing the surface-to-volume ratio and promoting rapid heat transfer.

Three different NR foil-based elastocaloric cooling devices are designed and implemented to operate within an engineering strain range of 300 to 700 % and transfer heat by mechanical

contact. The first investigated device is a monostable single-stage device, in which one actuator is employed for mechanical load cycling, while another one controls heat transfer. Spatial separation of hot and cold flows is achieved through alternating mechanical contact between the foil refrigerant and the parallel heat sink and heat source. A bistable actuation mechanism, utilizing a rotating lever arm for both mechanical loading and heat transfer, is introduced in the second single-stage device. The third device employs three cascaded foils that are thermally connected in series to enhance the device temperature span ΔT_{device}. An array of foil holders and a heat transfer unit, comprising a heat sink and heat source, are arranged in interlocking, comb-like structures. During operation of two and three foils, a temperature gradient is observed.

For all the investigated devices, the key performance parameters, including the ΔT_{device}, the initial cooling power $\dot{Q}_0$ and the device coefficient of performance COP_{device} exhibit a pronounced frequency and foil thickness dependence. The highest $\dot{Q}_0$ and COP_{device} of 214 mW and 5.7 are observed for the bistable single-stage device and a 290 µm thin NR foil. The optimum operation frequency is determined by the foil thickness and scales inversely with it. For decreasing the foil thickness from 650 to 290 µm, the optimum operation frequency increases from 350 to 424 mHz. Consequently, the absolute cooling power increases from 158 to 214 mW for the bistable single-stage device. By further decreasing the foil thickness to 60 µm, the specific cooling power increases to 6.7 Wg^{-1}. In addition, significant power savings of 64 % and reduced operating forces by a factor of 2.5 are observed, in comparison to the monostable single-stage device. Besides the frequency-dependence the absolute cooling power is significantly influenced by ΔT_{ad} and the thickness inhomogeneity due to manufacturing tolerances. The highest ΔT_{device} of 5.1 K is achieved by the cascaded device. However, the improvement resulting from two to three NR foils is marginal. A lumped element model (LEM) simulation indicates further improvement by increasing the heat transfer coefficient and reduced loading and unloading times. In addition, from elastocaloric cooling with shape memory alloys (SMAs), it is known that cascading is a powerful means to increase ΔT_{device}, if heat transfer is fast enough. This could be enhanced through various measures, such as thermally conductive fillers or surface coatings. Consequently, the potential for improvement is high and should be further elaborated.

In order to demonstrate the potential of NR-based elastocaloric materials for cooling applications, a preliminary long-term test, comprising 10^4 cycles, is performed. The ΔT_{device} remains stable throughout 10^4 cycles. Overall, the results emphasize the significant potential of NR-based elastocaloric devices as future sustainable cost-efficient cooling technology.

Kurzfassung

Kühltechnologien sind in der modernen Gesellschaft allgegenwärtig und spielen im Alltag eine unverzichtbare Rolle. Das anhaltende Wachstum von Industrie und Bevölkerung führt unweigerlich zu einem höheren Energiebedarf in diesem Technologiesektor. Herkömmliche Kompressionskältemaschinen sind mit einem hohen Stromverbrauch verbunden und basieren auf flüchtigen gasförmigen Kältemitteln mit einem erheblichen Treibhauspotenzial (GWP). Die elastokalorische Festkörperkühlung, die auf mechanisch induzierte Temperaturänderungen basiert, hat sich als vielversprechende umweltfreundliche Alternative zur Kompressionskältemaschine herausgestellt. Der elastokalorische Effekt und die damit verbundene reversible Temperaturänderung in Elastomeren basieren auf der Dehnungskristallisation (SIC) und die Entropieelastizität (EE). Elastomermaterialien wie Naturkautschuk (NR) sind kostengünstig und zeigen bei mechanischer Belastung ausgeprägte Temperaturänderungen. Darüber hinaus ist die SIC auch für die Ermüdungsbeständigkeit von NR unter dynamischer Belastung verantwortlich. Um eine verbesserte Wärmeübertragung zu ermöglichen, sind Folien aufgrund ihres hohen Oberflächen-zu-Volumen-Verhältnisses von besonderem Interesse. In der Literatur gibt es nur wenige Studien, die sich mit der Entwicklung von elastokalorischen Systemen auf Gummibasis befassen. Diese Arbeit konzentriert sich auf die Materialcharakterisierung und die Konstruktion von elastokalorischen Kühlsystemen im Miniaturbereich unter Verwendung von NR-Folien und festkörperbasierten Wärmeübertragung.

Es werden Folien mit einer lateralen Größe von 9 × 26,5 mm^2 untersucht, die aus Elastomerbändern mit einer Dicke von 60 bis 900 µm lasergeschnitten werden. Materialien wie handelsübliches NR, NR-Latex und NR, das mit verschiedenen Vernetzungsverfahren hergestellt wurde, werden verwendet. Der elastokalorische Effekt wird unter einachsiger Zugbelastung bewertet, während eine Infrarotkamera (IR-Kamera) die emittierte Strahlung erfasst, die mit der Oberflächentemperatur des Materials korreliert. Die reversible Temperaturänderung zeigt eine starke Abhängigkeit von der Dehnung, der Dehnungsgeschwindigkeit und der Vordehnung. Bei einer NR-Folie mit einer Dicke von 290 µm und einer maximalen technischen Dehnung von 700 % wird eine adiabatische Temperaturänderung ΔT_{ad} von etwa 20,3 K induziert. Dies entspricht einer Temperaturänderung von +10,0 K bei Belastung und von -10,3 K bei Entlastung. Die erforderliche Dehnungsrate, um quasi-adiabatische Belastungsbedingungen zu erreichen, steigt mit abnehmender Foliendicke. Für Folien mit einer Dicke von 290 µm ist eine nominelle Dehnrate von 9,3 s^{-1} erforderlich. Bei allen untersuchten Folien zeigen die nominellen Spannungs-Dehnungs-Kurven eine Hystereseschleife mit maximalen nominellen Spannungen im Bereich von wenigen MPa. Die benötigte Arbeit pro verrichtetem Zyklus entspricht der von der Hystereseschleife umschlossenen Fläche und steigt mit der maximalen nominellen Dehnung und Dehnrate. Im Gegensatz dazu nimmt diese bei kürzeren Haltezeiten unter konstanter Belastung sowie beim Betrieb mit Vordehnung ab. Eine nominelle Vordehnung von 300 % wird aufgrund des erhöhten Materialleistungskoeffizienten COP_{mat} von etwa 6 und einer verbleibenden ΔT_{ad} von 12,4 K als optimal identifiziert. Darüber hinaus verringert sich die Foliendicke, während die Oberfläche

zunimmt, wodurch das Oberflächen-zu-Volumen-Verhältnis steigt und ein schneller Wärmetransport begünstigt wird.

Drei verschiedene elastokalorische Kühlsysteme auf Basis von NR-Folien werden entwickelt und implementiert, um in einem nominellen Dehnungsbereich von 300 bis 700 % betrieben zu werden und Wärme durch mechanischen Kontakt zu übertragen. Das erste untersuchte Gerät stellt ein monostabiles einstufiges System dar, bei dem ein Aktor den mechanischen Lastzyklus übernimmt, während ein zweiter Aktor den Wärmetransport regelt. Eine räumliche Trennung von Wärmeströmen wird durch abwechselnden mechanischen Kontakt zwischen der Folie und der parallel angeordneten Wärmequelle sowie der Wärmesenke erreicht. Im zweiten einstufigen System wird ein bistabiler Mechanismus eingeführt, der einen rotierenden Hebelarm sowohl für die mechanische Belastung als auch für die Wärmeübertragung nutzt. Das dritte System verwendet drei hintereinandergeschaltete Folien, die thermisch in Serie verbunden sind, um die Temperaturspanne des Systems ΔT_{device} zu erhöhen. Ein Array aus Folienhaltern und eine Wärmetransfereinheit, bestehend aus Wärmesenke und Wärmequelle, sind als ineinandergreifende, kammartige Strukturen angeordnet. Während des Betriebs mit zwei beziehungsweise drei Folien wird ein Temperaturgradient beobachtet.

Für alle untersuchten Systeme zeigen die wichtigsten Leistungsparameter, darunter der ΔT_{device}, die initiale Kühlleistung $\dot{Q}_0$ und die Leistungszahl COP_{device}, eine ausgeprägte Abhängigkeit von der Frequenz und der Foliendicke auf. Die höchsten Werte für $\dot{Q}_0$ und COP_{device}, von 214 mW und 5,7 werden für das bistabile einstufige System und eine 290 µm dünne NR Folie erreicht. Die optimale Betriebsfrequenz wird durch die Foliendicke bestimmt und skaliert umgekehrt proportional zu dieser. Bei Verringerung der Foliendicke von 650 auf 290 µm steigt die optimale Betriebsfrequenz von 350 auf 424 mHz. Folglich erhöht sich die absolute Kühlleistung für das bistabile einstufige Gerät von 158 auf 214 mW. Durch eine weitere Reduktion der Foliendicke auf 60 µm steigt die spezifische Kühlleistung auf 6,7 Wg^{-1}. Darüber hinaus werden signifikante Energieeinsparungen von 64 % sowie eine Reduzierung der Betriebskräfte um den Faktor 2,5 im Vergleich zum monostabilen einstufigen System festgestellt. Neben der Frequenzabhängigkeit wird die absolute Kühlleistung wesentlich durch ΔT_{ad} sowie die Dickeninhomogenität infolge von Fertigungstoleranzen beeinflusst. Die höchste ΔT_{device} von 5,1 K wird durch das kaskadierte System erreicht. Die Verbesserung durch den Übergang von zwei auf drei NR-Folien ist jedoch marginal. Eine *lumped element model* (LEM) Simulation weist auf weitere Optimierungspotenziale durch Erhöhung des Wärmeübergangskoeffizienten sowie durch verkürzte Be- und Entlastungszeiten hin. Darüber hinaus ist aus der elastokalorischen Kühlung mit Formgedächtnislegierungen (FGLs) bekannt, dass Kaskadierung ein wirksames Mittel zur Erhöhung der ΔT_{device} ist, wenn die Wärmeübertragung schnell genug erfolgt. Dies könnte durch verschiedene Maßnahmen, wie beispielsweise wärmeleitende Füllstoffe oder Oberflächenbeschichtungen, verbessert werden. Folglich ist das Verbesserungspotenzial hoch und sollte weiter ausgearbeitet werden.

Um das Potenzial von NR-basierten elastokalorischen Materialien für Kühlungsanwendungen zu demonstrieren, wird ein vorläufiger Langzeittest mit 10^4 Zyklen durchgeführt. Die ΔT_{device} bleibt

über alle 10^4 Zyklen stabil. Insgesamt unterstreichen die Ergebnisse das erhebliche Potenzial von elastokalorischen Geräten auf NR-Basis als zukünftige nachhaltige kosteneffiziente Kühltechnologie.

Publications

Parts of this thesis and related work have been previously published and presented by the author in scientific journals and conferences.

In scientific journals:

C. Ludwig, J. Leutner, O. Prucker, J. Rühe, and M. Kohl, "Miniature-scale elastocaloric cooling by rubber-based foils", *J. Phys. Energy 6* (2023) 015009

C. Ludwig and M. Kohl, "Bistability-enhanced elastocaloric cooling device based on a natural rubber foil", *J. Appl. Phys. 136* (2024) 165001

As conference proceedings:

C. Ludwig, J. Leutner, O. Prucker, J. Rühe, and M. Kohl, "Natural Rubber Foil-Based Elastocaloric Cooling", *in ACTUATOR 2024 International Conference and Exhibition on New Actuator Systems and Applications (VDE VERLAG GmbH, Wiesbaden, 2024), pp. 132–135.*

As conference contributions:

C. Ludwig, J. Leutner, O. Prucker, J. Rühe, and M. Kohl, "Elastomer Foil-Based Elastocaloric Cooling", *ELASTOCALORICS2023,* June 27-28, 2023, Saarbruecken, Germany *(poster presentation)*

C. Ludwig, J. Leutner, O. Prucker, J. Rühe, and M. Kohl, "Rubber Driven Solid-State Elastocaloric Cooling Device Based on Miniature-Scale", *ACTUATOR24,* June 13-14, 2024, Wiesbaden, Germany *(oral presentation)*

C. Ludwig, J. Leutner, O. Prucker, J. Rühe, and M. Kohl, "Natural Rubber Foil-Based Elastocaloric Cooling using Bistable Actuation", *ELyT workshop 2025,* February 19-21, 2025, Lyon/ Annecy, France *(oral presentation)*

C. Ludwig, J. Leutner, O. Prucker, J. Rühe, and M. Kohl, "Bistability-Driven Elastocaloric Cooling: Utilizing Natural Rubber Foils", *ELASTOCALORICS2025,* May 13-15, 2025, Saarbruecken, Germany *(oral presentation)*

Contents

Abbreviations

CB	Carbon black
COP	Coefficient of performance
EE	Entropy-elasticity
FGL	Formgedächtnislegierung
GTR	Ground tire rubber
GNS	Graphene nanoplatelet
GWP	Global warming potential
IR	Infrared
LCP	Liquid crystal polymer
PFAS	Per- and polyfluoroalkyl
PPI	Pulse per inch
PCO	Polycyclooctene
PLA	Polylactic acid
PVDF	Fluoropolymer polyvinylidene fluoride
NiTi	Nitinol
NR	Natural rubber
SEBS	Styrene ethylene butylene styrene
SIC	Strain-induced crystallization
SIS	Styrene-isoprene-styrene
SMA	Shape memory alloy
SMP	Shape memory polymer

TPU	Thermoplastic polyurethane
TIC	Temperature-induced crystallization
TIM	Thermal interface material
UV	Ultraviolet

Parameters

A	Contact area
A_0	Initial cross-sectional area
α	Angle between heat sink and lever arm
Bi	Biot number
β	Angle between heat sink and heat source
COP_{device}	Device coefficient of performance
COP_{mat}	Material coefficient of performance
$cost_{mat}$	Material cost
c_p	Specific heat capacity
d	Initial thickness of the foil specimen (unloaded)
ε_{max}	Maximum engineering strain
ε_{min}	Minimum engineering strain
ε_{pre}	Engineering pre-strain
$\dot{\varepsilon}$	Engineering strain rate
f	device operation frequency
F	Absolut loading force
$\vec{F}$	Force vector
$\vec{F}_{clamp}$	Clamping force vector
$\vec{F}_{load}$	Loading force vector
$\vec{F}_N$	Force vector normal to the trajectory
$\vec{F}_T$	Force vector tangential to the trajectory
$\vec{F}_{clamp}$	Clamping force vector
$\vec{F}_x, \vec{F}_y$	Force vector along the x, y-axis

h	Heat transfer coefficient
h_{conv}	Convective heat transfer
h_{cond}	Conductive heat transfer
L	Characteristic length
L_0	Initial foil specimen length
λ	Thermal conductivity
$\vec{M}$	Applied torque vector
$\vec{M}_\rho, \vec{M}_\theta, \vec{M}_\varphi$	Bending moments about the ρ, θ, φ-axis
m_{source}	Source mass
$\dot{Q}_0$	Initial cooling power
$\dot{q}_0$	Specific initial cooling power
$\dot{q}_{ab}$	Specific absorbed heat
$\dot{Q}_{load}$	Cooling power under applied thermal load
$\dot{Q}_{out}$	Heat release
$\dot{Q}_{in}$	Heat absorption
ρ	Density
σ_{max}	Maximum engineering stress
σ_{re}	Remaining engineering stress
R	Radius
S_0	Initial foil specimen heat transfer area
t_{hold}	Hold time
t_{period}	Time period
t_{ramp}	Ramp time
t_{exp}	Experimental time constraints
$\dot{T}_{source}$	Initial temperature change

ΔT	Temperature change
ΔT_{ad}	Adiabatic temperature change
ΔT_c	Temperature change after unloading
ΔT_{device}	Device temperature span
ΔT_h	Temperature change after loading
ΔT_{i1}, ΔT_{i2}	Temperature change of intermediate elements
ΔT_{sink}	Sink temperature change
ΔT_s	Initial residual temperature increase
ΔT_{so}	Residual temperature increase
ΔT_{source}	Source temperature change
v	Velocity
w_0	Initial width
$\dot{W}$	Device input power
ΔW_{device}	Mechanical work input per cycle
ΔW_{mat}	Specific material work input
Δw_{mat}	Specific material work input

1 Introduction

1.1 Motivation

Cooling technologies are ubiquitous and play an indispensable role in modern everyday life. Air conditioning, food refrigeration, and thermal management of batteries and temperature-sensitive medical supplies illustrate the broad spectrum of cooling applications. Increasing industrialization and rising population inevitably lead to higher energy consumption in this technology sector. Approximately three billion cooling devices are currently in use worldwide, representing about 17 % of the total global electricity consumption [1]. Events such as the exceptionally hot summer of 2023 and the steadily rising average annual temperature [2] will lead to an increased demand for cooling units in the future [3].

The cooling market is dominated by vapor-compression technology, associated with high electricity consumption, and relies on volatile gaseous refrigerants with a substantial global warming potential (GWP). Achieving the climate goal of reducing overall greenhouse gas emissions by over 95 % by 2050 compared to 1990 levels necessitates a comprehensive transformation of cooling technologies [4]. Besides the GWP, per- and polyfluoroalkyl substances (PFAS) are included in many commonly used refrigerants. PFAS are persistent chemicals that resist degradation and are known for their potential harmful effects on human health and the environment. Due to their widespread impact and persistence, they are often referred to as *poison of the century*. The European Union is considering significant PFAS restrictions aimed at limiting the manufacture, marketing, and use of PFAS, including fluorinated greenhouse gases [5]. Consequently, the development of efficient innovative cooling technologies eliminating the dependence on gases with GWP is inevitable.

Elastocaloric cooling, which relies on temperature changes induced by mechanical loading, has emerged as a promising alternative. Superelastic shape memory alloys (SMAs) exhibit the elastocaloric effect with temperature changes exceeding 20 K, and their theoretical efficiency can approach the thermodynamic limit [6,7]. Due to the absence of harmful or flammable refrigerants, solid-state cooling based on the elastocaloric effect is classified as a viable substitute for vapor-compression technology [8]. Various macro-scale elastocaloric cooling demonstrators based on SMA materials, employing approaches such as the compression of NiTi-based superelastic tubes, have been reported lately [9–12]. Extraordinary temperature spans of up to 75 K [13] and cooling power exceeding 1.2 kW [14] are achieved using heat transfer fluids.

Nowadays, cooling requirements for miniature-scale devices are mainly fulfilled by thermoelectric coolers, which typically operate with COPs below 2.5 [15]. SMA film-based devices have demonstrated temperature spans of 27.5 K [16] and specific cooling power of 19 Wg^{-1} [17], highlighting their potential for miniature cooling applications. Film and foil refrigerants are

particularly advantageous for applications such as localized cooling of electronics and temperature regulation of lab-on-chips due to their high surface-to-volume ratios [18]. A major challenge in utilizing SMA refrigerants is the large stress range of 600-800 MPa required for superelastic cycling, aggravated by issues related to material availability and cost [19].

Elastomers such as natural rubber (NR) may provide a promising cost-efficient and environmentally friendly alternative [20]. The renewable origin and the potential for recycling waste tires, along with its non-toxic natural composition, are key factors contributing to environmental benefits [21]. Besides the sustainable factors, mass production of the material is already established, resulting in a remarkably low price of around 1.5 €kg^{-1}, in contrast to 100 €kg^{-1} for SMAs [22]. This could facilitate commercialization and potentially ease the demand for long lifetimes, as the refrigerant can be replaced more frequently [19]. Furthermore, a large adiabatic temperature change of around 20 K, induced by only several MPa of stress, is of special interest for cooling applications [19]. To yield a strong enough temperature effect, high strains of several hundred percent are needed [23,24].

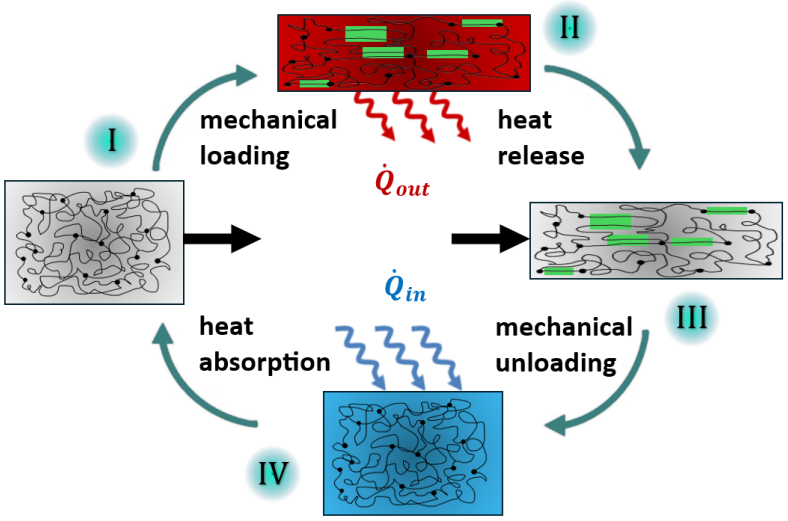

Figure 1: Schematic of a four-step elastocaloric cooling cycle based on elastomers. (I) mechanical loading of the elastocaloric refrigerant, (II) followed by heat release. (III) mechanical unloading, resulting in (IV) heat absorption. By separating the heat flows, both heating and cooling applications can be realized.

A schematic of the four-step elastocaloric cooling cycle based on elastomers is presented in Figure 1. The cycle starts with the mechanical loading in step I, followed by a temperature increase and heat release during step II. In step III, unloading takes place, leading to a temperature decrease, while step IV involves heat absorption for cooling.

The temperature change results from two effects, a conformational entropy change caused by the alignment of molecular chains and the strain-induced crystallization (SIC) [25,26]. The variation in the configurational disorder of polymer chains upon mechanical stimuli is also called entropy elasticity (EE) [27]. When stretched, a fraction of the polymer chains in the network

straighten and become ordered, and SIC arises in the rubber [28]. The crystallites melt, upon strain release. The fatigue resistance of NR under dynamic loading is associated with the SIC [29]. By the formation of semicrystalline zones around the crack tip, growth of cracks is prevented [30]. To date, only a limited number of studies have focused on the development of rubber-based elastocaloric devices [31–34].

To overcome the early stage of the research field and pave the way for feasible industrial applications, further investigation is needed. Given the promising environmental benefits, cost efficiency, and fatigue resistance of NR, further exploration of its potential for elastocaloric cooling is essential. This work aims to address current gaps by investigating the performance and durability of rubber-based elastocaloric cooling and to uncover its critical challenges. Ultimately, the goal is to contribute to the advancement of sustainable and efficient cooling technologies.

This work is performed in the framework of a research project funded by the German Science Foundation (DFG) with Prof. Rühe's research group at the University of Freiburg. Within this collaboration, the University of Freiburg focuses on material synthesis and the production of rubber sheets. This work, conducted at the Karlsruhe Institute of Technology, focuses on material characterization and the engineering of elastocaloric cooling devices using NR foils made from both commercially available and sheets fabricated in collaboration.

1.2 Objectives

One of the two main objectives of this work is to characterize NR materials for their suitability in elastocaloric cooling applications. The focus is on understanding their coupled thermal and mechanical properties, carried out by tensile tests combined with infrared thermography. Rubber materials such as commercially available NR, NR latex, and NR produced with different crosslinking methods, fabricated by cooperation partners, serve as active material, also referred to refrigerant. Building on the knowledge gained from material characterization, the second objective is to design and implement elastocaloric cooling devices that operate on the principle of solid-to-solid heat transfer. This includes the fabrication of compact functional prototypes, allowing spatial separation of heat flow, and the optimization of their operating parameters. Overall, three elastocaloric cooling devices based on NR foils are realized. Initially, a monostable single-stage device is investigated, serving as the initial baseline design and establishing a foundation for comparison with more advanced configurations. The objective of the bistable single-stage device is to further enhance performance parameters while reducing the number of required actuators. To reduce system complexity and facilitate commercialization, the number of actuators is intended to be kept to a minimum. Besides the single-stage devices, a cascaded device is developed to increase the device temperature span. To obtain a better understanding of the device, a lumped element model simulation of the thermal behavior is developed. Finally, the performance of these devices is evaluated to establish their potential for practical cooling applications and to identify directions for further improvement.

1.3 Outline

The following chapter provides an overview of the fundamental properties of NR materials and the elastocaloric effect, with a particular focus on its physical origin. To facilitate a deeper understanding of the elastocaloric effect on elastomers, the mechanisms of EE and SIC are explained in detail. Subsequently, adiabatic temperature changes reported in the literature for various elastomer-based materials are compared. Chapter three is dedicated to the current state of the art in elastocaloric cooling devices. Various system architectures and their respective operating principles are reviewed and analyzed in terms of performance, including a comparison between SMA- and elastomer-based cooling devices.

The fourth chapter focuses on the experimental characterization of elastomer foils. This includes specimen preparation based on both commercially available and NR sheets fabricated in collaboration. The experimental procedures are described in detail, with particular emphasis on the determination of mechanical and thermal properties under uniaxial tensile load conditions.

Building on this, the fifth chapter is dedicated to the demonstration of the elastocaloric effect in a functional cooling device based on elastomers. The implementation and operating principle of a NR-based elastocaloric cooling devices are presented. Three devices based on solid-to-solid heat transfer are evaluated and classified according to their performance. Particular emphasis is placed on the effects of operating frequency and foil thickness on the performance of each device. Among the three devices, two are single-stage concepts utilizing a single foil refrigerant, whereas the third features a cascaded architecture aimed at extending the achievable temperature span by operating three foils simultaneously.

Finally, the last chapter summarizes the key results obtained in the course of this work and provides an outlook on future research directions.

2 Background

2.1 Elastomers and the Elastocaloric Effect

As early as the beginning of the 19th century, Gough described that NR heats up when deformed and cools down upon release. He also described that NR undergoes thermal contraction when exposed to increased temperatures and expands upon cooling [35]. This behavior was later quantified by Joule [36]. The elastocaloric effect, and the associated reversible temperature change upon mechanical deformation in elastomers like natural rubber, is based on the strain-induced crystallization (SIC) and the entropy elasticity (EE) [25,26]. The EE is related to an entropy change resulting from the alignment of polymer chains during deformation [25]. In addition, the SIC, which depends on strain, strain rate, and temperature, [37] results in a first order phase transition [38] from an amorphous rubbery state to a semicrystalline state under deformation [39,40]. This crystallization and the subsequent melting are accompanied by a pronounced stress-strain hysteresis response. The SIC provides a substantial reinforcing mechanism for the rubber network [38,41,42]. The elastocaloric temperature change mainly originates from the latent heat accompanied by the SIC [25,26,43]. Although intensive research has been conducted in the field of SIC, the quantitative relationship between SIC and the resulting elastocaloric effect has not yet been sufficiently clarified. To provide a basis for understanding this correlation, both EE and SIC are discussed in detail in Chapters 2.3 and 2.4, while experimentally measured reversible temperature changes are summarized in Chapter 2.5. In addition, the occurrence of SIC in synthetic rubber and the effects of filler content and crosslink density are discussed in Subchapters 2.4.4, 2.4.5 and 2.4.6, respectively. For better understanding, an explanation of the NR material, including vulcanization, is presented beforehand, as this knowledge is necessary to comprehend SIC and EE.

2.2 Natural Rubber Based Materials

Cross-linked natural rubber can be found in many typical everyday products. In addition to its main application as truck and car tires, cross-linked NR is used in medical gloves, steering wheels and seals. The NR raw material is obtained from the sap of the rubber tree. The liquid milky sap, also known as latex, contains around 30 % NR [44]. Latex can be purchased as a partially cross-linked concentrate, and is used, for example, as an impregnation for clothing. The majority of latex is processed into solid rubber by coagulation and drying [45]. After the drying process, the rubber is pressed into bales [46]. Raw rubber can be stretched by 800-1000 % [47]. In order to process the rubber bales further, the viscosity must be reduced. This can be achieved by kneading in an internal mixer. This process step is called mastication [48]. Subsequently, shaping can be carried out by pressing, or mixing with rubber chemicals can take place. The final step is vulcanization of the shaped product.

While in English the term *rubber* is commonly used for both the raw material and the crosslinked product, whereas in German a distinction is made between *Kautschuk* (uncrosslinked) and *Gummi* (crosslinked) [44]. The term rubber also includes synthetically produced rubber.

In this work, the elastocaloric effect in NR-based materials with a defined compounding is investigated. Sheets are fabricated in collaboration with the University of Freiburg. In addition to classic sulfur vulcanization, a C,H-insertion crosslinking method is applied to produce recyclable sheets. This approach enables reshaping after failure due to fracture, which is not possible for conventionally vulcanized NR products. The method was developed by the University of Freiburg [49,50] and the sheet fabrication process is described in detail in [19]. In addition to tailored materials, commercially available products are also investigated. NR sheets based on sulfur crosslinking and NR latex are studied. Therefore, their fabrication and differences are briefly presented in the following two subchapters.

2.2.1 Vulcanization and Sheet Fabrication

In its uncured original state, NR is soft and sticky but already exhibits high restoring forces [46]. These properties can be further enhanced through cross-linking, also known as vulcanization. The name vulcanization comes from the high process temperatures and pressures [51]. Chemically, NR consists of cis-1,4-polyisoprene [52]. The polyisoprene forms long-chain polymer structures, the so-called macromolecules [53]. The individual macromolecules can be covalently linked through a chemical cross-linking reaction [54]. The crosslinking bridges are relatively short compared to the macromolecules and, in the case of crosslinking with sulfur, the most common type of crosslinking, consist of one to eight sulfur atoms [46]. The structure of cross-linked NR is illustrated in Figure 2. Due to the cross-linking, the restoring forces increase as a result of the significantly restricted mobility of the macromolecules [46]. The highly elastic end products after completion of a vulcanization process are called elastomers, rubber or vulcanizates (definition according to DIN 7724:1993).

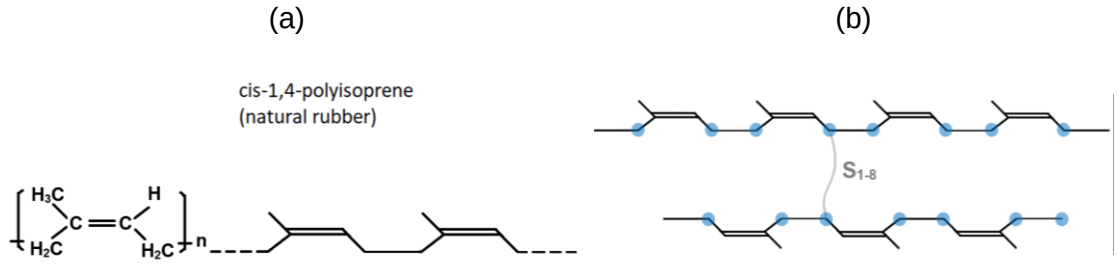

Figure 2: (a) The cis-1,4-polyisoprene macromolecule of NR. Adapted from [52] licensed under CC BY 4.0. (b) Principle of sulfur vulcanization with active crosslinking sites ($S_{1\text{-}8}$) and potential crosslinking sites (in blue) illustrated using cis-1,4-polyisoprene. Adapted from [55] licensed under CC BY 4.0.

Rubber products are shaped prior to cross-linking. After cross-linking, not only are the restoring forces improved, but undesirable properties such as stickiness and plasticity are also suppressed

[56]. The resulting vulcanizates can be stretched by several hundred percent and return almost completely to their original shape after release [46]. This behavior is referred to as rubber or entropy elasticity (EE) [57]. The modulus of elasticity, hardness, dynamic load-bearing capacity and strength increase with the crosslink density [46]. However, if the crosslink density is too high, the values decrease. In addition to sulfur vulcanization, rubber can also be cross-linked using peroxides. However, since sulfur vulcanization is the most common method, reference is made here to further literature [58].

2.2.2 Fabrication of Thin Latex Products

In some sectors of the rubber industry, raw field latex is directly utilized for manufacturing thin products such as medical gloves and balloons [59]. After extraction from the Hevea brasiliensis tree, the raw field latex is concentrated and mixed with ammonia at the plantation for mechanical stabilization, which is later used to produce prevulcanized NR latex [58]. In contrast to crosslinked NR products that are vulcanized in the solid state, NR latex products are typically produced through a prevulcanization step in the liquid state, followed by a postcuring process. [60]. During prevulcanization, the raw NR latex is mixed with a water-based dispersion containing a vulcanization agent. The resulting suspension can be shaped in a mould and vulcanized at elevated temperatures maintained for several hours, to obtain sheets with thicknesses in the range of tens to a few hundred micrometers [61,62].

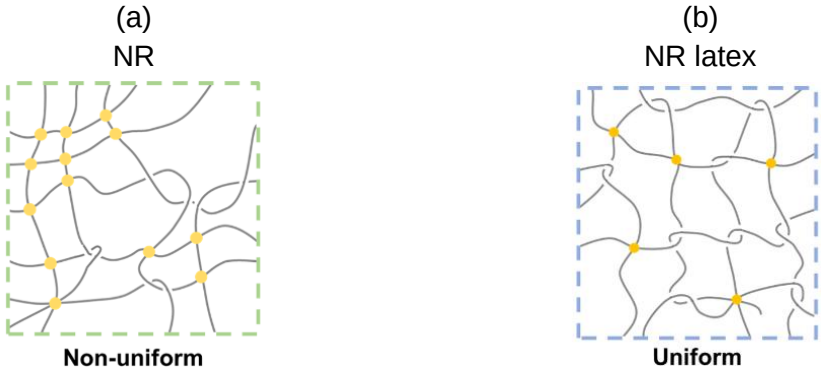

Figure 3: Schematic diagram of the microstructure of (a) vulcanized NR and (b) vulcanized NR latex. Yellow dots indicate the crosslinking points. NR latex exhibits a more uniform crosslinking network with higher entanglement. Adapted with permission from [59].

Due to the different fabrication methods, the resulting vulcanized rubber sheets differ in microstructure. When comparing sheets with identical total crosslink density, vulcanized NR latex has been reported to exhibit a more homogeneous and uniform crosslinking network with a higher entanglement content than conventionally vulcanized NR [59].

2.2.3 Synthetic Rubber Based Materials

NR-based products exhibit excellent mechanical and dynamic properties, but their thermal stability is limited, and they offer only slight resistance to oil and ultraviolet (UV) radiation [46]. In response to the demand for new properties and the desire for independence from plantation-based rubber, synthetic rubbers have been developed. One example is acrylonitrile butadiene rubber, also known as nitrile rubber and designated as NBR according to ISO 1629. Nitrile butadiene rubber (NBR) offers excellent resistance to oil and fuels derived from petroleum and is commonly used in sealing applications. [58]. In tire production, styrene butadiene rubber (SBR) is used alongside NR due to its high coefficient of friction in wet conditions and excellent abrasion resistance [46]. The synthetic counterpart to NR is isoprene rubber (IR). However, IR exhibits a significantly lower tendency to crystallize [63], resulting in considerably reduced tensile and tear strength compared to NR. A well-known synthetic rubber is chloroprene rubber (CR), commonly known as neoprene, which is valued for its excellent weather resistance and is often used in applications such as window frame seals [64]. It should be noted that, according to ISO 1629, the abbreviations are used synonymously for both uncured, raw and crosslinked rubbers.

In addition to monomer-based rubbers, a copolymer is a polymer derived from two or more different monomer species. In the case of styrene-isoprene-styrene (SIS), the material consists of a hard and glassy polystyrene (PS) end block. The middle block is the soft and rubbery polyisoprene (PI), responsible for the elastomeric behavior and a second polystyrene block. This triblock architecture enables the material to combine the elastic properties of rubbers with the processability of thermoplastics. Although covalent bonds are present within the chains, no covalent crosslinks are formed, as in chemical crosslinked vulcanized NR. Instead, only physical interactions, such as those between aggregated polystyrene end blocks acting as physical crosslinking points, and van der Waals forces between chains, are present [65]. Being free from chemical crosslinking, the triblock copolymer, which belongs to the class of thermoplastic elastomers (TPEs) similar to thermoplastic polyurethane (TPU), is compatible with standard plastic processing techniques like injection molding and melt extrusion, and could also be processed via 3D printing, enabling the fabrication of flexible geometries [66].

2.3 Entropy Elasticity

Typically, metals such as steel can be elastically strained by up to about 0.2 %, whereas elastomers such as NR can be strained by more than 1000 % without failure. Unlike metals, the elasticity of rubbers is governed by entropy rather than by enthalpy [67]. The elastic restoring force in metals arises from the variation in interatomic binding energy with strain. This principle was established as a fundamental concept in the modern theory of solids [68]. In rubber, the elastic restoring force arises from entropy changes caused by variations in the configurational disorder of polymer chains [27]. At room temperature, the coiled polymer chains in rubber, initially disordered, can be stretched and displaced relative to each other under the influence of a macroscopic force [25].

$$F = U - TS \quad \text{2-1}$$

During deformation, the polymer chains unravel and align, resulting in a higher state of order with fewer possible conformations and, consequently, a decrease in entropy, while the internal energy remains approximately constant [69,70]. For ideal elastic materials, the internal energy stays constant due to the freely rotatable polymer chains and the absence of significant intermolecular forces [71]. To describe this behavior thermodynamically, the Helmholtz free energy F, defined as the internal energy U minus the product of temperature T and entropy S, is used, 2-1. As the entropic contribution decreases, the negative term on the right-hand side of the equation becomes less negative, leading to an increase in the Helmholtz free energy. This increase is balanced by the mechanical work performed by the external force stretching the rubber [72]. Due to the reduction in entropy during the stretching process, heat is released [73]. According to the second law of thermodynamics, the original disordered state is restored upon removal of the external load. Consequently, entropy increases again as heat is absorbed by the environment. This disordered state represents the entropically favorable equilibrium condition. This material behavior is known as rubber or entropy elasticity (EE). The glass transition temperature, of approximately -72°C for natural rubber, separates the glassy-like, hard state from the entropy-elastic region [74].

To sum up, entropy elasticity describes the thermodynamically driven recovery of stretched rubber materials to their original configuration upon removal of the external load, resulting from the system´s tendency to maximize entropy. This concept can explain the elastic behavior of materials such as styrene-butadiene rubber (SBR), which remains amorphous under deformation [72]. However, for rubbers like NR, the situation is more complex due to their ability to crystallize under high deformation above 300 % strain [72]. This phenomenon is known as strain-induced crystallization (SIC). Moreover, SIC is the primary contributor to the elastocaloric effect observed in cross-linked natural rubber, alongside EE [43]. Therefore, SIC will be discussed in detail in the following section.

2.4 Strain-Induced Crystallization

Cross-linked natural rubber (NR) exhibits excellent mechanical properties, including high tensile strength and fatigue resistance [57]. In the undeformed state, the NR network consists of coiled, amorphous polymer chains connected by sulfur cross-linking bridges [25]. Under large deformations, these polymer chains align in parallel and form crystallites, resulting in a highly ordered configuration [39,40]. This means that part of the material crystallizes as a result of deformation [75]. The outstanding mechanical properties originate from strain-induced crystallization (SIC), which constitutes a reversible phase transformation [26]. The elastocaloric temperature change primarily results from the latent heat associated with SIC [25,26,43]. In Figure 4, the schematic of the NR network is shown, including coiled polymer chains connected by cross-linking bridges and strain-induced crystallites formed under macroscopic uniaxial tensile loading.

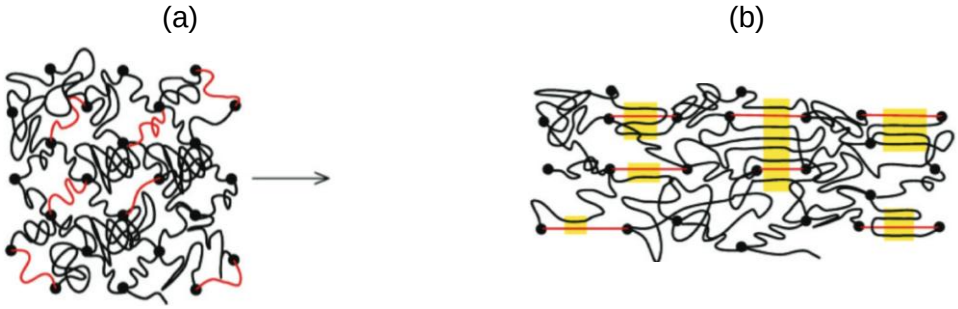

Figure 4: Schematic of nucleation and crystallization in a vulcanized natural rubber (NR) network, showing (a) the state before mechanical loading and (b) the semicrystalline state under high tensile strain. The load direction is indicated by the black arrow. Amorphous polymer chains are depicted as entangled structures connected by sulfur cross-linking bridges (black dots). Crystallites formed due to strain-induced crystallization (SIC) are highlighted in yellow. Together with entropy elasticity (EE), SIC mainly contributes to the elastocaloric effect in elastomer materials. Adapted with permission from [76].

Embedded within an amorphous matrix, the crystallites, which measure tens of nanometers, act as reinforcing fillers [38,41,42]. In comparison, many tough biological materials incorporate nanostructures within an amorphous matrix [29]. For example, spun spider silk fibers contain sheet-like crystallites that cross-link the elastic fibroin proteins into a polymer network, resulting in exceptional stiffness, strength and toughness [77]. In NR materials, stiffness, as indicated by engineering stress, increases with deformation because newly formed crystallites act as fillers, analogous to cross-linking points [24,38]. To assess the degree of crystallinity, the crystallinity index can be used, which is evaluated based on the reduction of the amorphous fraction upon stretching [39]. This definition is employed by [78] to evaluate the crystallinity of an NR sample under mechanical loading and unloading. Since the definition of the crystallinity index may vary across the literature, the specific calculation method should be carefully considered when comparing absolute values. In Figure 5, a schematic is presented illustrating the evolution of crystallinity for different maximum strain levels [78].

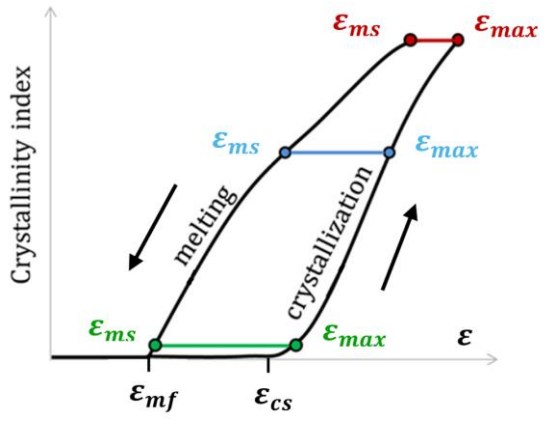

Figure 5: Schematic of the degree of crystallinity of the strain-induced crystallization (SIC) at various maximum strains in natural rubber (NR) during loading and unloading at room temperature. Legend: maximum strain ε_{max}; onset strain of SIC ε_{cs}; strain at which melting is completed ε_{mf}. Adapted with permission from [78].

The SIC in vulcanized NR typically begins at a tensile strain ε_{cs} of approximately 300 % at room temperature [37,38]. The onset of crystallization depends on several factors, including strain rate, ambient temperature, and rubber compounding, particularly the presence of additional fillers such as carbon black [38,79]. Consequently, the strain at which crystallization initiates vary across the literature and should always be reported together with the specific test conditions. The crystallites are already highly oriented at the onset [76] and align parallel to the direction of the macroscopic mechanical load [28,80]. The degree of crystallinity increases with applied strain [25], accompanied by the progressive disentanglement of coiled polymer chains [39]. In addition, oriented amorphous chains serve as precursors to crystallite formation [28,78]. As the mechanical strain increases to 600 %, the formation of additional crystallites is more and more impeded due to the accumulation of topological constraints in the amorphous phase adjacent to the existing crystallites [24]. Even at high strain levels of 600 %, approximately 75 % of the polymer chains remain unoriented [28] and retain their amorphous character [80]. Therefore, the notion, prevalent in many polymer textbooks, that polymer chains fully align under large deformations is shown to be inaccurate.

Upon removal of the external load, the melting of the crystallites begins [81]. In the fully relaxed state equal to complete unloading, all crystallites are completely dissolved [76]. The onset strain for crystallization during loading ε_{cs}, and the strain at which melting begins during unloading ε_{ms}, and the strain corresponding to the completion of melting ε_{mf} differ, following the relationship: $\varepsilon_{mf} < \varepsilon_{cs} < \varepsilon_{ms}$ [38]. However, the strain conditions under which crystallization is fully completed cannot be defined, as they depend on strain, strain rate, and the duration of deformation. As an example, when a NR specimen is subjected to uniaxial tensile load up to 500 % (ε_{max}), the onset of SIC, ε_{cs} is reported at 330 % and upon load removal, the crystallites completely melt at ε_{mf}, which equals 220 % [78]. Although the value of ε_{ms} is not explicitly mentioned, it must lie between ε_{mf} and ε_{max}. The authors report a maximum degree of crystallinity of 14 % at a maximum strain of 500 %. In Figure 5, the degree of crystallinity remains constant under a maintained maximum strain, likely due to the low strain rate of 4.2×10^{-3} s^{-1}, indicating that the maximum crystallinity is already reached during the mechanical loading process. Under rapid, quasi-adiabatic mechanical loading, an increase in the degree of crystallinity is to be expected, as explained in the following section.

2.4.1 Time and Temperature Dependency

Based on the findings of [79], approximately 50 % of the crystallization process, specifically the formation of crystallites, is completed within 5 ms. These findings are obtained from a rapid tensile test with a deformation time of 10 ms and a maximum strain of 400 %, performed on a cross-linked NR specimen. The remaining 50 % of the process takes place under constant maximum strain, either completing within the following 60 seconds or showing only minimal changes. Therefore, the degree of crystallinity continues to increase over time when the material is held at a constant maximum strain [37,38,79,81,82]. In Figure 6, the degree of crystallinity as a function of the holding time at maximum strain is shown for different maximum strains,

measured on a cross-linked NR specimen stretched at room temperature. The strain is applied rapidly, reaching the maximum deformation within less than 10 ms, and can therefore be approximated as a Heaviside step function. The short-term behavior shown in Figure 6 (b), occurring within less than 5 seconds, is relevant for elastocaloric cooling applications due to the cyclic nature of mechanical loading. After load removal, the melting process of induced crystallites is rapidly completed within a time frame of less than 10 ms, resulting in the disappearance of the crystallites [79]. This indicates that the rates of energy storage and release differ between crystallization formation and the melting processes.

To further evaluate SIC and its dynamic behavior, two different tests are conducted. A static test up to a strain of 365 % (above the SIC onset), held at the maximum strain for 5 minutes, serves as a reference due to the assumed equilibrium conditions. In the first dynamic test, the applied strain ranges from 0 to 365 %, while in the second dynamic test, the strain varies between 290 and 365 %. It has been reported that the degree of SIC is lowest in the first dynamic test, and higher in the second, as the crystallites do not fully melt between cycles. However, the degree of crystallization in both dynamic tests remains lower than that observed under static equilibrium conditions [79].

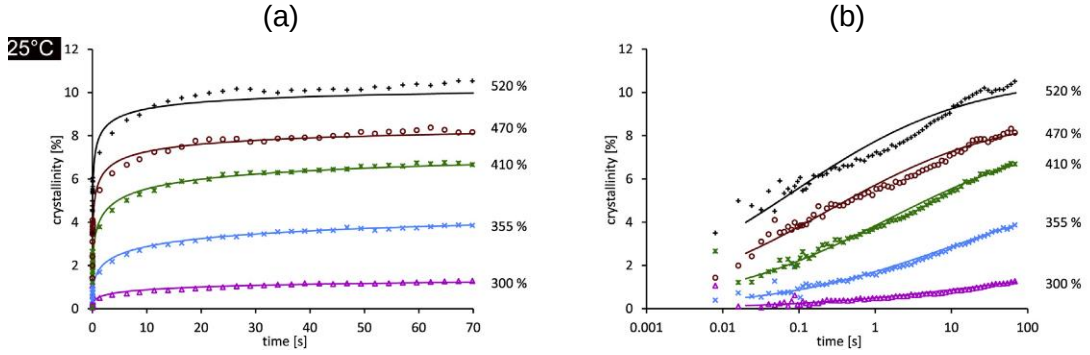

Figure 6: Evolution of the crystallinity index for different maximum strains as a function of time. The time corresponds to the holding period under a constant maximum strain. Starting from the undeformed state, a NR specimen is subjected to the maximum uniaxial tensile strain at t = 0 s. This strain is applied as a Heaviside step function within less than 10 ms. (a) Linear plot and (b) semi-logarithmic time plot. Short-term behavior (less than 5 s) is relevant for elastocaloric cooling due to cyclic mechanical loading. Adapted with permission from [37].

Since the quantitative influence of SIC on the elastocaloric temperature change is not yet fully understood, the hold time at maximum strain should be specified and considered for any meaningful comparison of reported temperature change values. This is particularly important, as it has been reported that the degree of crystallinity can change significantly within just a few seconds, which directly impacts the operating mode of elastocaloric cooling devices based on NR materials. Moreover, it should be noted that the degree of crystallinity, and consequently the elastocaloric temperature change, may be reduced during dynamic cycling.

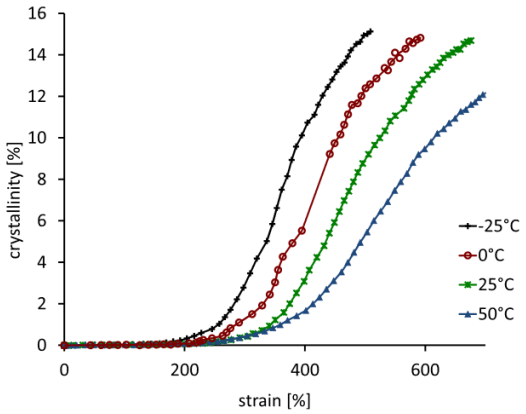

Figure 7: Evolution of the crystallinity index as a function of the applied maximum strain for the corresponding discrete ambient temperatures. Reproduced with permission from [37].

Besides the time-dependent behavior, the degree of crystallinity, and therefore the crystallinity index, is also influenced by the ambient temperature [30,37,38]. In Figure 7, the evolution of the crystallinity index as a function of the applied maximum strain and for different ambient temperatures is shown. As the temperature decreases, the onset of crystallization occurs at lower strains, and the crystallinity at a given strain increases almost linearly with strain [37]. For example, at 25°C, crystallization begins at approximately 300 % strain and the maximum crystallinity is around 15 %. These results are in qualitative agreement with earlier literature reports [30,38]. No SIC is observed at temperatures above 70 °C, as evidenced by the absence of a hysteresis loop in the stress-strain response of a NR specimen at 72 °C [83].

2.4.1.1 Temperature-induced Crystallization

When considering crystallization in NR, it is important to distinguish between strain-induced crystallization (SIC) and temperature-induced crystallization (TIC) [84]. This phenomenon is occasionally referred to in the literature as cold crystallization [85,86] or thermal quiescent crystallization to highlight the unstrained state [72]. NR can become crystalline either through straining at room temperature (SIC) or through exposure to low temperatures without the application of strain (TIC), typically occurring at or below 0°C [40]. TIC is most prominent around -25°C, where NR undergoes crystallization over the course of several hours [87,88]. A molecular-level interpretation of SIC, analogous to the well-established nucleation and growth models for TIC, is still lacking [89]. Furthermore, there is no consensus regarding the structure of SIC crystallites [90].

2.4.2 Macroscopic Mechanical Response

The macroscopic measurable responses induced by SIC are the temperature change and the stress-strain behavior [43,81]. In the stress-strain diagram, the loading and unloading process of a vulcanized NR specimen forms a hysteresis loop.

This means that the unloading curve does not coincide with the loading curve which is characterized by a lower stress level. SIC can lead to an increase in stress during the mechanical load process, this effect is referred to as stress hardening [38] The pioneering work on this subject was first documented by [25]. During unloading, the stress is significantly lower than during loading, although the degree of crystallinity is higher in the retraction phase [76,81]. Paradoxically, SIC can also cause a decrease in stress under constant mechanical load, this effect is called stress relaxation [63,81,91]. This is attributed to the alignment of molecular chains within the crystallites, which adopt an extended conformation oriented along the direction of the applied strain [25,63,92]. In simpler terms, the molecular chains become further disentangled and thus appear more stretched, resulting in a stress release. Suggesting that the chains are stretched within the crystallites, while the remaining amorphous regions are relaxed [76], similar to relaxed regions around crack tips due to SIC in NR [30]. However, even in the case of cross-linked rubber, there are contributions to stress relaxation not only from SIC but also from plastic flow, namely the mutual slippage of molecular chains, which is non-reversible and characterized by permanent plastic deformation [63]. Plastic deformation can be quantified in the unstrained state by the increase in length, which increases the initial length relative to specimens without a prior mechanical load history.

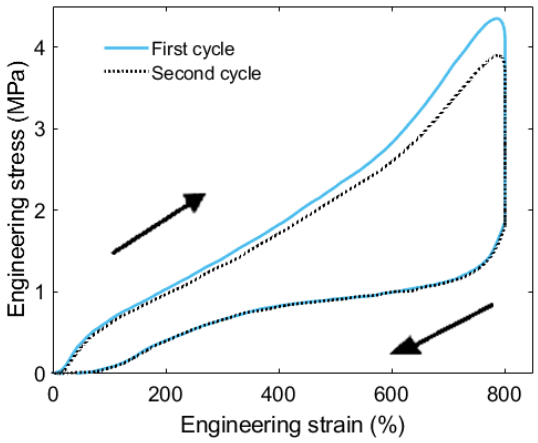

Figure 8: Stress-strain characteristics of an NR-based material. The first cycle exhibits the Mullins effect, while the vertical line is attributed to stress relaxation. Uniaxial mechanical loading and unloading are indicated by the black arrow.

In subsequent cycles under similar loading conditions, lower forces are required to achieve the same deformation compared to the initial cycle. This phenomenon is known as stress softening or the Mullins effect [93]. A typical stress-strain curve with hysteresis behavior and the Mullins effect is exemplified in Figure 8. To date, there is no general agreement on either the physical origin or the mechanical modeling of this effect [94]. However, the origin of the hysteresis is known. It arises from the process of SIC, involving the formation and transformation of crystallization [81]. The formation of the hysteresis loop is caused by a change in the microstructure of the material and is not attributed to intrinsic or thermal dissipation [24]. Intrinsic dissipation involves irreversible processes such as mechanical destruction and viscous flow [95]. Therefore,

in the case of NR, the mechanical energy used to deform the material is primarily stored elastically [96]. The energy storage occurs in the amorphous phase through chain alignment and the accumulation of topological constraints in the vicinity of crystallites [24]. After storage, the energy is released by crystallite melting. At this point, the differing kinetics of crystallite formation and melting should be noted [38,81].

2.4.3 Macroscopic Thermal Response

Under the assumption of an ideal elastomer, polymer chains are able to rotate freely, and the internal energy, U does not vary with molecular conformation [97]. Therefore, the internal energy of rubber remains nearly constant during deformation ($\Delta U = 0$) [69,70]. As a result, the applied mechanical work is directly released as heat, $\Delta W = \Delta Q$, in accordance with the first law of thermodynamics, as given in Equation 2-2 [98]. Conversely, during retraction, mechanical work is recovered at the expense of the absorbed heat.

$$\Delta U = \Delta Q - \Delta W \qquad \textbf{2-2}$$

In contrast to conventional entropy-elastic materials, NR undergoes SIC under high deformation. The SIC contributes additionally to the cooling of the material during mechanical load removal, as the latent heat Δh_f required for melting is absorbed from the surrounding [25,99]. Altogether, the temperature decrease upon unloading corresponds to the combined reversible effects of the latent heat and the mechanical work, and therefore correlates to the sum of Δh_f and ΔW [98]. The reverse effect of NR, with the specimen length decreasing upon heating and increasing upon cooling, was first reported in the year 1806 by Gough and later used as an indirect means to study the elastocaloric effect [35,100]. While these early studies relied on indirect observation of the elastocaloric response, recent research has focused on direct experimental methods. In these approaches, temperature changes are measured during mechanical loading and unloading, primarily under uniaxial tensile loading and using infrared thermography. An overview of the reversible elastocaloric temperature changes based on polymer materials reported in the literature is provided in Chapter 2.5.

2.4.4 Synthetic Rubber

NR stands out as the primary elastomer that undergoes SIC. In addition to NR, the SIC has also been observed in chloroprene rubber (CR), also known as neoprene [101–104], as well as in polybutadiene rubber (BR) and polyisobutylene-isoprene rubber (IIR), also known as butyl rubber [105]. The synthetic analog of NR, polyisoprene rubber (IR), also exhibits SIC [44]. However, it has been reported that crystallization in synthetic cis-1,4-polyisoprene rubber (IR)-based materials occurs more slowly than in crosslinked NR, and the overall degree of crystallization is lower [63,92], for both SIC and TIC. These findings are based on comparisons between NR and IR of identical composition, which also revealed that the onset of SIC is shifted to higher strain levels. While NR specimens begins to crystallize at around 300 % strain, IR must be stretched to

approximately 400 % to initiate SIC [92]. The observed differences are attributed to polymer chain defects in the synthetic IR. The reduced crystallization rate of IR is attributed to minor structural irregularities of approximately 1.4 to 2 % in its cis-isoprene chains, which consequently manifest macroscopically as lower tensile and tear strength at high strains [85,87]. Specifically, the cis-1,4 content is higher in NR and close to 100 %, and the ability to crystallize correlates with the average length of uninterrupted cis-configured segments in the polymer backbone [85]. Additionally, the authors report that deproteinizing the naturally present proteins in NR reduces the crystallization rate, likely by decreasing nucleation sites. The higher degree of crystallization in NR is due to a sterically pure polymer backbone, characterized by the absence of head-head and tail-tail structures and the presence of the desired head-tail structures [106,107].

Larger crystallite sizes upon deformation are reported in vulcanized natural rubber latex. This comparison is conducted at identical total cross-linking densities and is attributed to a more homogeneous network with higher entanglement compared to vulcanized NR [59]. In summary, the superior performance characteristics of NR products remain difficult to replicate using synthetic IR, despite structural similarities.

2.4.5 Filler

Carbon black and precipitated silica, as the primary reinforcing fillers, contribute to a substantial increase in tensile strength and improve abrasion resistance, tear strength, and damping properties [108]. The filler content is expressed in parts per hundred rubber (phr) by weight, meaning the rubber matrix is defined as 100 phr [58]. For example, if 10 g of carbon black is added to 100 g of crosslinked natural rubber, the resulting rubber contains 10 phr carbon black. It is well established in the literature that the presence of reinforcing fillers shifts the onset of SIC in NR to lower strain levels [90]. For example, for 20 phr carbon black (HS-HAF, Diablack N339) with an average particle size of 26-30 nm, the SIC onset shifts to 260 %, and for 40 phr to 230 %, compared to 300 % in unfilled NR [41].

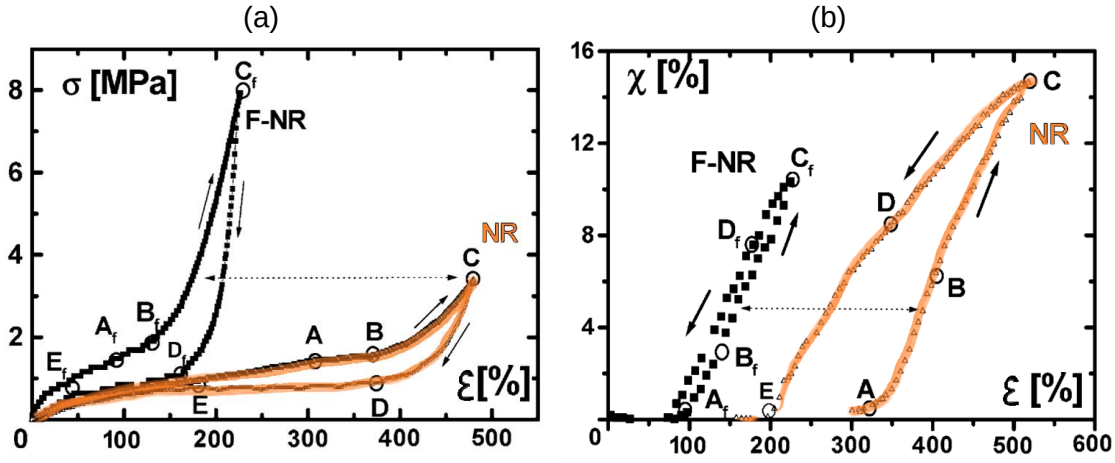

Figure 9: (a) Stress-strain curves of unfilled natural rubber (NR) and NR filled with 50 phr carbon black (N375) (F-NR) at different maximum strains, and the corresponding (b) crystallinity degree measured at room temperature (22 °C). The mechanical loading and unloading direction in (a) is clockwise, while in (b) it is counterclockwise due to the higher degree of crystallinity during retraction. Adapted with permission from [109].

A comparison of the stress-strain behavior and the corresponding degree of crystallinity for unfilled natural rubber (NR) and NR filled with 50 phr carbon black (N375) (F-NR) is presented in Figure 9 (a) and (b), respectively [109]. The filled NR specimen exhibits an earlier SIC onset and increased stiffness. In Figure 9 (a), mechanical loading and unloading proceed in a clockwise direction, whereas in Figure 9 (b), a counterclockwise direction is observed due to the higher degree of crystallinity during retraction. A gradual decrease is also reported by [72], where the onset is even below 100 % for NR filled with 60 phr of N234 carbon black, while the unfilled NR also exhibits an onset at 300 %. This shift in onset is attributed to locally increased strain, even though the overall macroscopic strain remains low [72]. There is broad consensus in the literature that the SIC onset shifts to lower strains in filled rubbers. However, the influence of fillers on the rate of crystallization remains less clearly defined. No studies report an increased crystallization rate or a higher maximum crystallinity in filled systems [41,83,109–112].

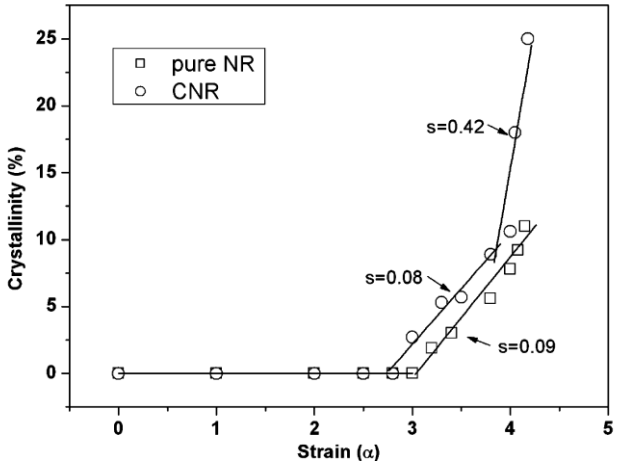

Figure 10: Degree of crystallinity as a function of the applied tensile strain for a 2 phr MWCNT-filled NR specimen (CNR) and an unfilled NR (pure NR) specimen. The filled specimen exhibits a dual crystallization mechanism and a shifted SIC onset to lower strains. Reproduced with permission [113].

Besides the well-established and widely used micron-sized carbon black filler, recent studies have reported the benefits of inorganic nanofillers [114]. Numerous studies have shown that the addition of nanoparticles significantly enhances SIC in NR [115–121]. For example, anisotropic nano clay fillers shift the SIC onset to lower strains and improve both the rate and the degree of crystallization under deformation in NR [115,116]. In addition, the planar structure of clay promotes the parallel alignment of polymer chains, thereby enhancing SIC [122]. More specifically, clay-filled NR exhibits an SIC onset at a strain of approximately 120 %, thus initiating is about 150 % earlier than in unfilled NR specimens under uniaxial deformation. Furthermore, after a strain of approximately 250 %, the slope of the degree of crystallization versus strain increases [119]. Therefore, a dual crystallization mechanism is assumed, with the first stage attributed to the orientation of clay layers at small strains, and the second to the conventional crystallization mechanism of unfilled NR [115,116,119]. The dual crystallization mechanism has also been reported in carbon nanotube-filled NR specimens. In Figure 10, the degree of crystallinity as a function of the applied strain is shown for the filled and unfilled NR specimens. Specifically, NR specimens filled with 2 phr of purified multiwalled carbon nanotubes (MWCNTs) with a diameter of 20 nm show a lower SIC onset strain, a higher degree of crystallinity, and increased tensile strength compared to unfilled NR specimens [113].

2.4.6 Crosslink Density

Crosslink density denotes the concentration of crosslink points within a polymer network, quantified as the number of crosslinks per unit volume [25]. Importantly, the number of monomer units between crosslinks decreases as the crosslink density increases, indicating that these two parameters are inversely related [25]. An increase in crosslink density typically enhances tensile strength by restricting chain mobility. However, excessive crosslinking can lead to brittleness and ultimately reduce strength [46,76]. In one study, crosslink density is increased by raising the amount of sulfur used in the vulcanization process, which reduced the number of monomer

units between crosslinks [38]. Another approach to varying the crosslink density in carbon-black-filled samples involves changing the concentration of the accelerator (CBS) [110]. There is a general agreement that the onset strain for SIC in sulfur-crosslinked natural rubber is largely independent of the crosslink density [38,76,123]. However, for highly crosslinked NR (from 1.61 to 1.95×10^4 molcm^{-3}), SIC is reported to decrease with increasing crosslink density [124]. In contrast, for low crosslink densities, there is no clear consensus, and further investigations are required. While [38] report that the degree of crystallinity increases with decreasing crosslink density, [124] observed the opposite trend, suggesting that below the optimum of 1.2×10^4 molcm^{-3}, the crystallization rate decreases as crosslink density decreases. Although several studies have investigated the influence of crosslink density on strain-induced crystallization (SIC) [38,76,110,124,125], it is still not fully understood. This complexity is further increased by the non-uniform distribution of crosslink density within a specimen and the inherent variation in polymer chain lengths, which makes establishing a clear relationship between network structure and SIC challenging in practice.

2.5 Elastocaloric Temperature Changes in Elastomer-Based Materials

The performance of elastocaloric cooling devices is strongly dependent on the properties of the refrigerant material, as it directly governs the achievable temperature change, cooling power, and efficiency. Among various classes of materials, elastomers have emerged as promising candidates for solid-state cooling applications. This chapter provides a comprehensive overview of elastocaloric temperature changes reported in the literature for elastomer-based materials. The focus lies primarily on natural rubber (NR) and thermoplastic triblock copolymers, such as styrene ethylene butylene styrene (SEBS), which have demonstrated significant potential for reversible, entropy-driven temperature changes under mechanical loading and unloading. By summarizing and comparing these reported temperature changes, the chapter aims to highlight the material-specific factors influencing elastocaloric performance and to provide a basis for evaluating their suitability in future device design and optimization.

An overview of the reported reversible elastocaloric temperature changes upon unloading ΔT_c and the peak-to-peak temperature span between loading and unloading ΔT_{ad} is presented in Table 1. Test conditions, including the maximum applied uniaxial tensile strain and the ambient temperature during testing, are specified for each reference. For one study, only the temperature change after loading is available, this value is indicated by *. In addition, two studies report results obtained under non-uniaxial deformation. These are labeled with ** and ***, corresponding to twisted and nearly biaxial deformation of a fiber and a membrane, respectively. For comparison, the reported elongation values are converted to strain to ensure consistency. An elongation of 1 corresponds to 0 % strain, while, for example, an elongation of 6 corresponds to a strain of 500 %. In addition, if not explicitly stated, the strain rate is calculated based on the strain range and the duration of deformation. As the distinction between engineering strain and

true strain is not specified in the referenced studies, the term “strain” is used as originally reported. This clarification is provided for consistency, as the present work refers to engineering strain throughout.

Table 1: Overview of reported reversible elastocaloric temperature change after unloading ΔT_c and a peak-to-peak temperature span ΔT_{ad} (from loading to unloading) for the corresponding maximum strain ε_{max} and room temperature values T_{RT} of different elastomer specimen materials. *Value obtained from the loading curve. Non-uniaxial deformation is indicated by ** and *, which correspond to twisting and inflation, respectively. Legend: natural rubber (NR), ground tire rubber (GTR), thermoplastic polyurethane (TPU), liquid crystal elastomers (LCE), shape memory polymer (SMP), fluoropolymer polyvinylidene fluoride (PVDF), styrene ethylene butylene styrene (SEBS) and graphene nanoplatelet (GNP).**

Specimen Material	ΔT_c (K)	ΔT_{ad} (K)	ε_{max} (%)	T_{RT} (°C)	Reference
NR	-3.7	7.0	500	23	[19]
NR	-10.3	20.3	700	23	[19]
NR	-8.7	14.2	600	23	[100]
NR	-9.4	17.4	500	23	[82]
NR	-12.2	-	600	23	[126]
NR	-19.1	-	**	23	[126]
NR	-41.3	68.0	**	-20	[127]
NR	-16.8	>23.0	***	22	[31]
NR + GTR	+6.5*	-	500	23	[21]
TPU	-7.7	-	400	23	[128]
LCE	-0.35	-	75	67	[129]
SMP	-2.8	5.6	300	70	[130]
SMP + carbon fabric	-1.3	2.3	50	70	[131]
PVDF	-1.8	-	10	25	[132]
P(VDF-TrFE-CTFE)	-2.15	5.0	12	27	[133]
SEBS	-15.3	29.8	600	26	[134]
SEBS + GNS	-18.0	-	600	25	[135]

A reversible elastocaloric temperature change of -8.7 K upon unloading is observed for a NR specimen with a thickness of 100 µm, while a peak-to-peak temperature span of 14.2 K is detected [100]. The temperature change is measured under uniaxial tensile loading at a strain rate of 3.0 s^{-1}, where the maximum strain of 600 % is maintained for 20 seconds. The best reported result in the literature for uniaxial tensile deformation shows an elastocaloric temperature change of 9.3 K after unloading from a maximum strain of 500 % [82], the values are provided in the supplementary information. Loading and unloading are performed at a strain rate of 10 s^{-1}, followed by a holding time of 200 s. The specimen, with a crosslink density close to 1.5×10^{-4} $molcm^{-3}$ and a thickness of 1 mm, experiences a resulting stress of approximately 2.5 MPa. In addition, the authors evaluate a synthetic polyisoprene rubber (IR) specimen with the same thickness. For a strain range of 250 to 500 %, a temperature change of less than -2.5 K

after unloading is reported, which is nearly half of the value observed for the NR specimen. This difference is attributed to the lower ability of IR to crystallize under deformation [63,92].

As an alternative to foil or film specimens, NR fibers are subjected to uniaxial tensile deformation of up to 600 % strain, resulting in a temperature decrease of -12.2 K [126]. Even greater temperature changes are reported for twisted fibers. When unplying seven-ply NR fibers with a diameter of 2.2 mm, a maximum temperature change of -19.1 K is reported. The average temperature change over the fiber surface is -14.4 K. While these results are obtained at room temperature, at temperatures of -20 °C, even higher temperature changes upon unloading, up to -41.3 K, are reported for a twisted and stretched cylindrical NR specimen with a diameter of 5 mm [127]. The high peak-to-peak temperature span of 68.0 K is attributed to both the presence of SIC and temperature-induced crystallization (TIC). The latter is introduced in Subchapter 2.4.1.1.

In addition to the non-uniaxial strain applied by twisting fibers, [31] present a rapid inflation-deflation experiment involving a NR membrane. The membrane with a thickness of 420 µm is almost biaxially stretched through balloon inflation and then adiabatically contracted within approximately 100 ms. A maximum temperature change of approximately -16.8 K is reported following deflation, based on data presented in Fig. 2e of [31]. The corresponding balloon volume is indicated to be between 200 and 220 cm^3.

An innovative and sustainable approach demonstrates a method for giving waste tires a second life by incorporating ground tire rubber (GTR) particles into NR, which is then vulcanized using a hot press. Upon applying a uniaxial tensile strain of up to 500 % at a strain rate of 0.9 s^{-1} and maintaining the strain for 60 s, a temperature change of -6.5 K during loading is reported [21].

In addition to NR, the elastocaloric effect is also observed in thermoplastic polyurethane (TPU) specimens. Under uniaxial tensile testing up to a strain of 400 %, the TPU specimen with a thickness of 0.2 mm exhibits a temperature change of -7.7 K upon unloading [128]. The strain rate is reported as 160 s^{-1}, with a holding time of 150 s. During cyclic operation over 5000 cycles at a frequency of 0.2 Hz, the authors report a peak-to-peak temperature span decrease of approximately 10 % per decade. This suggests that TPU-based specimens are likely not suitable for elastocaloric cooling applications, as such systems require high cyclic stability. Moreover, thermoplastic polyurethane (TPU) can be processed by additive 3D printing, enabling the fabrication of complex geometries. In the study by [136], 3D-printed TPU specimens based on Ultimaker TPU95A filament are evaluated. The additively manufactured specimens exhibit a peak-to-peak temperature span of 17.8 K for the first load cycle under uniaxial tensile loading at a strain rate of 5 s^{-1} and a maximum strain of 500 %. After ten cycles, the temperature span decreases to less than 7 K, showing a similar trend as reported by [128].

A minor elastocaloric temperature change has been observed, for example, in liquid crystal elastomers (LCEs). During the phase transition from the isotropic to the nematic state, which refers to the reorientation of polymer molecules from a disordered to an ordered, directionally aligned state, a temperature change of -0.35 K can be achieved at a strain of 75 % and an ambient temperature of 67 °C [129]. Due to their ability to elongate up to 400 % an elastocaloric effect of

several kelvin is expected [137]. In addition to LCEs, shape memory polymers (SMPs) also exhibit the elastocaloric effect [138]. Specifically, cross-linked poly(cyclooctene) also named as PCO specimens with a thickness of 1 mm are subjected to uniaxial tensile loading at a strain rate of 0.05 s^{-1}, which corresponds to quasi-adiabatic conditions. The PCO-based specimen undergoes plastic deformation of approximately 70 %. However, within the reversible regime, a temperature change of -2.8 K upon unloading from a maximum engineering strain of 300 % is reported [130]. The authors report a further improvement by incorporating carbon fibers. In specimens based on a composite material with a shape memory polymer (SMP) matrix reinforced with carbon fabric, a reversible strain of 50 % results in an elastocaloric temperature change of -1.3 K, representing a gain of 1.1 K compared to the pure SMP [131]. In the crosslinked fluoropolymer polyvinylidene fluoride (PVDF), an elastocaloric temperature change of -1.8 K can be observed at an ambient temperature of 25 °C and a strain of approximately 10 %, using a tensile-loaded film with a thickness of 0.3 mm and a resulting stress of 15 MPa [132]. Another polymer based on PVDF exhibits an even higher elastocaloric temperature change. A terpolymer is the result of a polymerization involving three different monomers. The terpolymer poly(vinylidene fluoride-trifluoroethylene-chlorotrifluoroethylene) or (PVDF-TrFE-CTFE) demonstrates an elastocaloric temperature change of -2.15 K upon unloading from a strain of 12 %, which is attributed to its entropic elasticity [133]. The measurement is performed on uniaxially stretched films with a thickness of 10 µm at a strain rate of 20 s^{-1}.

The highest reported non-NR-based temperature change of -15.3 K upon loading is measured in a triblock polymer specimen based on poly(styrene-b-ethylene-co-butylene-b-styrene), abbreviated as SEBS [134]. The SEBS specimen with high molecular chain-length uniformity, with a thickness of 0.4 mm, is uniaxially deformed up to a strain of 600 % at a strain rate of at least 15 s^{-1}. A peak-to-peak temperature span of 29.8 K is reported. This result can be improved by manipulating the ethyl side groups within the SEBS triblock polymer. This improvement is claimed to result from a reduced content of ethyl side groups, which otherwise hinder internal rotation. The increased structural regularity promotes crystallization, and the resulting larger reversible conformational adjustments (spatial arrangement) in the molecular chains lead to a temperature change of -16.3 K upon loading [139]. Furthermore, the authors report another enhancement by incorporating graphene nanoplatelets (GNS) into the SEBS polymer matrix. A maximum temperature change of -18.0 K upon unloading is observed for specimens with 1 wt.% GNS [135]. According to the authors, this improvement is attributed to the aggregation of elastic chains caused by shearing the interlaminar molecular chains, which is supported by the presence of the nanofillers and is believed to promote entropy changes in the elastocaloric polymer. The addition of 1 wt.% GNS also leads to a slight improvement in thermal conductivity, increasing from 0.17 to 0.20 $Wm^{-1}K^{-1}$ compared to the unfilled material.

To summarize, SEBS- and NR-based specimens exhibit the highest elastocaloric temperature responses among the reported elastomers. The largest temperature change upon unloading at room temperature, -19.1 K, is reported for twisted seven-ply NR fibers [126]. The second highest value, -16.8 K, is also reported under non-uniaxial loading conditions and corresponds to a NR membrane. Among specimens tested under predominantly uniaxial tensile loading, the highest

temperature change of -18.0 K is observed for SEBS specimens filled with graphene nanoplatelets (GNS). In [82] a temperature change upon unloading of -9.4 K at 500 % strain for a NR specimen is reported. Therefore, this can be directly compared with this work pre-published in [19]. For the same test conditions, minor results of -3.7 K are measured with another NR-based specimen. These differences highlight that not every NR-based specimen exhibits the same elastocaloric response, emphasizing the importance of tuning material parameters even within NR-based refrigerants. The fact that the elastocaloric temperature change during loading differs from that during unloading can be attributed to the distinct kinetic mechanisms of crystallite formation and melting [100,101].

2.6 Fatigue Resistance and Aging

For natural rubber, the occurrence of SIC correlates directly with its fatigue resistance [140]. A comprehensive review on mechanical fatigue, addressing the initiation and propagation of cracks due to cyclic loading in rubber components, is provided in [141]. For elastocaloric cooling applications, the mechanical fatigue resistance of the refrigerant under cyclic operation is of primary interest. The advantage of an increased minimum strain on the fatigue life of rubber is first mentioned by [142,143]. Cyclic tests under tensile load conditions with more than 10^7 cycles [144] are reported. In addition, by cycling within the SIC strain regimes between 200 and 500 % strain, 1.7×10^5 crack-free cycles under uniaxial tensile load are observed [145]. SIC in NR acts as a reinforcement mechanism and significantly increases fracture resistance [29]. The formation and growth of cracks are prevented by the development of semicrystalline zones surrounding the crack tip [30].

Besides the load history, environmental effects also influence fatigue life, such as oxygen, which diffuses into rubber products and leads to embrittlement by reducing elastic properties and crack growth resistance, while also inducing chemical reactions known as oxidative aging [141]. The exposure to ultraviolet (UV) light leads to chain scission and subsequent recombination, resulting in crack formation and ultimately failure, a mechanism that similarly applies to the influence of ozone [46,146]. Furthermore, crack growth in NR products initiates earlier when exposed to oxygen compared to vacuum conditions [147]. Quantitative analysis reveals a significant reduction in tensile strength and retention of elongation after 120 hours of UV radiation exposure at 40 °C (Zhou et al., 2023). The changes in surface morphology after 24, 48, and 72 hours and the corresponding tensile strength are presented in Figure 11 (a) and (b), respectively. These processes, which can ultimately lead to the complete degradation of the rubber material, are referred to as aging. Mechanical, especially dynamic, loading accelerates these aging processes [46].

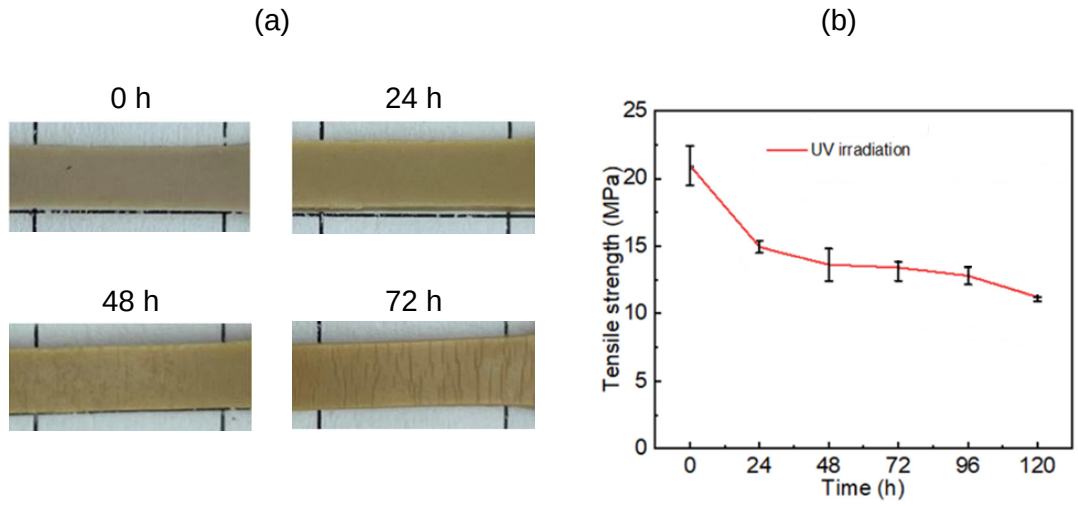

Figure 11: (a) Changes in the surface morphology of the NR specimen under UV irradiation and (b) the corresponding tensile strength. Adapted from [148] licensed under CC BY 4.0.

At the device level, aging effects might be mitigated by housing the elastocaloric cooling unit to shield it from UV radiation, thereby extending component lifetime, while optimized rubber compounding further reduces environmental degradation and prevents premature failure. Moreover, performing cyclic deformation of NR under vacuum conditions may prolong operational life by minimizing oxidative aging. Therefore, the material of the refrigerant plays a crucial role in enhancing mechanical durability under aging conditions. The following chapter presents the elastocaloric cooling devices reported in the literature, discussing their working principles and focusing on their performance and lifetime aspects.

3 State of the Art of Elastocaloric Cooling Devices

3.1 Caloric Cooling

Concerns regarding the limitations of conventional cooling technologies have led to a growing interest in alternative approaches. These alternatives aim to provide enhanced energy efficiency, compactness, and lower environmental impact, positioning them as promising candidates to gradually replace the widely used vapor-compression technology [149]. A particularly promising area of research concentrates on caloric cooling technologies, which utilize caloric effects linked to solid-to-solid phase transitions [150]. In caloric materials, applying and removing an external field induces a reversible entropy change, which leads to the corresponding caloric effect [151]. If the field change is performed under adiabatic conditions, the caloric effect manifests as a change in the temperature of the caloric material [152]. In contrast, under isothermal conditions the effect manifests as an isothermal entropy change in the material. The external field can be a magnetic, electric, or stress field, or a combination thereof. Depending on the type of field, the caloric effect can be categorized as the magnetocaloric effect, electrocaloric effect or mechanocaloric effect. The mechanocaloric effect comprises both the elastocaloric and barocaloric effects [153].

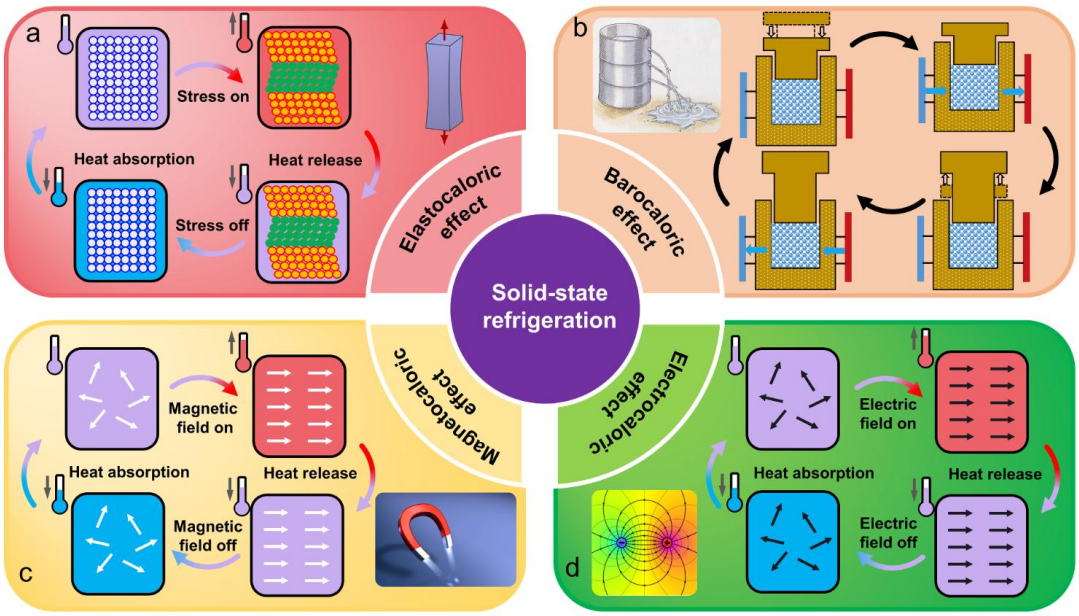

Figure 12: Schematic of solid-state cooling technologies based on (a) elastocaloric, (b) barocaloric, (c) magnetocaloric and (d) electrocaloric cooling. Reproduced with permission [154].

A change in the external magnetic field induces the magnetocaloric effect by causing the magnetic moments within the material to align [155,156]. Gadolinium, considered the benchmark

magnetocaloric material, exhibits an adiabatic temperature change at room temperature of up to 5.8 K for a magnetic field change of 2 T [157]. One of the main arguments against the commercialization of magnetocaloric cooling is the price of the magnetocaloric material and the magnet arrays as well as the large magnetic field required, which is due to the use of rare earth elements [158].

While in magnetocaloric materials the magnetic moments are aligned, the electrocaloric effect is achieved by aligning electric dipoles using electric fields [159]. In electrocaloric cooling, the breakdown of electrical insulation is a primary cause of failure and performance degradation [160]. An important milestone for electrocalorics is the development of a stack of films arranged as a multilayer capacitor [161]. The multilayer capacitor configurations based on lead scandium tantalat ceramic can achieve adiabatic temperature changes of up to 3.3 K under an applied electric field of 29.0 $V\mu m^{-1}$ [162]. However, the observed temperature changes remain lower than those achieved in materials exhibiting the elastocaloric effect.

The elastocaloric effect in elastomers is the oldest known caloric effect [35]. The elastocaloric effect is triggered by a uniaxial mechanical field [163]. The elastocaloric effect observed in elastomers such as NR, along with its origin and the resulting temperature changes, is discussed in detail in Chapter 2, as it is the subject of this work. In addition to elastomers, superelastic shape memory alloys (SMAs) also demonstrate the elastocaloric effect, although the underlying mechanism differs [164]. SMAs like NiTi alloys exhibit a reversible phase change between the crystallographic phases known as austenite and martensite in response to a change in the applied stress field [165].

The first-order, solid-solid phase transformation from a low-symmetry martensitic phase to a high-symmetry austenitic phase is diffusionless [166]. Under mechanical loading, latent heat is released, whereas during unloading, heat is absorbed. For NiTi-based alloys, it has been demonstrated that the elastocaloric temperature change is dependent on the alloy's composition [167]. For $Ni_{48.9}Ti_{51.1}$ wires subjected to a stress of 700 MPa and a strain of 6 %, loading induces a temperature increase of 25 K, while unloading results in a temperature decrease of 21 K, yielding a total adiabatic temperature change of 46 K [168]. The second mechanocaloric effect is the barocaloric effect.

The barocaloric effect arises when hydrostatic pressure is applied, leading to a change in volume. In NR-based materials, an adiabatic temperature change of approximately 25 K has been observed under a pressure of 390 MPa [169]. The barocaloric effect also occurs in magnetic shape memory alloys like FeRh [170] or electrocaloric ceramic materials like $BaTi_3$ [171]. Therefore, these materials exhibit more than one caloric effect, which leads to their classification as multicaloric materials [172–175].

Despite promising temperature changes, implementing barocaloric demonstrators remains challenging. This is primarily due to the difficulty of enabling spatial separation of the hot and cold heat flows while at the same time applying isostatic pressure changes under adiabatic conditions [22]. The application of uniaxial stress is technically less complex compared to

hydrostatic pressure, which necessitates uniform loading along all axes. For the elastocaloric effect, uniaxial loading and heat exchange can be spatially decoupled, thereby simplifying device design. Based on this advantage, NR-based materials are investigated in this work for its elastocaloric properties.

For device realization, the caloric materials must be subjected to cyclic loading and subsequent field removal under the corresponding external field. In Figure 12, a schematic overview of solid-state refrigeration technologies based on caloric materials is presented. In practical caloric cooling and heat-pumping devices, the inverse Brayton cycle is the most commonly employed [160]. Other thermodynamic processes can also be employed for caloric cooling [176]. Since the cycle is driven not by pressure but by cyclic variation of the external field, it constitutes an inverse Brayton-analog cycle.

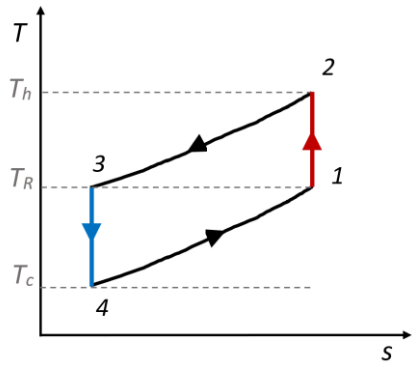

Figure 13: Temperature-entropy (T-s) diagram of the reversed Brayton cycle, serving as a reference framework for analyzing the caloric cooling process. The idealized elastocaloric cooling cycle starts with adiabatic loading 1→2, followed by heat transfer to the heat sink from the refrigerant at constant strain 2→3. Adiabatic unloading 3→4, after which heat is transferred from the heat source to the refrigerant at constant strain 4→1. Legend: room temperature T_R, temperature after adiabatic loading T_h, temperature after adiabatic unloading T_c.

The inverse Brayton cycle is schematically represented in the temperature-entropy (T-s) diagram shown in Figure 13. The idealized cycle is described for elastocaloric cooling based on elastomers. Starting at room temperature (T_R) and in the absence of an applied field, the elastocaloric material serving as the refrigerant is subjected to mechanical loading under adiabatic conditions (1→2). In detail, the loading process is isentropic, resulting in a temperature increase of the refrigerant (T_h). In the subsequent step, heat transfer under constant strain is carried out (2→3). Ideally, the temperature of the refrigerant is restored to room temperature. After adiabatic load removal, the temperature of the refrigerant decreases from T_R to T_c (3→4). In the final step, heat is absorbed under zero strain, causing the temperature of the refrigerant to rise back to T_R (4→1). The load cycling can then be repeated. During the heat transfer steps (2→3) and (4→1), the hot and cold heat flows are selectively directed to a heat sink and a heat source, respectively. This enables the realization of heat-pumping and cooling applications.

3.2 Comparison of Elastocaloric Cooling Based on SMAs and Elastomers

So far, only six elastocaloric cooling devices based on elastomers have been reported [31–34,135,177], in addition to the three devices developed within this work [19,178]. At the start of this study, only two devices had been reported [31,32]. The rapid increase in publications over a short period highlights the relevance and growing interest in this field of research. An overview of the reported devices is provided in Figure 14. A detailed description of the devices is provided in the subsequent sections of this chapter. To facilitate comparison, the reported devices are categorized according to their heat transfer mechanism.

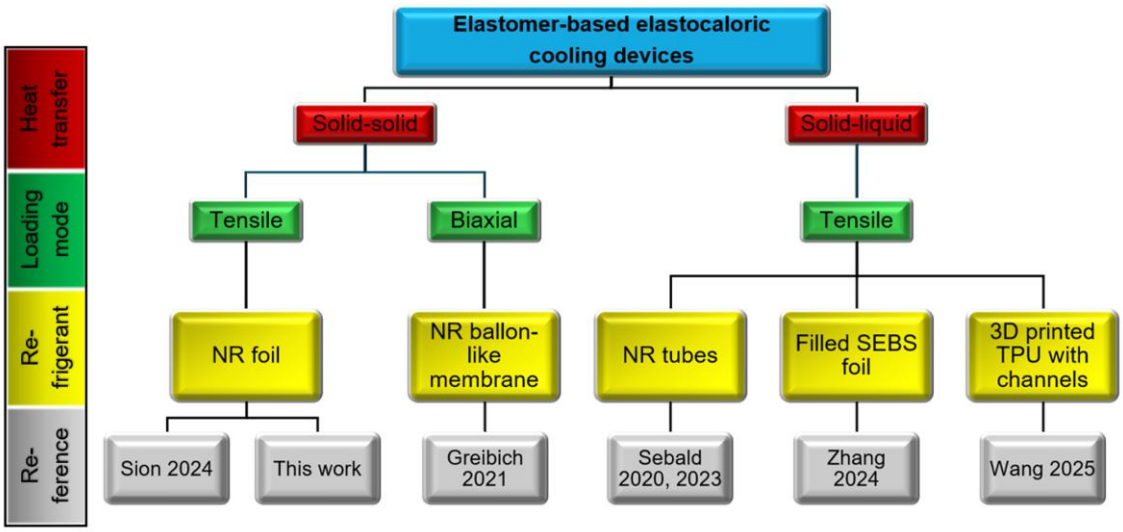

Figure 14: Overview of elastocaloric cooling devices based on elastomers, categorized by heat transfer mechanism, loading mode, refrigerant type and material, along with the corresponding references.

On the one hand, heat transfer is achieved through a solid-solid mechanism, and on the other hand through a solid-liquid mechanism. In both cases, the refrigerant (also referred to as the active material) is solid, with internal heat transfer occurring by conduction and limited by the material's thermal conductivity. In the solid-solid heat transfer mechanism, heat is rejected and absorbed from the refrigerant by a solid heat sink and source unit through mechanical contact. This mechanism, which is limited by the heat transfer resistance, is employed in the present work. In contrast, for the solid-liquid mechanism, a heat transfer fluid is employed to transfer heat to the hot and cold reservoirs, promoted by forced convection induced by the fluid flow.

Further categorization can be made based on the type of mechanical loading. To date, most devices are based on uniaxial tensile loading, with only one device employing nearly biaxial loading achieved through pneumatic expansion [31].

Although most devices are driven by tensile loading, the refrigerant types exhibit a wide spectrum. They range from balloon-like NR membranes and NR tubes to custom 3D-printed thermoplastic polyurethane (TPU) structures with fluid channels, and finally to foils.

In contrast to elastomer-based elastocalorics, a wide range of SMA-based cooling devices have been reported [154,179]. On the macroscale, fluid-based systems include wires operated in tension for air-conditioning applications [180], as well as tubes operated in compression [13,14,181,182]. Most recently, the combination of operation in compression and tailored material transition temperatures to extend the operating window has been demonstrated. Following this approach, the highest cooling power of over one kilowatt and temperature spans of 75 K reported for elastocaloric cooling devices have been achieved [13,14]. On the miniature scale, a film-based device employing solid-solid heat transfer and operating in tension has achieved a high specific cooling power of 19 Wg^{-1} [17]. Furthermore, cascaded systems, also operating in tension, have been developed to address the limitations imposed by the material's temperature range [16]. Therefore, if the adiabatic temperature change in the caloric materials is smaller than the required temperature span of the system, methods such as active regeneration or cascading can be employed [155]. Within cascading, multiple refrigerants are thermally connected in series, generating a temperature gradient within the system, while heat transfer is achieved through solid-solid mechanical contact [16]. Due to the gradient, refrigerants are pre-heated and pre-cooled, so that individual cycling occurs at different starting temperatures. In the figure, the corresponding T-s diagram is shown. Due to the gradient, refrigerants are pre-heated and pre-cooled, so that each cycle begins at a different starting temperature. The corresponding T-s diagram is shown in Figure 15. In contrast, the term active regeneration is typically associated with fluid-based systems [183]. Similarly, along the regenerator, each element performs its own thermodynamic cycle at a slightly different temperature [184]. These two concepts can be summarized under the framework of heat recovery.

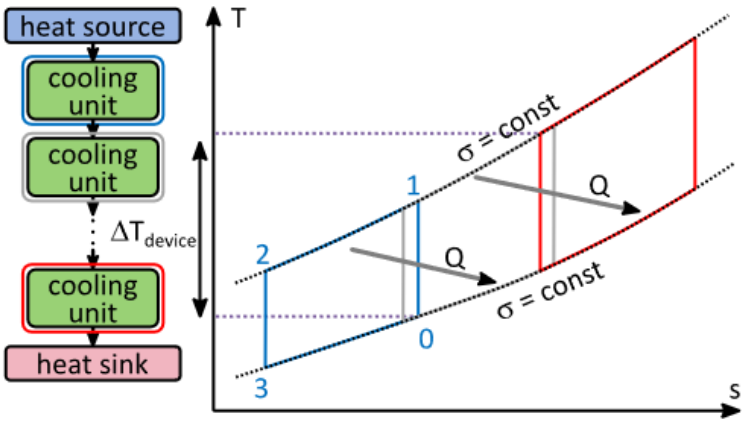

Figure 15: Temperature-entropy (T-s) diagram of the reversed Brayton cycle, for a cascaded device architectures with three refrigerants. Each refrigerant cycles at different temperatures, enabling an increased device temperature span. Adapted with permission from [185].

Due to its relevance to this work, the most important and recent cooling devices based on SMAs are presented in this chapter, followed by a detailed overview of devices based on elastomers. Prior to this, a comparison of the two material classes (elastomers and SMAs) and their respective impacts on device design, arising from material differences, is provided. An overview of the resulting advantages, disadvantages, and associated inferences is provided in Table 2.

First of all, the adiabatic temperature change observed in NR materials is around 20 K at room temperature [19]. Therefore, the effect size is promising when compared to other SMA alloys, such as NiTiFe with 36 K [186], NiTi with 42.5 K [187], or Ti-Ni-Cu-Co films with 23 K [16]. This makes NR a promising candidate for the realization of elastocaloric cooling devices.

While SMA-based materials need high stress fields, elastomer-based materials require high strains for a pronounced effect size. In detail, several hundreds of MPa, up to 900 MPa, and low strain of around 4 % are common for SMA [188]. In contrast, elastomers exhibit the elastocaloric effect under strains of several hundred percent, up to 700 %, but at much lower stress levels of only a few MPa [19]. Consequently, the stress and strain requirements are opposite for the two material classes. This leads to different design opportunities and challenges. On the one hand, the large strains of several hundred percent require distinct heat sink/source geometries and large actuation strokes, resulting in more complex device architectures, particularly for cascaded systems as presented in this work, compared to SMA-based architectures. On the other hand, the lower forces required for elastomer-based devices relax the demands on support structures, enabling the use of lightweight 3D-printed polymer components and low-cost motors, as exemplified in this work. Together with the low material price of around 1.5 €kg^{-1} for NR, which is two orders of magnitude lower than for SMA [22], NR is promising for commercialization. Furthermore, overloading due to actuation tolerances is less critical because of the flexible nature of the refrigerant. The NR foils in this study exhibit a high strain at failure, exceeding 1000 %, which further reduces the risk of damage.

Another key difference between the two material classes lies in their thermal properties. While the thermal conductivity λ of SMAs can be expected in the range of 8.6-18 Wm^{-1}K^{-1} [188], NR-based materials exhibit a much lower value of around 0.17 Wm^{-1}K^{-1} [189]. This places them within the range of thermal insulation materials. Since the thermal conductivity lowers heat transfer across the boundary to another medium, the heat transfer coefficient h for solid-to-solid contact is likewise reduced [190]. For SMA-based devices, a h value of approximately 1200 Wm^{-2}K^{-1} has been reported [186], whereas in NR systems the coefficient is about an order of magnitude lower [19,178]. This leads to limited internal heat transfer within bulk materials as well as across their interfaces. These factors must be addressed in the device design. Foils are employed in this work due to their high surface-to-volume ratio, which promotes rapid heat transfer especially in devices utilizing solid-solid heat transfer [19,191]. Similar to the approach in this work using thin foils, SMA-based devices have been reported to achieve a high surface-to-volume ratio by thin NiTi tubes.

Table 2: Comparison of using SMAs and elastomer-based refrigerant materials for elastocaloric cooling. Corresponding advantages, disadvantages, and inferences from the viewpoint of elastomer-based elastocaloric cooling technology. Typical values of the adiabatic temperature change ΔT_{ad}, maximum strain ε, stress σ, thermal conductivity λ at room temperature, heat transfer coefficient h and material $cost_{mat}$. References: [192][a], [19,178][b], [188][c], [186][d], [22][e].

	ΔT_{ad} (K)	ε (%)	σ (MPa)	λ $(Wm^{-1}K^{-1})$	h $(Wm^{-2}K^{-1})$	$cost_{mat}$ $(€kg^{-1})$
SMA	33 (NiTi)[a]	2-4[c]	500-900[c]	8.6-18[c]	1200[d]	100[e]
Elastomer	20 (NR)[b]	<700[b]	<10[b]	0.17[b]	80-170[b]	1.5[e]
Pros/ Cons	Promising effect size	Complex design	Low-load structures	Limited internal/boundary heat transfer		Low cost
Inferences	Attractive for device realization	Different geometry, large stroke	3D printed, low-cost actuation	Pre-strain, High surface-to-volume ratio (foils)		Attractive for commercialization

For example, values of 4.36 mm^{-1} [9] or even 7.51 mm^{-1} have been reported for the device achieving the highest temperature span recorded for elastocaloric cooling devices. This is surpassed by the foils used in this work, which exhibit a surface-to-volume ratio of 6.66 mm^{-1} for an initial thickness of 290 µm under 300 % strain, increasing to 12.5 mm^{-1} at 700 % strain [19]. For further comparison, as shown in Figure 16, the specific heat transfer area can also be considered, defined as the heat transfer area normalized by the mass of the refrigerant.

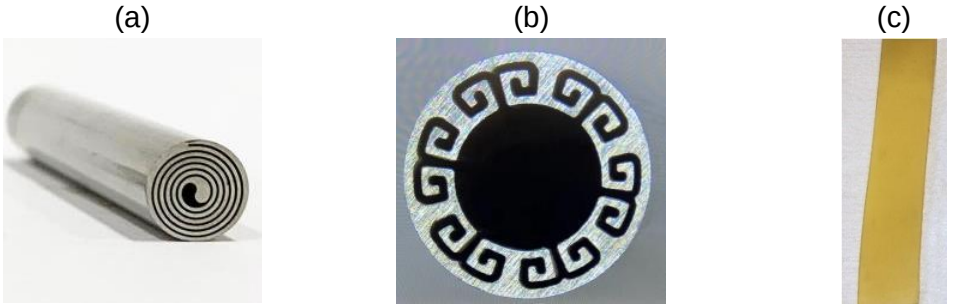

Figure 16: Comparison of the specific heat transfer area of (a) spiral cross-section, (b) multi-cell cross-section to increase of NiTi tubes and (c) NR foil, used in this work. Adapted with permission from [13].

The specific heat transfer area of 7.8 cm^2g^{-1} can be increased to 12.5 cm^2g^{-1} by employing a multi-cell cross-section instead of a spiral cross-section [13,182]. In comparison, the foil-based NR specimen used in this work achieves a specific heat transfer area of 18.5 cm^2g^{-1} [19]. For this calculation, a foil with an initial thickness of 650 µm is considered, taking only the surface facing the heat source into account. Under an engineering strain of 300 %, the value increases to 45.2 cm^2g^{-1} due to the enlarged surface. Therefore, by using elastic foils, expensive fabrication

methods of complex structures are not required to achieve a high surface-to-volume ratio and specific heat transfer area compared to SMA-based refrigerants.

3.3 Device Prototypes based on Elastomers

In the previous Chapter 2.5, an overview of the reversible adiabatic elastocaloric temperature changes reported in the literature for elastomer specimens is presented. However, a high temperature change on the material side alone does not guarantee good device performance, since the elastocaloric temperature changes generated within the refrigerant specimen must be effectively exchanged within a device through rapid heat transfer to be useable in practical cooling applications. Moreover, fatigue resistance under dynamic conditions must be considered due to the repetitive cyclic operation required for the cooling device. The reported devices in the relatively young research field of elastocaloric cooling based on elastomers are described in detail in this section. A summary of all the devices can be found in, including the corresponding operating conditions and performance parameters. They are subdivided according to the heat transfer mechanism, as illustrated in Figure 14.

3.3.1 Solid-Solid Heat Transfer

Apart from this work [19,178], only one reported study employs a solid-to-solid heat transfer mechanism combined with uniaxial tensile load cycling [34]. In Figure 17, a photograph of the device with parallel-oriented heat sink and source is presented. Similar to this work, NR-based foil specimens with two different thicknesses are tested. Load cycling is performed between 300 and 500 % strain at a strain rate of approximately $7s^{-1}$. The cooling power is determined under thermal load, resulting in 390 mW (0.430 Wg^{-1}) for the 600 µm foil. This is obtained at a frequency of 0.3 Hz, involving a heat transfer time of 3 s, resulting in a maximum temperature span of 1.8 K. The highest specific cooling power is obtained for the 400 µm foil, reaching 0.54 Wg^{-1} [34].

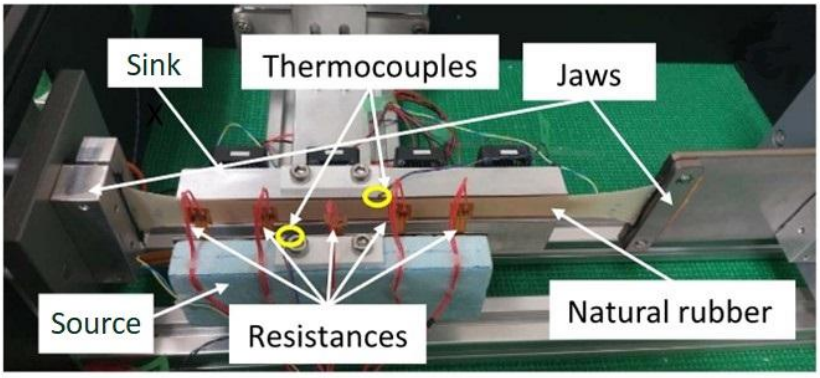

Figure 17: Photograph of the elastocaloric cooling device employing solid-to-solid heat transfer and uniaxial tensile loading of the NR refrigerant. Adapted from [34] licensed under CC BY 4.0.

Besides uniaxial tensile loading, nearly biaxial loading is achieved using an inflatable NR membrane with a thickness of 140 µm [31]. Similar to the previously presented device, heat is transferred through solid-solid contact. The adiabatic temperature span of the NR membrane is 23 K, based on a maximum adiabatic temperature change after unloading of around -16.5 K. The device performance is driven by two key mechanisms. The first is the strong elastocaloric effect resulting from nearly biaxial deformation, and the second is the snap-through instability that induces rapid quasi-adiabatic expansion and contraction in less than 100 ms. This results in a high specific cooling power of 20.9 Wg^{-1} [31] at frequencies of 1.1 Hz, comparable to that of SMA based devices at the miniature scale [193].

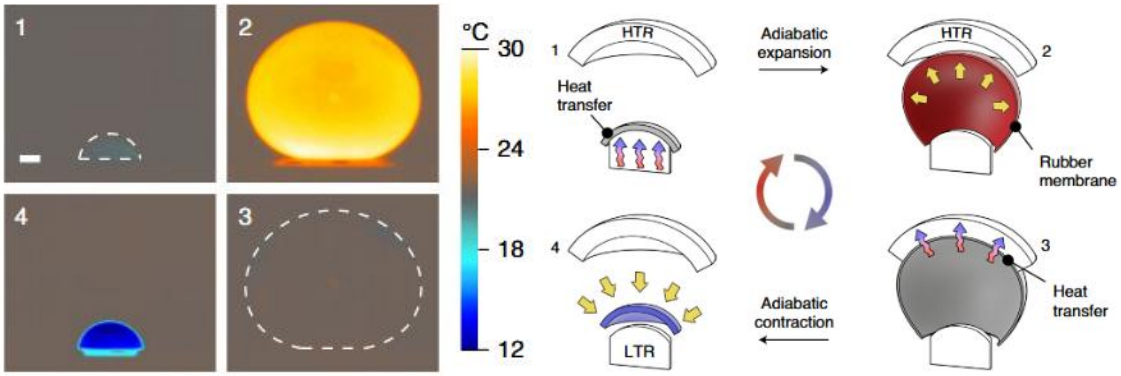

Figure 18: NR membrane based elastocaloric cooling device utilizing snap through instability for rapid mechanical, nearly biaxial load cycling. Heat transfer is accomplished by solid-to-solid contact, promoted by elevated contact pressure due to inflation of the balloon-like membrane. The surface temperature profile of the refrigerant during after loading (2) and unloading (3) is shown. Reproduced with permission [31].

The corresponding absolute cooling power is reported to be 877 mW, while the maximum device COP is 4.7 [31]. A maximum temperature span of 7.9 K is measured between the hot and cold reservoirs (HTR and LTR), which are composed of spherical caps, see Figure 18. The device transfers heat through mechanical contact enabled by the pressurized balloon like refrigerant driven by pneumatic actuation and remains stable over 10^3 cycles. Therefore, this device exhibits the highest operating frequency and specific cooling power among the reported elastocaloric cooling devices based on elastomers. For consideration as a cooling application, the lifetime is too low.

3.3.2 Solid-Liquid Heat Transfer

In contrast to this work, heat can be transferred using a heat transfer fluid. A regenerative fluid-based elastocaloric cooling device is presented, utilizing a deproteinized, cross-linked NR tube with a wall thickness of 1 mm [32]. While one end of the tube is fixed, the other one undergoes cyclic deflection facilitated by an actuator. The tube has an initial diameter of 5 mm, which reduces to 2 mm under a strain of 500 %, corresponding to an inner diameter of 1.47 mm. The heat exchange of the NR tube is achieved through an oscillating water-based fluid. As reported by [32] the thickness of the material layers significantly influences the system's performance.

Simulations indicate that the optimal layer thickness for both the fluid and the cross-linked NR tube ranges between 0.2 and 1 mm. At an operational frequency of 0.3 Hz, the fluidic prototype achieves a temperature span of 1.2 K.

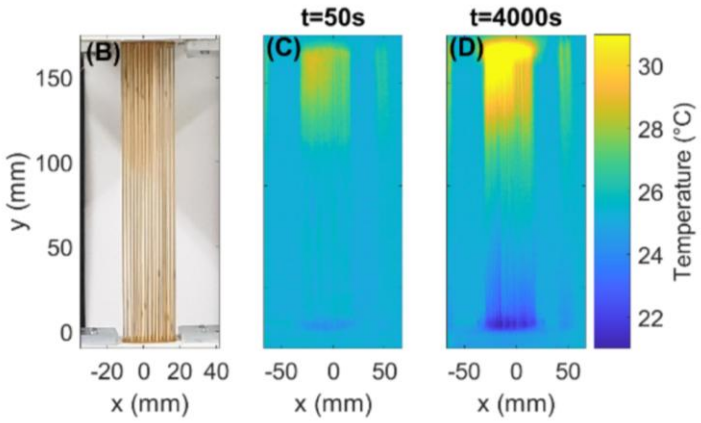

Figure 19: Elastocaloric cooling regenerator based on a parallel arrangement of 55 NR tubes with an initial diameter of 3.18 mm. Heat exchange is facilitated by water. The resulting temperature gradient is given after 50 and 4000 s. Reproduced with permission from [33].

In a subsequent study, the authors presented a similar system incorporating multiple tubes, which achieved a maximum device temperature span of 10 K at a frequency of 0.1 Hz [33]. The maximum adiabatic temperature change of the used rubber tubes is 13.8 K after unloading from 500 to 0 % of strain. The system operates at strains between 350 and 550 %, resulting in tube wall thicknesses of approximately 300 and 450 µm, respectively. In Figure 19, a photograph of the regenerator-based device with 55 NR tubes of an initial diameter of 3.18 mm is presented, and the corresponding temperature gradient developed after 50 and 4000 s is shown.

By cyclically pumping the water-based fluid through the interior of the tube, a temperature gradient along the tubes is built up during operation. Therefore, this device employs the principle of active regeneration, as previously described in Chapter 3.2. In detail, fluid flow occurs in opposite directions at maximum and minimum deformation. At maximum deformation, the fluid is pumped from the cold reservoir to the hot reservoir, cooling the heated-up NR tubes. Conversely, at minimum strain, the flow direction reverses, and the cold reservoir is cooled down. During deformation, no fluid flow takes place. Therefore, the operation can be subdivided into four steps. The cooling power is determined by measuring the heating power of a resistor placed in the insulated cold reservoir. The maximum cooling power under thermally loaded conditions, when the cold reservoir reached ambient temperature, is reported as 1.5 W, with a corresponding specific cooling power of 0.14 Wg^{-1}. The highest obtained device COP is 6. According to the study, the system has been subjected to 3×10^4 operating cycles [33]. By reversing the operating principle, heat can be converted into mechanical work. It has been reported that 4 J can be achieved per cycle [194].

3.3.2.1 Non-NR Elastomer Refrigerants

Another fluid-based elastocaloric cooling device uses a 3D-printed thermoplastic polyurethane (TPU) structure with rectangular microchannels, demonstrating that custom structures are feasible. The cubic TPU core (15 × 15 × 20 mm^3) houses 72 channels with a length of 20 mm and an opening size of 0.45 × 0.45 mm^2. While the TPU specimen exhibits a temperature change upon unloading of -2.3 K, the maximum temperature span of the device reaches 4.7 K, operating under 5.5-7.7 MPa and a strain range of 200-600 % [177]. A specific cooling power of 1.85 W g^{-1} is obtained at a frequency of 0.1 Hz.

The fourth reported device is also based on solid-liquid heat transfer. The device incorporates connected cooling units designed to counteract each other [135]. In the first unit, the foil specimen with a thickness of 1 mm is in the initial unstretched state, while simultaneously the second specimen in the other unit is in the stretched state. This configuration allows for work recovery. This means that the elastically stored energy due to deformation is reused, for example, for the actuation of a secondary refrigerant, as reported for SMA-based devices [186,195,196]. For the elastomer-based device, the uniaxial tensile strain applied to the specimens ranges from 100 to 500 %. The specimen material is poly(styrene-b-ethylene-co-butylene-b-styrene) (SEBS) filled with graphene nanoplatelets (GNS). Heat transfer is achieved by fluid flow, resulting in a maximum temperature change of -3.5 K of the water at the cold outlet. At zero temperature span, a cooling power of 5 W and a corresponding specific cooling power of 5.74 Wg^{-1} are reported, along with a device coefficient of performance COP_{device} of 8.3. Therefore, this device exhibits the highest absolute cooling power among the elastomer-based devices reported in literature.

Table 3: Overview of reported single-stage and regeneration-based elastocaloric cooling devices using elastomer refrigerants. The devices are characterized by the following values: The temperature change upon unloading ΔT_c of the refrigerant material and the operation parameters: the maximum strain range $\Delta\varepsilon$, the corresponding maximum engineering stress $\Delta\sigma$, the resulting device temperature span ΔT_{device}, the (specific) cooling power $\dot{Q}_0$ ($\dot{q}_0$) and the coefficient of performance COP_{device} and the maximum number of cycles. Legend: *regeneration-based devices (remaining devices are single-stage), **cooling power determined under thermal load; ***non-uniaxial.

Refrigerant	ΔT_c (K)	$\Delta\varepsilon$ (%)	$\Delta\sigma$ (MPa)	ΔT_{device} (K)	$\dot{Q}$ (W)	$\dot{q}$ (Wg^{-1})	COP_{device}	Cycles	Ref.
NR tube	-1	500-600	-	1.2	-	-	-	-	[32]
NR membrane	-16.5	***	-	7.9	0.8	20.9	4.7	10^3	[31]
NR tubes*	-	350-550	1.5	10.0	1.5**	0.14**	6.0	3×10^4	[33]
NR foil	-4.6	300-500	3.9	1.8	0.3**	0.54**	15.0	1.1×10^3	[34]
SEBS+ GNS bulk foil	-18.0	100-500	4	3.7	5.0**	5.74**	8.3	10^3	[135]
3D-printed TPU*	-2.3	200-600	7.7	4.7	2.5	1.85	1.7	-	[177]

3.4 Device Prototypes based on SMA

In contrast to the limited number of reported elastomer-based devices, several SMA-based demonstrators have been developed in recent years. Therefore, only a selection of SMA-based elastocaloric cooling devices is discussed in this section. Based on the relevance to this work, a single-stage cooling device and a cascaded device architecture at miniature scale are presented. An outlook is provided, highlighting the most promising devices for commercialization, which represents the outcome of more than a decade of intense research. Comparable performance levels could potentially be achieved with elastomer-based devices, leveraging their inherent advantages, provided that further research is conducted. An overview of the selected elastocaloric devices based on shape memory alloys reported in the literature is provided in Table 4.

3.4.1 Solid-Solid Heat Transfer

Elastocaloric cooling devices based on SMAs are presented in this subchapter, starting with solid-solid heat transfer concepts. At the macro scale, elastocaloric cooling devices have been realized using SMA wires [11] and ribbons [197,198], which are subjected to tensile loading and rely on solid-solid contact for heat transfer. On the miniature scale, foils are employed for rapid solid-solid heat transfer owing to their large surface-to-volume ratio [186,191]. The concept relies on free-standing SMA bridges that are deflected out of plane, which triggers the elastocaloric effect [186]. The U-shaped bridges serve as holders for the SMA films, with their ends fixed at a constant distance. Out-of-plane loading is induced through mechanical contact with a convex surface of the heat sink. The cyclic loading is achieved by the linear displacement of an actuator, enabling repeated contact. Devices based on a single film and on coupled two-film systems are examined [186,199,200]. The mechanical coupling of two antagonistic bridge pairs, each containing one SMA film, allows work recovery [186].

Further developments of these systems employing flexible springs have been reported [17]. The default layout, comprising a single bridge, is shown in Figure 20 (a) and (c). Asymmetry or misalignment deviations, which can be corrected by flexible spring structures, are shown in Figure 20 (b) and (d)-(f). The coupled bridges, which allow work recovery, are arranged in convex or concave configurations, as shown in Figure 20 (d) and (e), respectively.

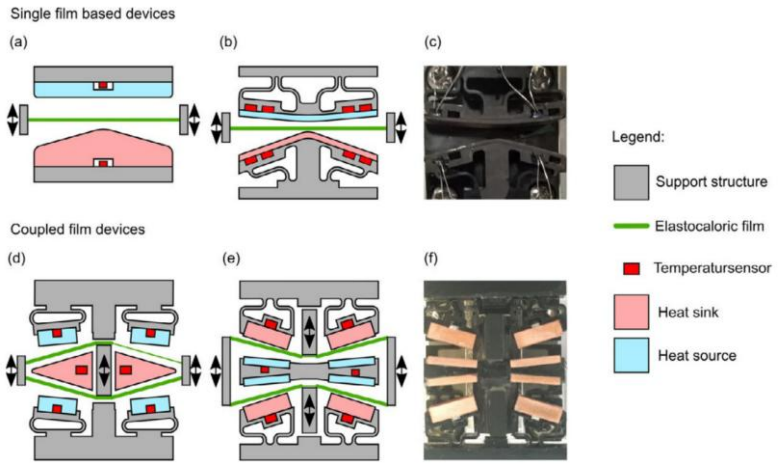

Figure 20: Schematics and photographs of suspended bridges based on SMA films, enabling out-of-plane loading. (a) Default layout based on a single bridge. (b) Improved design consisting of compliant spring-like structures and (c) the corresponding photograph. (d) Convex and (e) concave coupled bridges used for work recovery. (f) Photograph of corresponding experimental setup. Reproduced with permission [17].

The temperature evolution of the heat sink and heat source for the configuration shown in Figure 20 (b) is presented in Figure 21. The device performance exhibits a distinct frequency dependence, as also observed in this work [19,178]. At a frequency of 4 Hz, a high specific cooling capacity of 19 Wg^{-1} and a maximum temperature span of 14 K is achieved with a NiTiCuCo-based film [17].

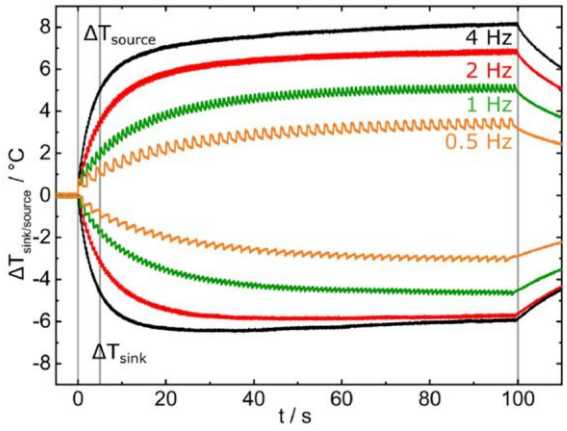

Figure 21: Temperature evolution of the heat sink and heat source for different frequencies. The device is based on a single SMA film and flexible support structures. Reproduced with permission from [17].

Therefore, the out-of-plane loading mechanism achieves the highest reported specific cooling power among SMA-based cooling devices. In addition, a cascaded device with in-plane loading, similar to this work, is demonstrated [193]. By operating three NiTiFe films, which are thermally connected in series, at an optimum frequency of 1 Hz, a high temperature span of 27.3 K is reported on the miniature scale.

3.4.2 Solid-Liquid Heat Transfer

The highest device temperature span of elastocaloric cooling devices is achieved through solid-liquid heat transfer and load cycling in compression. In the fluid-based system reported by [13], 75 K is achieved at a frequency of 0.33 Hz and a stress rate of 1 GPa s^{-1}, involving an applied stress of 900 MPa. The system manages to overcome the adiabatic temperature change of the material by employing active regeneration and multi material selection. This surpasses single-material devices, which exhibit a maximum temperature span of 50.6 K [182]. The multi-material cooling device uses NiTi SMAs with three different austenite finish temperatures. This means that the material's lattice is fully transformed to austenite at different temperatures. The transformation temperatures ranging from -2.5 to 48.0 °C and therefore create a possible operation span of over 100 K, see Figure 22. It should be mentioned that the adiabatic temperature change is temperature-dependent and differs for the different NiTi-based materials.

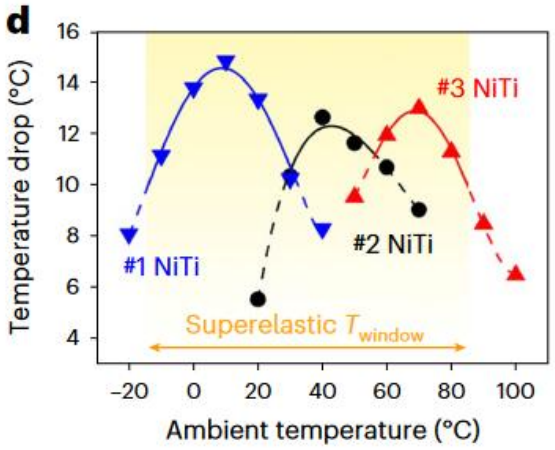

Figure 22: Adiabatic temperature change for the three selected NiTi SMAs at different ambient temperatures, realizing a possible operation region of over 100 K. Adapted with permission from [13].

The system architecture comprises 11 cascaded NiTi units, each 50 mm long and two distilled water-based loops enabling the heat exchange. During operation, cold and hot fluid loops are formed. The fluid pre-cools and pre-heats units 1-4 and 8-11, respectively, with lower and higher austenite finish temperatures. A schematic of the temperature gradient established along the cooling system, along with the corresponding austenite finish temperatures, is shown in Figure 23. The maximum temperature lift of 74.7 K is reached during the first 10^4 cycles and remains at 55 K after one million cycles [13]. In addition, a specific cooling power of up to 0.42 Wg^{-1} at a 50 K temperature span is reported, corresponding to an absolute cooling power of 12 W. Even higher cooling powers have been reported for a similar device architecture [14].

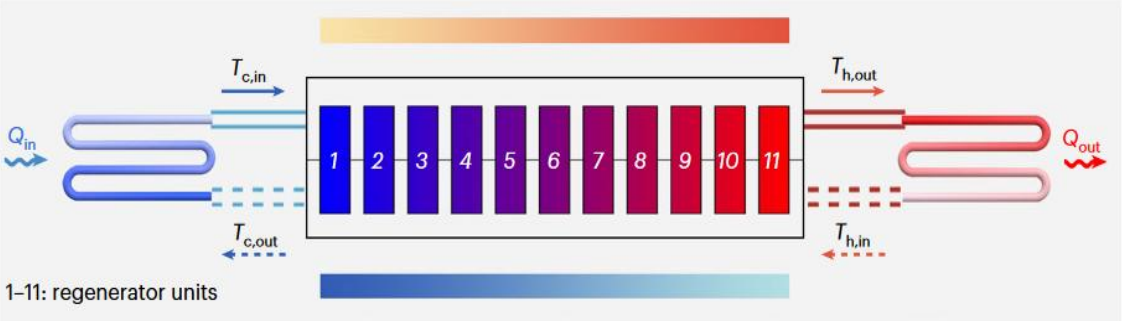

Figure 23: A schematic of the active regenerator device architecture comprising 11 NiTi units with different austenite finish temperatures A_f. Low temperature A_f (-2.5 K) used in the units 1-4 connected to the units 5-7 with A_f equal to 28 °C. The units 9-11 exhibit a high A_f of 48 °C. Adapted with permission from [14].

Fluid flow takes place in parallel through NiTi tubes connected in series. The connected tubes are subdivided into cells. Figure 24 (a) illustrates a schematic of a single cell, comprising four SMA tubes, two ceramic loading heads, and two ceramic liquid distributors. The cells operate at different temperature lifts of 0, 15, and 30 K, thereby promoting a temperature gradient along the device. Therefore, this strategy uses different austenite finish temperatures to promote the build-up of the device temperature span [17,201,202]. This strategy is also used to achieve the highest reported temperature span of 75 K in an elastocaloric cooling device [13]. The importance of strategies to enhance heat transfer is highlighted by increasing the thermal conductivity of the heat-transfer fluid and increasing the surface-to-volume ratio of the elastocaloric refrigerant. In the reported system, water containing graphene nanoparticles with diameters between 500 and 800 nm exhibits a 50 % increase in thermal conductivity compared with pure water, thereby improving heat transfer. In Figure 24 (b), the thermal conductivity of the nanofluid at different ambient temperatures is presented.

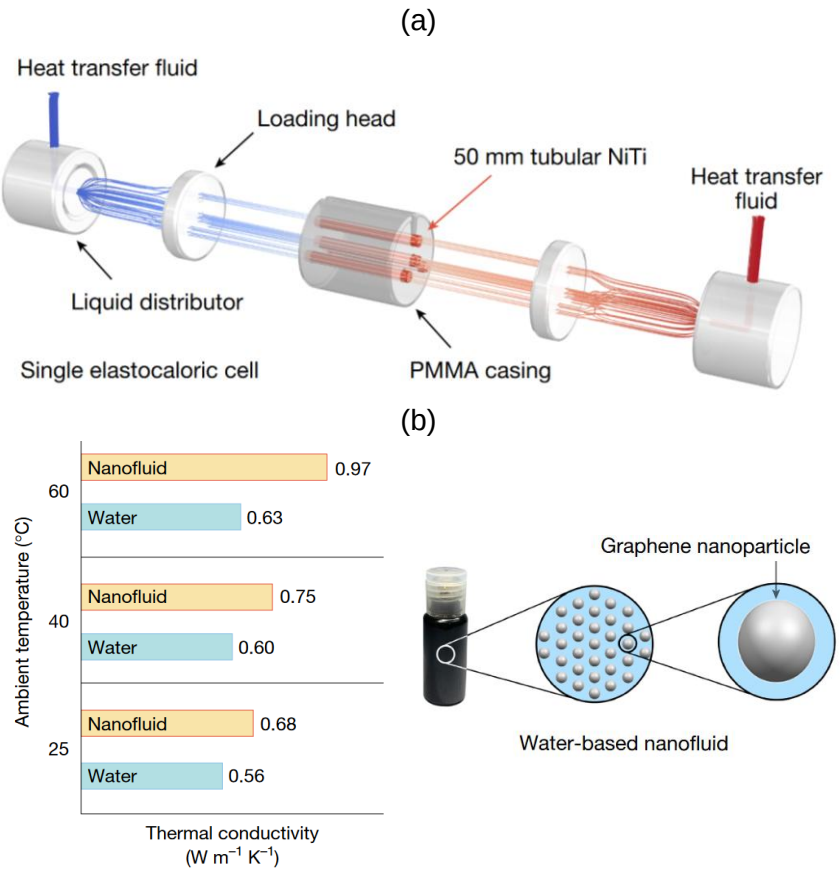

Figure 24: (a) Schematic of a single elastocaloric cell comprising four NiTi tubes, two ceramic loading heads, and two ceramic liquid distributors. (b) Increased heat transfer due to high surface to volume ratio and water based nano fluid with enhanced thermal conductivity due to graphene nanoparticles. Adapted with permission from [14].

At an operating frequency of 3.5 Hz and under thermal load, a cooling power of 1.284 kW is reported for zero temperature span during the first half-million cycles [14]. The frequency of 3.5 Hz consists of 0.05 s for loading and unloading, each followed by a 0.09 s holding phase. With an applied compressive stress of 950 MPa and the same operating frequency, it endures over two million cycles. In Table 4, an overview of the selected elastocaloric cooling devices based on SMAs is presented.

Table 4: Overview of selected elastocaloric cooling devices based on SMAs reported in the literature. The devices are characterized by the following values: The temperature change upon unloading ΔT_c of the refrigerant material and the operation parameters: the maximum strain range $\Delta\varepsilon$, the corresponding maximum engineering stress $\Delta\sigma$, the resulting device temperature span ΔT_{device}, the (specific) cooling power $\dot{Q}_0$ ($\dot{q}_0$) and the coefficient of performance COP_{device} and the maximum number of cycles. A negative strain value indicates compressive deformation. Legend: *cooling power determined under thermal load (zero temperature span), **cascaded devices, * regeneration-based devices (remaining devices are single-stage).**

Refrigerant	ΔT_c (K)	$\Delta\varepsilon$ (%)	$\Delta\sigma$ (MPa)	ΔT_{device} (K)	$\dot{Q}$ (W)	$\dot{q}$ (Wg^{-1})	COP_{device}	Cycles	Ref.
NiTiCuCo film	-14.5	>2.0	>400	12.6	0.22	19	6.7	400	[17]
NiTiFe films**	-16.0	4.5	-	27.3	0.19	3.4	-	-	[193]
NiTi tubes***	-	-3.0	900	74.7	12	0.42	10.2	10^6	[13]
NiTi tubes***	-22.0	-3.5	950	31.6	1284*	12.3*	7.9	2×10^6	[14]

4 Material Characterization

An overview of the material characterization process carried out on elastomer foils employed for the investigation of the elastocaloric effect is presented in this chapter. First, the elastomer sheet materials are introduced, together with a description of the procedure employed to prepare foil specimens. Subsequently, the thermal and mechanical characterization of the prepared specimens is addressed, with a primary focus on evaluating the elastocaloric effect. The experimental setup developed for uniaxial tensile loading is described in detail, including the instrumentation and boundary conditions employed. The investigation systematically varies the following mechanical parameters: maximum engineering strain, engineering strain rate, and engineering pre-strain. In addition, foils with different thicknesses are evaluated to assess their influence on the elastocaloric performance. The resulting data, including temperature evolution and stress-strain curves, are presented to illustrate the thermo-mechanical response under cyclic loading. From these results, performance metrics such as absorbed heat, mechanical work input, and the material coefficient of performance are derived. On this basis, the efficiency of the elastocaloric effect under various conditions is evaluated. Since the performance of elastocaloric cooling devices relies heavily on the properties of the active refrigerant, the characterization of promising elastomer foils is essential. This characterization provides the foundation for evaluating the overall device performance.

4.1 Specimen Material

In this section, an overview of the elastomer sheets used in this work is provided. Elastomers that exhibit the strain-induced crystallization (SIC) and the entropic elasticity (EE) are considered for the use as elastocaloric refrigerants. The elastomer selection comprises commercially available vulcanized natural rubber (NR) and NR latex sheets, as well as custom sheets fabricated in collaboration. The custom sheets comprise sulfur-vulcanized and C,H-ic vulcanized NR, as well as styrene-isoprene-styrene (SIS) copolymers with varying styrene content. Further information on the custom sheets can be found in Chapter 2.2, while details on their fabrication and compounding are provided in [19]. In Table 5, an overview of the materials, including their abbreviations and the corresponding material sources, is listed. Throughout the rest of this work, the term “Type” is used to identify the material of the specimens and subsequently refers to the foil refrigerant employed in the device. The elastomer sheets are used for the preparation of the foil specimens.

Foils with a thickness below one millimeter have been identified as beneficial for cooling applications based on the elastocaloric effect due to their rapid heat transfer [203]. However, commercially available natural rubber (NR) sheets are predominantly offered in thicknesses exceeding one millimeter.

Table 5: Material overview, including their abbreviations and the corresponding material manufacturer. The selection spans from vulcanized natural rubber (NR) through a styrene-isoprene-styrene copolymer to natural rubber latex. Material labels marked with an asterisk (*) indicate that detailed compounding information is unavailable due to the commercial origin of the material. The sheets labeled with "Fabricated in collaboration" employed in this study are custom fabricated by our collaborative partners at the University of Freiburg, Germany [19].

Type	Material	Manufacturer
K	Vulcanized NR*	IHSD-Klarmann
F	Sulfur vulcanized NR	Fabricated in collaboration
CHIC	C,H-ic vulcanized NR	Fabricated in collaboration
SIS	SIS Copolymer	Fabricated in collaboration
L	NR-latex*	MAPA GmbH
Lp	NR-latex*	Karex Industries Sdn. Bhd.

For instance, NR sheets from the company IHSD-Klarmann have a minimum sheet thickness of 650 µm. In the following specimens based on sheets of this company are labeled with a "K". To make it possible to also test specimens with the same material but thinner, specimens are engraved and thinned down by laser ablation. In addition to the commercially available sheets, custom sheets are employed to maintain control over the compounding and to allow more flexibility in sheet thickness. Specimens based on sulfur and C,H-ic vulcanization are used. For more details on the vulcanization process, see Chapter 2.2.1. The PS-PI-PS (SIS) copolymer sheets with three different styrene contents are tested, ranging from 14 to 22 %. For more information about the SIS copolymer, see Chapter 2.4.4. In addition to the custom sheets NR latex sheets are included in the study to assess the behavior of thin rubber foils. The use of commercially available NR latex sheets offers an advantage, as they are industrially produced with precisely controlled and uniform thickness. This makes them particularly suitable for investigating thickness-dependent effects. Specimens based on NR latex from the companies MAPA GmbH and Karex Industries Sdn. Bhd. are used. Figure 25 presents a photograph of the foil specimens used in this work, along with their corresponding labels.

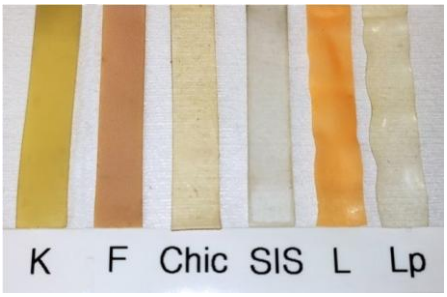

Figure 25: Photograph of foil specimens which are laser-cut from the sheet materials listed in Table 5, and their corresponding labels.

4.2 Specimen Preparation

This section is dedicated to the specimen preparation performed by laser cutting. A rectangular specimen geometry is chosen instead of the conventional tensile test specimen, commonly referred to as a "dogbone" shape. The dogbone geometry is avoided due to the inhomogeneous temperature profile induced by the elastocaloric effect that occurs at the fillet radius. Additionally, classical tensile testing until fracture is not required in this study, making the standard geometry unnecessary. In contrast, the rectangular specimen provides a homogeneous surface temperature distribution during testing. This is crucial for avoiding a temperature gradient formation within the heat sink/source in cooling devices. The selected specimen dimensions are 9 × 26.5 mm^2 [19]. In Figure 26 a schematic of the undeformed rectangular tensile specimen is presented. The total specimen length, denoted as L_g, includes both the gray-shaded end sections used for mechanical fixation and the central deformable region, shown in beige color. The section subjected to deformation is geometrically defined by its initial length L_0, the width w_0 , and thickness d. From these dimensions, the cross-sectional area $A_0 = d\, w_0$ can be calculated, which is relevant for stress analysis. Additionally, the area available for heat exchange with a heat source or sink is denoted as S_0, and considered in subsequent thermal analyses. The holder for specimen fixation is introduced in Chapter 5.1.1, as it is a critical component of the elastocaloric cooling device with respect to its lifetime.

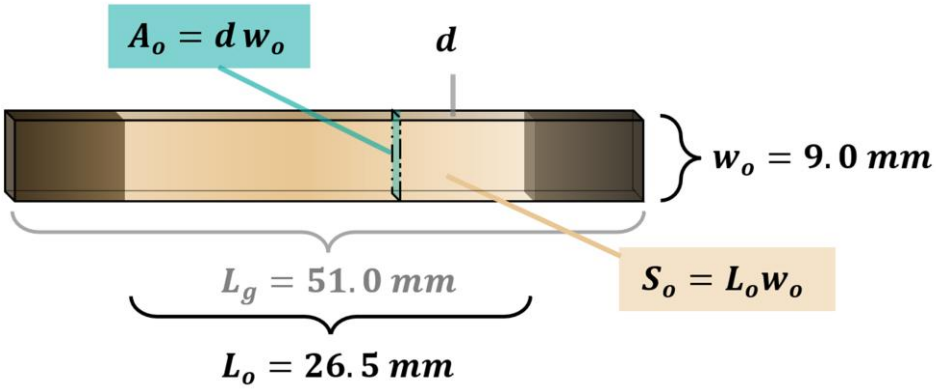

Figure 26: Schematic of the undeformed rectangular foil specimen subjected to uniaxial tensile load. The specimen geometry is given by the total length L_g, which includes the end sections used for fixation (indicated in gray) and the central deformable volume (indicated in beige color). The deformable section is characterized by the length L_0, width w_0 and thickness d. The initial cross-sectional area is given by A_0. The area available for heat transfer to a sink or source is denoted as S_0.

The sample geometry is cut from the elastomer sheets, introduced in Table 5 using a pulsed laser through material ablation [19]. The cutting edge is generated thermally. Since rubber cannot be melted, it undergoes oxidation and thermal decomposition under the laser beams energy input [46]. A laser cutter from Universal Laser Systems is used, equipped with a CO_2 laser operating at a wavelength of 10.6 µm and a focal spot size of 120 µm. The maximum output power of the laser is 40 W, with a maximum travel speed of 25 cms^{-1}. Smooth and homogeneous cut

edges are achieved using a low power setting of 20 %, a travel speed of 10 %, 700 pulses per inch (PPI), and by repeating the cutting process multiple times. For example, in the case of sheets of the material type “K” with a foil thickness of 650 µm, the cutting process must be repeated four times. To produce a continuous cutting edge, the PPI value is a critical parameter. For example, at 500 PPI, the cut edge of a sheet type “K” with a foil thickness of 650 µm is discontinuous, which becomes evident under deformation and manifests as a wavy, perforated cutting edge. The specimens generated by laser ablation are engraved at moderate power input to reduce their thickness [178].

4.3 Thermal and Mechanical Characterization

4.3.1 Experimental Methods and Test Setup

The experimental test setup to characterize the mechanical and thermal properties of the elastocaloric elastomer tensile specimens is depicted in Figure 27. The setup comprises an IR camera and a linear actuator with a force sensor and two rigid specimen holders. The linear actuator including an AC servo drive is provided by the company ESR Pollmeier GmbH. The right specimen holder is stationary and attached to the force sensor which captures the force needed to deform the specimen uniaxially. The other specimen holder is fixed to the slide block of the linear actuator which performs the displacement in x-direction. Force sensors with a maximum force of 100 N and 50 N are used, depending on the specimen thickness. The time-dependent surface temperature, located in the x-y plane, is evaluated by infrared thermography during the test. The infrared camera (FLIR A655sc) with close-up lens (T198066) achieves a resolution of 640 x 480 pixels with a pixel size of 25 µm and can record up to 120 fps. As the emitted thermal radiation is influenced by the surface characteristics and material properties, the emission coefficient is set to 0.92, based on values reported in the literature for rubber materials [189]. The literature value of the emission coefficient is confirmed by comparing the resulting surface temperatures with measurements from an embedded thermocouple [203]. The experiments are controlled and recorded through a computer utilizing FLIR ResearchIR and LabVIEW software, while the measurement data is analyzed using MATLAB.

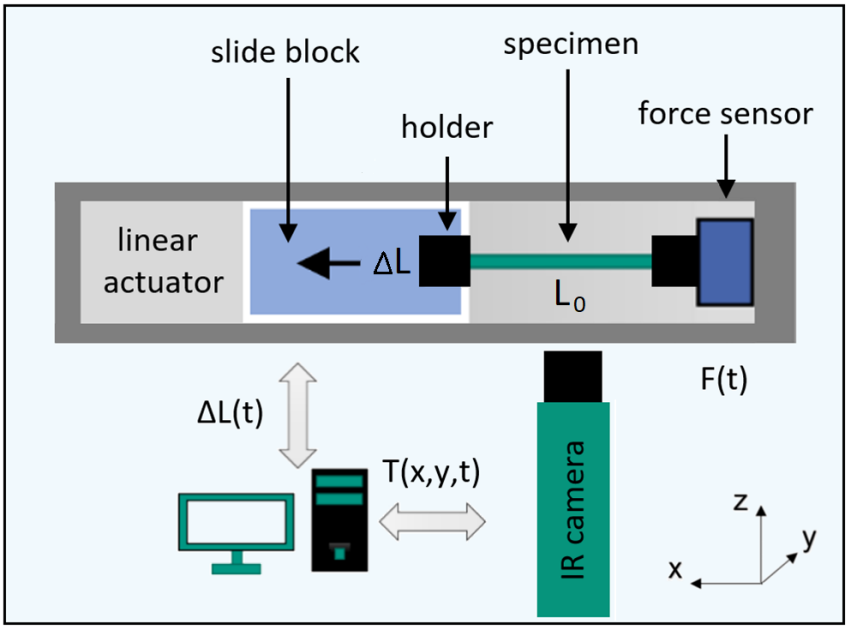

Figure 27: Top-view schematic of the experimental setup used for the mechanical and thermal characterization of elastocaloric elastomer foil specimens. The IR camera captures the emitted radiation of the surface which correlates to its temperature $T(x, y, t)$ of the clamped specimen during uniaxial tensile loading and unloading. To deform the specimen with an initial length of L_0,the linear actuator's slide displaces along the x-axis, inducing a length change of $\Delta L(t)$, as indicated by the black double arrow. During operation the force sensor records the force $F(t)$.

The mechanical properties of elastocaloric elastomers specimens are determined through uniaxial tensile tests, as the elastocaloric effect can be triggered by tensile strain. The mechanical behavior is characterized by stress σ and strain ε. The tensile stresses, strains, and strain rates are nominal quantities. They differ from the actual values (true strain), as the cross-sectional area of the specimen changes compared to the initial cross-section or more specifically, the specimen undergoes lateral strain. Consequently, it is referred to as engineering stress, strain, and strain rate. In tensile tests, the force F in x-direction is applied perpendicular to the cross-sectional area of the specimen under load. The resulting engineering stress is calculated as the ratio of the applied force to the undeformed initial cross-sectional area A_0, as given in Equation 4-1.

$$\sigma = \frac{F}{A_0} = \frac{F}{w_0 d} \qquad \textbf{4-1}$$

The resulting engineering strains arise from the applied engineering stresses. They can be calculated from the change in length ΔL, equal to the displacement of the slide block, relative to the initial length L_0, as given in Equation 4-2.

$$\varepsilon = \frac{\Delta L}{L_0} 100\ \% \qquad \textbf{4-2}$$

All tensile tests conducted as part of this work are performed at a constant engineering strain rate $\dot{\varepsilon}$. The strain rate $\dot{\varepsilon}$ is expressed in s^{-1} and is calculated based on the original specimen length

L_0 and the displacement rate $d\,L(dt)^{-1}$, or the slide block speed v, of the linear actuator, as given in Equation 4-3.

$$\dot{\varepsilon} = \frac{d\,\varepsilon}{d\,t} = \frac{1}{L_0}\frac{d\,L}{d\,t} = \frac{v}{L_0} \qquad \textbf{4-3}$$

With the setup, strain-rates up to 14 s^{-1} can be achieved, which is equal to a duration of half a second to reach the maximum engineering strain of 700 %.

4.3.2 Elastocaloric Temperature Change

The elastocaloric response resulting from mechanical loading and unloading of a NR foil type "K" with a thickness of 290 µm is shown in Figure 28. The temporal evolution of a single strain cycle, comprising uniaxial tensile loading and unloading, is shown in Figure 28 (a). The cycle begins with a rapid loading process at an engineering strain rate of 9.3 s^{-1} up to the maximum engineering strain ε_{max}, which is visualized by the path from ⓪ to ①. Consequently, a maximum engineering stress σ_{max} , is induced in the specimen, given in Figure 28 (b). Crystallites form due to the SIC and polymer chain orientation, which lowers the entropy. The elastocaloric effect leads to a temperature increase of the specimen due to release of latent heat. For further details on the origin of the elastocaloric effect in elastomers, refer to Chapter 2.3 and 2.4. In Figure 28 (c) the temperature response over time is given. The maximum temperature difference ΔT_h with respect to the ambient temperature of 23.0 °C is 7.4 K. Once the maximum load is reached, the tensile specimen is held in this state until its temperature stabilizes at ambient temperature, as indicated by ① to ②. During this time, additional crystallites are formed and may influence the temperature change upon unloading. For this reason, the holding time t_{hold} is maintained constant for all specimens in this study to ensure comparability. A stress relaxation during constant maximum strain is observed, which is reflected in the decline of the engineering stress, as shown in Figure 28 (b). Therefore, after the holding time of 120 s, quasi-adiabatic unloading takes place at significant lower engineering stress σ_{re}, compare ② to ③. The unloading endpoint is characterized by a complete absence in both engineering strain and stress. The result of unloading is a temperature decrease, as shown in Figure 28 (c), due to an entropy increase caused by melting crystallites and re-entangled polymer chains. The maximum temperature drop after unloading ΔT_c is -10.3 K. Subsequently, a holding time of 120 s follows, during which the temperature of the elastocaloric specimen decreases toward ambient temperature, given by the points ③ and ④. This marks the end of the first loading cycle. The corresponding surface temperature of the specimen is visualized in Figure 28 (d), which peaks at the points ① and ③. The peak-to-peak temperature difference ΔT_{ad} and therefore the full elastocaloric response is given as the product of the temperature change during loading ΔT_h and the temperature change during unloading ΔT_c, as given in Equation 4-4.

$$\Delta T_{ad} = \Delta T_h + |\Delta T_c| \qquad \textbf{4-4}$$

For comparison, temperature profiles over time of NR foils with two different thicknesses, 290 µm (black solid line) and 800 µm (green dashed line), of material types "K" are provided in Figure 28 (c). The thickness refers to the initial undeformed state. For the 800 µm thick foil and the resulting lower surface-to-volume ratio, the equilibration process with the surrounding environment takes more time. While the full equilibration of the 290 µm thick foil in the loaded state occurs within 18 s, the 800 µm thick foil requires 4.3 times longer. After unloading, the equilibration times are even longer. For the 290 µm foil, full equilibration is reached after 115 s, while for the thicker foil, it takes approximately twice as long. The differences arise from the change in foil thickness under deformation. This highlights the challenge of realizing devices with elastomers like NR, which have low thermal conductivity and slow heat transfer. A potential solution could be the reduction of the foil thickness [19,178]. For more details, see 4.3.4.

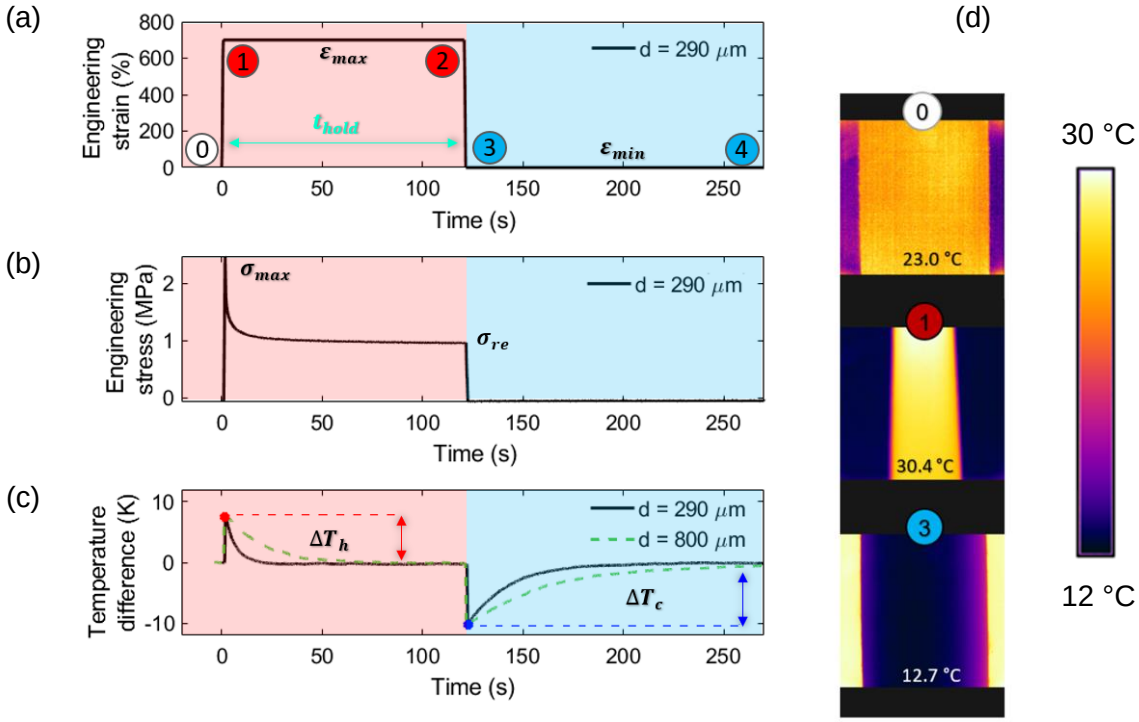

Figure 28: The elastocaloric effect in elastomers, exemplified for a natural rubber (NR) foil, is characterized by a reversible temperature change during rapid mechanical loading and unloading. The effect is associated with the strain-induced crystallization (SIC) and entropy elasticity (EE). Uniaxial tensile loading ⓪→① and unloading ②→③ are performed at an engineering strain rate of 9.3 s^{-1} on foils with a thickness of 290 µm. The engineering strain (a) is cycled between the undeformed state ε_{min} (at the points ⓪, ③ and ④) and the maximum engineering strain ε_{max} (at ① and ②) and maintained respectively during the time t_{hold}. The corresponding engineering stress (b) and temperature difference upon loading ΔT_h and unloading ΔT_c (c) are shown. For comparison, the temperature evolution of a foil with a thickness of 800 µm (dashed green line) is shown, demonstrating slower thermal equilibration (during loading ①→② and unloading ③→④) with the ambient environment. In part (d), two infrared images of the radiation emitted from the surface of the foil specimen at room temperature (23.0 °C) are shown. The corresponding maximum and minimum surface temperatures are 30.4 °C and 12.7 °C. Adapted from [19] licensed under CC BY 4.0.

4.3.3 Maximum Engineering Strain

It is well known that the temperature change in elastocaloric materials is strain-dependent, owing to its origin in strain-induced crystallization and entropy elasticity [20,23]. To evaluate the dependency on maximum engineering strain, the strain is varied in steps of 100 %, starting from 0 % and increasing up to 800 %, followed by unloading to the undeformed state. Loading and unloading are conducted at an engineering strain rate of 4.7 s^{-1}, with a hold time of 120 seconds at both the maximum and minimum strain states. The resulting temperature difference during loading ΔT_h (red dots) and during unloading ΔT_c (blue dots) as function of the maximum engineering strain are given in Figure 29 (a). The NR specimens type "K" with a thickness of 650 µm is used. In addition, the difference between the absolute temperature values are visualized by the green points. All tests are performed in a state free of the Mullins effect, after performing up to ten initial cycles to stabilize the material response. Within the strain range of up to approximately 300 %, minor and nearly linear temperature changes are observed. For the maximum engineering strain of 300 % ΔT_c is -1.3 K, decreasing further to -1.9 K at the next strain increment. At 400 % engineering strain, the temperature change upon loading and unloading is almost equal ($\Delta T_h \approx \Delta T_c$) and differ only by 0.1 K. Above 300 % of engineering strain, the temperature exhibits a pronounced nonlinear increase with $|\Delta T_c| < \Delta T_h$. A near doubling of the temperature difference is observed at a maximum engineering strain of 500 % compared to the preceding measurement point. At a maximum engineering strain of 700 %, ΔT_h is +8.8 K after loading and ΔT_c is -10.3 K after unloading, resulting in an adiabatic temperature ΔT_{ad} of 19.1 K [19]. Further increasing the maximum engineering strain to 800 % produces only a minor additional temperature change of approximately 8 %.

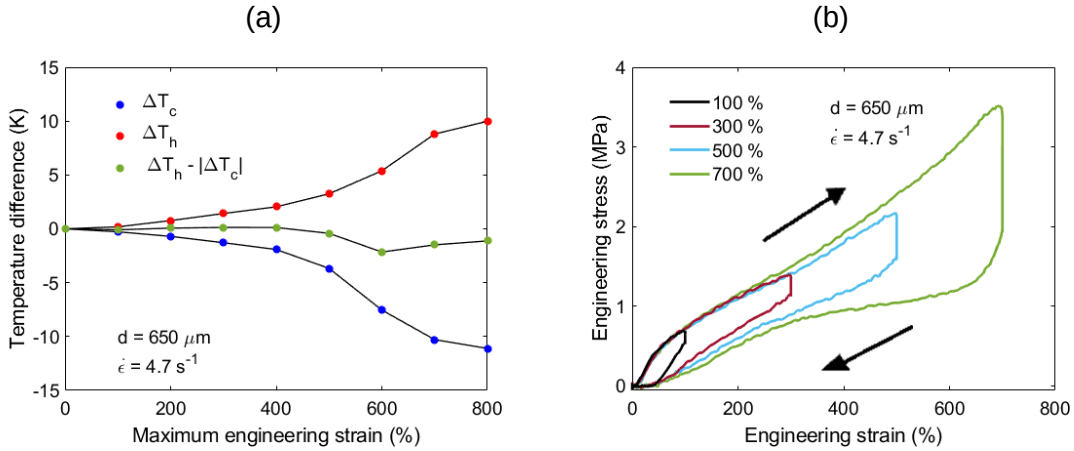

Figure 29: (a) The temperature difference during loading ΔT_h and unloading ΔT_c as a function of the maximum engineering strain for a NR foil type "K" of 650 µm thickness and (b) the corresponding engineering stress-strain response. Uniaxial tensile tests are performed with an engineering strain rate of 4.7 s^{-1}. The loading and unloading direction is indicated by the black arrows. The solid lines indicate the connections between the points. Adapted from [19] licensed under CC BY 4.0.

The linear temperature variation in the engineering strain range up to 300 % primarily reflecting the entropic elasticity associated with the alignment of molecular chains [43]. For engineering

strain above 300 % the nonlinear behavior can be explained by the formation of the strain-induced crystallization, eventually reaching saturation above 700 % [24]. Therefore, for all subsequent tests, a maximum engineering strain of 700 % is selected due to the significant temperature change.

In Figure 29 (b) the corresponding nonlinear stress-strain characteristics are given for different maximum engineering strains. The loading and unloading direction are indicated by black arrows. For engineering strains below 100 %, the NR foil exhibits near-elastic behavior. At engineering strains exceeding 200 %, the stress rises in a plateau-like fashion, but with a reduced slope indicating the progression of SIC [19]. The maximum induced engineering stress occurs at the end of the loading curve, resulting in 0.7 MPa for the engineering strain of 100 % (black curve). By further increasing the maximum engineering strain up to 700 % (green curve) the maximum stress is elevated up to 3.5 MPa. During temperature equalization, quantified by the time t_{hold} of 120 s, an engineering stress decrease occurs at a constant engineering strain, as shown by the vertical curve segment. For the maximum engineering strain of 700 % the engineering stress decreases by 1.6 MPa. Consequently, unloading occurs at substantially lower stress levels, thereby completing the loop into a hysteresis that encloses the area A_{hyst} [19]. The enclosed area increases with rising maximum engineering strain. For strains exceeding 500 %, a further downward shift with characteristic convex bulging as part of the unloading curve is observed, resulting in an additional enlargement of the enclosed area.

In general, in subsequent cycles under similar load conditions, reduced forces are required for deformation compared to the initial cycle. This phenomenon is known as stress softening or Mullins effect [93]. To date, there is no general agreement on either the physical origin or the mechanical modeling of this effect [94]. For the NR specimen type “K” the Mullins effect only occurs within the first load cycle, the hysteresis is stabilized after the first cycle. The Mullins effect has no effect on the temperature difference only on the needed work input. The plateau-like increase in engineering stress reflects the progression of strain-induced crystallization, characterized by the nucleation and transformation of crystalline structures [81]. Furthermore, the SIC at maximum strain also causes stress relaxation, leading to the typical hysteresis behavior [100]. While conventional texts attribute the origin of hysteresis to thermal dissipation, recent investigations may reveal that the hysteresis loop instead arises from microstructural changes within the material rather than intrinsic or thermal losses [24]. The area enclosed by the hysteresis loop represents the work input ΔW_{mat} required for elastocaloric cycling. Work recovery is assumed, meaning the hysteresis work during loading and unloading is considered, while the efficiency of the actuator is neglected.

In conclusion, the maximum stress is on the order of several megapascals, and in all cases a hysteresis loop is observed, with the enclosed area, representing the work input, increasing progressively with the maximum engineering strain [19].

For comparison, the custom NR foil type “F” is also evaluated under varying the maximum engineering strain. In Figure 30 (a) the temperature difference during loading ΔT_h (red dots) and during unloading ΔT_c (blue dots) as function of the maximum engineering strain are given. The

NR specimen type “F” with a thickness of 290 µm is used. In Figure 30 (b) the corresponding stress-strain curves are given. Tests are performed with an engineering strain-rate of 9.3 s^{-1}. In comparison, the results for the foil specimens type “K” and type “F” are similar, especially the engineering strain dependency. The results differ in the absolute value of ΔT_c, thereby indicating a lower elastocaloric temperature change for type “F”. For a maximum engineering strain of 700 %, specimen type “F” reaches -8.2 K, which, in terms of the absolute value, is 2 K lower [19]. In addition, the value of ΔT_{ad} is 13.5 K, which is therefore 70 % lower than that of foil type “K” with a thickness of 650 µm.

For comparison at the same thickness (290 µm) and under the same engineering strain rate, the results for foil type “F” and “K” are given in Table 6, page 53. The temperature differences ΔT_c and ΔT_h are lower for foil type “F” than for type “K”. It can therefore be assumed that the material exhibits a lower elastocaloric effect, at the same test conditions.

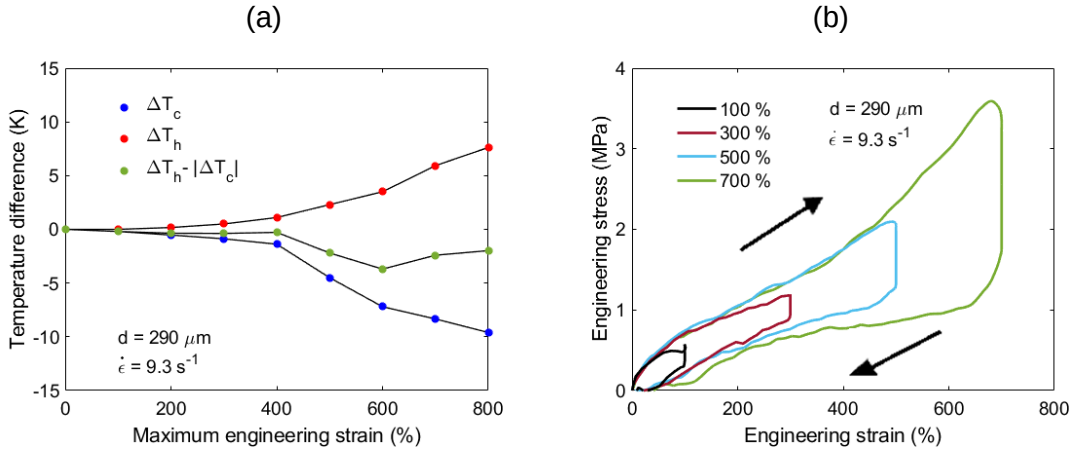

Figure 30: (a) The temperature difference during loading ΔT_h and during unloading ΔT_c as a function of the maximum engineering strain for a NR foil type “F” of 290 µm thickness and (b) the corresponding engineering stress-strain response. Uniaxial tensile tests are performed with an engineering strain rate of 9.3 s^{-1} and the loading and unloading direction is indicated by the black arrows. The solid lines indicate the connections between the points.

To calculate the coefficient of performance for the material, the specific absorbed heat q_{ab} and the specific work input per cycle Δw_{mat} are used, as given in Equation 4-5. Using the material density of the foil, ρ and the specific heat capacity at constant pressure c_p and the temperature change after unloading ΔT_c, q_{ab} can be calculated. The enclosed hysteresis area A_{hyst}, in a stress-strain diagram recorded during mechanical loading and unloading determines the work input per cycle.

$$COP_{mat} = \frac{Q_{ab}}{\Delta W_{mat}} = \frac{q_{ab}}{\Delta w_{mat}} = \frac{-c_p \, \Delta T_c \, \rho}{A_{hyst}} \qquad \textbf{4-5}$$

In Table 6, an overview of the elastocaloric material properties of the investigated foils with different initial thicknesses d is presented. The applied strain range is defined by $\varepsilon_{pre} - \varepsilon_{max}$. Chapter 4.3.6 discusses engineering pre-strain in detail, which is defined as mechanical cycling that starts and ends in a pre-deformed state.

The foil types “K”, “F”, and “Chic” are NR-based materials, whereas “SIS” corresponds to a co-polymer with varied styrene content, indicated in brackets. The foil types “Lp” and “L” are NR-latex-based materials. Further information on the materials is provided in Table 5.

Table 6: Overview of elastocaloric material properties of the investigated foils within this work with different initial thicknesses *d*. For material details of the NR foils (“K”, “F” and “Chic”), copolymer foils (“SIS” with styrene content in brackets) and NR latex foils (“L” and “Le”), see Table 5. The test condition parameters are the strain range, which is given by the engineering pre-strain ε_{pre}, the maximum engineering strain ε_{max} and the corresponding engineering strain rate $\dot{\varepsilon}$. The resulting parameters are the specific work input Δw, the temperature change upon unloading ΔT_c, the peak-to-peak temperature change ΔT_{ad}, the corresponding specific absorbed heat q_{ab} and the coefficient of performance for the material COP_{mat}.

Type	d (μm)	$\varepsilon_{pre} - \varepsilon_{max}$ (%)	$\dot{\varepsilon}$ (s^{-1})	Δw_{mat} (Jg^{-1})	ΔT_c (K)	ΔT_{ad} (K)	q_{ab} (Jg^{-1})	COP_{mat}
K	900	0-700	0.7	5.2	-10.0	17.4	18.8	3.6
K	900	300-700	0.7	1.7	-6.4	12.3	12.0	6.9
K	650	0-700	4.7	7.1	-10.3	19.0	19.5	2.7
K	650	0-700	9.3	8.5	-10.3	20.3	19.5	2.3
K	650	300-700	4.7	2.4	-7.8	12.4	14.6	6.0
K	650	300-700	9.3	3.6	-7.9	13.1	14.9	4.1
K	290	0-700	9.3	7.2	-10.0	17.4	18.9	2.6
K	290	300-700	9.3	4.2	-7.6	13.5	14.3	3.4
F	290	0-700	4.7	6.5	-7.9	12.7	9.3	1.4
F	290	0-700	9.3	6.8	-8.2	13.5	9.7	1.4
F	290	300-700	4.7	3.0	-5.5	8.0	10.3	3.4
F	290	300-700	9.3	2.9	-6.4	10.6	12.0	4.1
Chic	340	0-700	9.3	17.7	-11.4	23.1	21.6	1.2
Chic	340	300-700	9.3	3.5	-7.7	13.0	14.6	4.2
SIS(14)	600	0-700	4.7	6.4	-2.2	7.3	4.2	0.6
SIS(17)	600	0-700	4.7	4.4	-1.9	5.0	3.6	0.8
SIS(22)	600	0-700	4.7	4.3	-1.5	3.9	2.8	0.7
L	60	0-700	9.3	6.8	-7.1	9.5	13.4	1.9
L	60	0-700	14.0	5.8	-7.0	9.6	13.3	2.3
L	60	300-700	9.3	4.0	-2.1	4.7	4.0	1.0
L	60	300-700	14.0	4.3	-2.0	4.7	3.8	0.9
Lp	120	0-700	9.3	13.8	-9.2	12.2	17.4	1.3
Lp	120	0-700	14.0	15.0	-9.4	12.4	17.8	1.2
Lp	120	300-700	9.3	5.5	-4.3	6.6	8.1	3.2
Lp	120	300-700	14.0	5.7	-4.3	6.6	8.1	1.4

In Figure 31 (a), the engineering stress-strain curves of the copolymer foils of type “SIS” with styrene contents of 14, 17, and 22 % are presented. The tests are performed with an engineering strain rate of 4.7 s^{-1} and stretched up to a maximum engineering strain of 700 %. The thickness of the foils is 600 µm. The highest maximum engineering stress of 1.7 MPa and ΔT_c of -2.2 K is observed for the lowest styrene content of 14 %. This corresponds to the highest isoprene

content of 86 %. For the specimens with a higher styrene content of 17 and 22 %, the maximum engineering stress and ΔT_c are lower. In addition, for the lowest styrene content of 14 %, the upper curve corresponding to the loading path exhibits a steeper slope at engineering strains exceeding 100 %. The styrene content, which is coupled with the isoprene content, mainly influences the hysteresis shape. Therefore, it determines the work input needed to deform the specimen up to 700 % engineering strain. However, only a slight difference in ΔT_c is observed. Overall, the foils of type "SIS" are unsuitable for elastocaloric cooling, as they exhibit premature failure by fracture after less than five cycles and generate only minor temperature changes and COP_{mat}.

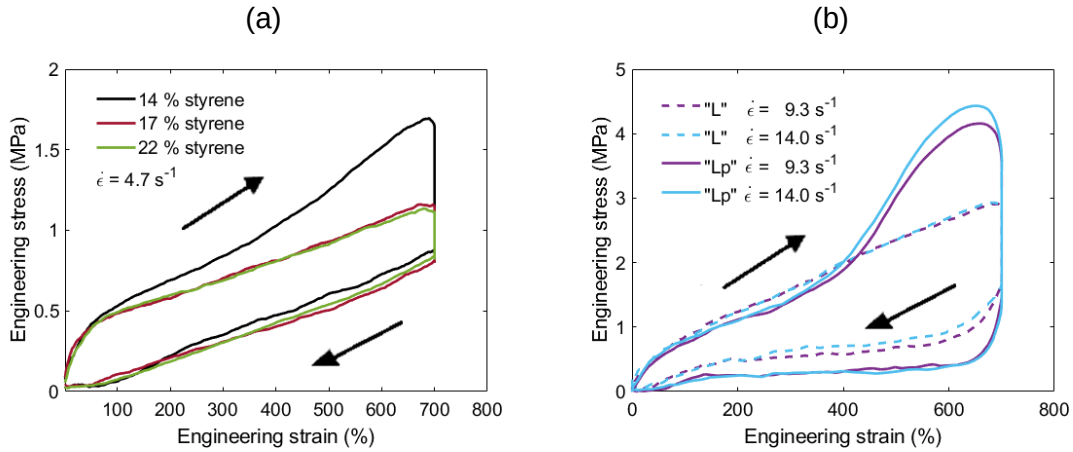

Figure 31: (a) Engineering stress-strain curves for the copolymer foil type "SIS" with a thickness of 600 µm for different styrene contents of 14, 17 and 22 % at an engineering strain rate of 4.7 s^{-1}. The "SIS" specimen with 14 % styrene content shows the highest elastocaloric temperature response among the "SIS" types, although it remains lower than that of the tested NR specimens. Due to its early mechanical failure, it is considered unsuitable for elastocaloric cooling. (b) Engineering stress-strain curves for the NR latex foil type "L" (dashed line) and "Lp" (solid line) with a corresponding thickness of 60 and 120 µm and the engineering strain rate of 9.3 (purple line) and 14.0 s^{-1} (light blue line) as indicated. The corresponding temperature response is listed in Table 6.

Among all tested foils, the NR latex-based foil type "Lp" exhibits the highest Δw_{mat}, which is unfavorable. In Figure 31 (b), the engineering stress-strain curves for the two selected NR latex types are shown. The foil type "Lp" displays a pronounced, enlarged hysteresis area. In comparison, the foil type "Lp" requires nearly twice the work input per cycle for the strain range between 0 and 700 %. For both NR latex-based foil types, increasing the strain rate from 9.7 to 14 s^{-1} does not lead to a significant temperature increase. However, it remains possible that quasi-adiabatic loading conditions are not achieved due to the low foil thicknesses of 120 µm and 60 µm. The quasi-adiabatic loading conditions are discussed in Chapter 4.3.5.

In summary, the evaluation of the tested foils reveals that only type "SIS" is deemed unsuitable, as discussed in the preceding sections. The remaining foils that were subjected to testing have been determined to be potentially suitable for elastocaloric cooling. Consequently, they are being evaluated in elastocaloric cooling devices. Owing to the highest COP_{mat}, the NR foils of type "K" and "Chic" represent the most promising foils in terms of elastocaloric performance among

those characterized. The performance of the corresponding devices are presented in Chapters 0 through 7.

4.3.4 Shape Change and Surface-to-Volume Ratio under Deformation

During deformation, significant shape changes occur. This is crucial because several hundred percent of strain is required to trigger the elastocaloric effect. Therefore, the shape change in all three dimensions is studied. Additionally, shape changes are important because the heat transfer during the deformed state and heat absorption during the undeformed or pre-strained state occur within different refrigerant geometries. This is relevant because the heat transfer time is also influenced by the thickness of the refrigerant specimen [19].

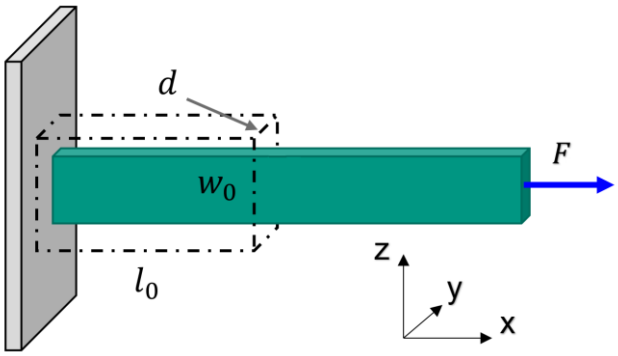

Figure 32: Schematic of the shape deformation behavior. The undeformed elastomer specimen is visualized by dashed lines while the solid green body denotes the sample under deformation. A uniaxial load is applied through the force component F along the x-axis. The initial length l_0 and the initial thickness d and w_0 describe the sample dimensions in x, y and z-direction, respectively.

In Figure 32, the three-dimensional deformation of the elastic specimen under uniaxial loading is visualized. The specimen's undeformed initial dimensions, visualized by dashed lines, are defined by the length l_0, the thickness d and the width w_0 which describe the geometric dimensions in the x-, y- and z-direction, respectively. By applying an uniaxial load in the x-direction with the force F, the dimensions of the specimen are altered. With increasing strain, the length of the specimen increases while the cross-sectional area of a tensile specimen decreases, illustrated by the green body in Figure 32. The schematic is simplified at the fixed support, as the actual deformation in this region would deviate from linear behavior. For a specimen made of material type "K" with an initial thickness of 650 µm, the thickness decreases to 270 µm and 190 µm at 300 % and 700 % engineering strain, respectively. The detailed values are listed in Table 7. The percentage change varies among the different materials due to differences in compounding, which seems to influence the viscoelastic behavior of the specimens.

Table 7: The thickness d and width w_o values of the specimen in the undeformed state and under uniaxial loading, for the NR foils of the material types "F" and "K".

Label	F	K
Thickness at zero strain, d (µm)	290	650
Thickness at 300 % engineering strain (µm)	150	270
Thickness at 700 % engineering strain (µm)	80	180
Width at zero engineering strain, w_0 (µm)	9000	900
Width at 300 % engineering strain (µm)	5000	5500
Width at 700 % engineering strain (µm)	4000	4000

Due to the elastic properties of the tensile specimens, measuring the thickness using common measuring tools such as a caliper is problematic, as the thickness varies depending on the manually applied contact pressure. The thickness of the specimens is measured using a height gauge (MT60M) and gauge stand (MS 200) from Heidenhain. The device is equipped with a measurement tip that applies a constant force of 1.0 ± 0.2 N during measurement and has a diameter of 1 mm. The thickness is averaged over the specimen area of 26.5 × 9 mm^2 by placing a rigid, flat spacer with a known height between the specimen or elastomer sheet and the measurement tip. Elastomers are generally regarded as nearly incompressible materials, meaning that the initial volume is approximately equal to the volume under load, $V_0 \approx V_{load}$ [204]. The influence of SIC on macroscopic volumetric change is neglected. Therefore, the resulting thickness under load can be approximated by the initial volume divided by the length and resulting width under load $d_{load} \approx l_0\, d\, w_0 (L_{load}\, w_{load})^{-1}$.

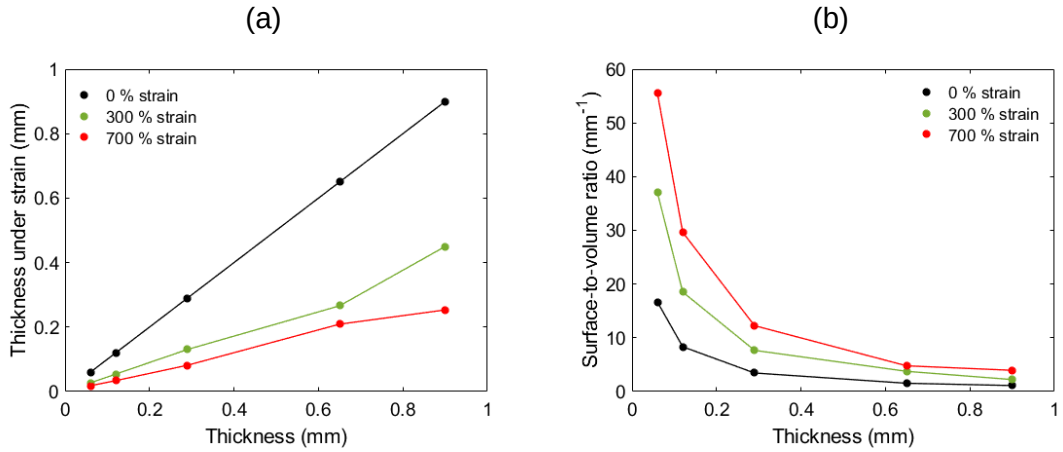

Figure 33: (a) Thickness change as function of the initial thickness for the maximum engineering strain of 0, 300 and 700 % and (b) the corresponding surface-to-volume ratio.

In Figure 33 (a), the thickness under strain is shown as a function of the initial thickness for engineering strains of 300 % (green dots) and 700 % (red dots). The black line indicates the initial thickness of the foils tested in this work, ranging from 60 to 900 µm. For example, for foils with an initial thickness of 120 µm, the thickness reduces to approximately 55 µm and 35 µm at

engineering strains of 300 and 700 %, respectively. Due to shape changes under deformation, the surface-to-volume ratio also changes. The surface-to-volume ratio can be expressed as $d(\varepsilon)^{-1}$.

In Figure 33 (b), the changes in surface-to-volume ratio are presented as a function of the initial thickness for engineering strains of 0 % (black dots), 300 % (green dots), and 700 % (red dots). The surface-to-volume ratio increases with increasing applied engineering strain and decreasing initial foil thickness. In summary, rapid heat transfer is promoted by the increase in surface-to-volume ratio in thinner foils and under deformation, which also enlarges the foil surface and, consequently, the heat transfer contact area.

4.3.5 Engineering Strain Rate and Quasi-Adiabatic Behavior

During mechanical loading and unloading heat transfer within the foil and the surrounding takes place. To avoid unwanted parasitic heat flow, loading and unloading needs to be fast enough, to measure the generated and absorbed heat [19]. It is known that SIC occurs within a few milliseconds [79]. Therefore, the strain rate can be gradually increased until quasi-adiabatic conditions are reached. In Figure 34, (a) two different time-dependent strain stimuli with an engineering strain rate of 0.1 and 9.3 s^{-1} and (b) the corresponding temperature evolution with respect to room temperature are given for a foil type "K". The maximum applied engineering strain is 700 % and the hold time t_{load} for temperature equalization back to room temperature after loading and unloading is 120 s. For the low engineering strain rate of 0.1 s^{-1} corresponding to a loading and unloading time t_{load} of around 70 s the temperature change ΔT_h is 1.3 K and ΔT_c is -3.1 K. While for an engineering strain rate of 9.3 s^{-1}, equal to t_{load} = 0.78 s, ΔT_h results in 7.4 K and ΔT_c is -10.3 K. The difference in the temperature change leads to the assumption that for the lower engineering strain rate no quasi-adiabatic conditions can be reached. In the following a detailed analysis of different engineering strain rates is given.

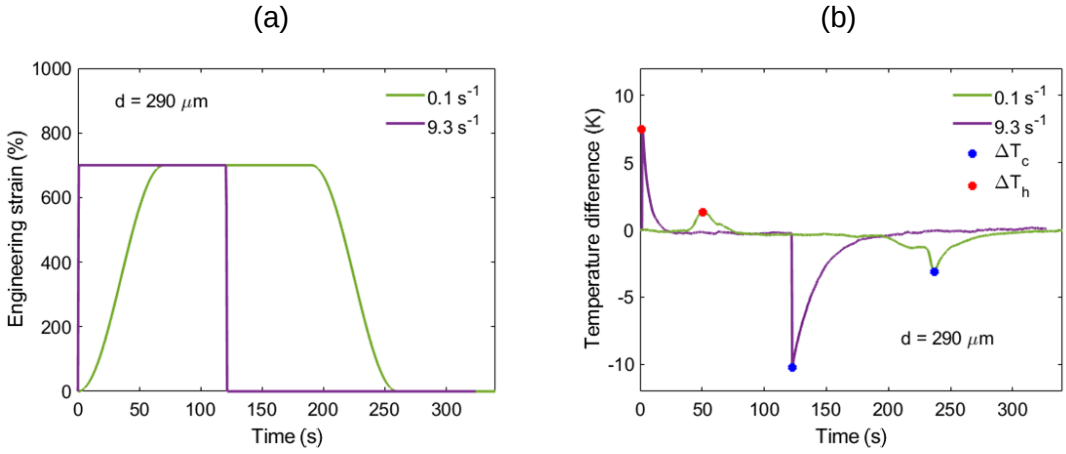

Figure 34: (a) The time-dependent applied engineering strain and (b) the corresponding temperature difference relative to room temperature over time, for the foil type "K" with a thickness of 290 µm. The engineering strain rate is 0.1 and 9.3 s^{-1}.

The influence of the engineering strain rate on the elastocaloric temperature difference is investigated for NR specimens composed of material types “F” and “K” with foil thicknesses of 290 and 650 µm. In Figure 35, the temperature differences upon loading ΔT_h (red dots) and unloading ΔT_c (blue dots) as a function of the engineering strain is given. Green dots are used to represent the difference in cooling and heating. To guide the eye and distinguish between material types, line connections are applied between the discrete measured temperature values. A solid line represents material type “K” with a foil thickness of 650 µm and a dotted line corresponds to type “K” with a foil thickness of 290 µm. A dashed line indicates type “F” with a foil thickness of 290 µm.

The engineering strain rate is varied between 0.1 and 14.0 s^{-1}. For an engineering strain rate of 14.0 s^{-1}, a temperature difference upon unloading of -10.3 K is reached for specimen’s type “K”, whereas a lower value of -8.3 K is observed for type “F”. Across all the curves, the steepest slope and thus the greatest change in the measured temperature difference is observed in the range between 0.1 and 1.0 s^{-1}. For instance, for the specimen with material type “K”, 88 % of the maximum ΔT_c value (achieved at 14.0 s^{-1}) is already reached at 1.0 s^{-1}. For engineering strain rates $\geq$ 1.0 s^{-1}, a saturation behavior is observed. Among all specimens, the values of ΔT_c for material type “F” consistently show the lowest values in terms of magnitude. To reach the maximum value of ΔT_c within a change of a 2.5 % deviation, different engineering strain rates $\dot{\varepsilon}_{ad}$ are needed. For the foils with a thickness of 290 µm an engineering strain rate of 9.3 s^{-1} is needed, while for the foils with a thickness of 650 µm, 4.7 s^{-1} is sufficient [19]. The values represented by the green dots are always negative, indicating that, in terms of magnitude, the temperature difference during unloading is greater than during loading $|\Delta T_c| > |\Delta T_h|$. As an exception, the condition $|\Delta T_c| \approx |\Delta T_h|$ applies to specimen type “K” with the highest foil thickness of 650 µm at the maximum strain rate.

This indicates that the needed engineering strain rate to create quasi adiabatic conditions $\dot{\varepsilon}_{ad}$ for loading and unloading is thickness dependent. Moreover, there is an observed difference in loading and unloading for a $\dot{\varepsilon}_{ad}$. While during unloading $\dot{\varepsilon}_{ad}$ of 9.3 s^{-1} is sufficient for a foil with an initial thickness of 290 µm. Quasi-adiabatic conditions cannot be achieved during loading, even at the maximum strain rate of 14.0 s^{-1}. This means a fraction of the generated heat is absorbed by the surroundings. The effect can even be quantified by comparing the final values of the specimens type of type “K”. For an engineering strain rate of 14.0 s^{-1}, it is found that 25 % of the generated heat is rejected to the surroundings during loading for the foil with a thickness of 290 µm, in comparison to the 650 µm foil.

The origin of this observation can be explained by the SIC formation mechanism, since it is mainly responsible for the elastocaloric temperature change. The melting of crystallites starts at lower strains than crystallization. For more details, this is discussed in Chapter 2.4 and illustrated in Figure 5. In addition, during loading the foil thickness decreases, while unloading the thickness increases back to the initial thickness. This means crystallites formation and melting takes place at different foil thicknesses and thinner foils exchange heat more rapidly, leading to a higher required engineering strain rate to reach quasi adiabatic conditions upon loading [19].

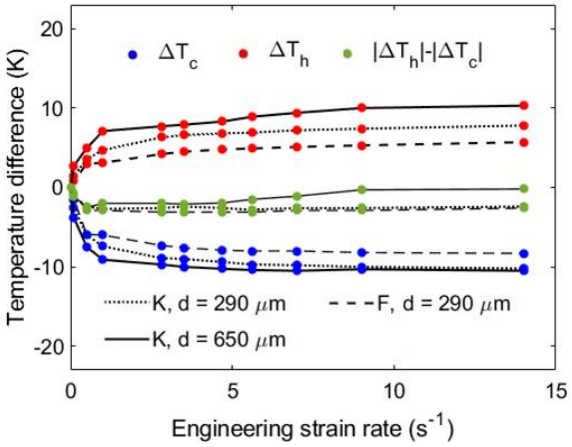

Figure 35: Engineering strain rate dependent temperature difference for NR specimens. For high engineering strain rates $\dot{\varepsilon}_{ad}$ no parasitic heat flow to the surrounding takes place and therefore quasi-adiabatic conditions are reached. For foils with a thickness of 650 µm $\dot{\varepsilon}_{ad}$ is 4.7 s^{-1}, while for foils with a thickness of 290 µm $\dot{\varepsilon}_{ad}$ of 9.3 s^{-1} is needed. The connection between the measurement points serves as a guide for the eye. Adapted from [19] licensed under CC BY 4.0.

The stress-strain response at various strain rates for NR foil type "K" with a thickness of 650 µm is presented in Figure 36 (a). The curves, which exhibit typical hysteresis behavior, are free from the Mullins effect. The maximum engineering stress, occurring at the end of the loading phase, varies depending on the applied engineering strain rate and reaches values on the order of a few MPa. Specifically, the maximum engineering stress increases with increasing engineering strain rate, ranging from 2.3 to 3.6 MPa for engineering strain rates between 0.1 and 14.0 s^{-1}, respectively. The increase in stress is accompanied by a corresponding rise in the hysteresis area. The loading curves are identical up to 100 % engineering strain, after which they begin to diverge, as evidenced by different curve slopes, leading to an increase in work input. The work input ranges from 4.3 to 9.8 Jg^{-1} for the minimum to maximum engineering strain rates. At an engineering strain rate of $\dot{\varepsilon}_{ad}$ = 4.7 s^{-1}, the work input is 7.2 Jg^{-1}. For temperature equalization after loading, the maximum strain of 700 % is kept constant for 120 s, during this hold time a stress relaxation is observed, given by the vertical drop in the stress-strain curve. The drop increases with an increasing engineering strain rate, although all curves converge to a final stress level of approximately 1.8 MPa. Due to the stress relaxation induced by SIC unloading takes place at significantly reduced stress levels [205]. Unloading exhibits negligible dependence on the engineering strain rate. The corresponding work input, absorbed heat per cycle, and the resulting COP_{mat} is given in Figure 36 (b). By increasing the needed work input to deform the foil, also the COP_{mat} is affected. An increase in the engineering strain rate from 4.7 to 14.0 s^{-1} results in a 22 % decrease in the coefficient of performance COP_{mat}, reducing it from an initial value of 2.7.

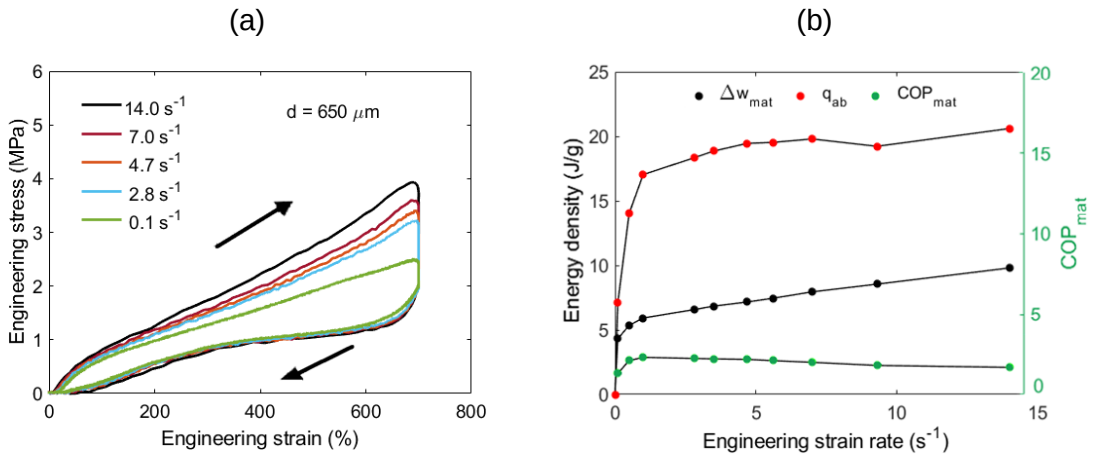

Figure 36: (a) Engineering stress-strain curves of a NR foil type "K" with a thickness of 650 µm under uniaxial tension at various engineering strain rates $\dot{\varepsilon}$, ranging from 0.1 up to 14.0 s^{-1}. (b) The corresponding work input and specific absorbed heat and the resulting COP_{mat}. Adapted from [19] licensed under CC BY 4.0.

The increased hysteresis observed with higher engineering strain rates can be assumably explained by the stress relaxation behavior. For higher strain rates the relaxation mainly takes place after loading, while for lower engineering strain rates, stress relaxation already takes place during loading and therefore lowers the stress. Similar stress-strain behavior is observed for foils type "F". Moreover, the increased stress attributed to higher strain rates aligns well with findings in the literature [91,206]. Overall, higher engineering strains and strain rates lead to an increase in the work input [19]. Subsequently, the COP_{mat} is altered, which should be considered when evaluating the performance.

4.3.6 Pre-Strain Characteristics

In comparison to shape memory alloys, elastomers require a relatively large deformation, with strains reaching several hundred percent, to generate significant elastocaloric temperature changes. This drawback limits both the size of a cooling device and its operating frequency due to the time required for the mechanical displacement. By applying a constant mechanical pre-strain in tension, the actively required displacement needed to achieve a certain strain can be reduced. For instance, to achieve a total strain of 700 % by using a pre-strain of 300 %, the displacement is reduced by 42 %. In Figure 37 the initial specimen geometry, equal to 0 % of engineering strain and an initial length L_0, as well as the geometry under 300 % engineering pre-strain is visualized. The 300 % engineering pre-strain is maintained statically and forms the starting and ending points of the loading and unloading phases. In addition, the surface of the specimen is increased by 48 %, enabling a larger heat transfer interface facilitating heat absorption from the source to the refrigerant. The increase in the surface-to-volume ratio is even more significant, quantified at 240 %. The calculation of the percentage increase in surface area and surface-to-volume ratio is based on the specimen type "K" with a thickness of 650 µm. In the case of modified compounding and the associated differences in geometric changes under deformation, deviations in the percentage change may occur.

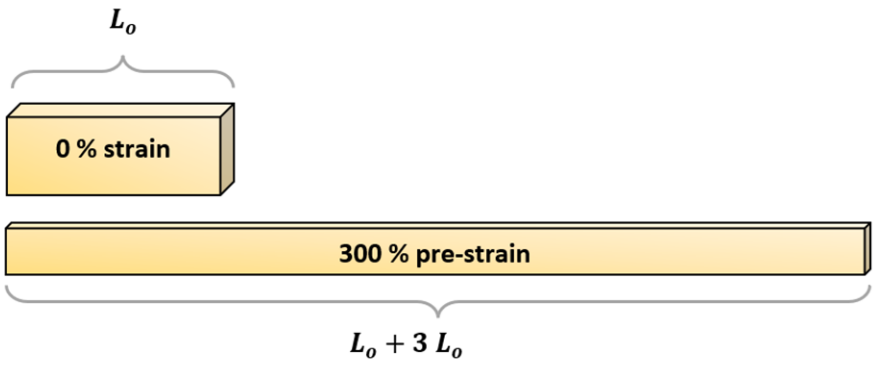

Figure 37: Illustration of the specimen geometry in the initial undeformed state (0 % strain) and after application of 300 % engineering pre-strain. The corresponding changes in surface area and surface-to-volume ratio are visually represented.

In the following, it is investigated how the pre-strain influences the ΔT_{ad}, work input Δw_{mat} and resulting coefficient of performance of the material COP_{mat}. Applying a pre-strain is beneficial in two ways: the heat transfer area is increased for cooling, and the required work input is lower [19]. However, this comes at the cost of a reduced ΔT_{ad}. This is exemplified by an NR foil of type "K" with a thickness of 650 µm. The temperature differences during loading ΔT_h (red dots) and unloading ΔT_c (blue dots) as a function of the engineering pre-strain are shown in Figure 38 (a). With increasing engineering pre-strain ΔT_{ad}, decreases. At 300 % engineering pre-strain, ΔT_{ad} decreases by 35 % to an absolute value of 12.4 K, compared to the case without applied engineering pre-strain [19]. For an engineering pre-strain of 600 %, ΔT_{ad} result in 3 K.

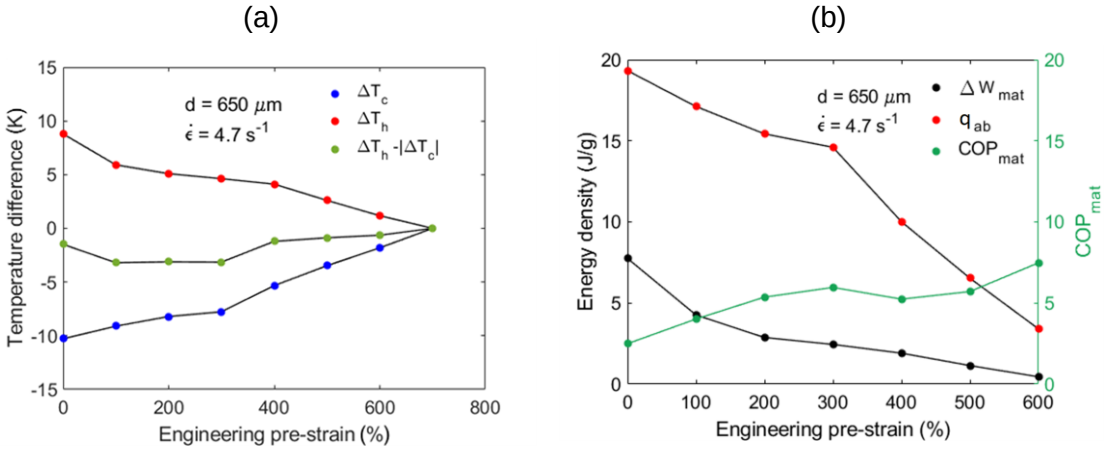

Figure 38 (a) The temperature difference during loading ΔT_h and during unloading ΔT_c as a function of the maximum engineering pre-strain for a NR type "K" with a thickness of 650 µm. The engineering strain rate of 4.7 s^{-1} and a maximum engineering strain of 700 % is applied. (b) The corresponding work input Δw_{mat} the absorbed heat q_{ab} and the resulting COP_{mat}. The solid lines indicate the connections between the points. Adapted from [19] licensed under CC BY 4.0.

The reduction of ΔT_c corresponds to a decrease in the absorbed heat. The absorbed heat q_{ab}, the Δw_{mat}, and the resulting COP_{mat}, as a function of the engineering pre-strain, are shown in Figure 38 (b). Both q_{ab} and Δw_{mat} decrease with increasing engineering pre-strain. The resulting

COP_{mat} increases with increasing engineering pre-strain. A local maximum is observed at 300 % engineering pre-strain, where the COP_{mat} reaches a value of 6, which is nearly two and a half times higher than the initial value [19]. The highest COP_{mat} of 7.5 is obtained at 600 % engineering pre-strain.

Therefore, the engineering strain range of 300 to 700 % is identified as the optimum cycling range for elastocaloric cooling devices based on NR foils, as discussed in the following chapters [19]. This is justified by the elevated COP_{mat} of 6 and ΔT_{ad} of 12.4 K, which remains adequate for effective cooling [19]. In addition, the surface area available for heat transfer increases by 48 %, and the surface-to-volume ratio rises by 240 % compared to the undeformed state.

5 Single-Stage Elastocaloric Cooling Device

In this chapter, the implementation and characterization of demonstrator devices for miniature-scale elastocaloric cooling using natural rubber (NR) foil specimens are presented. The foil specimens feature a lateral size of 26.5 × 9 mm^2, with thicknesses ranging from 60 to 800 µm. The development of the devices is based on the material characterization presented in Chapter 4, in which the elastocaloric effect is investigated under uniaxial tensile loading conditions for various types of foil specimens. The following specimens investigated are considered potentially suitable for foil-based elastocaloric cooling. They range from commercially available NR material (type "K") to synthetically fabricated NR provided by cooperation partners of the University of Freiburg (type "F"). This also includes a recyclable NR formulation developed using a novel cross-linking approach (type "Chic"). In addition, NR latex (type "L"), sourced from a commercial supplier, is also included in the study due to its availability in thin foil form with thicknesses down to 60 µm. An overview of the thermal and mechanical properties of the different foil specimens, along with their corresponding types, is provided in Table 6.

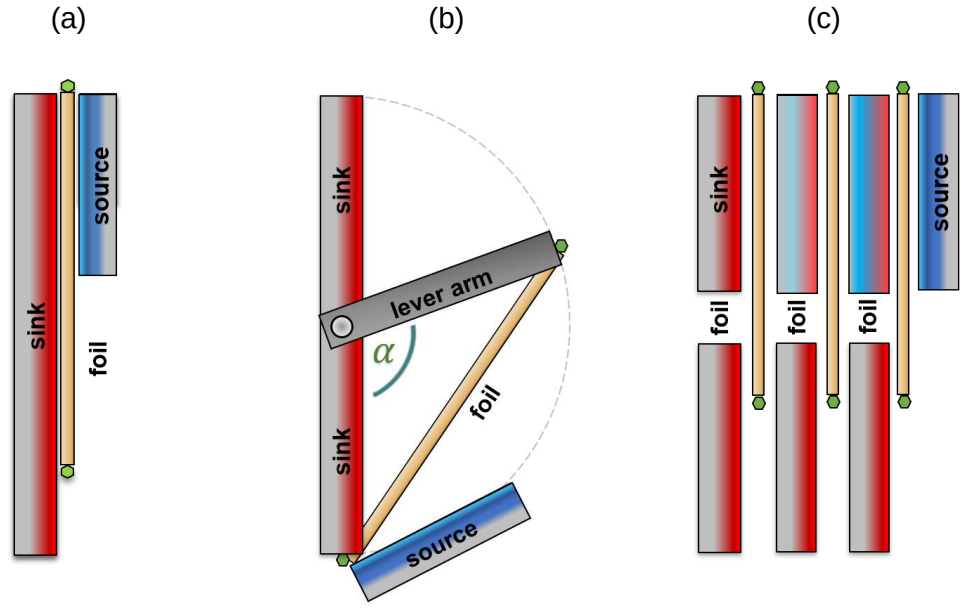

Figure 39: Devices developed within this work. (a) Monostable single-stage (b) bistable single-stage and (c) cascaded device.

A total of three different elastocaloric cooling devices based on natural rubber (NR) foils are developed within this work. Heat transfer is accomplished by solid-to-solid mechanical contact. Two single-stage devices utilize one foil refrigerant: one is driven by two actuators, while the other employs a bistable actuation mechanism characterized by power savings and reduced

actuation forces. The third device design comprises three cascaded foils thermally connected in series, which require an enhanced design architecture discussed in detail in Chapter 7.

The implementation includes the design and fabrication of key device components, such as custom foil holders. The benefits of applying an engineering pre-strain to the foil specimen are discussed with respect to both the design and heat transfer. The setup used for synchronized data acquisition and peripheral communication, and control enables the coordination of cyclic mechanical excitation and heat transfer timing. This also allows the investigation of different operating frequencies of the elastocaloric cooling device. The acquired data are used to derive performance metrics such as the device temperature span, cooling power, and coefficient of performance. These metrics serve to compare different foil types and thicknesses, thereby evaluating their influence on the overall device performance.

5.1 Device Implementation

To realize a cooling application, the spatial separation of heat flow must be employed. In a cooling device, the heat source is the region where heat is absorbed from, while the heat sink is the region where heat is rejected. The separation process and the elastocaloric effect itself are enabled by cyclic operation and are realized through external actuators. The device designs presented herein utilize solid-to-solid heat transfer through alternating foil surfaces, enabling the foil refrigerant to heat the heat sink and cool the heat source. To keep system complexity low, fluid-free architectures with a minimal number of external actuators are designed. While one actuator enables the mechanical loading cycle, a second actuator facilitates heat transfer. To further reduce the number of actuators, a single-stage bistable device configuration is introduced. Besides minimizing system complexity, the implementation also takes cost efficiency into account. Since material cost is one of the main arguments for using NR as a refrigerant, a key requirement is that the cooling device remains cost-efficient, which necessitates avoiding the use of expensive, large-scale hydraulic or pneumatic equipment that could increase both the overall cost and footprint. This inevitably requires good thermal contact between the rubber-based refrigerant and both the heat source and the heat sink. Moreover, as the cooling power is currently limited and inadequate for air conditioning, the application focuses on the miniature scale, requiring a compact design. The implementation of a cooling device based on elastocaloric elastomers requires large strokes due to the strain dependence of the elastocaloric temperature span, as discussed in Chapter 4.3.3. The active stroke, which arises from the engineering strain range, and therefore sets a minimum size limit in one dimension of the device. The remaining dimensions, corresponding to the foil's width and thickness, are negligible when considering the minimum achievable size of the device. For a maximum engineering strain of 700 % and a static engineering pre-strain of 300 %, which define both the initial and final states of the mechanical loading and unloading phases, the active stroke can be reduced by 43 %. An engineering pre-strain of 300 percent is selected due to the enhanced performance observed at this operating point, as identified in Chapter 4.3.6. Additionally, the surface area of the specimen increases by 48 %, thereby enlarging the heat transfer interface and enhancing heat absorption from the heat

source to the refrigerant. The corresponding increase in the surface-to-volume ratio is even more pronounced, amounting to 240 %. These values are calculated based on specimen type “K” with an initial thickness of 650 µm. Besides the length change, the contact area is changed due to the viscoelastic properties of the foil specimen when in contact with the heat sink, in comparison to contact with the heat source. This is attributed to the cyclic mechanical loading and the resulting shape change of the specimen in all three dimensions. Details are provided in Chapter 4.3.4.

Since the engineering strain in the loading direction is defined as a multiple of the initial length L_0, it should be kept as small as possible. The achievable minimum length depends on the holder concept. In this case, a length of 26.5 mm is attained. Even shorter lengths are possible, but this comes with a trade-off in terms of high-cycle stability. High-cycle stability is also ensured by selecting a design with minimized friction, which helps prevent early device failure caused by foil specimen breakage due to surface damage. This is achieved by eliminating relative motion between the foil specimen and the heat sink or source, which are arranged as flat, parallel surfaces. Other, more compact designs capable of realizing high engineering strains, such as those using meander structures guided over deflection rollers, increase friction on the surface of the foil specimens. In addition, they hinder the realization of heat transfer separation due to the reduced accessibility of the foil surface. Another compact design can be realized using an inverted V-shaped heat sink. However, additional friction is introduced at the top of the cusp, as deformation is induced by sliding the foil surface over this point. A device based on this concept has been published by the author [203]. Considering high-cycle stability, the holder design plays a critical role and is therefore discussed in detail in the following section.

To sum up, applying an engineering pre-strain not only proves beneficial in terms of performance, by reducing the required work input per cycle, but also promotes rapid heat transfer and decreases the active stroke. In addition, elastic specimens require special clamping, particularly at high strains and under repeated mechanical load cycles, due to their significant lateral deformation. As a result of volume conservation, high strains lead to a substantial reduction in specimen thickness and width.

5.1.1 Specimen Holder Design

Different specimen holder designs are tested to evaluate their suitability for ensuring cyclic stability and their appropriateness for use in an elastocaloric device. In Figure 40 (a)-(d) the schematics and photographs of different specimen holders are shown. The external clamping force $\vec{F}_{clamp}$ and the uniaxial tensile loading force $\vec{F}_{load}$, oriented perpendicular to the clamping direction, are indicated. In Figure 40 (a) conventional rigid metallic holders with grip jaws featuring rough surfaces from the company ZwickRoell are given. The normal force $\vec{F}_{clamp}$ induces friction through a preset clamping force, thus providing frictional engagement. Failure occurs when $\vec{F}_{load}$ exceeds the frictional force generated by the pre-stress, as the clamping force does not increase accordingly. More importantly, the separation between the grip jaws remains constant

while the specimen thickness decreases under tensile loading. This mismatch creates a gap between the stationary jaws and the specimen, ultimately leading to specimen slipping. An adhesively bond specimen holder configuration is shown in Figure 40 (b). Each specimen end is glued to a T-shaped 3D-printed flat suspension, which provides geometric locking. Failure occurs at the transition zone due to stress concentration. Both configurations (a) and (b) fail within a single load cycle. A line-pressure specimen holder configuration, in which the specimen is clamped between a flat and a curved block is represented in Figure 40 (c). Failure occurs after a few cycles in the line-pressure region. By incorporating an elastic intermediate layer, the resulting frictional force and the gap between the stationary holder and the specimen can adapt to the deformed specimen. However, the elastic holder configuration presented in Figure 40 (d) fails. The elastic layer does not fully recover its shape after each cycle, leading to cumulative deformation. A fraction of the elastic layer is positioned outside the holder. In summary, configuration (b) is adhesively bonded and geometrically locked by a T-shaped suspension, whereas configurations (a), (c), and (d) rely on frictional engagement generated by the normal force arising from $\vec{F}_{clamp}$.The configurations (c) and (d) fail after less than five load cycles due to specimen breakage or slippage from the holder. Consequently, none of the presented holder designs are suitable for repeated cyclic loading in elastocaloric testing.

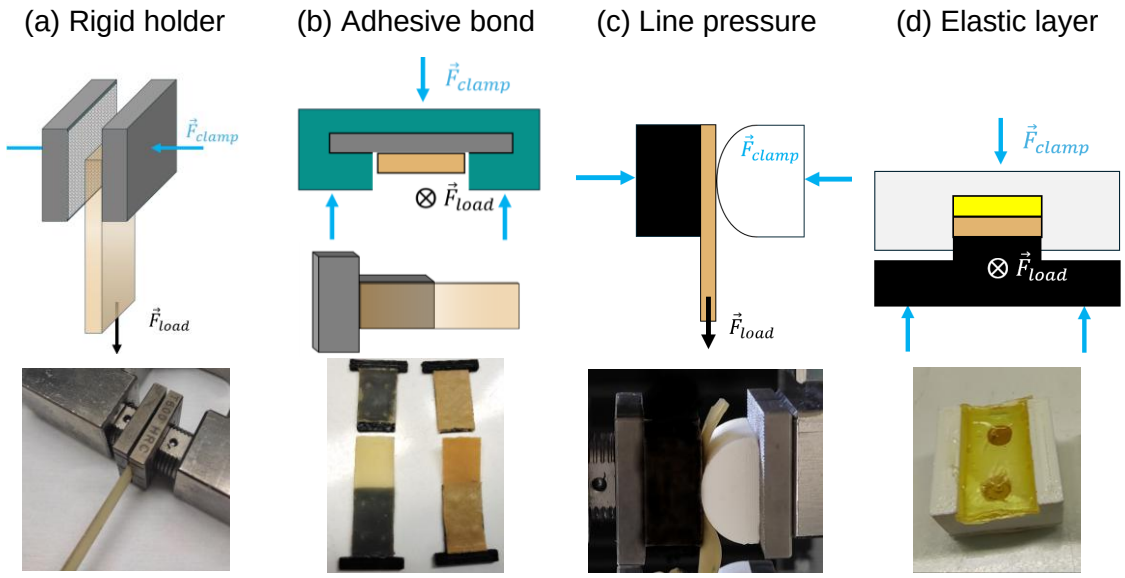

Figure 40: Schematics and photographs of the tested foil holders, along with the corresponding external clamping force $\vec{F}_{clamp}$ and the uniaxial tensile loading force $\vec{F}_{load}$. The configurations range from conventional rigid holders (a) with rough surfaces, where the specimen slips under load, to adhesive bonding connection (b) which ultimately fails at the transition zone under load (see photograph). In the line-pressure configuration (c), the specimen is clamped between a flat and a curved block, failing after several load cycles at the line-contact region. In the sandwich configuration (d), which incorporates an elastic intermediate layer, the specimen begins to slip under load after several cycles. While configuration (b) is adhesively bonded and geometrically locked by a T-shaped suspension, configuration (a), (c), and (d) rely on frictional engagement generated by the normal force resulting from $\vec{F}_{clamp}$.

Therefore, the elastocaloric cooling specimen holder must enable three-dimensional shape change of the foil during loading and complete shape recovery upon unloading. In addition, it

must accommodate various foil thicknesses, avoid stress concentrations that could lead to premature failure, and remain compact and cost-effective.

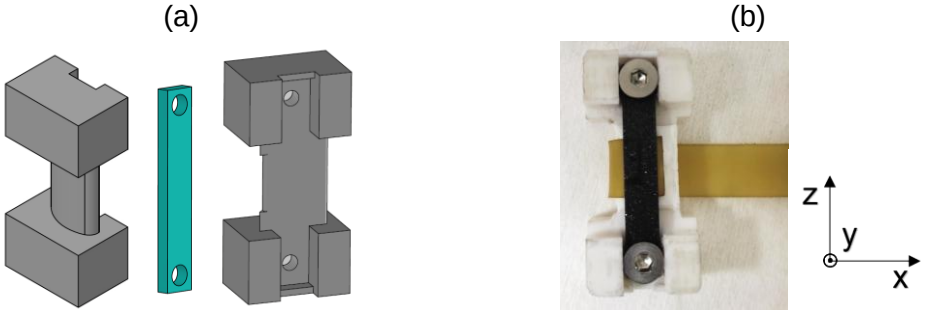

Figure 41: (a) 3D schematic and photograph of the foil holder shown from the side and rear, highlighting the threaded holes and the corresponding counter clamping bar (visualized in turquoise) part with through-holes. The rectangular clamping bar is positioned along the flat rear side of the convex half-roller, pressing the foil against the holder to ensure fixation. (b) Photograph (rear view) of a foil fixed at one end, with the required clamping force generated by short M3 screws.

In Figure 41 (a), the three-dimensional schematic of the elastocaloric cooling foil holder design is shown from side and rear views. The design is based on a half-roller featuring a convex surface on one side and a flat surface on the other. The half-roller is centered and integrated into cooling devices by form-fit suspension using cuboidal extensions at each end. Each holder is manufactured with dimensions of 35 × 16 × 11 mm^3. For fixation, the foil is wrapped around the convex surface and clamped at the flat rear side, as illustrated in the photograph in Figure 41 (b). The clamping force is applied by two M3 screws, which are inserted through the through-holes of a rectangular counter clamping bar (visualized in turquoise) and tightened into corresponding threaded holes in the rear part of the holder. This configuration allows foils with different initial thicknesses to be securely fixed.

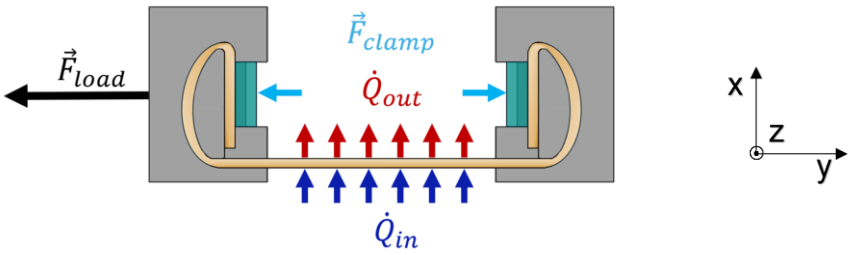

Figure 42: Schematic of the foil holder, incorporating a half-roller with a flat convex surface profile. Top view with cross-section of one pair of antagonistic holders, illustrating the applied external clamping force $\vec{F}_{clamp}$ and the uniaxial tensile loading force $\vec{F}_{load}$. The foil specimen (shown in beige color) is wrapped around the convex structure and clamped at its ends via frictional engagement. The time-alternating heat release and absorption of the foil refrigerant, represented by $\dot{Q}_{out}$ and $\dot{Q}_{in}$, occur during mechanical load cycling. The compact and cost-efficient holder design enables a three-dimensional shape change of the foil, characterized by an increase in length (y-axis) and a decrease in width (z-axis) and thickness (x-axis).

In Figure 42, the top view with cross-sectional detail of the concept of a pair of antagonistic foil holders is presented. The applied external clamping force $\vec{F}_{clamp}$ and the uniaxial tensile loading force $\vec{F}_{load}$ are indicated. During mechanical load cycling, one holder is displaced relative to the other, which remains stationary. As a result, an increase in foil length (y-direction) and a reduction in width (z-direction) and thickness (x-direction) are induced, while the foil is guided in a friction-locked manner across the convex surface. Due to the deformation, the elastocaloric effect is activated, leading to a temperature increase in the foil. Upon mechanical unloading, full shape recovery is enabled, and a reverse phase transformation is triggered, resulting in a temperature decrease. The time-alternating heat absorption and release, denoted by $\dot{Q}_{out}$ and $\dot{Q}_{out}$, are transferred across the foil surface in the y-z plane.

5.1.2 Device Fabrication

The heat sink and heat source include copper plates that serve both as thermal masses and as heat-conducting elements, facilitating the transfer and temporary storage of thermal energy. The copper plates, supplied by Goodfellow and featuring a purity of 99.9 %, have a thickness of 0.75 mm. The selected thickness arises from experimental constraints to balance thermal sensitivity and mass effects. Plates with greater thickness exhibit temperature changes that may fall below the detectable range, particularly during the initial phase of heat transfer and when used in combination with thin refrigerant foils, because the thermal mass ratio between the heat source and the refrigerant increases. Similar to thin foils, thin copper plates promote heat transfer. During loading and unloading, undesired parasitic heat flow to the surroundings occurs due to the copper plate's exposure to air. This reduces the achievable temperature span between the heat sink and the heat source. Therefore, thinner copper plates are avoided. The selected copper plate thickness represents a compromise suitable for all tested foil thicknesses ranging from 60 to 650 µm. While adapting the copper plate thickness to match the specific refrigerant foil thickness may enhance the resulting temperature change, this approach is not suitable for comparative analysis across different samples. Therefore, to ensure consistent experimental conditions, a uniform copper plate thickness is maintained.

The required in-plane dimensions of the copper plates are produced by mechanical sawing performed with a table saw. To obtain a mirror-like surface finish on the copper areas intended for direct mechanical heat transfer, the plates are sanded using abrasive paper with successive grit sizes of 1200, 1800, 2000, and 2500, with the addition of distilled water to aid the process. The edges of the plates are also beveled and smoothed by polishing to prevent surface damage and subsequent refrigerant degradation, which could lead to early device failure. The contact surface for the temperature sensor, located on the rear side of the copper plates, is also polished to remove any existing copper oxide layer. For temperature monitoring during device operation, platinum resistance temperature sensors with dimensions of $2.3 \times 2.1 \times 0.9$ mm^3 (length × width × height) are used. Pt100 sensors, with tolerance Class A, are employed for this purpose. The sensors are attached using adhesive. After pressing the sensor onto the bare copper surface, small drops of adhesive are applied to the side edges and adjacent copper areas.

This prevents the formation of an undesired intermediate layer, which could distort the measurement results. In the following step, four connection wires are soldered to each sensor to enable four-wire temperature measurement. The copper plate is then bonded to the PLA structure using cyanoacrylate adhesive. All bonding surfaces are cleaned with isopropanol prior to adhesive application. To minimize parasitic heat flow at the rear side, thermal insulation of aramid felt are placed in designated recesses between the heat sink/source support structures and the copper plates.

The load-bearing structures of the heat sinks/source and the foil holders are manufactured using 3D printers, enabling rapid and cost-efficient production of the desired geometries. The three-dimensional structures are designed using Autodesk Inventor and exported as STL files. These are then converted into GCODE files using the 3D printing software Cura and PrusaSlicer. Polylactide (PLA) filaments are processed with Ultimaker 2+ and Prusa MINI printers each equipped with a 0.4 mm nozzle. A layer thickness of 0.15 millimeter is used, while the infill density of the internal structures is adapted to the external mechanical load and varies between 50 and 100 %. An infill density of 100 % provides additional design flexibility, particularly in applications that require subsequent mechanical processing such as the integration of tapped holes. Post-processing of holes is particularly necessary for those printed orthogonally to the base plate, as they tend to become oval during printing. Through-holes and threaded holes can be successfully created by drilling, provided that sufficient lubrication, such as silicone oil, is used. This prevents the chips formed during machining from melting and adhering inside the borehole or along its edges.

5.1.3 Data Acquisition and Peripheral Communication and Control

For synchronized real-time data acquisition and system control, a compact reconfigurable input/output system (cRIO) from National Instruments (NI) is used. The control is implemented using a program coded in Laboratory Virtual Instrument Engineering Workbench (LabVIEW), which is directly deployed on the cRIO-9067 with onboard data logging and can be accessed via a PC.

Peripheral communication is realized using a master-slave architecture based on an EtherCAT network. In this architecture, a single master act as controller and communicates deterministically (with low jitter) with multiple slave devices over Ethernet to enable fast, synchronized automation. In the presented setup, the master is the LabVIEW real-time controller on the cRIO, which communicates via its Ethernet port with slave devices including actuators and I/O sensor modules. A single data frame is sent out by the master and passes sequentially through all connected devices. Each device reads and writes its designated bytes on the fly before forwarding the frame, which ultimately returns to the master, thus forming a daisy-chained bus topology. For motion control, the data frame contains the target position declared by the cRIO controller and is transmitted to the alternating current (AC) servo drives. These drives supply the modulated current for the ironless linear actuators manufactured by ESR Pollmeier GmbH. The linear actuator model ML 1612 features a maximum stroke of 256 mm and a rated force of 116 N.

Short-term peak forces of up to 400 N can be applied, and velocities of up to 9 ms^{-1} can be achieved. To close the loop and enable motion control, the servo drive feeds back the actual position and velocity signal to the master controller. For the monostable single-stage and cascaded elastocaloric cooling devices, two actuators positioned orthogonally to each other are controlled simultaneously to enable load cycling and facilitate heat transfer.

In addition to the control functionality, the master-slave architecture also enables data acquisition of elapsed time, actuator position and velocity, applied force, and the temperatures of the heat sink and heat source, recorded every 10 ms. Data acquisition is carried out via sensor-specific, signal-conditioning input/output modules integrated into the chassis as part of the controller. To measure the applied force, U9C miniature load cells with nominal capacities of 50 N and 100 N from Hottinger Brüel & Kjær (HBK) are used. These strain gauge-based transducers are characterized by an HBK accuracy class of 0.2. The force signals are acquired using the NI-9237 module, which provides four different analog input channels and can be directly inserted into the cRIO chassis. In addition to the force measurement module, two resistance temperature detector (RTD) input modules of type NI-9217 are used. Each module supports four Pt100 temperature sensors via 4-wire RTD measurement.

5.1.4 Modulation of Operation Frequency

Based on the material characterization, rapid mechanical loading and unloading are necessary to minimize heat exchange with the surrounding air and thereby utilize the full temperature span induced by the elastocaloric effect. For further details, see Chapter 4.3.5. The mechanical excitation phase is followed by a heat transfer phase, during which heat is transferred from the refrigerant to the device and vice versa. Therefore, the operation frequency is determined by the durations of mechanical loading and unloading t_{ramp} and the holding time t_{hold} required to enable heat transfer, as illustrated in Figure 43 (a). Consequently, the mechanical excitation of the actuator, which is responsible for loading and unloading the foil, follows a sinusoidal signal with a rise-dwell-fall-dwell pattern. The amplitude of the mechanical excitation is defined by the maximum engineering strain ε_{max}, and it starts and ends at the minimum engineering strain ε_{pre}.

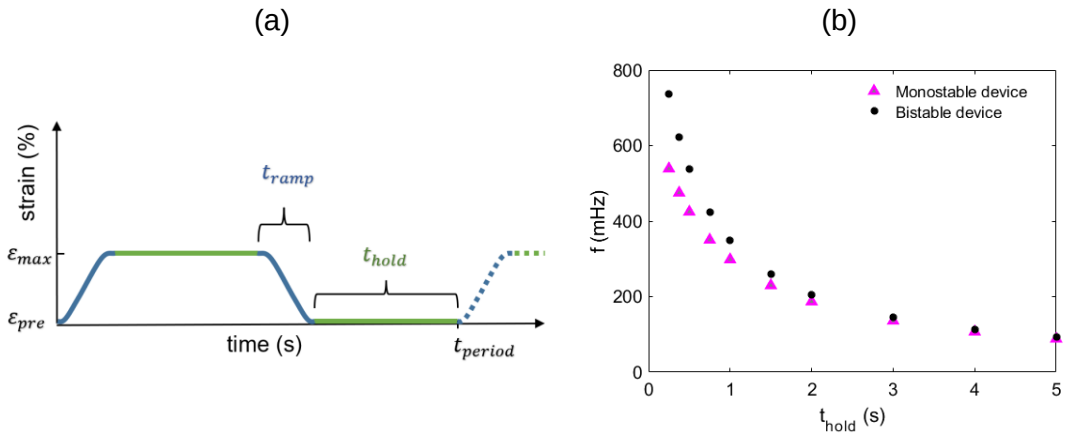

Figure 43: (a) The operation frequency is determined by the time durations of mechanical loading and unloading t_{hold} and the holding time t_{hold} required to enable heat transfer via mechanical contact between the foil refrigerant and the heat sink or heat source. The frequency is modulated by varying t_{hold}, while t_{ramp} is maintained constant at 430 ms. (b) Discrete operation frequencies as a function of t_{hold} for monostable and bistable elastocaloric cooling devices are shown. Adapted from [19] licensed under CC BY 4.0.

To match the mechanical and thermal response times of the device, the operating frequency is modulated. This modulation is achieved by varying t_{hold}, enabling the identification of optimal operating conditions. The frequency is defined as the inverse of the period of one cooling cycle, $f = {t_{period}}^{-1}$. Due to experimental constraints arising from the need to actuate two linear actuators simultaneously within the monostable devices, additional 250 ms are considered. In Figure 43 (b), the operating frequencies as a function of t_{hold} are shown for both the monostable and bistable elastocaloric cooling devices. The bistable device can be driven by only one actuator and can therefore achieve higher frequencies, as given in Equation 5-1.

$$f(t_{hold}) = \begin{cases} (2\,t_{hold} + 2\,t_{ramp} + t_{exp})^{-1} & Monostable\ device \\ (2\,t_{hold} + 2\,t_{ramp})^{-1} & Bistable\ device \end{cases} \quad \textbf{5-1}$$

5.2 Monostable Single-Stage Device

A straightforward and intuitive configuration for a single-stage elastomer foil-based device consists of two parallel, planar heat sink and heat source units. These units come into mechanical contact with the refrigerant following mechanical loading and unloading, respectively. Thereby establishing this configuration as an initial baseline design for elastocaloric cooling devices. In Figure 44, the schematic is presented. The thermal energy generated and absorbed within the elastomer foil due to the elastocaloric effect is selectively transferred to the heat sink and heat source. This enables spatial separation of the hot and cold heat flow. The geometry and dimensions of the heat sink and heat source are designed to match the rectangular contact area of the foil specimen. Due to the elastic properties of the material, the length and width of the contact area change during deformation. Mechanical loading induces deformation in the specimen, resulting in an increase in length and a decrease in width and foil thickness. Therefore, the copper plate of the heat sink, which absorbs heat, is 4 mm wide in the y-direction and is 2.25 times

narrower than the copper plate of the heat source. In contrast, its length in the y-direction is twice that of the source plate.

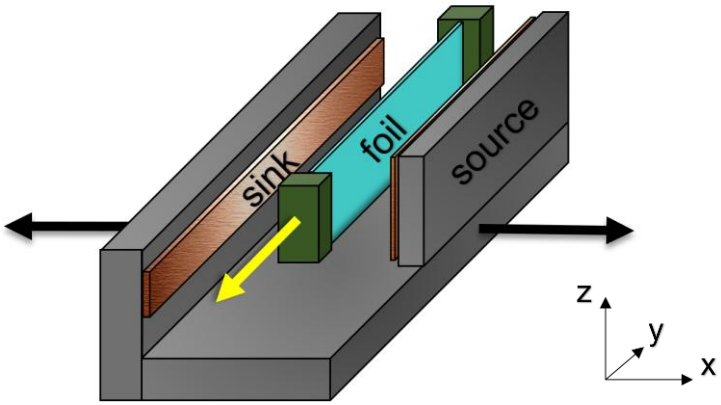

Figure 44: Three-dimensional schematic of the monostable single-stage elastocaloric cooling device based on NR foils, at its neutral, initial position. The device comprises a plane-parallel heat sink/source unit. The yellow arrow along the y-axis indicates the uniaxial tensile loading (strain range: 300 to 700 %) direction of the foil refrigerant. The black arrows along the x-axis indicate the movement of the heat sink/source unit to establish mechanical contact and enable heat transfer. The heat sink and heat source dimensions are adapted to the strain-dependent heat transfer area of the foil.

Since the heat sink and heat source alternate contact with the foil, integrating them into a single unit is advantageous. The combined heat-sink/source unit is mounted on a linear actuator for translation (indicated by the black arrows) along the x-axis from its neutral position. Translation in the positive x-direction establishes mechanical contact between the heat sink and the foil, whereas movement in the negative x-direction engages the heat source.

For load cycling indicated by the yellow arrow, a second actuator oriented perpendicular to the first displaces one end of the foil, including the specimen holder, along the y-axis, while the heat-sink/source unit remains in its neutral position as visualized in Figure 44.

5.2.1 Operation Principle

In Figure 45, the operating principle of the elastocaloric monostable single-stage cooling device with uniaxial tensile load cycling is presented. The NR foil is at room temperature in its initial state. In step I, quasi-adiabatic mechanical uniaxial loading of the foil, indicated by the black force vector $\vec{F}_y$, induces a release of latent heat due to entropy elasticity (EE) and strain-induced crystallization (SIC), resulting in an increase in the foil's temperature. In the subsequent step II, the generated heat is transferred to the heat sink through movement in the x-direction, indicated by the force vector $\vec{F}_x$, enabling a solid-to-solid mechanical contact. As a result, the heat sink temperature rises while the refrigerant cools back to room temperature. This is followed by rapid unloading, which initiates the reverse transformation and causes cooling of the foil refrigerant, corresponding to step III. Upon contact with the heat source, latent heat is absorbed,

which reduces the temperature of the heat source and simultaneously restores the refrigerant to room temperature, corresponding to the final step IV. Within the four-step cooling cycle, an engineering strain range of 300 to 700 % is used.

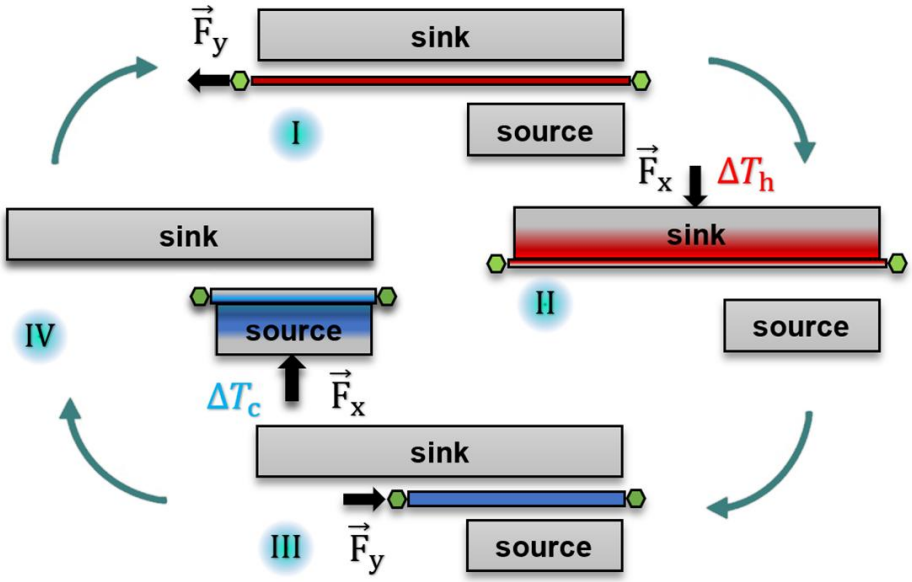

Figure 45: Schematic of the monostable single-stage elastocaloric cooling cycle. The cooling cycle consists of four steps, beginning with the mechanical loading of the foil specimen which is fixed between two holders, shown as green octagons and heating (I) followed by the heat rejection to a heat sink (II) and the unloading and cooling (III) and finalized by the heat absorption from a heat source (IV). $\vec{F}_y$ and $\vec{F}_x$ indicated by black arrows denote the forces responsible for tensile loading/unloading (300-700 % of engineering strain) of the foil and for ensuring mechanical contact with the heat sink/source, respectively. Adapted from [19] licensed under CC BY 4.0.

5.2.2 Lumped Element Model Device Simulation

To predict performance metrics of the elastocaloric cooling device, such as cooling power, a lumped element model (LEM) is employed. The lumped element approach simplifies the analysis of thermal systems and is therefore utilized in simulations. Thermal interactions at the various interfaces and the consequent heat flow within the system are captured in the model, which is implemented using MATLAB Simulink, Simscape. A schematic of the LEM of the single-stage elastocaloric cooling device, comprising key components acting as thermal capacitors, such as the elastomer foil, copper elements serving as heat sink and heat source, and polymeric support structures, is presented in Figure 46. The elastocaloric effect in the NR foil is implemented by a heat pulse applied at the end of each loading and unloading cycle, alternating between heating and cooling. The resulting adiabatic temperature change is uniformly distributed throughout the refrigerant foil. The amount of heat is experimentally investigated, see Table 6. The device is divided into discrete elements, each assumed to be thermally thin and characterized by a uniform internal temperature. Thermal coupling between elements is modeled using heat resistances defined as $R = h^{-1}A^{-1}$, where h is the heat transfer coefficient and A denotes the

contact area. Multiple modes of heat transfer are considered, including convection to the ambient air and conduction between adjacent NR segments limited by h_{cond}. Convective heat transfer at the free surfaces of the foil is described using a coefficient of h_{conv}.

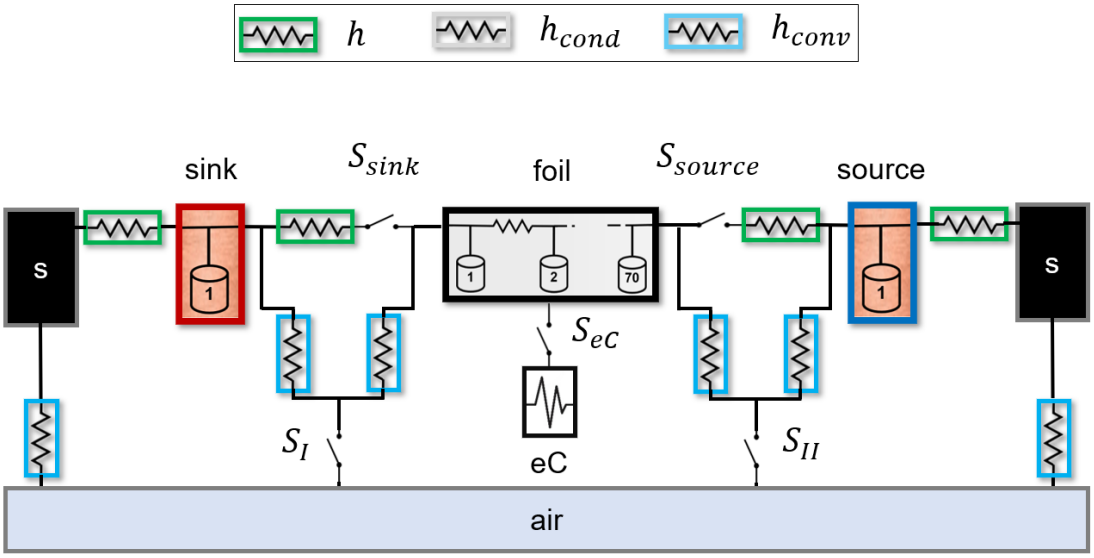

Figure 46: Schematic of the lumped element model (LEM) of a single-stage elastomer foil-based elastocaloric cooling device. The device is subdivided into elements represented as thermal capacitors, which are connected by heat resistances allowing bidirectional heat transfer. While convective heat transfer to the air is defined by h_{conv}, the heat transfer between the sink/source and the foil is limited by h. The foil is discretized into thermally thin segments ($Bi < 0.1$), which are interconnected by heat conduction h_{cond}. The four-step cooling cycle is implemented through time-dependent switching elements ($S_I, S_{II}, S_{sink}, S_{source}$ and S_{eC}). Legend: s—support; eC—elastocaloric. Adapted from [19] licensed under CC BY 4.0.

The time-dependent and location-dependent temperature within the elements is governed by internal heat transfer and heat exchange at the boundary surfaces. The Biot number (Bi) quantifies the ratio between conductive heat transfer within the body and the heat transfer between a body and its environment over the boundary surfaces, as given in Equation 5-2. The variable λ denotes the thermal conductivity of the material, h is the heat transfer coefficient between the material and its adjacent environment, and L is the characteristic length. In the case of contact between the foil and the heat sink or source elements, the characteristic length is defined by the foil thickness d and can be expressed as $L = d/2$.

$$Bi = \frac{h\,L}{\lambda} \qquad 5\text{-}2$$

In the limiting case where the Biot number approaches zero (Bi → 0), the temperature within a body becomes spatially uniform and varies only with time. Under these conditions, the body is considered *thermally thin* and can be represented as a *lumped element*. Simscape enables the modeling of physical systems, such as electric motors or cooling devices, within the Simulink environment. A Biot number below 0.1 is considered as practical approach for obtaining reliable results and is therefore used for the model implementation [190]. To meet this condition, the

system must be discretized into multiple segments. Since the thermal conductivity and heat transfer coefficient are fixed parameters, lumped elements can only be achieved by adjusting the segment thickness. For the calculation, a thermal conductivity of $\lambda = 0.15\ Wm^{-1}K^{-1}$ for NR at room temperature is used [189]. As the heat transfer coefficient is initially unknown, a high value of $h = 1000\ Wm^{-2}K^{-1}$, representing two ideal metal bodies pressed together at ambient pressure, is assumed [190]. A high value is used, as this results in a finer segmentation and therefore covers smaller values. A maximum segment thickness of 30 µm is calculated accordingly. In order to perform predictions using the LEM simulation for foils with a thickness of, for example up to 2 mm, 70 segments are required.

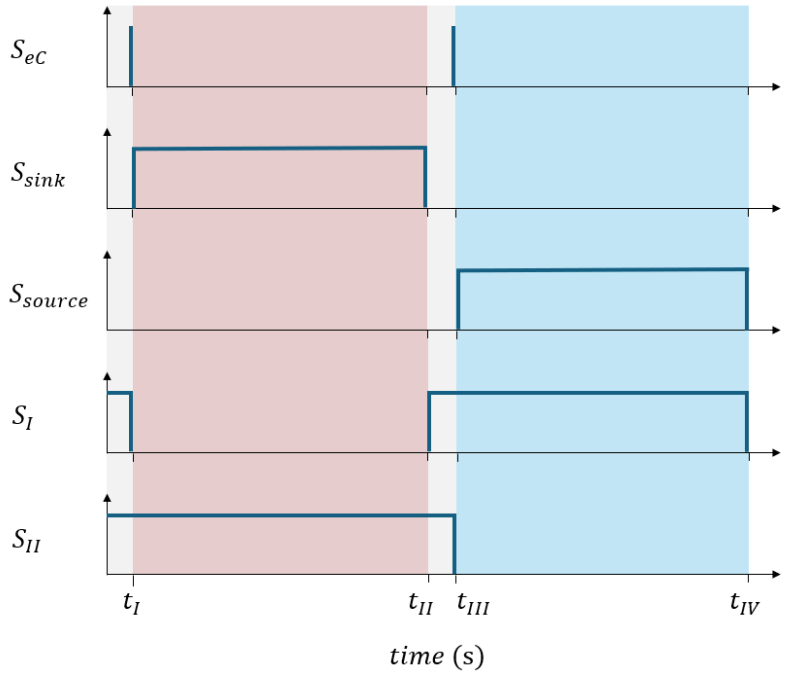

Figure 47: Time-dependent binary switch states used in the lumped element model. The diagram shows the binary switching states of key components over one full cycle of the four-step elastocaloric cooling process in the single-stage device. The variables S_I and S_{II} represent the switching functions controlling the thermal pathways to the surrounding air and between the elements. S_{eC} indicates the activation state of the elastocaloric effect. S_{sink} and S_{source} denote the connection states between the foil and the heat sink or heat source, respectively. Each switching function takes a value of 1 (active heat transfer/closed) or 0 (inactive heat flow/open), with transitions occurring in accordance with the timing of the cooling cycle steps. The synchronization of these states governs the sequential heat flow and the activation of the elastocaloric effect, which is triggered by a Dirac impulse. Legend: $t_I = t_{ramp}, t_{II} = t_I + t_{hold}, t_{III} = t_{II} + t_I, t_{IV} = t_{III} + t_{hold} = t_{period}$

Besides the discretization into thermally thin elements, a key aspect of the model is the characterization of thermal contact between the foil and the copper sink/source elements, as well as the time-dependent bidirectional heat flow within the elements, which is implemented using event-triggered switching mechanisms. The time-dependent switches and their binary state diagram representing the four-step cooling cycle are shown in Figure 47. The binary state 1 corresponds to active heat flow due to a closed switch, while the binary state 0 corresponds to no heat flow due to an open switch condition. The switch S_{eC} enables a heat pulse for cooling and

heating of the foil segments and thus replicates the elastocaloric effect, which is implemented as a Dirac impulse. Adiabatic conditions are imposed during the pulse by encapsulating the foil, thereby eliminating heat transfer to the surrounding. After the elastocaloric effect takes place, heat transfer by mechanical contact between the heat sink and heat source elements and the foil is correspondingly enabled by the switches S_{sink} and S_{source}. The heat transfer accomplished by mechanical contact is limited by the heat transfer coefficient h. The simulated temperature curves for the heat sink and heat source are. The heat transfer coefficient is determined by iteratively adjusting its value in the simulation, starting from 10 $Wm^{-2}K^{-1}$, until the simulated temperature profiles of the heat sink and heat source closely match the experimental data. The optimal h corresponds to a cooling power deviation below 10 % for the optimum frequency. For NR foil thicknesses of 650 and 290 µm, h is estimated to be approximately 120 $Wm^{-2}K^{-1}$ and 80 $Wm^{-2}K^{-1}$, respectively [19]. Moreover, the foil is in contact with the heat sink and heat source elements on only one side, while the opposite side remains exposed to air. The foil and the heat sink/source are exposed to air during periods without mechanical contact. Heat flow to the air is implemented by the switches S_I and S_{II}. The parameters used in the LEM simulations are listed in Table 8.

Table 8: Parameters for LEM simulation of the elastocaloric cooling performance of NR foils of 900, 650 and 290 µm thickness. Adapted from [19] licensed under CC BY 4.0.

Label	K	K	L
Thickness at zero strain (µm)	900	650	290
Thickness at 300 % strain (µm)	450	270	150
Thickness at 700 % strain (µm)	290	180	80
Width at zero strain (mm)	9	9	9
Width at 300 % strain (mm)	4.5	5.5	5
Width at 700 % strain (mm)	3.5	4	4
Specific heat capacity ($Jg^{-1}K^{-1}$)	1.88	1.88	1.88
Density (gmm^{-3})	$833 \cdot 10^{-6}$	$833 \cdot 10^{-6}$	$1026 \cdot 10^{-6}$
Mass (mg)	179	129	72
Thermal conductivity ($Wm^{-1}K^{-1}$)	0.15	0.15	0.15

Although the elastocaloric effect is maximal under adiabatic conditions, residual heat within the foil resulting from incomplete heat transfer necessitates the implementation of heat exchange between the foil and the surrounding air in the model. The back side of the support structure, acting as thermal insulation, continuously transfers heat to the surroundings by convection. The model also incorporates strain-dependent variations in the foil geometry, including changes in thickness, width and length, to accurately capture the evolution of the contact area and heat transfer duration. Based on the simulated time-dependent temperature profiles in the sink and source elements, both the cooling power and the coefficient of performance (COP_{device}) of the device are evaluated as functions of operational frequency and foil thickness.

5.2.3 Performance Results of the Monostable Single-Stage Device

In Figure 48 (a) the time-dependent temperature evolution of the heat sink and heat source for the monostable single-stage device employing a NR foil type “K” with a thickness of 650 µm is presented. The applied engineering strain ranges from 300 to 700 %, with an operating frequency of 136 mHz and a corresponding hold time t_{hold} of 3 s. A strain rate of 9.3 s^{-1} is used for rapid mechanical tensile loading and unloading, corresponding to a time frame of 430 ms. An additional tolerance of 250 ms is accounted for due to experimental constraints. The temperature difference is referenced to the room temperature of 23.0 °C.

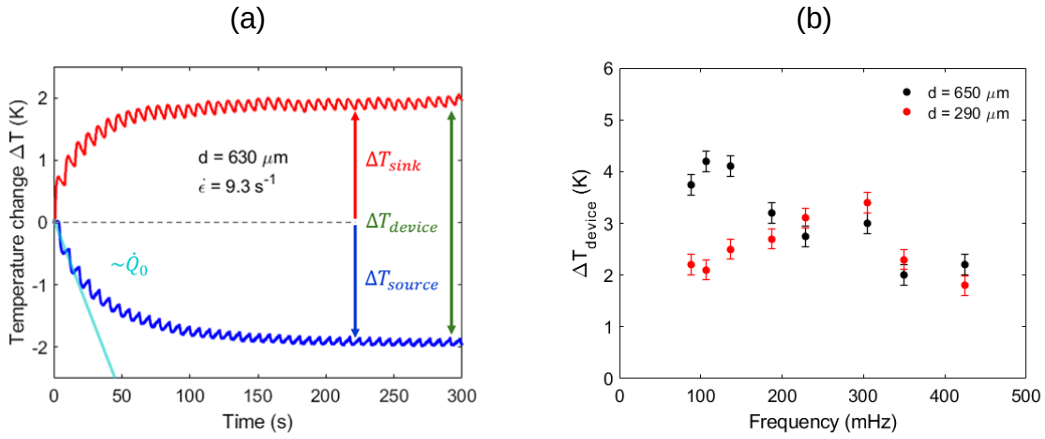

Figure 48: (a) Temperature evolution of the heat sink (red line) and heat source (blue line) of the monostable single-stage elastocaloric cooling device, relative to ambient conditions of 23.0 °C. A frequency of 136 mHz and a NR foil with a thickness of 650 µm type “K” is used. The applied engineering strain ranges from 300 to 700 % and the engineering strain rate of 9.3 s^{-1} result in loading and unloading durations of $t_{ramp} = 430\ ms$. (b) The device's temperature span ΔT_{device} versus frequency for NR foils with 650 and 290 µm and the corresponding type “K” (black dots) and “F” (red dots). Error bars reflect the uncertainty of the temperature sensors used in the measurements. Adapted from [19] licensed under CC BY 4.0.

At the beginning, each loading cycle induces a progressive increase in the temperature difference between the heat sink and the heat source. This increase occurs during the heat exchange phases and corresponds to step II and step IV. This corresponds to heat rejection to the heat sink and heat absorption from the heat source and the foil refrigerant, respectively. Within the first cycle, the temperature difference at the heat sink (red curve), rises by 0.7 K. Upon unloading, the temperature difference at the heat source (blue curve) decreases by 0.5 K. Approximately 24 % of the total temperature change is transferred within the first cycle at the heat source.

The device temperature span is decreased by parasitic heat transfer. During unloading (step III) and subsequent heat transfer to the heat source (step IV), the heat sink temperature difference decreases by 0.1 K. Conversely, during loading (step I) and heat transfer to the heat sink (step II), the heat source temperature difference increases by 0.1 K. Consequently, this leads to a characteristic oscillatory pattern in the temperature response curves, attributed to parasitic heat transfer to the surrounding.

Following the initial temperature changes, saturation and thus a stabilized temperature response are observed. Saturation is defined as a temperature change that is less than 10 % of the final temperature. It is reached after approximately 50 seconds at the heat sink and about 100 seconds at the heat source. Under stationary conditions a temperature change ΔT_{source} of -2.1 K is reached at the heat source. At the heat sink, a temperature change ΔT_{sink} of the same magnitude but opposite sign is observed. Consequently, the sum of the temperature changes is defined as the temperature span of the device ΔT_{device}, as given in Equation 5-3. For the optimum operation frequency of 136 mHz, ΔT_{device} results in 4.1 K.

$$\Delta T_{device} = \Delta T_{sink} + |\Delta T_{source}| \quad \textbf{5-3}$$

The temperature changes ΔT_{source} and ΔT_{device}, together with the cooling power $\dot{Q}_0$, serve as key metrics for assessing the performance of the device. The initial cooling power can be derived from the initial temperature change $\dot{T}_{source}$, the mass of the heat source m_{source}, and the specific heat capacity c_p, as given in Equation 5-4. The initial temperature change of the source is determined by the temperature drop during the first cooling cycle ΔT^0_{source}. It starts from zero and is completed within the first period t_{period}. Consequently, the initial temperature change of the heat source is given by $\dot{T}_{source} = \Delta T^0_{source} {t_{period}}^{-1}$. The c_p of copper is 0.381 $Jg^{-1}K^{-1}$ and m_{source} is 5.3 g. Therefore, the initial cooling power of the device is proportional to the slope of the linear turquoise line, as illustrated in Figure 48 (a).

$$\dot{Q}_0 = c_p\, m_{source} |\dot{T}_{source}| \quad \textbf{5-4}$$

To further investigate the influence of operating frequency on the device temperature span ΔT_{device}, the frequency is varied between 88 and 424 mHz, corresponding to hold times t_{hold} ranging from 5.0 to 0.5 s. Figure 48 (b) presents the temperature span ΔT_{device} as a function of operating frequency. The results for NR foil type “K” with a thickness of 650 µm are shown as black dots, while those for NR foil type “F” with a thickness of 290 µm are indicated by red dots. Error bars represent the uncertainty of the Class A Pt100 temperature sensors used in the measurements. The temperature span ΔT_{device} exhibits a pronounced frequency-dependent behavior, reaching a maximum of 3.4 K at 305 mHz for NR foil type “F” with a thickness of 290 µm. At the same frequency, the thicker NR foil type “K” yields a ΔT_{device} that is 0.4 K lower, as it already attains its maximum value of 4.2 K at a lower frequency of 107 mHz.

In addition to ΔT_{device} and $\dot{Q}_0$ the device coefficient of performance COP_{device} serves as a final key parameter for evaluating the overall performance. To determine the COP_{device}, the mechanical work input per cycle ΔW_{device} must be calculated. The work is derived from the recorded force versus displacement response. The required work corresponds to the area enclosed by the hysteresis loop, obtained via the closed line integral, as given in Equation 5-5. Here, F represents the applied force, and y denotes the actuator stroke or displacement used to mechanically load and unload the foil. Work recovery is assumed without considering the actuator’s efficiency. For more details, see Chapter 3.3.2.1.

$$\Delta W_{device} = \oint F\, dy \qquad \text{5-5}$$

If the operating frequency is known, the COP_{device}, based on the cooling power $\dot{Q}$, can be determined from the ratio of the initial cooling power $\dot{Q}_0$ to the mechanical input power $\dot{W}$ calculated as the product of the mechanical work per cycle and the operating frequency f, as given in Equation 5-6.

$$COP_{device} = \frac{\dot{Q}}{\dot{W}} = \frac{\dot{Q}_0}{f \Delta W_{device}} \qquad \text{5-6}$$

Since the shape of the engineering stress-strain hysteresis loop depends on the hold time t_{hold}, the mechanical work per cycle ΔW_{device} is a function of t_{hold}. In Table 9 the resulting mechanical power input $\dot{W}$, calculated from ΔW_{device}, for different operating frequencies and the corresponding t_{hold} values are presented. The results are shown for NR foil type "K" with a thickness of 650 µm and type "F" with a thickness of 290 µm. While ΔW_{device} decreases with decreasing t_{hold}, due to the narrowing of the hysteresis loop, the resulting $\dot{W}$ increases with increasing frequency, which corresponds to decreased t_{hold}. Overall, both ΔW_{device} and thus $\dot{W}$ are lower for the thinner foil.

Table 9: The work input ΔW_{device} increases with increasing hold time t_{hold} due to the enlarged hysteresis, while the resulting mechanical input power $\dot{W}$ increases with increasing frequency f and foil thickness d. Determined for the NR foils type "K" and "F" with the corresponding thickness 650 and 290 µm. The experimentally determined work input corresponds to an engineering strain range of 300 to 700 %. Frequencies correspond to the single-stage device with linear actuation, the bistable device architecture allows higher frequencies, resulting in higher input powers.

$f(mHz)$	$t_{hold}(s)$	$d = 650\ \mu m$		$d = 290\ \mu m$	
		$\Delta W_{device}\ (mJ)$	$\dot{W}\ (mW)$	$\Delta W_{device}\ (mJ)$	$\dot{W}(mW)$
107	4.0	196.7	21.0	105.9	11.3
136	3.0	191.9	26.1	105.2	14.3
171	2.0	176.8	30.2	92.1	15.7
305	1.0	154.8	47.2	88.7	27.1
424	0.5	154.3	65.4	67.8	28.7

In Figure 49 (a) the cooling power $\dot{Q}_0$ as a function of frequency is presented. Experimentally determined results for the NR foil type "K" with a thickness of 650 µm (black dots) and type "F" with a thickness of 290 µm (red dots) are complemented by results from LEM simulations, represented by solid lines. The simulation model is described in Chapter 5.2.2. In Figure 49 (b) the corresponding device coefficient of performance COP_{device} as a function of frequency is shown. The cooling power exhibits a pronounced maximum at an optimal operating frequency, which shifts to higher frequencies as the NR foil thickness decreases. This behavior corresponds to the frequency-dependent variation of ΔT_{device}, given in Figure 48 (b). At 136 mHz, the 650 µm NR foil reaches its maximum cooling power of 123 mW, corresponding to a specific cooling power

of 954 mWg^{-1} and a COP_{device} of 4.7. Therefore, 136 mHz is identified as the optimum frequency for this foil. For NR foil type "F" with a thickness of 290 µm, the maximum cooling power is 78 mW at the optimum frequency of 230 mHz, corresponding to a specific cooling power of 1082 mWg^{-1} and a COP_{device} of 4.0. The optimum $\dot{Q}_0$ and COP_{device} are achieved at their respective frequencies for both foils. The corresponding LEM simulation of the cooling power aligns with the frequency-dependent maximum. Nevertheless, it exhibits a more gradual decline at higher frequencies, which is attributed to the assumption of frequency-independent convective heat transfer to the environment within the LEM model.

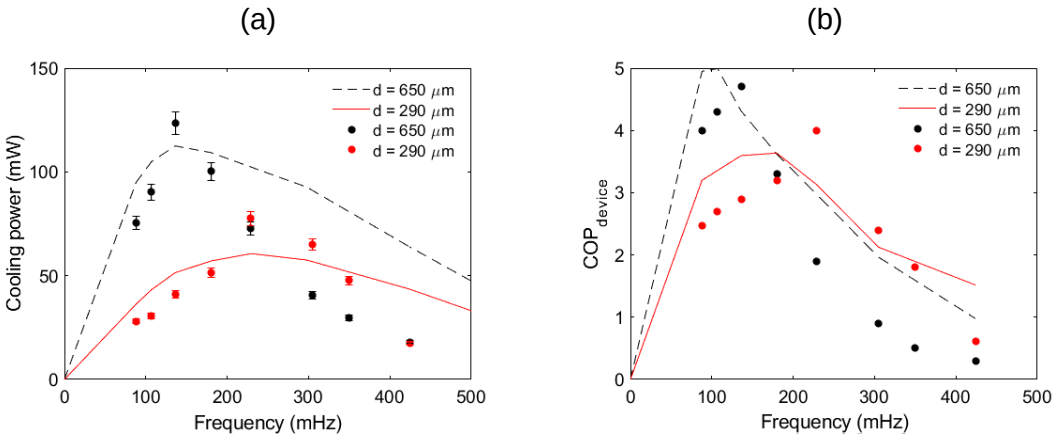

Figure 49: (a) Cooling power as a function of frequency, evaluated through both LEM simulations (solid and dashed line) and experimental tests (dots) on the monostable single-stage elastocaloric cooling device with linear actuation with a NR foils of 650 and 290 µm thickness and the corresponding type "K" (black dots) and "F" (red dots). Error bars represent the average variation within the measurement series. (b) Device coefficient of performance COP_{device} versus frequency. Adapted from [19] licensed under CC BY 4.0.

In Table 10 the experimental results for the monostable single-stage elastocaloric cooling device using NR foil types "K" and "F" with corresponding thicknesses d of 650 µm and 290 µm are summarized, respectively. The results are obtained under an engineering strain range of 300 to 700 % and an engineering strain rate of 9.3 s^{-1}.

At frequencies below the optimum, the efficiency decreases due to insufficient heat exchange between the foil refrigerant and heat sink/source. Conversely, at frequencies exceeding the optimum, the contact time for heat transfer by mechanical contact becomes too short, while the mechanical work input continues to increase. During mechanical loading and unloading, no heat transfer occurs through mechanical contact between the foil refrigerant and the device. However, undesired parasitic heat transfer to the surroundings takes place, causing minor oscillations in the device's temperature evolution. Therefore, the deformation speed t_{ramp} should be kept short [19]. Larger loading/unloading rates are avoided, as they impose high demands on actuator performance and lead to an undesirable increase in work input per cycle. In addition, high engineering strain rates are required to deform thin foils under quasi-adiabatic conditions. For further details, see Chapter 4.3.5. The higher optimal frequency observed for thinner foils indicates faster heat transfer, enabling an increased number of cooling cycles within the same

time frame. This improvement is associated with the reduced mass of the refrigerant, which contributes to enhance the specific cooling power $\dot{q}_0$.

Table 10: Overview of experimental data obtained from the monostable single-stage elastocaloric cooling device. The results correspond to NR foils of type "K" and "F" and the foil thickness d of 650 and 290 µm, respectively. The applied engineering strain ranges from 300 to 700 % and mechanical loading and unloading are performed at an engineering strain rate of 9.3 s^{-1}. The (specific) cooling power $\dot{Q}_0$ ($\dot{q}_0$) and the input power per cycle $\dot{W}$ depend on the operation frequency f and determine the coefficient of performance COP_{device}. The device temperature change is evaluated by the temperature change of the source ΔT_{source}, and the device temperature span ΔT_{device}, each determined under stationary conditions. Adapted from [19] licensed under CC BY 4.0.

Type	d (μm)	f (mHz)	$\dot{Q}_0$ (mW)	$\dot{q}_0$ (mWg^{-1})	$\dot{W}$ (mW)	COP_{device}	ΔT_{source} (K)	ΔT_{Device} (K)
K	650	88	76	584	18.7	4.0	-2.0	3.8
K	650	107	90	698	21.0	4.3	-2.1	4.2
K	650	136	123	954	26.1	4.7	-2.0	4.1
K	650	171	100	776	30.2	3.3	-1.5	3.2
K	650	229	73	562	38.0	1.9	-1.2	2.8
K	650	305	41	584	47.2	0.9	-1.2	3.0
K	650	350	30	229	54.6	0.5	-0.8	2.0
K	650	424	18	140	65.4	0.3	-0.6	2.2
F	290	88	28	391	11.3	2.5	-1.2	2.2
F	290	107	31	428	11.3	2.7	-1.1	2.1
F	290	136	41	572	14.3	2.9	-1.3	2.5
F	290	171	52	718	15.7	3.2	-1.4	2.7
F	290	230	78	1082	19.4	4.0	-1.7	3.1
F	290	305	65	908	27.1	2.4	-1.7	3.4
F	290	350	48	665	26.4	1.8	-1.2	2.3
F	290	424	17	734	28.7	0.6	-0.5	1.6

A maximum ΔT_{device}, $\dot{Q}_0$ and COP_{device} are observed at an optimal frequency, which shifts toward higher frequencies as the NR foil thickness decreases. The maximum cooling power of 123 and 78 mW is reached at 136 and 230 mHz for NR foil thicknesses of 650 and 290 µm, respectively [19]. The devices demonstrate a maximum ΔT_{device} value of up to 4.2 K and a COP_{device} of 4.7, reached for the 650 µm foil type "K" [19]. The $\dot{q}_0$ increases as the foil thickness decreases, reaching approximately 1.1 Wg^{-1} at a thickness of 290 µm and foil type "F".

The thickness-dependent heat transfer dynamics are further analyzed using LEM simulations. In Figure 50 (a), the optimal frequency required to achieve the maximum cooling power is presented as a function of the foil thickness.

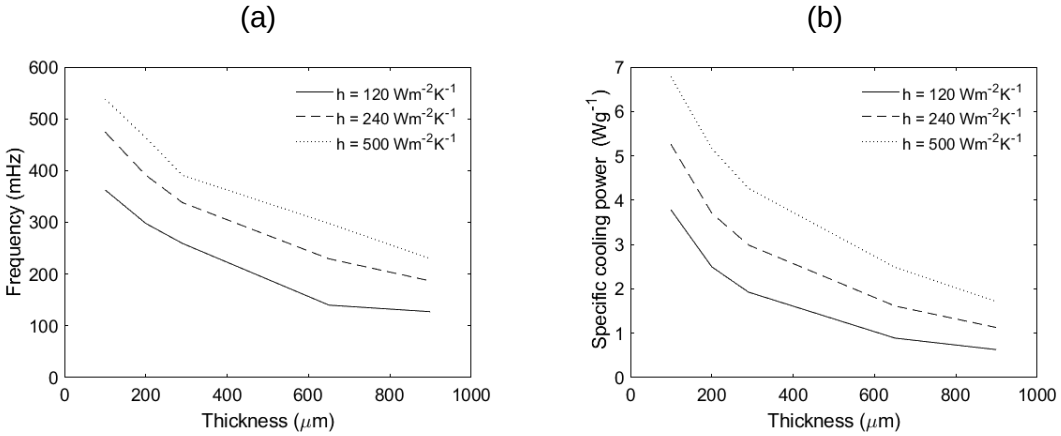

Figure 50: (a) LEM simulations of the optimal operation frequency required to achieve the maximum cooling power during cycling of the monostable single-stage elastocaloric cooling device as a function of NR foil thickness d, evaluated for various heat transfer coefficients h as indicated and the (b) corresponding simulations of the specific cooling power. Adapted from [19] licensed under CC BY 4.0.

Results are provided for discrete heat transfer coefficients h of 120, 240, and 500 Wm^{-2}K^{-1}, with the assumption that h is independent of thickness. A significant increase in the optimal frequency is observed with decreasing NR foil thickness and increasing heat transfer coefficient. In the simulation a lower adiabatic temperature change ΔT_{ad} are used for foils with a thickness of 290 µm and below, corresponding to type "F". For thicker foils ΔT_{ad} of type "K" is used. In Figure 50 (b), the corresponding simulated dependence of the specific cooling power on foil thickness is illustrated. With decreasing foil thickness, the specific cooling power increases. In detail, by reducing the foil thickness from 290 to 100 µm, the specific cooling power is increased to approximately 3.8 Wg^{-1}, under the assumption of a constant heat transfer coefficient of h = 120 Wm^{-2}K^{-1}. Furthermore, the cooling performance is significantly improved with increasing h. For a foil thickness of 290 µm, and a moderate increase in h from 120 to 240 Wm^{-2}K^{-1} results in a specific cooling power of about 3 Wg^{-1}. By further increasing h to 500 Wm^{-2}K^{-1} and reducing the foil thickness to 100 µm, it is indicated by the simulation that a specific cooling power close to 7 Wg^{-1} can be reached by operating the device at approximately 550 mHz. These results demonstrate that both foil thinning and enhanced heat transfer are effective strategies to optimize elastocaloric device performance [19]. Substantial potential for performance gains is highlighted by the simulation trends through improvements in material properties and device design.

5.2.4 Long-Term Test

To evaluate the potential of NR-based elastocaloric materials for cooling applications, a preliminary long-term cycling test comprising 10^4 cycles is carried out. This test aims to provide initial insights into the NR foil's mechanical stability and elastocaloric performance over extended operational periods, which are critical factors in assessing its viability for practical use in cooling systems.

In Figure 51 (a), the evolution of the engineering stress-strain curves from the initial 50 cycles up to 10^4 cycles is presented for NR foil type "K" with a thickness of 650 µm. The test is performed using the monostable, single-stage elastocaloric cooling device operating at a frequency of 424 mHz, with a hold time of 0.5 s and an engineering strain rate of 9.3 s^{-1}. During the first 50 cycles, the maximum engineering stress reaches 1.9 MPa. This value decreases progressively with cycling and reaches 1.6 MPa after 10^4 cycles, corresponding to a reduction of approximately 18 %. Typical stress relaxation is observed during the holding period and starts at the maximum engineering strain of 700 %. This relaxation behavior is consistent across all operation cycles and decreases with increasing cycle number, correlating with the decrease in maximum engineering stress. The point of load removal remains constant across all cycles and occurs at 1.4 MPa. Up to approximately 2,500 cycles, the unloading paths remain similar. However, beyond this point, unloading occurs at higher engineering strains. As a result, the loading and unloading curves progressively align with increasing number of cycles, leading to a reduction in the area enclosed by the hysteresis loop, which is proportional to the mechanical work input. In comparison to the initial 50 cycles, the work input decreases by approximately 57 %, reaching a value of 1.18 Jg^{-1} after 10^4 cycles.

Following the 10^4th cycle, the specimen is fully unloaded to 0 % engineering strain before an additional test is conducted. The result of this test is represented by the turquoise dash-dot line. The work input for the 10001st cycle deviates by only 2 % from that of the initial 50 cycles, despite slight differences in the shape of the hysteresis loop. Specifically, the maximum engineering stress for the 10001st cycle is approximately 12 % lower, reaching 1.7 MPa. Additionally, the hysteresis loop exhibits a higher engineering stress level at the start of the loading phase and a more pronounced drop during unloading.

In Figure 51 (b) the corresponding temperature change of the heat source ΔT_{source} and the device temperature span ΔT_{device} versus the amount of operation cycles is shown. The error bars represent the measurement uncertainty associated with the Pt100 Class A temperature sensors. Additionally, the 10001st cycle, performed after full mechanical load removal, is indicated by data points with a turquoise filling. The temperature change remains stable over the tested number of cycles and does not vary beyond the measurement uncertainty. This also holds true for the 10001st cycle.

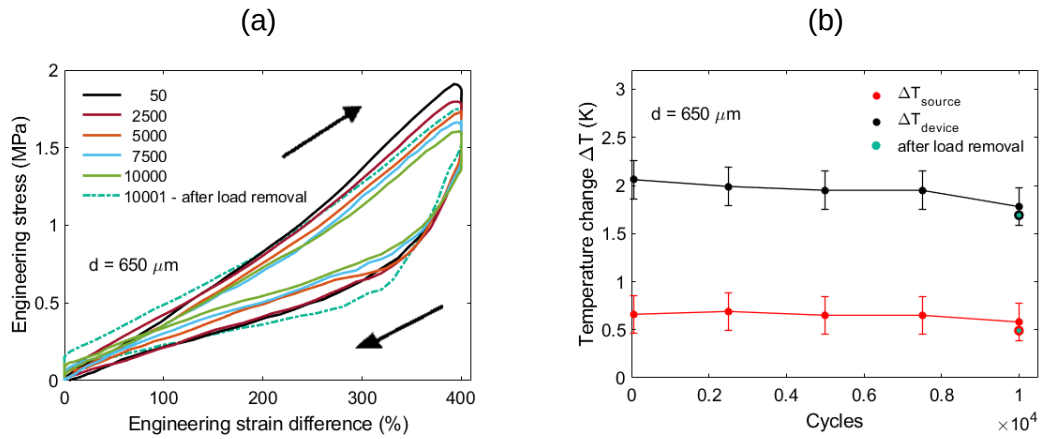

Figure 51: The cyclic stability of the monostable single-stage elastocaloric cooling device evaluated in a long-term test of 10^4 cycles. The engineering strain ranges from 300 to 700 % and the engineering strain rate is 9.3 s^{-1}. (a) Engineering stress-strain curve evolution ranging from the first 50 to 10^4 cycles. A NR foil type "K" of 650 µm thickness and a frequency of 424 mHz ($t_{hold} = 0.5\ s$) is employed. After 10^4 cycles, the mechanical load is removed, and an additional test is performed (dash-dot line). The work input during cycle 10001, which is proportional to the area enclosed by the hysteresis loop, is equal to that of the initial 50 cycles. (b) The corresponding temperature change of the heat source (magnitude) ΔT_{source} and the device temperature span ΔT_{device} versus the amount of operation cycles. The dot with the turquoise filling corresponds to the result after mechanical load removal. The error bars are determined by the measurement uncertainty of the Pt100 class A temperature sensors. Adapted from [19] licensed under CC BY 4.0.

Since the point of load removal remains constant across all cycles, the usable force available for work recovery upon unloading is unaffected. The 10001st cycle, performed after full load removal, demonstrates that the narrowing of the hysteresis loop is at least partially a reversible effect. This is supported by the fact that the hysteresis behavior in this cycle closely resembles that of the initial 50 cycles. However, complete load removal enables complete crystal melting, which is reflected in the partial return to the original hysteresis shape and nearly identical mechanical work input. This suggests that narrowing is not solely due to fatigue or molecular chain breaking, leading to plastic deformation. The results indicate a likely connection to strain-induced crystallization (SIC), as the operating strain range of 300 to 700 % does not permit complete melting of the crystalline regions. Furthermore, it is assumed that the load cycling over 10^4 cycles allows a gradual buildup of crystallinity. The buildup of crystalline regions may enable deformation with decreased resistance, which in turn reduces the mechanical effort needed for cyclic operation.

Consequently, the decrease in work input also implies a reduction in the input power required to operate the elastocaloric cooling device. This leads to improved energy efficiency. The temperature change remains stable throughout 10^4 cycles and is unaffected by full mechanical load removal, confirming the thermal reliability of the system under long-term operation [19]. However, since 10^4 cycles correspond to only approximately two days of operation, further investigations are required to fully assess the operational lifetime of the device. In addition, to confirm the proposed mechanism, the degree of crystallinity under comparable loading conditions must be further investigated.

6 Bistable Single-Stage Device

For the single-stage device operating in uniaxial tensile mode, two actuators are required to drive the system, which is not favorable for the realization of cooling applications. By contrast, the bistable device architecture shown in Figure 52 requires only a single actuator to operate the cooling device. The device is intended to maintain two stable states. Furthermore, general requirements common to all elastocaloric cooling devices are considered, namely the need to load and unload the refrigerant and to spatially separate the hot and cold flows. The design is inspired by mechanisms similar to those used in garage doors, where a spring maintains the structure in the open position. In the present device, the foil refrigerant itself functions as the spring element. The foil is clamped between two holders, H1 and H2. Holder H1 is fixed to the base plate, while H2 is attached to the lever arm and follows a semicircular trajectory during actuation. To enable loading and unloading of the foil, the rotating lever arm is employed, which brings the foil into contact with the heat sink and then the heat source in periodic alteration, enabling heat transfer. The semicircular trajectory, enabled by the rotation of the lever arm, is chosen because it allows spatial separation of the foil in the loaded and unloaded states.

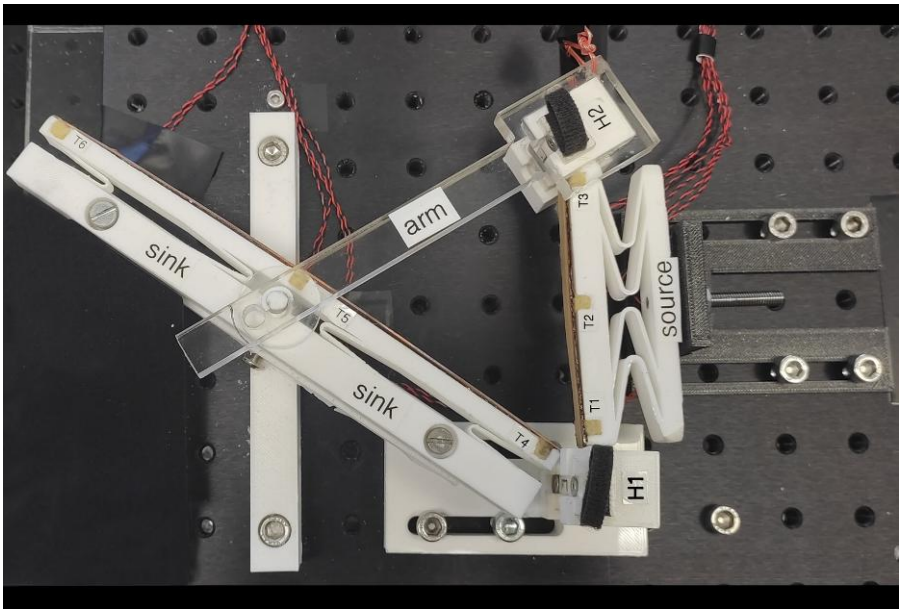

Figure 52: Photograph of the single-stage bistable elastocaloric cooling device (top view), comprising a heat sink and a heat source with flexible, spring-like compliant support structures, two foil holders (H1, H2), and a rotating lever arm. The design is intended to maintain two stable states and to be operated by a single actuator. The lever arm facilitates both the loading and unloading of the elastocaloric foil and enables mechanical contact between the foil and the heat sink/source units for heat transfer. The V-shaped arrangement of the heat source and heat sink at unequal lengths follows the shape and position of the foil in its loaded and unloaded states. The temperature evolution during operation is monitored using Pt100 sensors (T1-T6). In the image, the device is shown in its 300 % pre-strained condition, in which the foil (in beige color) is clamped between the two holders and in contact with the source.

In these two states, the foil forms a ‘V’ shape with unequal arm lengths. Therefore, in this design, the heat sink and heat source are no longer arranged parallel to each other. Instead, the system adopts an asymmetric V-shaped configuration, with the heat sink and source units forming the arms of the 'V' at unequal lengths. Three Pt100 sensors are embedded in each of the heat source (T1, T2, T3) and the heat sink (T4, T5, T6) units to measure the temperature evolution during operation. During heat transfer to the heat sink and heat source, two stable points corresponding to the minimum and maximum deformation of the foil are present. These stable end points represent energy minima in the system’s potential landscape, where no force is required to maintain the state, thus enabling significant power savings for the driving motor.

The monolithic heat source and sink supports are flexible, spring-like compliant structures that increase the contact area between the clamped foil and the heat source and sink by promoting surface conformity. In addition to the contact pressure, and the thermal conductivity and the surface roughness of the contact areas, of the materials involved, the actual contact area is a crucial factor for efficient heat transfer [17,186,190,207]. The structures are 3D printed using polylactide (PLA) and allow bidirectional bending moments around the θ- and ρ-axes, as well as displacement along the φ-axis. Despite the inherent stiffness of bulk PLA, the structure exhibits spring-like behavior due to its geometry, which incorporates flexible features such as thin beams connected by curved segments. These elements form a compliant mechanism that allows elastic deformation under load without the need for traditional joints. In Figure 53, a schematic of the spring-like compliant heat source including the heat transfer element (a cooper plate) is visualized. As a result, the support structure is capable of compensating for misalignments among the involved components. Thereby also reducing the precision requirements during the fabrication of the support itself, the holders, and even the foil.

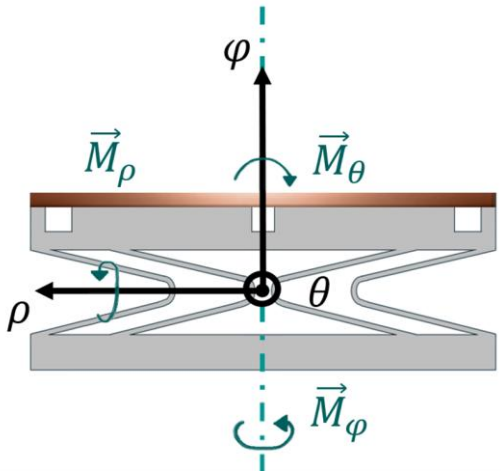

Figure 53: Schematic of the spring-like heat source including the heat transfer element (copper plate). The design allows bending moments ($\vec{M}_\theta, \vec{M}_\rho \neq 0$; $\vec{M}_\varphi = 0$) and therefore enables improved mechanical contact with the elastomer foil for enhanced heat transfer. The $\theta - \varphi$ plane forms the plane of symmetry.

The beam dimension of the support structure in the $\rho - \varphi$ plane is 1 mm, while in the $\varphi - \theta$ plane it is 13 mm, resulting in an aspect ratio of 13. This means that the structure is significantly

stiffer in the $\varphi - \theta$ plane compared to the $\rho - \varphi$ plane, introducing directional compliance which is important for its mechanical response under load. The spring constant in compression, is 3 Nmm^{-1} in the central region and 2.7 Nmm^{-1} in the outer sections near the edges, exhibiting linear behavior within the tested displacement range of up to 1.5 mm. The stiffness gradient facilitates the conforming of the stationary heat source to the foil in motion, which follows a circular trajectory at one end, thereby ensuring mechanical contact during operation. The absolute value of the spring constant is chosen such that the elastically stored energy is sufficient to tilt the heat source and thereby establish mechanical contact with the foil. The measurement of the spring constant, which considers both the monolithic PLA support structure and the heat transfer element (a copper plate), is performed under compression in the negative φ-direction.

6.1.1 Operation Principle

During operation of the bistable cooling device, a superimposed deformation of the support of the heat source is induced. Combining compression on one side and tension on the opposite side due to a bending moment, and displacement in the negative φ-direction. A schematic representation of the elastocaloric cooling cycle, based on bistable actuation, is shown in Figure 54. The operation principle involves four steps. In the initial phase step I, the foil is mechanically loaded under quasi-adiabatic conditions with a strain rate of 9.3 s^{-1}, which leads to the release of latend heat. To mechanically load the foil fixed between the holders (indicated as green dots) and allow thermal contact with the heat source and sink, a single actuator operating via a rotating lever arm is employed. Rotation occurs around the θ-axis, originating at the lever arm support, and is driven by an external torque $\vec{M}$.

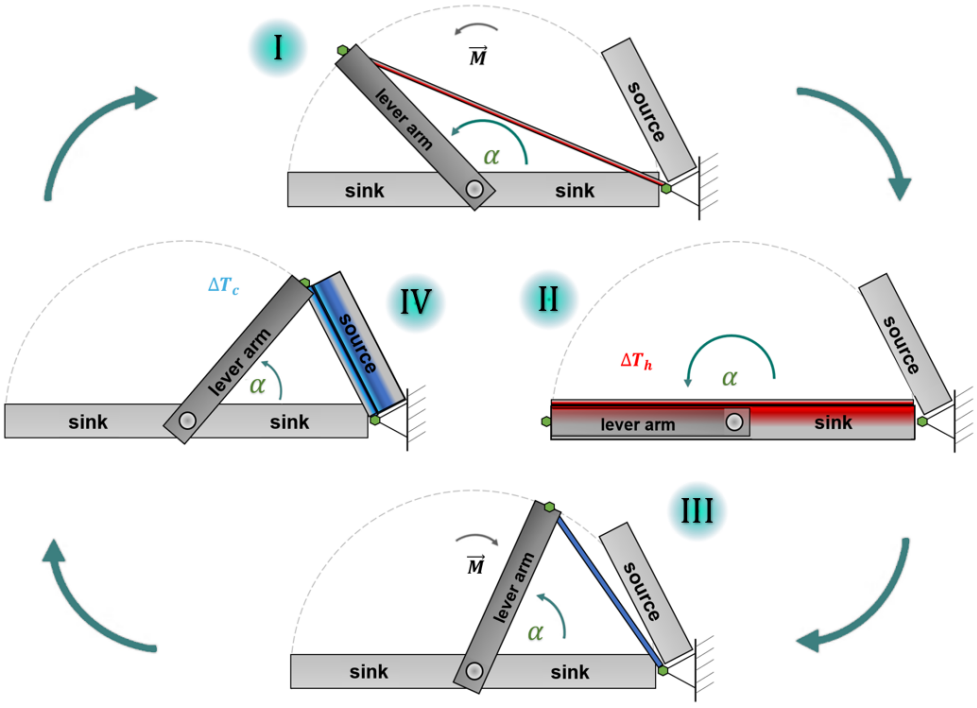

Figure 54: Schematic of the elastocaloric cooling cycle based on bistable actuation with a rotating lever arm. The cycle consists of four distinct steps: (*I*) mechanical loading, (*II*) followed by heat rejection to a heat sink, (*III*) unloading accompanied by cooling, and (*IV*) heat absorption from a heat source. The foil specimen is fixed between two holders, shown as green octagons, with black arrows indicating the quasi-adiabatic rotational loading and unloading directions. Adapted from [178] licensed under CC BY-NC 4.0.

The foil undergoes a nonlinear displacement change ΔL, which can be described by a sinusoidal function, as given in Equation 6-1. The input parameter $51° \leq \alpha \leq 180°$, resulting from the semicircular trajectory of the lever arm with the radius R, visualized as dashed gray line. The Radius is defined by the maximum engineering strain of 700 % and therefore results into $R = 4L_0$, where L_0 is the initial length of the foil specimen.

$$\Delta L = 2R \sin(\frac{\alpha}{2}) \qquad \textbf{6-1}$$

The angle α is defined between the axis of the heat sink and the rotating lever arm. At $\alpha = 180°$, the foil is in mechanical contact with the heat sink and attributed to a maximum strain of 700 %, corresponding to step II of the operation cycle and the first stable point. Within this step heat is absorbed from the heat sink during the holding time t_{hold} and thereby decreasing the foil's temperature. Subsequently, quasi-adiabatic unloading occurs, enabling a reverse phase transformation that results in a decrease in the foil temperature, corresponding to step III. In the final step IV, corresponding to the second stable point under 300 % pre-strain, heat is absorbed from the heat source to the foil by mechanical contact. By contacting the heat source with the foil, a compression of the support structure in negative φ- direction takes place, as well as a tilting motion about the θ-axis. This motion is induced by the interaction between the foil, its holder (H2), and the heat source at the heat source edge, generating a positive torque $\vec{M}_\theta$. The torque originates from the elastically stored energy in the foil, which is a result of the applied

300 % pre-strain. The heat source is cooled down during the time t_{hold} efficiently by the increased contact area due to the compliant support structure and corresponds to the final to step IV.

6.1.2 Force Evolution

In addition to the perquisite of only a single actuator to drive the system, the bistable device offers further advantages. Specifically, the lower forces required to operate the system makes it attractive for parallelization, enabling the simultaneous use of multiple foils to increase the overall absolute cooling power. The reduction in actuation force is realized through a dedicated loading and unloading mechanism, wherein the foil is strained via a rotating lever arm. During actuation, a fraction of the applied load is redirected to the bearing, thereby reducing the effective force demand on the actuator.

The decomposition of the force vectors, including the device schematic for three steps of operation, is illustrated in Figure 55. In all three configurations, the tensile force required to uniaxially stretch the elastic specimen is represented by the blue vector $\vec{F}$. This tensile force vector can be decomposed into two mutually orthogonal components. One is the tangential force vector $\vec{F}_T$ (green), which represents the force component actively supplied by the motor and is oriented tangentially to the circular trajectory (dashed line) defined by the rotation of the lever arm. The normal force vector $\vec{F}_N$ (orange), which is perpendicular to the trajectory and is passively sustained by the bearing of the lever arm. Therefore, the tensile force can be described as the vector product of the $\vec{F}_T$ and $\vec{F}_N$, as given in Equation 6-2, where $\vec{t}$ and $\vec{n}$ are unit vectors in the tangential and normal directions, respectively. The unit vectors $\vec{t}$ and $\vec{n}$ define a non-inertial (non-fixed) coordinate system with its origin at the free end of the rotating lever arm (red circle), positioned at a radius R from the rotation axis (dark blue circle). The coordinate axes move rigidly with the lever arm along its trajectory. The angle β is defined as $\beta = (180° - \alpha)/2$.

$$\begin{aligned} \vec{F} = \vec{F}_T + \vec{F}_N = & \ F \sin\left(\frac{180° - \alpha}{2}\right)\vec{t} + \ F \cos\left(\frac{180° - \alpha}{2}\right)\vec{n} \\ & = F\, cos\left(\frac{\alpha}{2}\right)\vec{t} + \ F\, sin\left(\frac{\alpha}{2}\right)\vec{n} \ ; \\ & \alpha \in [51°; 180°] \end{aligned} \qquad \textbf{6-2}$$

In Figure 55 (a) the pre-strained condition of the bistable device is shown, corresponding to step IV in Figure 54. At this point, the elastic foil is held at a pre-strain of 300 %, corresponding to the first mechanically stable position. The system remains stationary in this configuration without requiring external force input, as the force is absorbed by the support of the heat source. In this state, the absolute value of the normal force exceeds that of the tangential force, as indicated by the relative vector lengths.

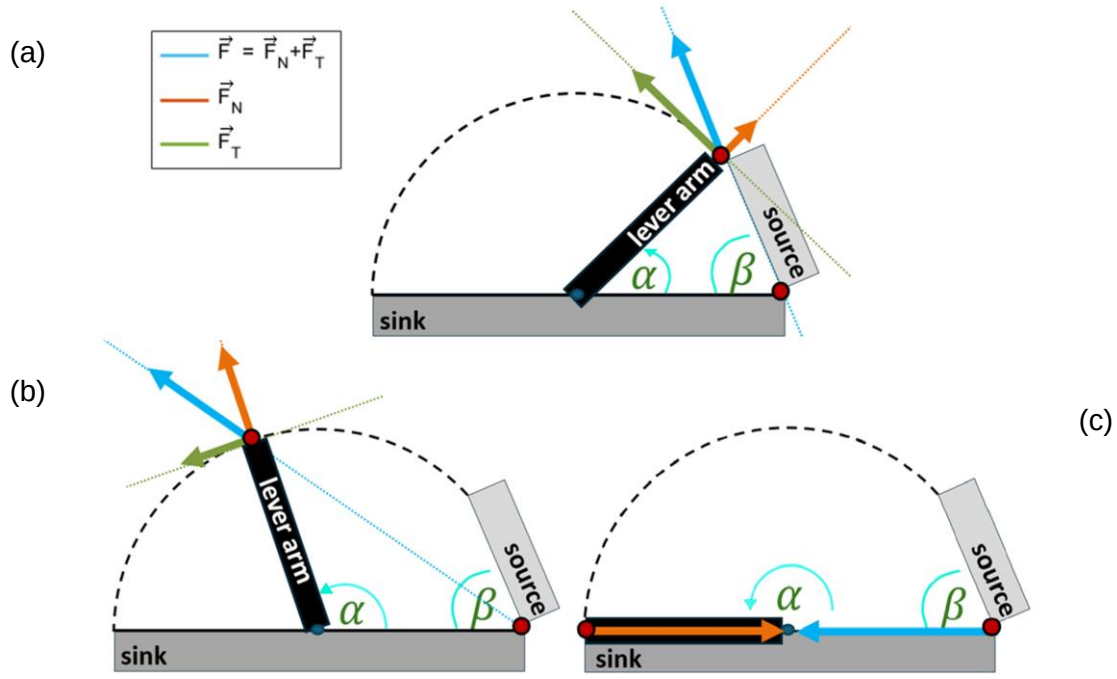

Figure 55: Schematics of the decomposition of the loading force vector of the bistable single-stage device for different operation steps. (a) Ranging from the unloaded initial stable position corresponding to step IV (equal to 300 % pre-strain) over (b) a in between position attributed to 500 % of strain. (c) The second stable end position equal to the maximum deformation of 700 % strain corresponding to step II. The total tensile force needed to uniaxially stretch the elastic specimen is indicated by the blue vector $\vec{F}$. It can be decompositioned into the force vector provided by the motor to drive the system, which is tangential to the trajectory of the rotating lever arm $\vec{F}_T$ (green) and the normal force vector $\vec{F}_N$ with respect to the trajectory (orange) is passively sustained by the bearing of the lever arm. The angle $\alpha \in [51°; 180°]$ is defined as the angle between the heat sink and the lever arm.

As the device transitions from the initial stable state to the second stable point, it passes through an intermediate configuration, depicted in Figure 55 (b). At this point, the tensile strain within the foil increases to approximately 500 % and $|\vec{F}_N| > |\vec{F}_T|$ applies, indicating that the majority of the force required to strain the foil is absorbed by the bearing of the lever arm. This intermediate state is mechanically unstable and must be traversed during actuation between the two stable states. Figure 55 (c) illustrates the final stable position of the system, where the foil reaches its maximum deformation of 700 % strain, corresponding to Step II. The mechanical advantage of this configuration lies in the bearing's ability to absorb the normal component of the force, thereby reducing the effective actuation force required from the motor. This force decomposition is critical for understanding the mechanical efficiency of the system and the reduced energy demand during operation, as the motor can be turned off at stable points and remain unpowered.

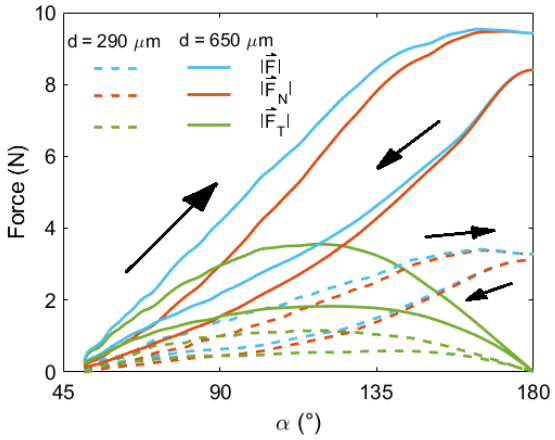

Figure 56: Absolute forces as a function of the angle α in the bistable actuation mechanism for NR foil thicknesses ranging from 290 to 650 µm, represented by dashed and solid lines for material types "K", respectively. The total tensile force $|\vec{F}|$ (blue), the motor-provided force $|\vec{F}_T|$ (green), and the normal force relative to the lever arm trajectory $|\vec{F}_N|$ (orange) are given. The angle $\alpha \in [51°; 180°]$ is defined as the angle between the heat sink and the lever arm. Black arrows indicate the directions of mechanical loading and unloading. Adapted from [178] licensed under CC BY-NC 4.0.

In Figure 56, the absolute force evolution as a function of the angle α is presented for two different NR foil thicknesses: 290 µm (dashed line) and 650 µm (solid line), corresponding to the material types "K". The absolute tensile force, shown in blue, exhibits the typical hysteresis behavior associated with loading and unloading. A maximum force occurring at the maximum displacement, which corresponds to the maximum angle α. Due to the pre-strained condition, this angle starts at 51° rather than at zero. The directions of loading and unloading are indicated by black arrows. During the transition between the two stable states, the normal force is absorbed by the bearing of the lever arm, its absolute value is indicated in orange. As a consequence, the maximum required force provided by the motor, indicated in green, is shifted to the transition region at $\alpha = 120°$, corresponding to step I. Additionally, this maximum force is reduced by a factor of 2.5, resulting in a maximum force of 1.1 N for the 290 µm thin foil, which corresponds to a maximum torque of 0.12 Nm [178]. For the NR foil with a thickness of 650 µm, the maximum torque is 0.38 Nm. In contrast, the displacement change ΔL is 1.6 times larger compared to the monostable single-stage device loaded in tensile mode by linear actuation, as presented in Chapter 5.2. The calculated start angle for 300 % engineering pre-strain is 60°, but it deviates and results in $\alpha = 51°$ due to the alignment of all components in the experimental setup.

6.1.3 Performance Results of the Bistable Single-Stage Device

To systematically evaluate the impact of mechanical actuation and the influence of geometric parameters on the performance of the bistable elastocaloric device, NR foils with varying thicknesses and operation frequencies are investigated. In addition, the effects of different elastocaloric temperatures ΔT_{ad}, resulting from variations in material composition, are examined. Influences arising from fabrication tolerances are also examined.

For an initial, detailed comparison, two foil thicknesses and three discrete excitation frequencies are selected. To ensure direct comparability, the same material type, “K” is used, as it exhibits an identical ΔT_{ad}, previously characterized in Table 6. The key device performance parameters, including the temperature difference ΔT_{device}, cooling power $\dot{Q}_0$, and coefficient of performance COP_{device}, are introduced in Chapter 5.2.3.

In Figure 57, the time-dependent temperature change relative to room temperature (23 °C) at the heat sink and heat source is illustrated. The bistable elastocaloric cooling device is operated at frequencies of 90, 200, and 424 mHz. The frequencies are modulated by the hold times t_{hold} of 5.0, 2.0, and 0.75 s, respectively, during which heat is transferred between the NR foil refrigerant and the heat sink or source. The device is equipped with NR foil type “K” in two thicknesses: 650 µm (a) and 290 µm (b). Load cycles are applied within an engineering strain range of 300 to 700 % at an engineering strain rate of 9.3 s^{-1}, corresponding to a deformation time of approximately 430 ms. A progressive increase in the temperature difference between the heat sink and heat source is observed with each loading cycle. The rise in temperature is induced during the heat transfer phases between the foil refrigerant and the heat sink (step II) and heat source (step IV). Outside these phases, a slight decrease in the temperature difference occurs due to parasitic effects. After approximately 75 seconds, the temperature difference stabilizes, and a temperature span, ΔT_{device}, is established. A minimum temperature difference of 2.2 K and 2.6 K is reached at the lowest frequency of 90 mHz for the foil thicknesses of 290 and 650 µm, respectively. In contrast, the maximum temperature difference of 4.2 K is achieved with the 290 µm foil at the maximum visualized frequency of 424 mHz. At this frequency, the 650 µm foil yields the second-highest temperature difference among the investigated cases. The oscillatory behavior observed in the temperature curves decreases with increasing frequency. For the 290 µm foil and the heat source, the amplitude of temperature oscillations ranges from 0.3 K at 90 mHz to 0.1 K at 424 mHz. For the 650 µm foil, the oscillation amplitude ranges from 0.2 K to 0.1 K over the same frequency range. The cooling power, which is proportional to the initial slope of the temperature rise (see Chapter 5.2.3 for detailed calculations), is lowest at the minimum frequency, reaching approximately 80 mW for both foil thicknesses. At the highest frequency of 424 mHz, the cooling power of the 290 µm foil increases to 212 mW, which is 78 mW higher than that of the thicker foil. This corresponds to a COP_{device} of 5.5 for the 290 µm foil and 2.9 for the 650 µm foil.

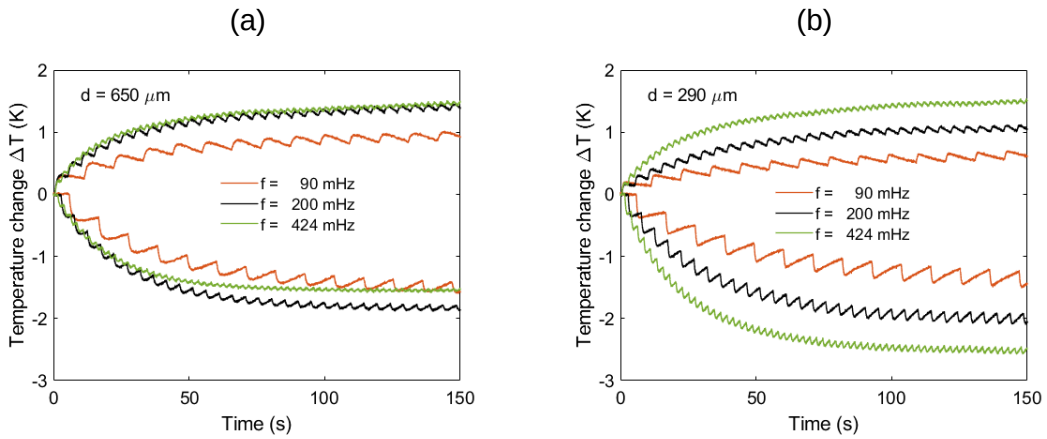

Figure 57: The temperature evolution of the heat sink and source, relative to ambient temperature of 23.0 °C, are shown for the bistable elastocaloric cooling device. The NR foil type "K" with a thickness of (a) 650 and (b) 290 µm is operated at frequencies ranging from 90 to 424 mHz, with an engineering strain rate of 9.3 s^{-1} used for mechanical tensile loading and unloading. The applied engineering strain ranges from 300 to 700 %. Adapted from [178] licensed under CC BY-NC 4.0.

The observed oscillations originate from alternating heat exchange between the foil refrigerant and the heat sink or heat source, and parasitic heat flow to the surroundings during the mechanical loading phases. This dynamic results in small temperature fluctuations superimposed on the overall temperature evolution.

At first consideration, it may appear counterintuitive that the thinner foil outperforms the thicker one, given that a greater volume of material in the thicker foil leads to a larger amount of absolute heat being generated and absorbed. However, the thinner foil enables faster heat transfer, due to its reduced thermal mass and shorter diffusion paths. Moreover, it is essential to rapidly transfer out the heat generated during loading. Otherwise, the usable temperature difference in the subsequent step III is reduced, because the reverse phase transformation, and therefore the temperature decrease, starts at a higher absolute temperature. This phenomenon is discussed in detail in Chapter 6.1.4. As a result, a higher cooling power $\dot{Q}_0$ can be achieved, as indicated by the steeper initial negative slope of the temperature curve measured at the heat source. In addition, a larger temperature difference ΔT_{device} is established during operation at higher frequencies.

6.1.3.1 Device Temperature Changes

To further investigate the influence of operating frequency on the device temperature span ΔT_{device}, the frequency is varied between 90 and 737 mHz, corresponding to holding times t_{hold} ranging from 5.0 to 0.25 s. In Figure 58, the temperature change at the heat source ΔT_{source} (red dots) and the temperature span across the device ΔT_{device} (black dots) are presented as a function of operating frequency. Since ΔT_{source} is negative by definition, its absolute value is displayed to facilitate a more intuitive comparison, such that larger values correspond to improved thermal performance.

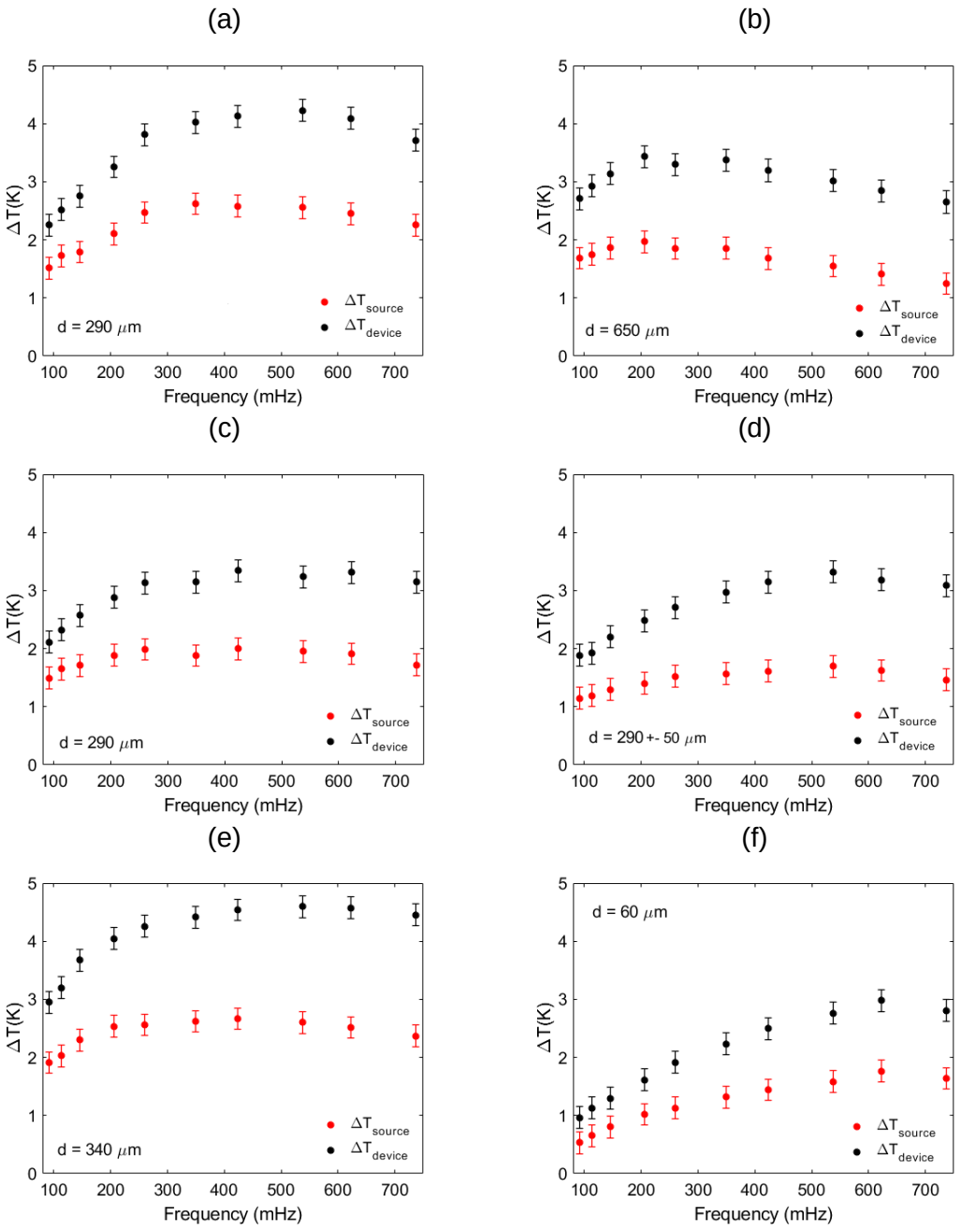

Figure 58: Temperature change of the heat source (magnitude) ΔT_{source} (red dots) and the device temperature span ΔT_{device} (black dots) versus frequency for the bistable elastocaloric cooling device for the NR foils type (a) "K", (b) "K", (c) "F", (d) "F" (d) "Chic" and (e) "L", for the corresponding foil thickness d. The engineering strain ranges from 300 to 700 % and the engineering strain rate is 9.3 s^{-1}. The error bars are determined by the measurement uncertainty of the temperature sensor. The temperature change is with respect to a room temperature of 23.0 °C. Adapted from [178] licensed under CC BY-NC 4.0.

All measurements are performed with an engineering strain ranging from 300 to 700 %, and mechanical loading and unloading are conducted at an engineering strain rate of 9.3 s^{-1}. The error bars are derived from the measurement uncertainty of the Class A Pt100 temperature sensors and result in a maximum deviation of less than $\pm$0.2 K for the determined temperatures. The NR foil type "K" is shown in Figure 58 (a) and (b) for foil thicknesses of 290 and 650 µm,

respectively. To assess the influence of different adiabatic temperature changes ΔT_{ad} resulting from variations in NR composition, foil type “F” is also studied with a selected thickness of 290 µm. The results are shown in Figure 58 (c), allowing for a direct comparison with Figure 58 (a). Additionally, due to the challenges in fabricating sheets with uniform thickness, a foil type “F” with varying thickness (290 ± 50 µm) is investigated, as shown in Figure 58 (d). This enables direct comparison among Figure 58 (a), (c), and (d). Another NR foil labeled as type “Chic,” with a comparable thickness of 340 µm, is studied to evaluate the performance of a recyclable foil refrigerant. This foil exhibits a similar ΔT_{ad} to type “K” and the results are given in Figure 58 (e). Finally, to evaluate the performance of ultrathin NR foils, a latex-based specimen labeled as type “L”, with a thickness of 60 µm, is examined, as shown in Figure 58 (f). Among all the studied foils, the minimum value of ΔT_{source} of -0.5 K is observed for the NR foil type “L” with a thickness of 60 µm, while the highest values of 2.6 and 2.7 K are reached for NR foils type “K” and “Chic”, with corresponding thicknesses of 290 and 340 µm, at frequencies of 350 and 424 mHz, respectively. The minimum value of ΔT_{device} of 1 K, coincides with the minimum value of ΔT_{source} while the maximum also coincides with the maximum ΔT_{device} and reaches 4.6 K at frequencies of 538 mHz and above for the NR foil type “Chic”, as shown in Figure 58 (e). The second highest ΔT_{device} value, reaching 4.2 K, is obtained for the NR foil type “K” with a thickness of 290 µm at a frequency of 538 mHz. For all other foils (Figure 58 (b), (c), (d) and (f)) ΔT_{device} remains below 3.5 K. When comparing the foils with a thickness of 290 µm but differing material properties (Figure 58 (a), (c), (d)), the NR foil type “K,” which exhibits the highest ΔT_c of -7.6 K, shows the largest temperature change among the 290 µm foils. This results in ΔT_{source} of -2.6 K, as shown in Figure 58 (a). For NR foil type “F”, which has a reduced ΔT_c of -6.5 K, the maximum ΔT_{source} is -2.0 K, as shown in Figure 58 (c). This indicates that approximately 30 to 34 % of the elastocaloric temperature change induced by the foil's material upon unloading is transferred to the heat source. In the case of an additional thickness variation of ±50 µm, the ΔT_{source} decreases further to 1.7 K, as presented in Figure 58 (d).

For all tested foils, both ΔT_{source} and ΔT_{device} exhibit broad maxima, characterized by relatively flat curvature near the peak, rather than sharply defined local maxima. For example, in the case of the thickest NR foil (650 µm), the broad maximum occurs between 200 and 350 mHz. For the foils with thicknesses around 300 µm (290 and 340 µm), even flatter maxima are observed in the range of approximately 350 to 550 mHz. Only for the thinnest foil (60 µm), no pronounced optimum behavior can be identified, as the maximum is shifted toward the upper end of the tested frequency range, above 600 mHz. To further investigate the influence of thickness in this regime, the NR foil type “Lp” with a thickness of 120 µm is also tested. However, the results are not shown here in detail, as they closely resemble those of the 60 µm foil, with a deviation in maximum values of only +0.1 K, occurring at the same frequencies despite the doubled foil thickness. In addition, the foil type “K” is further reduced in thickness by laser ablation, which highlights the limitations in achieving a homogeneous thickness, resulting in 160 ± 50 µm. The measured values of ΔT_{source} and ΔT_{device} are similar to those presented in Figure 58 (a) for the NR foil with 290 µm, although the maximum values are 0.2 K lower and therefore do not indicate any improvement.

The results demonstrate a clear dependence of the device temperature span on both operating frequency and foil properties. In contrast, the cooling power shows a more pronounced frequency dependence, which will be discussed in the following section.

6.1.3.2 Cooling Power

In Figure 59 (a), the cooling power of the bistable device as a function of frequency is given for different natural rubber (NR) foil types “K”, “F”, “Chic” and “L”, for foil thicknesses ranging from 60 to 650 µm. In Figure 59 (b) the corresponding specific cooling power is presented. The observed frequencies range from 93 to 737 mHz. For all tested NR foils, a nonmonotonic dependence of the cooling power on frequency is observed. The cooling power is observed to increase from its lowest value at low frequencies, reach a peak at an intermediate frequency, and decrease again as the frequency is further increased. For the thickest foil (650 µm) of type “K”, the maximum cooling power of 158 mW is observed at a frequency of 350 mHz. When the thickness is reduced to 340 and 290 µm, the frequency corresponding to the maximum cooling power is shifted to higher values, near 425 mHz. The maximum cooling power for the NR foil types “K” (290 µm) and “Chic” (340 µm) are found to be nearly identical, both reaching approximately 215 mW. For the NR foil type “F” with a thickness of 290 µm and 290 ± 50 µm, lower maximum cooling powers of approximately 173 mW and 118 mW, respectively, are observed, both occurring at the same optimal frequency of about 424 mHz. The thinnest tested foil (60 µm) type “L” reaches the maximum cooling power at a frequency of approximately 622 mHz, with the lowest peak value of about 115 mW.

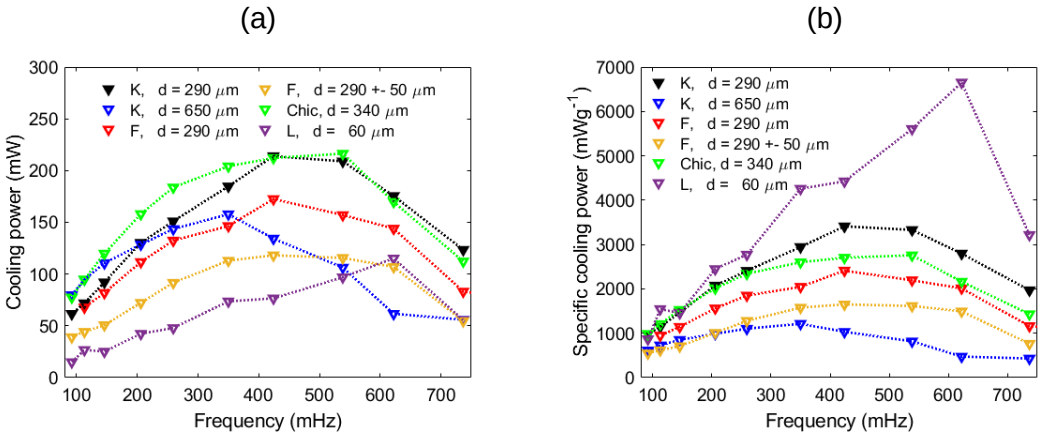

Figure 59: (a) Cooling power $\dot{Q}_0$ versus frequency for the bistable single-stage elastocaloric cooling device with NR foils type, “K, F, Chic and L” for different thicknesses d and (b) the corresponding specific cooling $\dot{q}_0$. The engineering strain ranges from 300 to 700 % and the engineering strain rate is 9.3 s^{-1}. The dotted lines indicate the connections between the points. The optimum operation frequency range is determined by the foil thickness and scales inversely with it, remaining independent of the material's adiabatic temperature change ΔT_{ad}. In contrast, the absolute cooling power is strongly influenced by the frequency, ΔT_{ad} and the thickness inhomogeneity due to manufacturing tolerances, highlighting its critical role in overall performance. Adapted from [178] licensed under CC BY-NC 4.0.

The corresponding specific cooling power, normalized by the foil mass, is presented in Figure 59 (b). Due to normalization, the optimal frequencies coincide with those observed for the absolute cooling power. The thinnest NR foil type “L” exhibits the highest maximum specific cooling

power, approximately 6.7 Wg^{-1}, while the thickest foil yields the lowest value, around 1.2 Wg^{-1}. The curves are well separated across the entire frequency range, indicating no overlap between the data sets, except for frequencies below 200 mHz where some partial convergence is observed. This separation demonstrates that the specific cooling power remains consistently higher for the respective thinner foils. In other words, a general trend is observed where thinner foils result in superior performance throughout the full frequency range (146 to 737 mHz), apart from NR foil type "Chic" (340 µm), which does not follow this trend. These results emphasize the importance of tuning the operating frequency to match the thermal and mechanical response times of the system. Furthermore, differences in maximum cooling power, resulting temperature spans, and optimal frequencies among the various foil types and thicknesses suggest that both geometric and material parameters play a critical role in device performance. A direct comparison between the NR foil types "K" and "F", both with a thickness of 290 µm, reveals the influence of material-related temperature change due to the elastocaloric effect, as listed in in Table 6. For the peak-to-peak material temperature change ΔT_{ad}, foil type "F" shows a value approximately 1.7 K lower than that of type "K". This results in a temperature difference which is about 0.6 and 0.9 K lower for ΔT_{source} and ΔT_{device}. The temperature difference ΔT_c is found to be 1.1 K lower for foil type "F" when comparing absolute values, which directly relates to a lower cooling power across all frequencies. Specifically, the 1.1 K reduction in temperature difference results in a decrease of approximately 41 mW in maximum cooling power. If the foil thickness additionally varies (290 ± 50 µm), the influence on the cooling power becomes even more pronounced, resulting in a 45 % reduction to 118 mW, compared to 214 mW for the homogeneous NR foil type "K".

Table 11: Comparison of material properties (ΔT_c, ΔT_{ad}) and the resulting performance of the bistable elastocaloric cooling device. The foil thickness is given by d. The temperature change upon unloading ΔT_c, and the quasi-adiabatic peak-to-peak temperature change ΔT_{ad}, are measured under an engineering strain range of 300 to 700 % and an engineering strain rate of 9.3 s^{-1}. These mechanical loading parameters are maintained during device operation, resulting in the optimum cooling power $\dot{Q}_0$ and specific cooling power $\dot{q}_0$ at the corresponding optimum frequency f. The device temperature change is evaluated by the temperature change of the source ΔT_{source}, and the device temperature span ΔT_{device}, each determined under stable conditions.

Type	d (μm)	ΔT_c (K)	ΔT_{ad} (K)	f (mHz)	$\dot{Q}_0$ (mW)	$\dot{q}_0$ (Wg^{-1})	ΔT_{source} (K)	ΔT_{Device} (K)
K	160±50	-6.6±1	11.3±2	425	145	3.4	-2.4	4.0
K	290	-7.6	13.4	425	214	3.3	-2.6	4.2
K	650	-7.9	13.1	350	158	1.2	-2.0	3.4
F	290	-6.5	11.7	425	173	2.4	-2.0	3.3
F	290±50	-5.4±1	8.6±2	425	118	1.6	-1.7	3.3
Chic	340	-7.7	13.0	538	216	2.8	-2.6	4.7
Lp	120	-4.3	6.6	538	96	3.8	-1.9	3.1
L	60	-2.1	4.7	622	115	6.7	-1.8	3.0

For comparison, the foil material properties and the resulting performance of the bistable elastocaloric cooling device are summarized in Table 11. The observed frequency dependence

indicates the existence of an optimal operating range for the bistable elastocaloric device. At low frequencies, parasitic heat effects dominate and reduce both the cooling power and the associated temperature changes. At high frequencies, the limited time available for heat exchange is likely to constrain the performance. The maximum cooling power is therefore observed at an intermediate frequency, representing a balance between actuation rate and thermal transfer efficiency. The results further indicate that the optimal frequency increases with decreasing foil thickness, while the maximum achievable cooling power and temperature span are strongly influenced by the material's elastocaloric temperature change and the thickness inhomogeneity.

6.1.3.3 Coefficient of Performance

To evaluate the performance of the bistable elastocaloric device, the coefficient of performance COP_{device} is calculated based on the mechanical input power per cycle $\dot{W}$. In Figure 60, $\dot{W}$ is shown for NR foils of type "K" with a thickness of 650 µm (blue dots) and 290 µm (green dots), as a function of the operating frequency. The mechanical power $\dot{W}$ is determined for an engineering strain range from 300 to 700 % and an applied engineering strain rate of 9.3 s^{-1}. It increases with both frequency and foil thickness. The discrete frequencies correspond to hold times of t_{hold} = 5, 4, 3, 2, 1, 0.5 s.

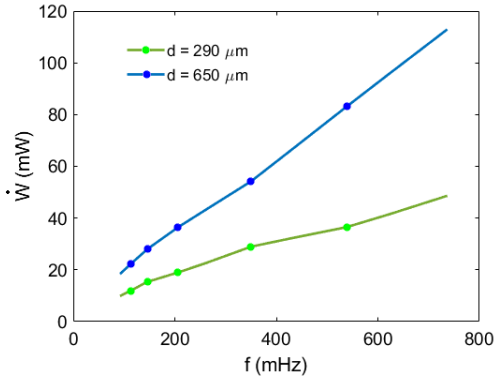

Figure 60: Input power per cycle $\dot{W}$ as a function of frequency for the bistable elastocaloric cooling device employing NR foils of type "K" with thicknesses of 290 and 650 µm. Resulting from an applied engineering strain ranging from 300 to 700 % and an engineering strain rate of 9.3 s^{-1}. The increasing discrete frequencies correspond to hold times of t_{hold} = 5, 4, 3, 2, 1, 0.5 s. Adapted from [178] licensed under CC BY-NC 4.0.

In Figure 61, the coefficient of performance COP_{device} is shown as a function of operating frequency for the bistable elastocaloric cooling device using NR foils type "K" with thicknesses of 290 and 650 µm. The definition of the COP_{device} is introduced in Chapter 5.2.3. The highest observed COP_{device} of 5.7 is achieved with the NR foil type "K" at a thickness of 290 µm, occurring at frequencies of 206 and 259 mHz [178]. In comparison, for the same foil type with an increased thickness of 650 µm, the COP_{device} reaches only 4.3 at the lowest studied frequency of 92 mHz. The NR foil type "Chic" exhibits a lower COP_{device} due to its higher stiffness, which requires a higher work input to achieve the necessary deformation. This leads to an increased

input power per cycle and, consequently, a reduced maximum COP_{device} of 4.4. In contrast, the latex-based foil with a thickness of 60 µm achieves the second highest COP_{device} reaching 5.6.

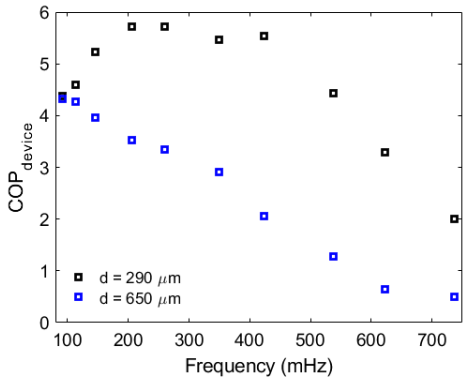

Figure 61: Coefficient of performance COP_{device} versus frequency of the bistable elastocaloric cooling device using NR foil type "K" with thicknesses of 290 and 650 µm. Adapted from [178] licensed under CC BY-NC 4.0.

The results show that the COP_{device} is strongly influenced by both foil thickness and operating frequency, with thinner foils generally exhibiting higher performance. The highest COP_{device} of 5.7 is achieved using the 290 µm NR foil type "K", while thicker and stiffer foils result in reduced efficiency. Notably, the maximum COP_{device} does not coincide with the frequency yielding maximum cooling power, due to the increased input work required at higher operating rates. Although the optimum COP_{device} for the 650 µm foil may lie at lower frequencies not covered here, such conditions are less practical for cooling applications due to the associated drop in cooling power.

6.1.4 Heat Transfer Characterization

The performance characteristics of the tested elastocaloric demonstrators exhibit a strong dependence on the frequency of the applied cyclic loading. These findings underline the critical role of heat transfer processes and emphasize that precise control over thermal dynamics is essential for enhancing device efficiency. To gain deeper insight into the heat transfer mechanisms, a lumped-element model (LEM) simulations using MATLAB Simscape, presented in section 5.2.2 is conducted. These simulations are designed to assess the impact of foil thickness on the foil's temperature response during operation. In the model, the NR foil is divided into thermally thin elements connected via thermal resistances. The convective heat exchange at the exposed surfaces is characterized by a heat transfer coefficient $h_{conv} = 25\ Wm^{-2}K^{-1}$. A particular focus is placed on the thermal interface resistance between the NR and the sink/source, which is found by iteratively comparing simulated and measured temperature changes to correspond to a heat transfer coefficient of approximately $h = 170\ Wm^{-2}K^{-1}$ [178]. The model also accounts for mechanical deformation, incorporating the strain-induced variations in thickness, length and width of the NR foil to accurately reflect changes in the contact area and the associated thermal exchange duration. In Figure 62 (a) the simulated temperature evolution of

the NR foil during one operation cycle for various foil thicknesses over a holding time of 0.75 s and a resulting frequency of 427 mHz is given. Additional simulation results for a 1.0 s holding time and a resulting frequency of 350 mHz are provided in Figure 62 (b). For foil thicknesses of 650 and 290 µm, the temperature drop during step II and III remains incomplete within 0.75 s, resulting in residual temperature ΔT_s of 2.1 K and 0.7 K, respectively, starting from an initial temperature difference of 5.2 K [178]. This incomplete cooling leads to heat accumulation over successive cycles, adversely affecting thermal performance [178]. The simulation results suggest that thinner foils can mitigate this issue. For example, at a foil thickness of 100 µm, the residual temperature increase ΔT_s. is eliminated within less than 0.75 s. The remaining heat affects the subsequent temperature change at the heat source during unloading. Specifically, the initial temperature decrease becomes decreased, and the subsequent temperature rise during contact with the heat source also remains incomplete, leading to non-zero values of ΔT_{so}. Even with the 100 µm foil, a complete return to the original temperature and $\Delta T_{so} = 0$ is not achieved within the given holding time.

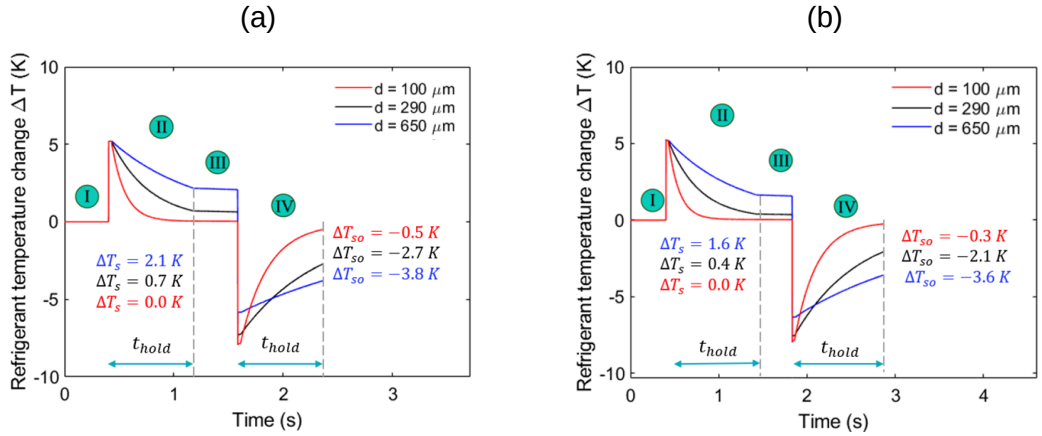

Figure 62: (a) Temperature evolution of the refrigerant during device operation for 100, 290 and 650 µm foil thickness and a frequency of 424 mHz which refers to a hold time t_{hold} of 0.75 s, due to LEM simulation and (b) the corresponding results for a frequency of 350 mHz and which refers to $t_{hold} = 1.0\ s$. The temperature difference ΔT_s and ΔT_{so} correspond to the residual temperture increase after step II and step IV. Adapted from [178] licensed under CC BY-NC 4.0.

To further investigate the influence of achieving a full temperature drop at contact to the heat sink ($\Delta T_{so} = 0$) on cooling performance, an elastocaloric cooling cycle beginning at step III is examined. In this scenario, the pre-strained NR foil of 700 % strain at ambient temperature is released, and the resulting temperature decrease and associated cooling power are measured. At 700 % engineering strain, the thickness of the 650 and 290 µm foils is reduced to approximately 180 and 80 µm, respectively. Assuming $\Delta T_{so} = 0$ can be consistently maintained across cycles, ideal cooling power values are estimated.

Table 12: Summary of the results for the bistable device regarding the remaining temperature increase ΔT_s. The measured cooling power $\dot{Q}_0$ and specific cooling power $\dot{q}$, for NR foils of type "K" with thicknesses d of 290 and 650 µm, evaluated at different holding t_{hold}. Higher cooling power can be achieved when operating without heat accumulation $\Delta T_s = 0$ in the foil-based refrigerant, due to rapid heat transfer. Adapted from [178] licensed under CC BY-NC 4.0.

$d\ (\mu m)$	$t_{hold}\ (s)$	$\Delta T_s\ (K)$	$\dot{Q}_0\ (mW)$	$\dot{q}\ (Wg^{-1})$
290	0.75	0.7	213	3.410
290	0.75	0.0	306	4.880
650	1.0	1.6	158	1.213
650	1.0	0.0	331	2.543

A summary of these results is presented in Table 12. For the 650 µm foil type "K", operated at the optimum frequency of 350 mHz and corresponding holding time of 1.0 s, the cooling power nearly doubles, from 158 to 331 mW. Similarly, for the 290 µm foil type "K" at an optimal frequency of 425 mHz and a holding time of 0.75 s, the cooling power rises from 214 to 306 mW, corresponding to a specific cooling power of 4.8 Wg^{-1}. These simulation trends highlight the substantial potential for performance enhancement, particularly by promoting rapid heat transfer at the heat sink and therefore avoid heat accumulation and ensuring complete heat transfer to the source.

6.1.5 Long-Term Test

A preliminary long-term test with 10^4 cycles is conducted to assess the mechanical stability and elastocaloric performance of NR-based devices, providing initial insights into their suitability for cooling applications. In Figure 63 (a), the temperature change of the heat source ΔT_{source} and the device temperature span ΔT_{device} versus the amount of operation cycles is shown. The error bars represent the measurement uncertainty associated with the Pt100 Class A temperature sensors. The test is performed with a NR foil type "K" with a thickness of 650 µm. The bistable, single-stage elastocaloric cooling device operates at a frequency of 737 mHz, with a corresponding hold time of 0.25 s and an engineering strain rate of 9.3 s^{-1}. In Figure 63 (b), the corresponding mechanical work input to operate the device $\dot{W}$ versus the amount of performed cycles is given.

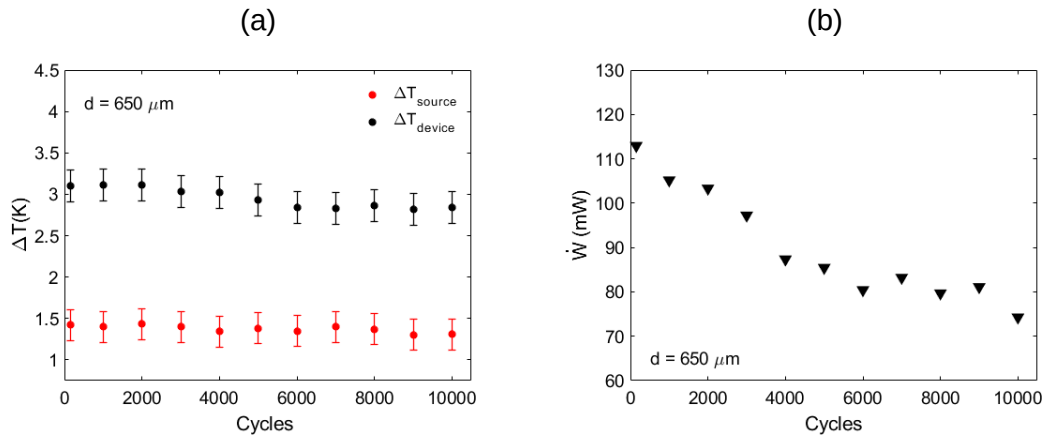

Figure 63: The cyclic stability of the bistable elastocaloric cooling device evaluated in a preliminary long-term test during 10^4 cycles. (a) Temperature change of the heat source (magnitude) ΔT_{source} and the device temperature span and ΔT_{device} versus the amount of operation cycles for a NR foil type "K" of 650 µm thickness and a frequency of 737 mHz and a strain rate of 9.3 s^{-1}. The applied engineering strain ranges from 300 to 700 %. The error bars are determined by the measurement uncertainty of the Pt100 class A temperature sensors. (b) The corresponding input power $\dot{W}$ versus the amount of operation cycles, which decreases by 54 % over 10^4 cycles, thereby enhancing the device's performance. Adapted from [178] licensed under CC BY-NC 4.0.

The temperature change remains consistent across the tested cycles and stays within the bounds of measurement uncertainty. In contrast, a significant reduction in input power $\dot{W}$ is observed with increasing cycle number. After 5000 cycles, the initial input power of 113 mW has already decreased by 32 %. Following 10^4 cycles, only 74 mW are required to perform one cooling cycle, corresponding to a total reduction of approximately 53 % compared to the initial cycle. This trend aligns with the behavior observed in a preliminary long-term test of the monostable single-stage device, see Chapter 5.2.4, where both ΔT_{source} and ΔT_{device} remain stable over 10^4 cycles, while the required work input and consequently $\dot{W}$ decrease, which significantly enhances the device's efficiency.

7 Cascaded Elastocaloric Cooling Device

Besides the single-stage designs employing only one foil refrigerant, the cascaded device architecture utilizes multiple foils that are thermally coupled. By thermally coupling the foils in series, the device can overcome the material's intrinsic adiabatic temperature change ΔT_{ad}, which sets the upper limit for single-stage devices [16]. Each foil refrigerant cycles at different temperatures, enabling an increased device temperature span. Further details are provided in Figure 15. This approach has been exemplified in miniature-scale devices using shape memory alloy (SMA) film refrigerants, where the effective temperature span exceeds the intrinsic material limit [16,185,193]. In SMA-driven devices, the units responsible for thermal coupling are typically of equal length to the heat source and heat sink. When incorporating elastic refrigerant materials into the device architecture, the variation in foil length during load cycling must be considered. Additionally, the intermediate elements responsible for transversal heat exchange must function both as heat sink and heat source. As a result, they must accommodate strain levels ranging from 300 to 700 %. To provide sufficient space for the holder arrays during operation, the intermediate units are divided into two sections, separated by a gap, as illustrated in Figure 64. The holder arrays, which include multiple foils, and the heat transfer units, which comprise both heat sink and heat source elements, form two interlocking comb-like structures. In this work, three foils are used to investigate the behavior of the cascaded device employing natural rubber (NR) as the active material.

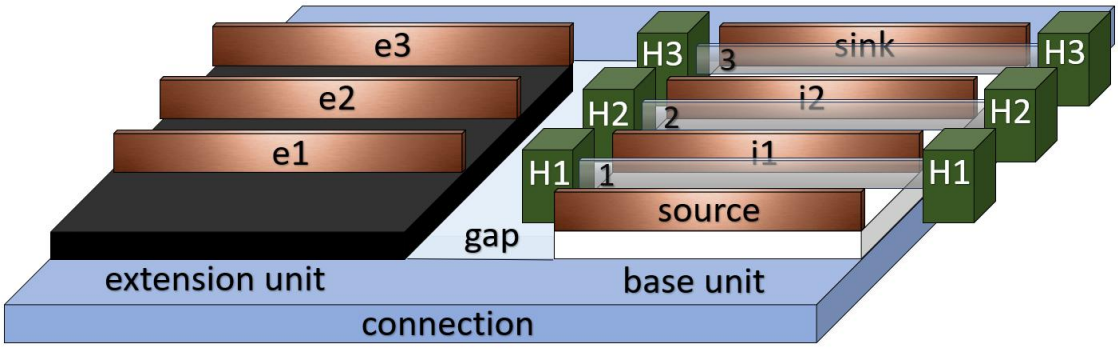

Figure 64: 3D Schematic of the cascaded elastocaloric cooling device, designed to achieve an increased device temperature span by thermally coupling three elastomer foils (1, 2, 3) in series. The device comprises a base unit with a heat source, two connection units (i1, i2), and a heat sink. A gap is included to provide space for the specimen holders (H1, H2, H3) during unloading. During loading, the extension unit absorbs heat via three elements (e1, e2, e3). The base and extension units are mechanically connected and, together with the holder array and foils, form a pair of interlocking comb-like structures.

The cascaded elastocaloric device consists of a specimen holder array (H1, H2, H3), a base unit, and an extension unit, which are mechanically connected via a frame and separated by a gap. The base unit comprises a heat source, a heat sink, and two intermediate elements (i1, i2) that

are arranged in a comb-like structure. The extension unit includes three elements e1, e2, and e3 that absorb heat during the loaded state and thus function as heat sink, also arranged in a comb-like configuration. The holder array is capable of accommodating three foils, labeled as 1, 2, and 3. It comprises six subunits, visualized as green cuboids, which form three holder pairs. Each pair can clamp one elastomer foil, which is illustrated as a gray semi-transparent sheet in the schematic. Holder pairs H1, H2, and H3 are associated with foils 1, 2, and 3, respectively. The three right-side holders are stationary and connected to a load cell (not shown in the schematic), which measures the mechanical work input during cyclic operation. The three opposing left-side holder subunits, are fixed to a holder support, as shown in Figure 65 (a), which corresponds to the pre-strained state. During unloading, the holder support is positioned above the extension unit. This configuration allows the foils, along with their corresponding left-side holder units, to be inserted between the extension unit elements e1 to e3 during loading. The resulting loaded state is shown in Figure 65 (b). By forming two interlocking comb-like structures, with a gap that accommodates the holder arrays, this design eliminates the need for three or more separate actuators to drive the device. Only two actuators are required to operate the device. One actuator loads and unloads the foils by displacing the left-side holder array. The second actuator brings the base and extension units into contact with the foils in the loaded and pre-strained states, enabling heat transfer. This movement occurs perpendicular to the load direction.

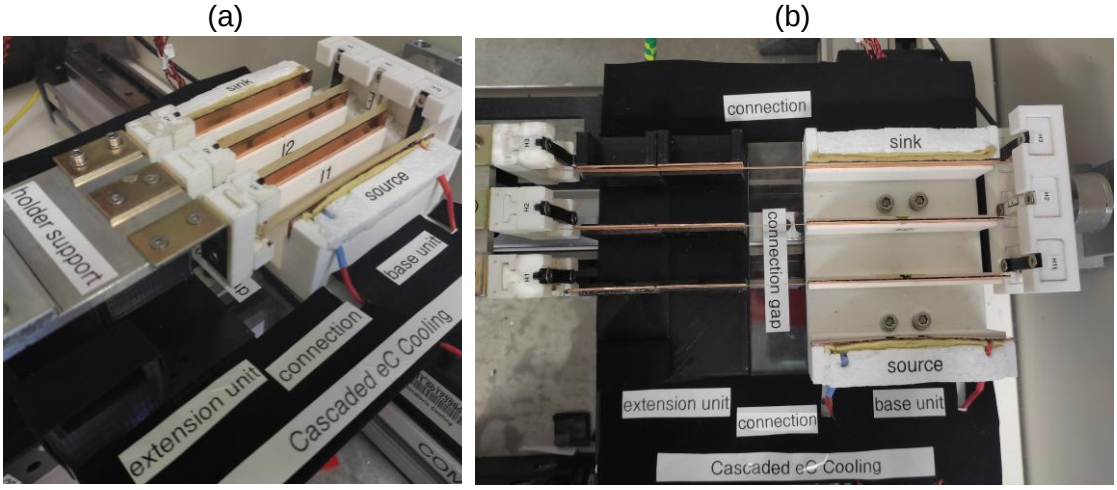

Figure 65: Photographs of the cascaded elastocaloric cooling device under (a) 300 % engineering pre-strain (side view) and (b) maximum deformation, corresponding to 700 % engineering strain (top view). The pre-strained condition represents the transition between step III and step IV (foil are in neutral position), while condition (b) corresponds to step II.

7.1.1 Operation Principle

The cascaded device operates on the same basic principle as the single-stage devices described in this work, following a sequence of four steps. However, multiple foils are employed which are thermally connected in series. An additional transverse heat flow occurs in the out-of-plane direction of the foils, across the heat source, i1, i2 and the heat sink. In Figure 66, the operating principle of the cascaded elastocaloric cooling device utilizing NR foils is illustrated. In step I, the

three NR foils are uniaxially loaded under quasi-adiabatic conditions by rapidly displacing the left-sided holder array with a tensile force $\vec{F}_y$ along the y-axis. The temperature of the foils increases as a result of the elastocaloric effect.

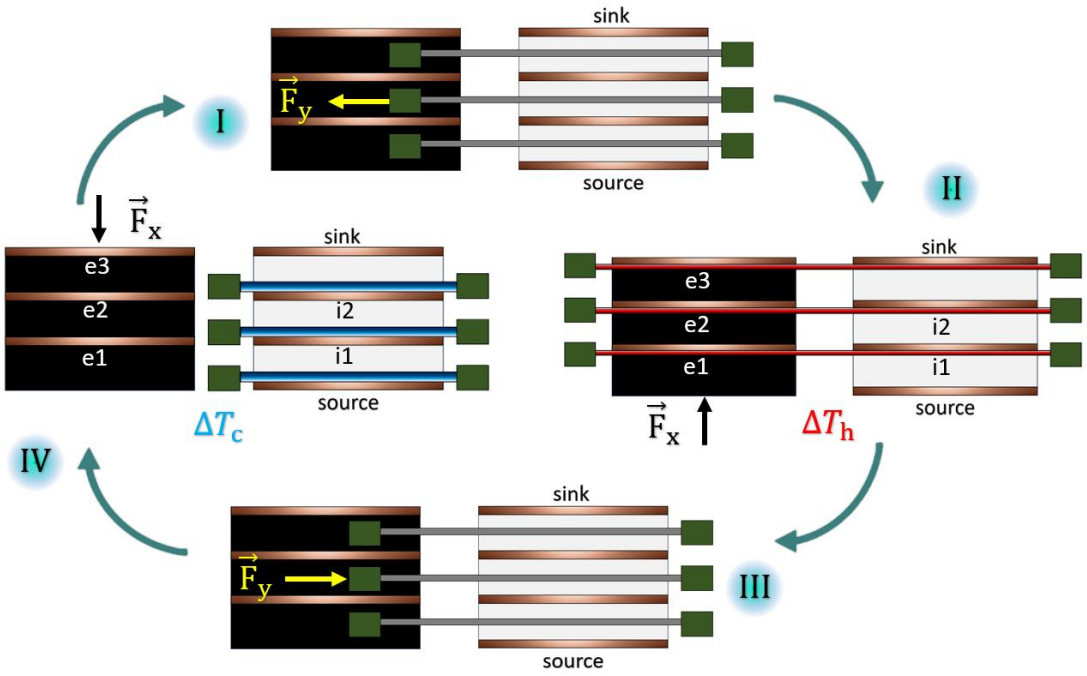

Figure 66: Schematic (top view) of the cascaded elastocaloric cooling cycle comprising three foil refrigerants, which consists of four steps: (I) mechanical quasi-adiabatic uniaxial tensile loading, heating and (II) subsequent heat rejection by mechanical contact to the heat sink and the intermediate elements (i1, i2) and extension units (e1, e2, e3) which also function as heat sink. (III) The unloading is associated with cooling, and (IV) heat absorption from the heat source and the intermediate elements (i1, i2). The yellow arrow indicates the loading and unloading force $\vec{F}_y$, while $\vec{F}_x$ is represented by the black arrow.

In step II, heat is rejected through mechanical contact to the elements i1, i2 and the heat sink within the base unit, as well as to elements e1, e2 and e3 within the extension unit. Mechanical contact is enabled by simultaneously displacing the base and extension units using the force $\vec{F}_x$, which is oriented perpendicular to the loading direction. In step III, quasi-adiabatic unloading of the foils takes place, leading to a temperature decrease due to the reverse phase transformation. In the final step IV, heat is absorbed from the heat source and from the elements e1 and e2, which were heated during step II. Consequently, the intermediate elements function as both a heat sink and a heat source, enabling heat transfer across their front and back surfaces. Therefore, these elements must be free-standing and cannot be thermally insulated on the back side. The thermal coupling in series between the foils is given by heat exchange in the out-of-plane direction. As a result, the first foil, positioned between the heat source and element i1, is cooled by mechanical contact with element i1. Therefore, the reverse phase transformation is initiated at a lower temperature compared to single-stage devices. A temperature gradient builds up, which is discussed in detail in the following chapter.

7.1.2 Results on Temperature Span

To systematically investigate the influence of cascading multiple foils, the temperature evolution over time is first evaluated for a single foil, as shown in Figure 67 (a). All temperature changes are reported relative to the ambient room temperature of 23.0 °C. The experiment is conducted using a NR foil of type "K" with a thickness of 650 µm. The foil undergoes uniaxial load cycling at an engineering strain rate of 9.3 s^{-1}, ranging from 300 to 700 % engineering strain. Given a holding time t_{hold} of 3 s, a ramp time t_{ramp} of 430 ms and an additional tolerance of 250 ms due to experimental constraints, the optimal operating frequency is 136 mHz.

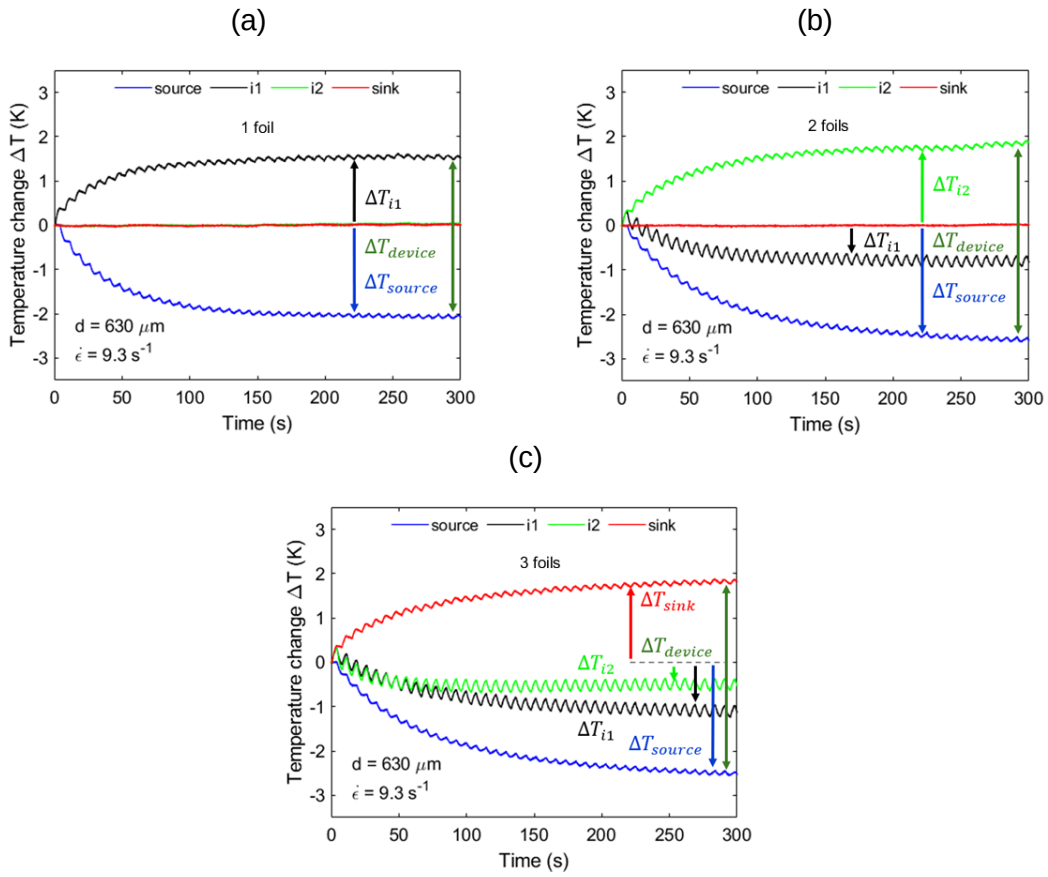

Figure 67: Temperature evolution of the monostable cascaded elastocaloric cooling device, relative to ambient conditions of 23.0 °C, measured at a frequency of 136 mHz ($t_{hold} = 3\ s$) employing a NR foil with a thickness of 650 µm type "K". The applied engineering strain ranges from 300 to 700 % and the engineering strain rate of 9.3 s^{-1} results in loading and unloading durations of $t_{ramp} = 430\ ms$. The device is equipped with (a) one foil, (b) two foils and (c) three foils. For the operation with two foils, the intermediate unit i1 is alternately heated by foil 1 and cooled by foil 2. For the three-foil configuration, in addition i2 is heated by foil 2 and cooled by foil 3 resulting in the temperature changes ΔT_{i1} and ΔT_{i2}. An improved device temperature span ΔT_{device}, can be achieved by cascading two foils in series, with the first foil being precooled via the intermediate element i1. A temperature gradient is built up along the device. For the operation of three foils, ΔT_{i1} is increased from -0.9 to -1.3 K, but ΔT_{source} remains at -2.6 K as for two foils.

In the single-foil setup, the temperatures of element i2 and the heat sink remain at room temperature. Saturation is reached after approximately 120 s, defined as less than 5 % change relative to the final temperature. Under these conditions, a temperature change at the heat source

ΔT_{source} of -2.1 K is observed, while the temperature difference at element i1, ΔT_{i1} is 1.6 K. This results in a total device temperature span ΔT_{device} of 3.6 K.

For two and three cascaded foils, a temperature gradient is observed along the base unit, spanning the heat source, intermediate elements, and the heat sink. In the two-foil configuration, the first foil, positioned between the heat source and element i1, rejects heat to element i1, which is cooled from the opposite side by the second foil. Cooling and heating intervals are phase-shifted by half a period. As a result, the first foil is able to transfer the generated heat during loading more effectively compared to single-foil operation. Due to the fact that $\Delta T_{i1} < 0$ applies after the first two cycles, the first foil rejects heat to a cooled intermediate element rather than to a heated sink. This reduces heat accumulation within the foil and, ideally, allows it to be cooled below ambient temperature. Consequently, the reverse phase transformation in the subsequent unloading step can occur at a lower temperature. This behavior leads to an increased device temperature span ΔT_{device}, primarily due to an increasing ΔT_{source} up to -2.6 K.

For the operation with three foils, the temperature of the intermediate element i1, which cools the first foil by mechanical contact, is further decreased by around -0.3 K, reaching an absolute value of -1.3 K. This marginal difference appears insufficient to further enhance ΔT_{source}. The limitation arises from the heat transfer coefficient, which governs the efficiency of thermal exchange at the mechanical interface between the NR foil and the copper plates. Additionally, the low intrinsic thermal conductivity of the NR foil (below 0.16 $Wm^{-1}K^{-1}$) influences the heat transfer coefficient and further restricts internal heat transfer, thereby limiting the overall thermal performance. One option to mitigate limitations caused by internal heat transfer within the foil, is to decrease foil thickness. In the following thin foils with thicknesses down to 60 µm are tested.

In Figure 68, an overview of the temperature change as a function of the frequency for the cascaded elastocaloric cooling device using different NR foil types is presented. Figure 68 (a)-(c) shows the results obtained using “K” type foils with thicknesses of 800, 650 and 290 µm, respectively. In Figure 68 (d), type “L” foils with a thickness of 60 µm are used. The resulting temperature gradients for device operation with one, two, and three foils, indicated by dotted, solid, and dashed lines, respectively, are shown. When operating with a single foil, the device temperature change ΔT_{device} is the sum of ΔT_{source} and ΔT_{i1}. In the case of operating with two foils, the device temperature change ΔT_{device} is the sum of ΔT_{source} and ΔT_{i2}. When operating with three foils, ΔT_{device} is the sum of ΔT_{source} and ΔT_{sink}.

For all tested foils, the same general trend can be observed. The optimum frequency, corresponding to the minimum of the ΔT_{source} curves, varies with the foil thickness. The foil thickness and the operating frequency exhibit an inversely proportional relationship, which is consistent with the behavior observed for the single-stage devices under investigation. For foils with a thickness of 800 µm, the optimum frequency is 88 mHz, whereas for foils with a thickness of 60 µm, frequencies above 400 mHz are favorable. Furthermore, at the optimum frequency, the absolute temperature changes at both the heat source and the heat sink reach their maximum values. The smallest absolute values of ΔT_{source} are obtained in single-foil operation, which

consequently limits ΔT_{device}. By operating the device with two or more foils, ΔT_{device} can be increased. However, the improvement from two to three foils is only marginal. The highest ΔT_{device} of 5.1 K is achieved when operating two foils with a thickness of 800 µm at a frequency of 88 mHz. While the highest ΔT_{source} is -3.2 K and observed for the same frequency but with three foils.

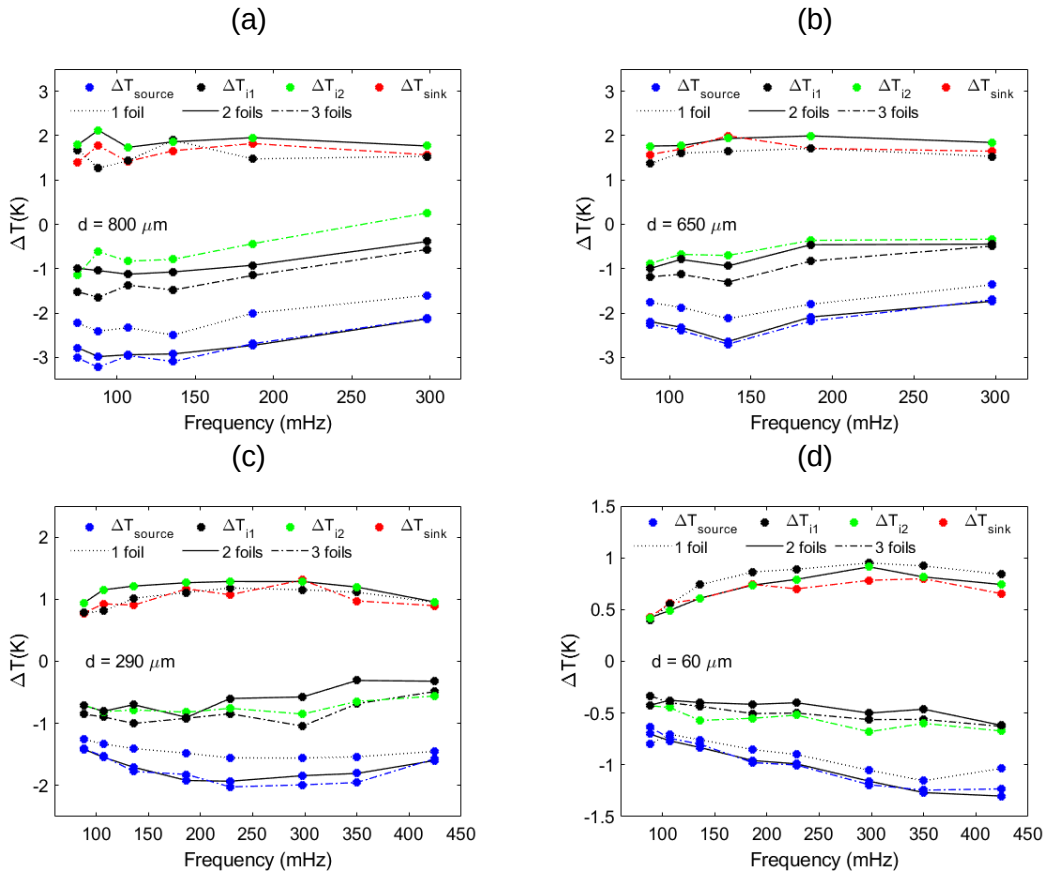

Figure 68: Temperature change versus frequency of the cascaded elastocaloric cooling device, employing NR foils type "K" (a-c) for the corresponding foil thickness d. In panel (d) the results for the NR foil type "L" are presented. The applied engineering strain ranges from 300 to 700 % and the engineering strain rate of 9.3 s^{-1} results in loading and unloading durations of $t_{ramp} = 430\ ms$. The temperature changes are given for one foil (dotted line), two foils (solid line) and three foils (dashed line). The optimum operating frequency (minimum ΔT_{source}) increases with decreasing foil thickness and remains unaffected by the number of foils employed. An improved device temperature span ΔT_{device}, can be achieved by cascading two foils in series, thereby increasing the absolute value of ΔT_{source}. However, across all investigated foil thicknesses, the incorporation of a third foil does not result in any further performance enhancement.

When the number of cascaded foils is increased from one to two, a ΔT_{i1} of -1.0 K is observed at the optimum frequency of 88 mHz, as shown in Figure 68 (a). This results in an additional temperature improvement of -0.8 K in ΔT_{source}. By comparing the solid connection line with black dots (two foils) to the dashed and dotted connection line with black points (three foils), it can be seen that the internal temperature gradient increases with more foils. Increasing the number of 800 µm foils from two to three further cools the intermediate element i1, improving ΔT_{i1} by approximately -0.5 K. However, even though the absolute temperature of the intermediate

element increases when an additional foil is added, the overall temperature span ΔT_{device} remains almost unaffected. Specifically, improving ΔT_{i1} by around 60 % to the absolute value of -1.6 K leads to an additional improvement of -0.2 K of ΔT_{source}. For foils with thicknesses of 290 and 650 µm, approximately 50-60% of the intermediate temperature change ΔT_{i1} can be used to improve ΔT_{source} by cascading. The resulting improvement in ΔT_{source} compared to a single foil, ranges between -0.4 and -0.6 K. In the case of cascading 60 µm foils, the transfer efficiency is even lower. It appears that the cascaded device is less suitable for thinner foils, such as the 290 and 60 µm ones. This is evident from the direct comparison with the bistable single-stage device as listed in Table 12. The achieved ΔT_{source} for one foil in the cascaded device is less than that of the bistable device. By comparison, the absolute value of ΔT_{source} achieved with the bistable device is approximately 1 K higher. In contrast, the 650 µm foils exhibit comparable temperature differences across all device types.

Table 13: Comparison of the heat source temperature difference ΔT_{source} and the device temperature span ΔT_{device} for the monostable single-stage, bistable single-stage, and cascaded devices using various NR foils. The foils with a thickness d are operated at their corresponding optimum frequency f.

Device	Foils	Type	d (μm)	f (mHz)	ΔT_{source} (K)	ΔT_{Device} (K)
Monostable single-stage	1	K	650	136	-2.0	4.1
Bistable single-stage	1	K	650	350	-2.0	3.4
Cascaded	1	K	650	136	-2.1	3.7
Cascaded	2	K	650	136	-2.6	4.5
Cascaded	3	K	650	136	-2.7	4.7
Monostable single-stage	1	F	290±50	230	-1.7	3.1
Bistable single-stage	1	F	290±50	425	-1.7	3.3
Bistable single-stage	1	K	290	425	-2.6	4.2
Cascaded	1	K	290	297	-1.6	2.8
Cascaded	2	K	290	297	-1.8	3.1
Cascaded	3	K	290	297	-2.0	3.4
Bistable single-stage	1	L	60	424	-1.4	2.5
Cascaded	1	L	60	424	-1.0	1.9
Cascaded	2	L	60	424	-1.3	2.0
Cascaded	3	L	60	424	-1.2	1.9

The ΔT_{device} and heat transfer dynamics are further analyzed using LEM simulations, for the operation of three cascading foils with a thickness of 290 µm. Figure 69 shows experimental results (blue dots) and corresponding simulation results (blue solid line) for various heat transfer coefficients h on the ΔT_{device} as a function of frequency.

The simulation results of the ΔT_{device} align with the experimental results, exemplified by a negligible deviation of below 3 %, for the optimum frequency. With increasing h, the ΔT_{device} increases and shifts towards higher optimum operation frequencies. In detail, by increasing h from 120 to 1000 $Wm^{-2}K^{-1}$, ΔT_{device} increases from 3.4 to 6.0 K and the corresponding optimum frequency shifts from 287 to 538 mHz. A negligible increase in ΔT_{device}, amounting to less than 2 %, is observed when h is further increased to 2000 $Wm^{-2}K^{-1}$.

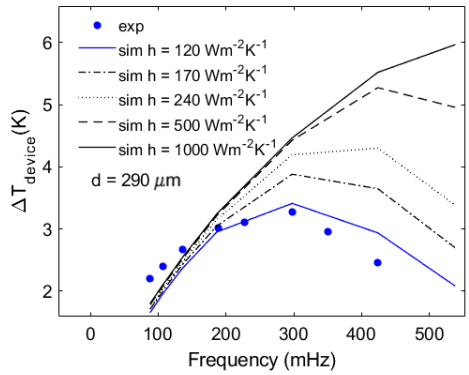

Figure 69: Device temperature span ΔT_{device} as a function of frequency, evaluated through both LEM simulations (lines) and experimental tests (blue dots) on the cascaded elastocaloric cooling device. Three NR foils with the thickness of 290 µm are cascaded. The optimum frequency and ΔT_{device} increase with increasing heat transfer coefficient h.

The ΔT_{device} can be further increased by decreasing the mechanical loading and unloading times t_{ramp} and therefore increasing the engineering strain rate $\dot{\varepsilon}$. The t_{ramp} is set to 110 ms, corresponding to an engineering strain rate of approximately 36 s^{-1}, which aligns with the fastest loading and unloading conditions reported in literature [31]. An overview of the resulting ΔT_{device} for one and three cascaded foils, due to experiment and simulation is summarized in Table 14. A t_{hold} of 0.25 s corresponds to a frequency of around 1.4 Hz. For this frequency and a h of 1000 $Wm^{-2}K^{-1}$ the simulation indicates an enhanced ΔT_{i1} of -6 K and ΔT_{i2} of -2.8 K after 300 s. This results in an increased ΔT_{source} of -9.3 K and a ΔT_{sink} of 1.9 K, therefore exceeding ΔT_c of -7.9 K. The resulting ΔT_{device} of 11.9 K is close to ΔT_{ad}. A similar trend is identified for one foil, nevertheless the maximum ΔT_{device} of 6.6 K remains below the ΔT_{ad}.

The highest reported ΔT_{device} for a cascaded device based shape memory alloys (SMAs) and solid-to-solid heat transfer is 27.3 K, with a corresponding ΔT_{source} of 10.6 K [193]. In detail, the reported device employs three NiTiFe films with a ΔT_{ad} of 36 K, in contrast to the ΔT_{ad} of 13.5 K for the NR foil operating between 300 and 700 % engineering strain. This indicates that

cascaded NR-foil-based cooling devices have the potential to compete with alternative cooling systems provided that the improvements above are successfully implemented.

Table 14: The device temperature span ΔT_{device} of the cascaded elastocaloric cooling device as a function of the heat transfer coefficient h and the engineering strain rate corresponding to the optimum frequency f. The results are determined by LEM simulations and experiments for one and three cascaded NR foils type "K" with a thickness of 290 µm. The ΔT_{device} increases with increasing h, $\dot{\varepsilon}$ and by cascading.

Method	Foils	h $(Wm^{-1}K^{-1})$	$\dot{\varepsilon}$ (s^{-1})	f (mHz)	ΔT_{Device} (K)
Experiment	1	120	9.3	297	2.8
Simulation	1	120	9.3	297	2.7
Simulation	1	120	36.0	1400	4.1
Simulation	1	1000	9.3	538	4.1
Simulation	1	1000	36.0	1400	6.6
Experiment	3	120	9.3	297	3.4
Simulation	3	120	9.3	297	3.3
Simulation	3	120	36.0	450	4.8
Simulation	3	1000	9.3	538	6.0
Simulation	3	1000	36.0	1400	11.9

In summary, the cascaded device is capable of enhancing ΔT_{source} and ΔT_{device} by thermally coupling the foils in series. Its performance exhibits a pronounced dependence on both operation frequency and foil thickness, consistent with the behavior observed in the single-stage devices. The LEM simulation reveals an increasing ΔT_{device} by increasing h and $\dot{\varepsilon}$, for both the single-stage and the cascaded device. This aligns with the increasing trend of the specific cooling power $\dot{q}_0$, with increasing h for the single-stage device. For more details, see Chapter 5.2.3.

7.1.3 Cooling Power under Thermal Load

To determine the cooling power under thermal load, a resistor heated by an electric current is directly attached to the back side of the heat source. Specifically, a meander-shaped wire made of constantan is adhered to the copper plate. Care was taken to avoid the use of any intermediate layer that could hinder heat transfer. By heating the resistor, a homogeneous surface temperature of the heat source is generated, as verified by infrared thermography, while the electrical resistance remains constant within the tested temperature range.

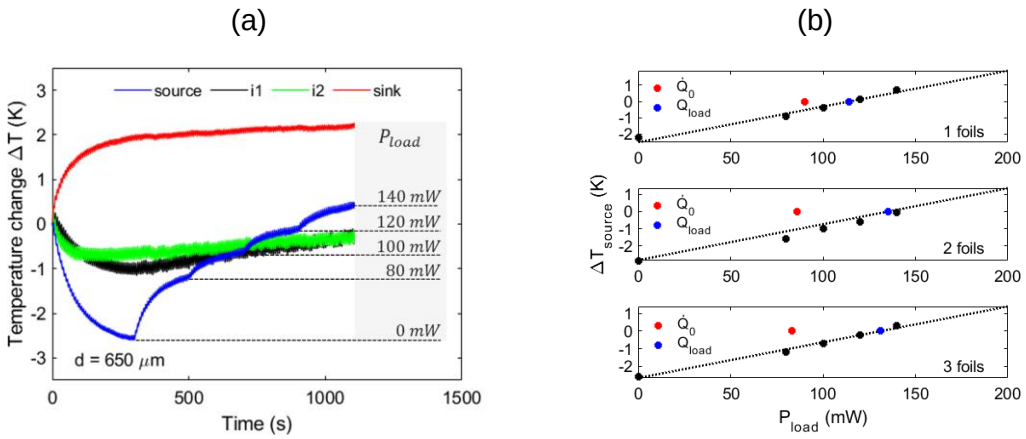

Figure 70: (b) Temperature evolution of the monostable cascaded elastocaloric cooling device with and without thermal load, relative to ambient conditions of 23.0 °C. Measured at a frequency of 136 mHz ($t_{hold} = 3\ s$) employing three NR foils with a thickness of 650 µm type "K". The applied engineering strain ranges from 300 to 700 % and the engineering strain rate of 9.3 s^{-1} results in loading and unloading durations of $t_{ramp} = 430\ ms$. After 300 seconds, the back side of the heat source is heated by a load resistor, with the input power increasing from 80 to 140 mW. (b) The corresponding source temperature change is shown for different applied thermal load and for configurations using 1, 2, and 3 foils. The resulting cooling power under load Q_{load} (blue dot) is determined by linear regression. For comparison, the initial cooling power $\dot{Q}_0$ (red dot) under unloaded conditions is also provided.

In Figure 70 (a), the temperature evolution of the monostable cascaded elastocaloric cooling device without and with thermal load P_{load} is shown. Three NR foils of type "K" operate at a frequency of 136 mHz, corresponding to a hold time t_{hold} of 3 s and an engineering strain rate of 9.3 s^{-1}. The applied engineering strain ranges from 300 to 700 %. For the first 300 s, the device operates without thermal load, allowing the full ΔT_{device} to develop. At 300 s, the first phase of thermal loading begins with 80 mW. Subsequently, ΔT_{source} decreases, while ΔT_{sink} remains constant. The thermal load is increased stepwise up to 140 mW. By applying P_{load} of 80 mW, ΔT_{source} is reduced to -1.2 K. The reduction of the ΔT_{source} is proportional to P_{load} and even ΔT_{i1} and ΔT_{i2} are reduced. By applying 140 mW of thermal load, ΔT_{i1} and ΔT_{i2} still remain negative and correspondingly result in -0.6 and -0.5 K from its initial values of -1.1 and -0.8 K. In Figure 70 (b), the corresponding ΔT_{source} under thermal load is shown for the operation with one, two, and three foils. The cooling power under load is determined by linear regression of the measured data points (indicated as black dots) and the intersection with the y-axis ($\Delta T_{source} = 0$). The initial cooling power $\dot{Q}_0$ (red dot) and the cooling power under thermal load Q_{load} (blue dots) can be compared. For employing one foil, Q_{load} is 114 mW and therefore 27 % larger than $\dot{Q}_0$. For two and three foils the difference is even higher. In both cases, Q_{load} is around 57 % larger than $\dot{Q}_0$. With two foils, Q_{load} results in 135 mW. When comparing absolute values with literature, caution must be taken, as the cooling power depends on how it is determined. In addition, for $\dot{Q}_0$, the remaining cooling capacity of the intermediate elements i1 and i2 is not considered, as only the slope of the heat source is used for the calculation. However, under thermal load, the temperatures ΔT_{i1} and ΔT_{i2} are affected and rise, as shown in Figure 70 (a). Consequently, Q_{load} may overestimate the cooling power, whereas $\dot{Q}_0$ provides a conservative estimate, representing a lower limit.

The maximum cooling power achieved in this work [19] is lower than that reported in the literature [34] for a similar device with a 600 µm NR foil. The higher cooling power reported in the literature is determined under thermal load. However, the specific cooling power is nearly twice as high. This suggests that the higher cooling power reported elsewhere is likely achieved using a larger refrigerant mass. This interpretation is supported by the higher specific cooling power of 1.1 Wg^{-1} [19] compared to 0.54 Wg^{-1} [34] for the device reported in literature. Furthermore, the device temperature span in the reference work [34] is more than twice as low as in this work [19] and is obtained at a lower operating frequency of 136 mHz. These results suggest that the device developed in this work is particularly well suited for miniature-scale elastocaloric cooling.

To compare the different device types investigated in this work, operated with the 650 µm foil, the bistable single-stage device exhibits the highest $\dot{Q}_0$ of 158 mW. The second-highest $\dot{Q}_0$ is obtained for the monostable single-stage device, with approximately 123 mW. It is not surprising that the lowest $\dot{Q}_0$ is recorded for the cascaded device, as it behaves like a monostable single-stage device but includes an additional gap at the heat sink. This gap reduces the area available for heat transfer, which negatively affects the cooling performance (see Chapter 6.1.4). However, the primary objective of the cascaded device is to enhance the ΔT_{device}, which is successfully demonstrated.

Conclusions

In modern society, cooling technologies are omnipresent and play an indispensable role in everyday life. The demand for cooling applications such as air conditioning, food preservation, and thermal management of batteries is expected to steadily increase. Elastocaloric solid-state cooling, which relies on temperature changes induced by mechanical loading, has emerged as a promising alternative to conventional vapor-compression technology. By avoiding the use of refrigerant gases with high global warming potential (GWP) as well as per- and polyfluoroalkyl substances (PFAS), this approach offers a more sustainable pathway for cooling applications. Elastocaloric cooling based on elastomers such as natural rubber (NR) offers environmentally friendly advantages due to its non-toxic composition and derivation from a renewable resource. In addition, a low price of around 1.5 €kg^{-1} and existing mass production may further facilitate commercialization.

The elastocaloric effect and the associated reversible temperature change upon mechanical deformation in elastomers are based on strain-induced crystallization (SIC) and entropy elasticity (EE). The EE describes the alignment of molecular chains induced by a mechanical stimulus. When subjected to tensile stress, a fraction of the polymer chains in the network straighten and become ordered. The SIC arises in the rubber material and latent heat is released. Furthermore, the SIC is associated with the fatigue resistance of NR under dynamic loading. After load removal, the crystallites melt and heat is absorbed. The elastocaloric cooling cycle comprises four steps. The cycle starts with the mechanical loading of the NR refrigerant, causing a temperature increase and heat release. Subsequently, unloading occurs, resulting in a temperature decrease and the absorption of heat for cooling. In order to achieve large adiabatic temperature changes, high strains of several hundred percent are needed. To enable rapid heat transfer, foil refrigerants are of special interest due to their high surface-to-volume ratio. In literature, only a limited number of studies have concentrated on the development of rubber-based elastocaloric devices. The focus of this work is on understanding the coupled thermal and mechanical properties of NR foil refrigerants as well as their implementation in a new generation of miniature-scale elastocaloric cooling devices that operate on the principle of solid-to-solid heat transfer. The device performance is evaluated to assess their potential for the utilization in practical cooling applications, and to identify possibilities for further improvement.

In this work, foil refrigerants of 9 × 26.5 mm^2 lateral size are investigated, which are laser-cut from NR sheets with thicknesses ranging from 60 to 900 µm. Sheet materials such as commercially available NR, NR latex, and NR produced with different crosslinking methods are employed. The elastocaloric effect is evaluated under uniaxial tensile loading, while an infrared (IR) camera captures the emitted radiation, which correlates with the material surface temperature. Mechanical parameters like the maximum engineering strain, engineering strain rate, and engineering pre-strain are investigated with respect to their influence on the induced elastocaloric temperature evolution and engineering stress-strain curves. Maximum engineering strains of up

to 700 % and a sufficiently high engineering strain rate of 9.3 s^{-1} are required to induce an adiabatic temperature change ΔT_{ad} of approximately 20.3 K.

This corresponds to a NR foil with a thickness of 290 µm and a temperature change of +10.0 K upon loading and of -10.3 K upon unloading. A maximum engineering stress of 3.5 MPa and a stress relaxation of 1.6 MPa under constant maximum deformation are observed. Rapid load cycling must be performed to reduce undesired parasitic heat exchange. The required engineering strain rate to achieve quasi-adiabatic loading conditions depends on the foil thickness. For the foils with a thickness of 290 µm, an engineering strain rate of 9.3 s^{-1} is required, while for the foils with a thickness of 650 µm, 4.7 s^{-1} is sufficient. For all examined foils, the engineering stress-strain curves exhibit a hysteresis loop, characterized by an unloading curve with lower stress levels. The hysteresis increases with increasing maximum engineering strain and strain rate, as stress relaxation during loading occurs. Thus, the work input required for a single cooling cycle increases due to the enlarged area enclosed by the hysteresis loop. In contrast, stress relaxation decreases with shorter hold times, which has a positive effect on operation at higher frequencies. For increasing strain, the foil thickness decreases while the surface area enlarges. Thereby, the surface-to-volume ratio increases and heat transfer is enhanced.

Operating with pre-strain is beneficial not only for enhancing heat transfer but also for reducing the required work input and active displacement. However, this advantage comes at the cost of a reduced adiabatic temperature change ΔT_{ad}. An engineering pre-strain of 300 % is identified as optimum due to its increased material coefficient of performance COP_{mat} of around 6 and remaining ΔT_{ad} of 12.4 K. This corresponds to a NR foil with a thickness of 650 µm and an engineering strain rate of 4.7 s^{-1}. In addition, the surface area available for heat transfer increases by 48 %, and the surface-to-volume ratio rises by 240 % compared to the undeformed state. In addition to conventional sulfur-vulcanized NR sheets, recyclable NR materials are developed at the University of Freiburg using a novel crosslinking approach. The recyclable NR foils (type “CHIC”) are identified to have a promising elastocaloric performance. An overview of the investigated NR foils and their performance metrics is summarized in Table 15.

Table 15: Overview of elastocaloric material properties of the investigated foils with different initial thicknesses d. For material details of the NR foils ("K", "F" and "Chic") and NR latex foil ("L"), see Table 5. The test condition parameters are the strain range, which is given by the engineering pre-strain ε_{pre}, the maximum engineering strain ε_{max} and the corresponding engineering strain rate $\dot{\varepsilon}$. The resulting parameters are the specific work input Δw, the temperature change upon unloading ΔT_c, the peak-to-peak temperature change ΔT_{ad}, the corresponding specific absorbed heat q_{ab} and the coefficient of performance for the material COP_{mat}.

Type	d (μm)	$\varepsilon_{pre} - \varepsilon_{max}$ (%)	$\dot{\varepsilon}$ (s^{-1})	Δw_{mat} ($J g^{-1}$)	ΔT_c (K)	ΔT_{ad} (K)	q_{ab} ($J g^{-1}$)	COP_{mat}
K	650	0-700	9.3	8.5	-10.3	20.3	19.5	2.3
K	650	300-700	9.3	3.6	-7.9	13.1	14.9	4.1
K	290	0-700	9.3	7.2	-10.0	17.4	18.9	2.6
K	290	300-700	9.3	4.2	-7.6	13.5	14.3	3.4
F	290	0-700	9.3	6.8	-8.2	13.5	9.7	1.4
F	290	300-700	9.3	2.9	-6.4	10.6	12.0	4.1
Chic	340	0-700	9.3	17.7	-11.4	23.1	21.6	1.2
Chic	340	300-700	9.3	3.5	-7.7	13.0	14.6	4.2
L	60	0-700	9.3	6.8	-7.1	9.5	13.4	1.9
L	60	300-700	9.3	4.0	-2.1	4.7	4.0	1.0

Three different elastocaloric cooling devices are designed and realized based on the comprehensive material characterization of the NR foils. One general design goal is to minimize the number of driving actuators and eliminate expensive, large-scale hydraulic or pneumatic components to ensure a cost efficient and leakage free device. Consequently, heat is transferred between the foil refrigerant and the heat sink and heat source via solid-to-solid mechanical contact. The first device under investigation is a monostable single-stage device, in which one actuator is employed for mechanical load cycling, while another one facilitates heat transfer. The heat sink and heat source units are oriented in parallel and alternately contact the refrigerant during mechanical loading and unloading, respectively. This enables spatial separation of the hot and cold heat flows. The dimensions of the heat sink and heat source are designed to match the rectangular contact area of the foil, which changes throughout the cooling cycle. The contact time for heat transfer strongly influences key performance parameters, including the device temperature span ΔT_{device}, the initial cooling power $\dot{Q}_0$ and the device coefficient of performance COP_{device}. Hold times, ranging from 0.5 to 5.0 s, are tested and optimized for each foil thickness. At frequencies above the optimum, the contact time for heat transfer becomes too short, while the required mechanical work input increases. Conversely, at frequencies below the optimum, efficiency decreases due to insufficient heat exchange between the foil and the heat sink or heat source. During mechanical loading and unloading, no heat transfer occurs through mechanical contact between the foil refrigerant and the device. However, undesired parasitic heat transfer to the surroundings causes minor oscillations in the device's temperature evolution. Therefore, the deformation time should be minimized with respect to the previously identified threshold for quasi-adiabatic load cycling for each specific foil thickness. Higher strain rates are avoided, as they impose high demands on the actuator performance and lead to an undesirable increase in input power per cycle.

Table 16: Key results of the monostable single-stage elastocaloric cooling device. The results are archived with NR foils of type "K" and "F" and the corresponding foil thickness d of 650 and 290 µm. The engineering strain ranges from 300 to 700 % and mechanical loading and unloading is performed at an engineering strain rate of 9.3 s^{-1}. The (specific) cooling power $\dot{Q}_0$ ($\dot{q}_0$) and the input power per cycle $\dot{W}$ depend on the operation frequency f and determine the coefficient of performance COP_{device}. The device temperature change is evaluated by the temperature change of the source ΔT_{source}, and the device temperature span ΔT_{device}, each determined under stationary conditions. Highlights are marked in bold. Adapted from [19] licensed under CC BY 4.0.

Type	d (μm)	f (mHz)	$\dot{Q}_0$ (mW)	$\dot{q}_0$ $(mW g^{-1})$	COP_{device}	ΔT_{source} (K)	ΔT_{Device} (K)
K	650	136	**123**	954	**4.7**	-2.0	**4.1**
F	290	230	78	**1082**	4.0	-1.7	3.1

It is shown that the performance exhibits a pronounced dependence on both foil thickness and operation frequency. A maximum ΔT_{device} of 4.1 K, a COP_{device} of 4.7 and an absolute cooling power of 123 mW are demonstrated for the single-stage device with a 650 µm foil operating between the engineering strain range of 300-700 %. The key performance metrics are given in Table 16. Lumped Element Model (LEM) simulations reveal the optimum frequency to maximize the cooling power. For NR foils with thicknesses of 650 and 290 µm, the predicted frequencies of 136 and 230 mHz, align with the experimental results. Furthermore, LEM simulations indicate that improving heat transfer properties and further decreasing the foil thickness can lead to significant enhancements in device performance.

The second device under investigation introduces a bistable actuation mechanism, to further reduce the number of actuators. The bistable actuation mechanism, utilizing a rotating lever arm for both mechanical loading and heat transfer. Two stable points corresponding to the minimum and maximum deformation of the foil are present. These stable end points represent energy minima in the system's potential landscape. No force is required to maintain this state, thus enabling significant power savings for the driving motor. In addition, at the stable positions heat is transferred between the foil refrigerant and the heat sink and heat source. In the case of the 290 µm thick NR foil and the optimal frequency of 424 mHz, the overall time without energy demand during operation reaches 64 % of the total cycling time. The highest ΔT_{device} of 4.7 K and ΔT_{source} of -2.6 K is observed for the recyclable NR foil with a thickness of 340 µm. In contrast to the monostable single-stage device, the loading forces are reduced by factors of 2.8 and 2.5 for foil thicknesses of 650 and 290 µm, respectively. For decreasing the foil thickness from 650 to 290 µm, the optimum operation frequency increases from 350 to 424 mHz. Consequently, the absolute cooling power increases from 158 to 214 mW. The COP_{device} reaches values up to 5.7 for foil refrigerants of 290 µm thickness. It is demonstrated that foils of reduced thickness exhibit superior performance compared to those of greater thickness. At first consideration, this may appear counterintuitive, given that a greater volume of material in the thicker foil leads to a larger amount of absolute released and absorbed latent heat. However, the thinner foil enables faster heat transfer, due to its reduced thermal mass and increased surface-to-volume ratio ration. Moreover, a fast heat transfer to the heat sink is essential to prevent heat accumulation and consequently enable complete transfer of cold to the heat source. By further decreasing the

foil thickness to 60 µm, the specific cooling power increases to 6.7 Wg^{-1}. The corresponding increase in specific cooling power and optimal operation frequency with decreasing foil thickness are illustrated in Figure 71.

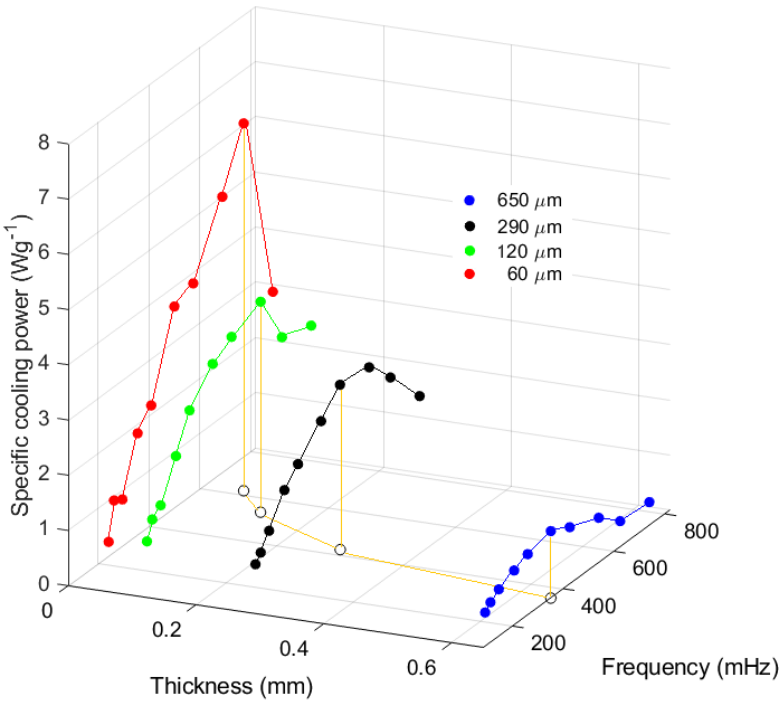

Figure 71: Specific cooling power as a function of the foil thickness and the operation frequency. The results correspond to the bistable single-stage elastocaloric cooling device. The optimum frequencies are highlighted by white dots.

The optimum operation frequency is determined by the foil thickness and scales inversely with it, remaining independent of the material's adiabatic temperature change ΔT_{ad}. The performance is significantly influenced by the frequency, ΔT_{ad} and the thickness inhomogeneity due to manufacturing tolerances, highlighting its critical role. For a decreased ΔT_{ad} by 1.7 K, the resulting ΔT_{device} is 0.9 K lower. Furthermore, the maximum observed source temperature change ΔT_{source} of 2.6 K decreases to 2.0 K. In addition, the $\dot{Q}_0$ is 41 mW lower for foils with a thickness of 290 µm. If the foil thickness additionally varies by ± 50 µm, the influence on the cooling power becomes even more pronounced, resulting in a 45 % reduction to 118 mW, compared to 214 mW for the foil with a homogeneous thickness. The inhomogeneous thickness leads to an inhomogeneous temperature distribution within the foil and therefore locally reduced ΔT_{ad}. The key results of the bistable single-stage elastocaloric cooling device are summarized in Table 17.

Table 17: Key results of the bistable elastocaloric cooling device. The results are archived with (latex) NR foils of type "K", "F", "Chic" and ("L") and the corresponding foil thickness d. The engineering strain ranges from 300 to 700 % and mechanical loading and unloading is performed at an engineering strain rate of 9.3 s^{-1}. The optimum cooling power $\dot{Q}_0$ and specific cooling power $\dot{q}_0$ correspond to the optimum frequency f. The device temperature change is evaluated by the temperature change of the source ΔT_{source}, and the device temperature span ΔT_{device}, each determined under stable conditions. Highlights are marked in bold.

Type	d (μm)	f (mHz)	$\dot{Q}_0$ (mW)	$\dot{q}_0$ (Wg^{-1})	COP_{device}	ΔT_{source} (K)	ΔT_{Device} (K)
K	650	350	158	1.2	4.3	-2.0	3.4
K	290	425	**214**	3.3	**5.7**	**-2.6**	4.2
F	290±50	425	118	1.6	3.6	-1.7	3.3
F	290	425	173	2.4	5.2	-2.0	3.3
Chic	340	538	**216**	2.8	4.4	**-2.6**	**4.7**
L	60	622	115	**6.7**	**5.6**	-1.8	3.0

The third device under investigation comprises three cascaded foils that are thermally connected in series to enhance the ΔT_{device}. An array of foil holders and a heat transfer unit, comprising a heat sink and heat source, are arranged in interlocking, comb-like structures. The key results of the cascaded elastocaloric cooling device are summarized in Table 18. During the operation with two and three foils, a temperature gradient is observed. By increasing the number of 800 µm foils from one to two, the intermediate element results in a temperature change ΔT_{i1} of -1.0 K. The foil in contact with the heat source is pre-cooled by the intermediate element. This corresponds to an increased ΔT_{source} of -3.0 K in contrast to -2.2 K for the operation with one foil. Consequently ΔT_{device} increases to 5.1 K, representing the highest value achieved in this work. The improvement resulting from two to three foils is marginal, as it leads to a non-significant enhancement of ΔT_{i1} up to -1.5 K and ΔT_{source} of -3.2 K. This emphasizes the crucial need to address the limitations in both internal and interfacial heat transfer, caused by the intrinsically low thermal conductivity of NR materials, which falls within the range of thermal insulators. LEM simulations indicate that improving heat transfer properties lead to significant enhancements in ΔT_{device}.

In addition to performance optimization through variation of the operation frequency and foil thickness, as well as enhancement of ΔT_{device} by cascading multiple foils, this work also investigates the cyclic stability of the device. To demonstrate the potential of NR-based elastocaloric materials for cooling applications, a preliminary long-term cycling test, comprising 10^4 cycles, is successfully carried out with both single-stage devices. The test is realized through the successful implementation of compact, custom-designed foil holders. A decreased input power with an increasing number of operation cycles is observed, indicating improved energy efficiency of the elastocaloric cooling device. In addition, the temperature change remains stable throughout 10^4 cycles and is unaffected by full mechanical load removal, confirming the thermal reliability of the system under long-term operation. Overall, these findings are highly promising and underline the strong potential of NR-based elastocaloric devices for future sustainable cooling technologies.

Table 18: Key results of the cascaded elastocaloric cooling device. The engineering strain ranges from 300 to 700 % and mechanical loading and unloading is performed at an engineering strain rate of 9.3 s^{-1}. Comparison of the temperature change of the source ΔT_{source} and the device temperature span ΔT_{device}, for the operation with one, two and three NR foils. Foils with a thickness d are operated at their corresponding optimum frequency f. Highlights are marked in bold.

Type	Foils	d (μm)	f (mHz)	ΔT_{source} (K)	ΔT_{Device} (K)
K	1	800	88	**-2.2**	**3.7**
K	2	800	88	**-3.0**	**5.1**
K	3	800	88	**-3.2**	**5.0**
K	1	650	136	-2.1	3.7
K	2	650	136	-2.6	4.5
K	3	650	136	-2.7	4.7
K	1	290	297	-1.6	2.8
K	2	290	297	-1.8	3.1
K	3	290	297	-2.0	3.4
L	1	60	424	-1.0	1.9
L	2	60	424	-1.3	2.0
L	3	60	424	-1.2	1.9

Outlook

This work demonstrates the potential of solid-state NR-based elastocaloric devices as promising candidates for future cooling technologies. However, the preliminary long-term test with 10^4 cycles corresponds to approximately two days of operation. Therefore, further investigations are required to fully assess the operational lifetime of the device and to enable its transition toward practical implementation and increase the technology readiness level (TRL). In addition, the degree of crystallinity under comparable loading conditions should be examined to gain a better understanding of the decreasing input power, which corresponds to the area enclosed by the stress-strain hysteresis loop.

Besides the lifetime of the foil refrigerant, the operational characteristics of the actuator require optimization with respect to the applied loading mode. When a linear actuator is employed for mechanical loading and unloading, a ramp-type displacement profile is typically utilized. This mode induces high acceleration during the loading phase, followed by abrupt deceleration during unloading, which adversely affects the actuator's lifetime. This could be avoided through the utilization of a rotary motor that is equipped with a clutching mechanism for mechanical loading. Conversely, the unloading process is accomplished by permitting the elastic foil to snap back to its original position, or by constraining it at an intermediate state to maintain pre-strained conditions. The elastic energy stored in one foil refrigerant could also be utilized to load a second foil. Therefore, the antagonistically operating foils can be employed to enable work recovery and improve the overall system efficiency.

In addition to work recovery, an important aspect is the thermal isolation of the device. The surfaces used for heat transfer at the heat sink and heat source are exposed to parasitic heat flow during mechanical loading and unloading of the foil. This could be mitigated by integrating an elastic thermal switch that covers the surface and permits heat transfer only upon direct contact with the foil refrigerant. Alternatively, operating the device under vacuum would suppress convection and may allow for higher device temperature spans and cooling power.

As demonstrated, higher adiabatic temperature changes of the material lead to higher cooling power. Therefore, further work should also focus on material optimization to achieve performance improvements. Thermally conductive fillers may further enhance rapid heat transfer. In addition, they can shift the onset of strain-induced crystallization (SIC) to lower strain levels, thereby enabling a more compact design. Ideally, the resulting thermal conductivity of the foil refrigerant should be anisotropic, with a preferred direction out of plane towards the heat sink and heat source. This may also facilitate an improved heat transfer coefficient, corresponding to higher cooling power and larger device temperature spans, as indicated by the simulations conducted in this work. Another approach to enhance the heat transfer coefficient is to increase the contact pressure. Enhanced contact pressure can be achieved by positioning the foil refrigerant between a split heat source, allowing both halves to exert compression forces on the foil.

Depending on the cooling application, it may be necessary to upscale the elastocaloric cooling device through parallelization to meet the cooling power requirements of specific applications.

With continued advances in materials and device design, elastomer foil-based elastocaloric cooling has the potential to emerge as a sustainable and cost-effective solid-state alternative to conventional cooling technologies.

List of Figures

List of Tables

References

[1] United Nations Environment Programme and International Energy Agency. Cooling Emissions and Policy Synthesis Report: Benefits of cooling efficiency and the Kigali Amendment. UNEP Nairobi and IEA, Paris: 2020.

[2] Esper J, Torbenson M, Büntgen U. 2023 summer warmth unparalleled over the past 2,000 years. Nature 2024;631:94–7. https://doi.org/10.1038/s41586-024-07512-y.

[3] Frank T. Climate change impacts on building heating and cooling energy demand in Switzerland. Energy Build 2005;37:1175–85. https://doi.org/10.1016/j.enbuild.2005.06.019.

[4] European Commission. 2030 climate and energy goals for a competitive, secure and low-carbon EU economy. 2014.

[5] European Union. Regulation (EU) 2024/573 of the European Parliament and of the Council of 7 February 2024 on fluorinated greenhouse gases, amending Directive (EU) 2019/1937 and repealing Regulation (EU) No 517/2014. Official Journal of the European Union; 2024.

[6] Moya X, Mathur ND. Caloric materials for cooling and heating. Science 2020;370:797–803. https://doi.org/10.1126/science.abb0973.

[7] Qian S, Geng Y, Wang Y, Ling J, Hwang Y, Radermacher R, et al. A review of elastocaloric cooling: Materials, cycles and system integrations. Int J Refrig 2016;64:1–19. https://doi.org/10.1016/j.ijrefrig.2015.12.001.

[8] Goetzler BYW, Zogg R, Young JIM, Johnson C. Alternatives to Vapor-Compression HVAC Technology. Ashare J 2014.

[9] Ahčin Ž, Dall'Olio S, Žerovnik A, Baškovič UŽ, Porenta L, Kabirifar P, et al. High-performance cooling and heat pumping based on fatigue-resistant elastocaloric effect in compression. Joule 2022;6:2338–57. https://doi.org/10.1016/j.joule.2022.08.011.

[10] Bachmann N, Fitger A, Maier LM, Mahlke A, Schäfer-Welsen O, Koch T, et al. Long-term stable compressive elastocaloric cooling system with latent heat transfer. Commun Phys 2021;4:1–6. https://doi.org/10.1038/s42005-021-00697-y.

[11] Chen Y, Wang Y, Sun W, Qian S, Liu J. A compact elastocaloric refrigerator. The Innovation 2022;3:100205. https://doi.org/10.1016/j.xinn.2022.100205.

[12] Cheng S, Xiao Y, Li X, Lin H, Hua P, Sheng L, et al. Elastocaloric effect characterization of a NiTi tube to be applied in a compressive cooler. AIP Adv 2022;12:125202. https://doi.org/10.1063/5.0117216.

[13] Zhou G, Li Z, Wang Q, Zhu Y, Hua P, Yao S, et al. A multi-material cascade elastocaloric cooling device for large temperature lift. Nat Energy 2024;9:862–70. https://doi.org/10.1038/s41560-024-01537-3.

[14] Zhou G, Zhang L, Li Z, Hua P, Sun Q, Yao S. Achieving kilowatt-scale elastocaloric cooling by a multi-cell architecture. Nature 2025;639:87–92. https://doi.org/10.1038/s41586-024-08549-9.

[15] He W, Zhang G, Zhang X, Ji J, Li G, Zhao X. Recent development and application of thermoelectric generator and cooler. Appl Energy 2015;143:1–25. https://doi.org/10.1016/j.apenergy.2014.12.075.

[16] Bruederlin F, Bumke L, Quandt E, Kohl M. Cascaded SMA-Film Based Elastocaloric Cooling. 2019 20th Int. Conf. Solid-State Sens. Actuators Microsyst. Eurosensors XXXIII TRANSDUCERS EUROSENSORS XXXIII, 2019, p. 1467–70. https://doi.org/10.1109/TRANSDUCERS.2019.8808605.

[17] Bruederlin F, Bumke L, Chluba C, Ossmer H, Quandt E, Kohl M. Elastocaloric Cooling on the Miniature Scale: A Review on Materials and Device Engineering. Energy Technol 2018;6:1588–604. https://doi.org/10.1002/ente.201800137.

[18] Ludwig C, Leutner J, Prucker O, Rühe J, Kohl M. Natural Rubber Foil-Based Elastocaloric Cooling. ACTUATOR 2024 Int. Conf. Exhib. New Actuator Syst. Appl., 2024, p. 132–5.

[19] Ludwig C, Leutner J, Prucker O, Rühe J, Kohl M. Miniature-scale elastocaloric cooling by rubber-based foils. J Phys Energy 2023;6:015009. https://doi.org/10.1088/2515-7655/ad0cff.

[20] Xie Z, Sebald G, Guyomar D. Elastocaloric effect dependence on pre-elongation in natural rubber. Appl Phys Lett 2015;107:081905. https://doi.org/10.1063/1.4929395.

[21] Candan N 1, Vives E 2, Fernández AI 3, Oguz O 4, Corvee G 5, Federico CE, et al. Observation of heterogeneities in elastocaloric natural/wastes rubber composites 2022:1331–47. https://doi.org/10.3144/expresspolymlett.2022.96.

[22] Xie Z, Sebald G, Guyomar D. Comparison of elastocaloric effect of natural rubber with other caloric effects on different-scale cooling application cases. Appl Therm Eng 2017;111:914–26. https://doi.org/10.1016/j.applthermaleng.2016.09.164.

[23] Guyomar D, Li Y, Sebald G, Cottinet P-J, Ducharne B, Capsal J-F. Elastocaloric modeling of natural rubber. Appl Therm Eng 2013;57:33–8. https://doi.org/10.1016/j.applthermaleng.2013.03.032.

[24] Le Cam J-B. Energy storage due to strain-induced crystallization in natural rubber: The physical origin of the mechanical hysteresis. Polymer 2017;127:166–73. https://doi.org/10.1016/j.polymer.2017.08.059.

[25] Flory PJ. Principles of polymer chemistry. 1. Ithaca, NY: Cornell University Press; 1954.

[26] Katz JR, Bing K. Ist Rohkautschuk teilweise kristallisiert? Z Für Angew Chem 1925;38:439–41. https://doi.org/10.1002/ange.19250382003.

[27] Kuhn W. Dependence of the average transversal on the longitudinal dimensions of statistical coils formed by chain molecules. J Polym Sci 1946;1:380–8. https://doi.org/10.1002/pol.1946.120010505.

[28] Toki, Sics, Ran, Liu, Hsiao, Murakami, et al. New Insights into Structural Development in Natural Rubber during Uniaxial Deformation by In Situ Synchrotron X-ray Diffraction. Macromolecules 2002;35:6578–84. https://doi.org/10.1021/ma0205921.

[29] Zhang HP, Niemczura J, Dennis G, Ravi-Chandar K, Marder M. Toughening effect of strain-induced crystallites in natural rubber. Phys Rev Lett 2009;102:245503. https://doi.org/10.1103/PhysRevLett.102.245503.

[30] Trabelsi S, Albouy P-A, Rault J. Stress-Induced Crystallization around a Crack Tip in Natural Rubber. Macromolecules 2002;35:10054–61. https://doi.org/10.1021/ma021106c.

[31] Greibich F, Schwödiauer R, Mao G, Wirthl D, Drack M, Baumgartner R, et al. Elastocaloric heat pump with specific cooling power of 20.9 W g–1 exploiting snap-through instability and strain-induced crystallization. Nat Energy 2021;6:260–7. https://doi.org/10.1038/s41560-020-00770-w.

[32] Sebald, Komiya, Jay, Coativy, Laurent. Regenerative cooling using elastocaloric rubber: Analytical model and experiments. J Appl Phys 2020. https://doi.org/10.1063/1.5132361.

[33] Sebald G, Lombardi G, Coativy G, Jay J, Lebrun L, Komiya A. High-performance polymer-based regenerative elastocaloric cooler. Appl Therm Eng 2023;223:120016. https://doi.org/10.1016/j.applthermaleng.2023.120016.

[34] Sion M, Jay J, Coativy G, Komiya A, Sebald G. Natural rubber based elastocaloric solid-state refrigeration device: design and performances of a single stage system. J Phys Energy 2024;6:025003. https://doi.org/10.1088/2515-7655/ad20f4.

[35] Gough. VII. A description of a property of caoutchouc, or indian rubber; with some reflections on the cause of the elasticity of this substance. In a letter to Dr.Holme. Philos Mag 1806:39–43. https://doi.org/10.1080/14786440608563329.

[36] Joule. V. On some thermo-dynamic properties of solids. Philos Trans R Soc Lond 1859;149:91–131. https://doi.org/10.1098/rstl.1859.0005.

[37] Brüning K, Schneider K, Roth SV, Heinrich G. Kinetics of strain-induced crystallization in natural rubber: A diffusion-controlled rate law. Polymer 2015;72:52–8. https://doi.org/10.1016/j.polymer.2015.07.011.

[38] Trabelsi S, Albouy P-A, Rault J. Crystallization and Melting Processes in Vulcanized Stretched Natural Rubber. Macromolecules 2003;36:7624–39. https://doi.org/10.1021/ma030224c.

[39] Mitchell GR. A wide-angle X-ray study of the development of molecular orientation in crosslinked natural rubber. Polymer 1984;25:1562–72. https://doi.org/10.1016/0032-3861(84)90148-4.

[40] Treloar LRG. The Elasticity and Related Properties of Rubbers. Rep Prog Phys 1973;36:755–826. https://doi.org/10.1088/0034-4885/36/7/001.

[41] Poompradub S, Tosaka M, Kohjiya S, Ikeda Y, Toki S, Sics I, et al. Mechanism of strain-induced crystallization in filled and unfilled natural rubber vulcanizates. J Appl Phys 2005;97:103529. https://doi.org/10.1063/1.1900927.

[42] Treloar LRG. The Physics of Rubber Elasticity. 3rd ed. Oxford: Oxford University Press UK; 2005.

[43] Xie Z, Wei C, Guyomar D, Sebald G. Validity of Flory's model for describing equilibrium strain-induced crystallization (SIC) and thermal behavior in natural rubber. Polymer 2016;103:41–5. https://doi.org/10.1016/j.polymer.2016.09.038.

[44] Berghus, Bird, Friemann, Humme, Kempermann, Italiaander, et al. Handbuch für die Gummi-Industrie. 2. Bayer AG; 1991.

[45] Röthemeyer F, Sommer F, editors. Kautschuk Technologie: Werkstoffe – Verarbeitung – Produkte. 3rd ed. Hanser; 2013.

[46] Abts G, editor. Einführung in die Kautschuktechnologie. 2. München: Hanser; 2019.

[47] Türk O. Stoffliche Nutzung nachwachsender Rohstoffe: Grundlagen - Werkstoffe - Anwendungen. Wiesbaden: Springer Fachmedien Wiesbaden; 2014.

[48] Limper Andreas. Mixing of rubber compounds. München: Hanser; 2012.

[49] Liotier J, Piock T, Rühe J. Universal Cross-Linking of Nonfunctional Polymers through C,H-Insertion Reactions. Macromolecules 2025;58:1859–66. https://doi.org/10.1021/acs.macromol.4c02184.

[50] Kost J, Bleiziffer A, Rusitov D, Rühe J. Thermally Induced Cross-Linking of Polymers via C,H Insertion Cross-Linking (CHic) under Mild Conditions. J Am Chem Soc 2021;143:10108–19. https://doi.org/10.1021/jacs.1c02133.

[51] Bovenkerk K, Braun H, Dörflinger R, Doll W, Fischer U, Heinzler M, et al. Fachkunde für Metallberufe. 44th ed. Wuppertal: Europa Lehrmittel; 1981.

[52] Scoti M, De Stefano F, Zanchin G, Leone G, De Rosa C, Ricci G. Synthesis, Structure, and Properties of Poly(isoprene)s of Different Constitutions and Configurations from Catalysts Based on Complexes of Nd, Co, and Fe. Macromolecules 2023;56:4629–38. https://doi.org/10.1021/acs.macromol.3c00615.

[53] Staudinger, Fritschi. Über Isopren und Kautschuk. 5. Mitteilung. Über die Hydrierung des Kautschuks und über seine Konstitution. Helv Chim Acta 1922. https://doi.org/10.1002/hlca.19220050517.

[54] Koltzenburg S, Maskos M, Nuyken O. Polymere: Synthese, Eigenschaften und Anwendungen. Berlin, Heidelberg: Springer Spektrum; 2014.

[55] Cataldo F. Thermochemistry of Sulfur-Based Vulcanization and of Devulcanized and Recycled Natural Rubber Compounds. Int J Mol Sci 2023;24:2623. https://doi.org/10.3390/ijms24032623.

[56] Frede W. Taschenbuch für Lebensmittelchemiker: Lebensmittel - Bedarfsgegenstände - Kosmetika - Futtermittel (German Edition). 2. Dordrecht: Springer; 2006.

[57] Domininghaus H, Elsner P, Eyerer P, Hirth T. Kunststoffe: Eigenschaften und Anwendungen. 7. Berlin; Heidelberg: Springer; 2008. https://doi.org/10.1007/978-3-540-72401-8.

[58] Ciesielski A. An Introduction to Rubber Technology(1). Shropshire: Rapra Technology Limited; 2000.

[59] Zhang J, Huang S, Kong L, Sakdapipanich J, Zhang R, Xie Z, et al. Unveiling the Hierarchical Microstructure of Prevulcanized Natural Rubber Latex Film and Its Impact on Mechanical Properties. Macromolecules 2024;57:11727–37. https://doi.org/10.1021/acs.macromol.4c02599.

[60] Mathew G, Kuriakose AP. A new binary accelerator system for the sulfur vulcanization of natural rubber latex. J Appl Polym Sci 1993;49:2009–17. https://doi.org/10.1002/app.1993.070491118.

[61] Sasidharan KK, Joseph R, Palaty S, Gopalakrishnan KS, Rajammal G, Pillai PV. Effect of the vulcanization time and storage on the stability and physical properties of sulfur-prevulcanized natural rubber latex. J Appl Polym Sci 2005;97:1804–11. https://doi.org/10.1002/app.21918.

[62] Winsunthorn S, Bonfils F, Pochat-Bohatier C, Bouyer D, Deratani A, Dupuy C. Comparative study of the elasticity and permeability of vulcanized films made with skim and cream natural rubber latex. J Appl Polym Sci 2008;108:960–8. https://doi.org/10.1002/app.27580.

[63] Tosaka M, Kawakami D, Senoo K, Kohjiya S, Ikeda Y, Toki S, et al. nooo_doppelt_Crystallization and Stress Relaxation in Highly Stretched Samples of Natural Rubber and Its Synthetic Analogue 2006.

[64] Ikeda Y, Kato A, Kohjiya S, Nakajima Y. Rubber Science: A Modern Approach. Singapore: Springer; 2018.

[65] Hadjichristidis N, Pispas S, Floudas G. Block Copolymers: Synthetic Strategies, Physical Properties, and Applications. John Wiley & Sons; 2003.

[66] Feng H, Lu X, Wang W, Kang N-G, Mays JW. Block Copolymers: Synthesis, Self-Assembly, and Applications. Polymers 2017;9:494. https://doi.org/10.3390/polym9100494.

[67] Guth E, Mark H. Die Elastizität des Kautschuks und ihr Zusammenhang mit dem Strukturmodell. Naturwissenschaften 1937;25:353–9. https://doi.org/10.1007/BF01491815.

[68] Seitz F, Johnson RP. Modern Theory of Solids. II. J Appl Phys 1937;8:186–99. https://doi.org/10.1063/1.1710281.

[69] Meyer KH, Ferri C. Sur l'élasticité du caoutchouc. Helv Chim Acta 1935;18:570–89. https://doi.org/10.1002/hlca.19350180176.

[70] Nash LK. Entropy and rubbery elasticity. ACS Publ 1979. https://doi.org/10.1021/ed056p363.

[71] Pellicer J, Manzanares JA, Mafé S. Ideal systems in classical thermodynamics. Eur J Phys 1997;18:269. https://doi.org/10.1088/0143-0807/18/4/005.

[72] Brüning K. In-situ Structure Characterization of Elastomers during Deformation and Fracture. 2014.

[73] Göritz D, Müller FH. Die kalorimetrische Erfassung der Dehnungskristallisation Polymerer. Kolloid-Z Z Für Polym 1970;241:1075–9. https://doi.org/10.1007/BF02137415.

[74] Loadman MJR. The glass transition temperature of natural rubber. J Therm Anal 1985;30:929–41. https://doi.org/10.1007/BF01913321.

[75] Schwab G-M. Physikalisch-chemische Grundlagen der chemischen Technologie. Leipzig: Spamer; 1927.

[76] Tosaka M, Murakami S, Poompradub S, Kohjiya S, Ikeda Y, Toki S, et al. Orientation and Crystallization of Natural Rubber Network As Revealed by WAXD Using Synchrotron Radiation. Macromolecules 2004;37:3299–309. https://doi.org/10.1021/ma0355608.

[77] Gosline JM, Guerette PA, Ortlepp CS, Savage KN. The mechanical design of spider silks: from fibroin sequence to mechanical function. J Exp Biol 1999;202:3295–303. https://doi.org/10.1242/jeb.202.23.3295.

[78] Candau N, Laghmach R, Chazeau L, Chenal J-M, Gauthier C, Biben T, et al. Strain-Induced Crystallization of Natural Rubber and Cross-Link Densities Heterogeneities. Macromolecules 2014;47:5815–24. https://doi.org/10.1021/ma5006843.

[79] Brüning K, Schneider K, Roth SV, Heinrich G. Kinetics of Strain-Induced Crystallization in Natural Rubber Studied by WAXD: Dynamic and Impact Tensile Experiments. Macromolecules 2012;45:7914–9. https://doi.org/10.1021/ma3011476.

[80] Murakamia, Seno, Toki, Kohjiya. Structural development of natural rubber during uniaxial stretching by in situ wide angle X-ray diffraction using a synchrotron radiation. Polymer 2002. https://doi.org/10.1016/S0032-3861(01)00794-7.

[81] Toki, Fujimaki, Okuyama. Strain-induced crystallization of natural rubber as detected real-time by wide-angle X-ray diffraction technique 2000. https://doi.org/10.1016/S0032-3861(99)00724-7.

[82] Haissoune H, Coativy G, Chazeau L, Lebrun L, Sebald G, Chenal J-M. Critical parameters governing elastocaloric effect in polyisoprene rubbers for solid-state cooling. Polymer 2024;307:127234. https://doi.org/10.1016/j.polymer.2024.127234.

[83] Rault J, Marchal J, Judeinstein P, Albouy PA. Stress-Induced Crystallization and Reinforcement in Filled Natural Rubbers: 2 H NMR Study. Macromolecules 2006. https://doi.org/10.1021/ma0608424.

[84] Andrews EH, Owen PG, Singh A. The influence of morphology on the mechanical properties of crystalline polymers. Pure Appl Chem 1971;31:91–112. https://doi.org/10.1351/pac197231010091.

[85] Burfield DR, Tanaka Y. Cold crystallization of natural rubber and its synthetic analogues: The influence of chain microstructure. Polymer 1987;28:907–10. https://doi.org/10.1016/0032-3861(87)90161-3.

[86] Chenal J-M, Chazeau L, Bomal Y, Gauthier C. New insights into the cold crystallization of filled natural rubber. J Polym Sci Part B Polym Phys 2007;45:955–62. https://doi.org/10.1002/polb.21105.

[87] Gent AN, Kawahara S, Zhao J. Crystallization and Strength of Natural Rubber and Synthetic cis-1,4-Polyisoprene. Rubber Chem Technol 1998;71:668–78. https://doi.org/10.5254/1.3538496.

[88] Luch D, Yeh GSY. Morphology of strain-induced crystallization of natural rubber. Part II. X-Ray studies on cross-linked vulcanizates. J Macromol Sci Part B 1973;7:121–55. https://doi.org/10.1080/00222347308212577.

[89] Mandelkern L. Crystallization of Polymers: Volume 2: Kinetics and Mechanisms. vol. 2. 2nd ed. Cambridge: Cambridge University Press; 2004. https://doi.org/10.1017/CBO9780511535413.

[90] Huneau B. Strain-Induced Crystallization of Natural Rubber: a Review of X-ray Diffraction Investigations. Rubber Chem Technol 2011;84:425–52. https://doi.org/10.5254/1.3601131.

[91] Allen G, Gee G, Read BE. Stress relaxation in elastomers by visco-elastic mechanisms. Part 1.—Natural rubber at high rates of strain and low temperatures. Trans Faraday Soc 1959;55:1651–9. https://doi.org/10.1039/TF9595501651.

[92] Trabelsi S, Albouy P-A, Rault J. Stress-Induced Crystallization Properties of Natural and Synthetic CIS-Polyisoprene. Rubber Chem Technol 2004;77:303–16. https://doi.org/10.5254/1.3547825.

[93] Mullins L, Tobin NR. Stress softening in rubber vulcanizates. Part I. Use of a strain amplification factor to describe the elastic behavior of filler-reinforced vulcanized rubber. J Appl Polym Sci 1965;9:2993–3009. https://doi.org/10.1002/app.1965.070090906.

[94] Diani J, Fayolle B, Gilormini P. A review on the Mullins effect. Eur Polym J 2009;45:601–12. https://doi.org/10.1016/j.eurpolymj.2008.11.017.

[95] Le Cam J-B. Fast Evaluation and Comparison of the Energy Performances of Elastomers from Relative Energy Stored Identification under Mechanical Loadings. Polymers 2022;14:412. https://doi.org/10.3390/polym14030412.

[96] Samaca Martinez JR, Le Cam J-B, Balandraud X, Toussaint E, Caillard J. Mechanisms of deformation in crystallizable natural rubber. Part 2: Quantitative calorimetric analysis. Polymer 2013;54:2727–36. https://doi.org/10.1016/j.polymer.2013.03.012.

[97] Pellicer J, Manzanares JA, Zúñiga J, Utrillas P, Fernández J. Thermodynamics of Rubber Elasticity. J Chem Educ 2001;78:263. https://doi.org/10.1021/ed078p263.

[98] Katzenberg F, Heuwers B, Tiller J. Superheated Rubber for Cold Storage. Adv Mater Deerfield Beach Fla 2011;23:1909–11. https://doi.org/10.1002/adma.201100408.

[99] Katz JR. Was sind die Ursachen der eigentümlichen Dehnbarkeit des Kautschuks? Kolloid-Z 1925;37:19–22. https://doi.org/10.1007/BF01436231.

[100] Xie Z, Sebald G, Guyomar D. Comparison of direct and indirect measurement of the elastocaloric effect in natural rubber. Appl Phys Lett 2016;108:041901. https://doi.org/10.1063/1.4940378.

[101] Dart SL, Anthony RL, Guth E. Rise of Temperature on Fast Stretching of Synthetics and Natural Rubbers. Ind Eng Chem 1942;34:1340–2. https://doi.org/10.1021/ie50395a020.

[102] Krigbaum WR, Dawkins JV, Via GH, Balta YI. Effect of strain on the thermodynamic melting temperature of polymers. J Polym Sci Part -2 Polym Phys 1966;4:475–89. https://doi.org/10.1002/pol.1966.160040316.

[103] Krigbaum WR, Roe R-J. Diffraction study of crystallite orientation in a stretched polychloroprene vulcanizate. J Polym Sci A 1964;2:4391–414. https://doi.org/10.1002/pol.1964.100021010.

[104] Tsuji M, Shimizu T, Kohjiya S. TEM Studies on Thin Films of Natural Rubber and Polychloroprene Crystallized under Molecular Orientation II. Highly Prestretched Thin Films. Polym J 2000;32:505–12. https://doi.org/10.1295/polymj.32.505.

[105] Toki S, Sics I, Hsiao BS, Murakami S, Tosaka M, Poompradub S, et al. Structural developments in synthetic rubbers during uniaxial deformation by in situ synchrotron X-ray diffraction. J Polym Sci Part B Polym Phys 2004;42:956–64. https://doi.org/10.1002/polb.10679.

[106] Cooper W, Smith RK. Melting transitions in diene polymers. J Polym Sci A 1963;1:159–68. https://doi.org/10.1002/pol.1963.100010113.

[107] Hackathorn MJ, Brock MJ. The Determination of “Head-Head” and “Tail-Tail” Structures in Poly(Isoprene)S. Rubber Chem Technol 1972;45:1295–302. https://doi.org/10.5254/1.3544739.

[108] Gent AN. Engineering with Rubber| Hanser Fachbuch. 3rd ed. Carl Hanser Verlag GmbH & Co. KG; 2012.

[109] Trabelsi S, Albouy P-A, Rault J. Effective Local Deformation in Stretched Filled Rubber. Macromolecules 2003;36:9093. https://doi.org/10.1021/ma0303566.

[110] Chenal J-M, Gauthier C, Chazeau L, Guy L, Bomal Y. Parameters governing strain induced crystallization in filled natural rubber. Polymer 2007:6893–901. https://doi.org/10.1016/j.polymer.2007.09.023.

[111] Dupres S, Long DR, Albouy P-A, Sotta P. Local Deformation in Carbon Black-Filled Polyisoprene Rubbers Studied by NMR and X-ray Diffraction. Macromolecules 2009;42:2634–44. https://doi.org/10.1021/ma900006y.

[112] Gehman SD, Field JE. X-Ray Structure of Rubber-Carbon Black Mixtures. Ind Eng Chem 1940;32:1401–7. https://doi.org/10.1021/ie50370a027.

[113] Weng G, Huang G, Qu L, Nie Y, Wu J. Large-Scale Orientation in a Vulcanized Stretched Natural Rubber Network: Proved by In Situ Synchrotron X-ray Diffraction Characterization. J Phys Chem B 2010;114:7179–88. https://doi.org/10.1021/jp100920g.

[114] Nie Y, Gu Z, Wei Y, Hao T, Zhou Z. Features of strain-induced crystallization of natural rubber revealed by experiments and simulations. Polym J 2017;49:309–17. https://doi.org/10.1038/pj.2016.114.

[115] Carretero-González J, Retsos H, Verdejo R, Toki S, Hsiao BS, Giannelis EP, et al. Effect of Nanoclay on Natural Rubber Microstructure. Macromolecules 2008;41:6763–72. https://doi.org/10.1021/ma800893x.

[116] Carretero-González J, Verdejo R, Toki S, Hsiao BS, Giannelis EP, López-Manchado MA. Real-Time Crystallization of Organoclay Nanoparticle Filled Natural Rubber under Stretching. Macromolecules 2008;41:2295–8. https://doi.org/10.1021/ma7028506.

[117] Hernández M, Sanz A, Nogales A, Ezquerra TA, López-Manchado MA. Structure and Segmental Dynamics Relationship in Natural Rubber/Layered Silicate Nanocomposites during Uniaxial Deformation. Macromolecules 2013;46:3176–82. https://doi.org/10.1021/ma4002353.

[118] Nie Y, Qu L, Huang G, Wang B, Weng G, Wu J. Improved resistance to crack growth of natural rubber by the inclusion of nanoclay. Polym Adv Technol 2012;23:85–91. https://doi.org/10.1002/pat.1826.

[119] Nie Y, Huang G, Qu L, Wang X, Weng G, Wu J. New insights into thermodynamic description of strain-induced crystallization of peroxide cross-linked natural rubber filled with clay by tube model. Polymer 2011;52:3234–42. https://doi.org/10.1016/j.polymer.2011.05.004.

[120] Nie Y, Huang G, Qu L, Zhang P, Weng G, Wu J. Structural evolution during uniaxial deformation of natural rubber reinforced with nano-alumina. Polym Adv Technol 2011;22:2001–8. https://doi.org/10.1002/pat.1709.

[121] Qu L, Huang G, Liu Z, Zhang P, Weng G, Nie Y. Remarkable reinforcement of natural rubber by deformation-induced crystallization in the presence of organophilic montmorillonite. Acta Mater 2009;57:5053–60. https://doi.org/10.1016/j.actamat.2009.07.007.

[122] Liang Y, Guo Y, Wang E, Cakmak M. Details of Molecular Organization during Strain-Induced Crystallization in Natural Rubber/Clay Systems As Revealed by Real-Time Mechano-Optical Behavior. Macromolecules 2015;48:2299–304. https://doi.org/10.1021/acs.macromol.5b00231.

[123] Ikeda Y, Yasuda Y, Hijikata K, Tosaka M, Kohjiya S. Comparative Study on Strain-Induced Crystallization Behavior of Peroxide Cross-Linked and Sulfur Cross-Linked Natural Rubber. Macromolecules 2008;41:5876–84. https://doi.org/10.1021/ma800144u.

[124] Chenal J-M, Chazeau L, Guy L, Bomal Y, Gauthier C. Molecular weight between physical entanglements in natural rubber: A critical parameter during strain-induced crystallization. Polymer 2007;48:1042–6. https://doi.org/10.1016/j.polymer.2006.12.031.

[125] Tosaka M, Kohjiya S, Murakami S, Poompradub S, Ikeda Y, Toki S, et al. Effect of Network-Chain Length on Strain-Induced Crystallization of NR and IR Vulcanizates. Rubber Chem Technol 2004;77:711–23. https://doi.org/10.5254/1.3547846.

[126] Wang R, Fang S, Xiao Y, Gao E, Jiang N, Li Y, et al. Torsional refrigeration by twisted, coiled, and supercoiled fibers. Science 2019;366:216–21. https://doi.org/10.1126/science.aax6182.

[127] Liu B, Wang Y, Zhu Z, Theodorakis PE, Song J, Bennacer Rachid. A lower temperature difference of the elastocaloric effect by natural rubber. Int J Refrig 2023;155:163–72. https://doi.org/10.1016/j.ijrefrig.2023.08.004.

[128] Coativy G, Haissoune H, Seveyrat L, Sebald G, Chazeau L, Chenal J-M, et al. Elastocaloric properties of thermoplastic polyurethane. Appl Phys Lett 2020;117:193903. https://doi.org/10.1063/5.0023520.

[129] Trček M, Lavrič M, Cordoyiannis G, Zalar B, Rožič B, Kralj S, et al. Electrocaloric and elastocaloric effects in soft materials. Philos Trans R Soc Lond 2016;374. https://doi.org/10.1098/rsta.2015.0301.

[130] Hong SB, An Y, Yu W-R. Characterization and modeling of elastocaloric effects of shape memory poly(cyclooctene). Appl Phys Lett 2019. https://doi.org/10.1063/1.5082357.

[131] Hong SB, An Y, Yu W-R. Elastocaloric effects of carbon fabric-reinforced shape memory polymer composites. Funct Compos Struct 2019. https://doi.org/10.1088/2631-6331/ab0c4c.

[132] Patel S, Chauhan A, Vaish R, Thomas P. Elastocaloric and barocaloric effects in polyvinylidene di-fluoride-based polymers. Appl Phys Lett 2016. https://doi.org/10.1063/1.4942000.

[133] Yoshida Y, Yuse K, Guyomar D, Capsal J-F, Sebald G. Elastocaloric effect in poly(vinylidene fluoride-trifluoroethylene-chlorotrifluoroethylene) terpolymer. Appl Phys Lett 2016. https://doi.org/10.1063/1.4953770.

[134] Zhang S, Yang Q, Li C, Fu Y, Zhang H, Ye Z, et al. Solid-state cooling by elastocaloric polymer with uniform chain-lengths. Nat Commun 2022;13:9. https://doi.org/10.1038/s41467-021-27746-y.

[135] Zhang S, Fu Y, Nie X, Li C, Zhou Y, Wang Y, et al. Shearo-caloric effect enhances elastocaloric responses in polymer composites for solid-state cooling. Nat Commun 2024;15:6567. https://doi.org/10.1038/s41467-024-50870-4.

[136] Wang K, Engelbrecht K, Bahl CRH. Additive manufactured thermoplastic elastomers for low-stress driven elastocaloric cooling. Appl Mater Today 2023;30:101711. https://doi.org/10.1016/j.apmt.2022.101711.

[137] Sánchez-Ferrer, Finkelmann. Thermal and Mechanical Properties of New Main-Chain Liquid-Crystalline Elastomers. Mol Cryst Liq Cryst 2009. https://doi.org/10.1080/15421400903065861.

[138] Hong SB, Hong SJ, Kang T-H, Youk JH, Yu W-R. Optical and shape memory properties of semicrystalline poly(cyclooctene) upon cold-drawing. J Polym Phys 2017. https://doi.org/10.1002/polb.24415.

[139] Zhang S, Fu Y, Li C, Nie X, Chen J, Zhou Y, et al. Polymer elastomer near plastic-to-rubber critical transition produces enhanced elastocaloric effects. Cell Rep Phys Sci 2022;3:101147. https://doi.org/10.1016/j.xcrp.2022.101147.

[140] Choi IS, Roland CM. Intrinsic Defects and the Failure Properties of cis-1,4-Polyisoprenes. Rubber Chem Technol 1996;69:591–9. https://doi.org/10.5254/1.3538386.

[141] Mars WV, Fatemi A. Factors that Affect the Fatigue Life of Rubber: A Literature Survey. Rubber Chem Technol 2004;77:391–412. https://doi.org/10.5254/1.3547831.

[142] Busse WF. Tear Resistance and Structure of Rubber. Ind Eng Chem 1934;26:1194–9. https://doi.org/10.1021/ie50299a015.

[143] Jenkin CF. Report on materials of construction used in aircraft and aircraft engines. London: H. M. Stationery off.; 1920.

[144] Cadwell SM, Merrill RA, Sloman CM, Yost FL. Dynamic Fatigue Life of Rubber. Ind Eng Chem Anal Ed 1940;12:19–23. https://doi.org/10.1021/ac50141a006.

[145] Sebald G, Xie Z, Guyomar D. Fatigue effect of elastocaloric properties in natural rubber. Philos Trans R Soc Math Phys Eng Sci 2016;374:20150302. https://doi.org/10.1098/rsta.2015.0302.

[146] dos Santos KAM, Suarez PAZ, Rubim JC. Photo-degradation of synthetic and natural polyisoprenes at specific UV radiations. Polym Degrad Stab 2005;90:34–43. https://doi.org/10.1016/j.polymdegradstab.2005.01.038.

[147] Gent AN, Hindi M. Effect of Oxygen on the Tear Strength of Elastomers. Rubber Chem Technol 1990;63:123–34. https://doi.org/10.5254/1.3538236.

[148] Zhou M-Z, Wang H-R, Guo X, Wei Y-C, Liao S. Synergistic effect of thermal oxygen and UV aging on natural rubber. E-Polym 2023;23. https://doi.org/10.1515/epoly-2023-0016.

[149] Kitanovski A, Plaznik U, Tomc U, Poredoš A. Present and future caloric refrigeration and heat-pump technologies. Int J Refrig 2015;57:288–98. https://doi.org/10.1016/j.ijrefrig.2015.06.008.

[150] Goetzler W, Zogg R, Young J, Johnson C, U.S. Department of Energy. Energy Savings Potential and RD&D Opportunities for Non-Vapor-Compression HVAC Technologies. 2014. https://doi.org/10.2172/1220817.

[151] Fähler S, Rößler UK, Kastner O, Eckert J, Eggeler G, Emmerich H, et al. Caloric Effects in Ferroic Materials: New Concepts for Cooling. Adv Eng Mater 2012;14. https://doi.org/10.1002/adem.201290005.
[152] Moya X, Kar-Narayan S, Mathur ND. Caloric materials near ferroic phase transitions. Nat Mater 2014:439–50.
[153] Lu B, Liu J. Mechanocaloric materials for solid-state cooling. Sci Bull 2015;60:1638–43. https://doi.org/10.1007/s11434-015-0898-5.
[154] Li L, He S, Xiao F, Zeng Y, Liu Y, Zhou Y, et al. Cooling innovations: Elastocaloric shape memory alloys, manufacturing, simulation, and refrigerator. Prog Mater Sci 2025;153:101477. https://doi.org/10.1016/j.pmatsci.2025.101477.
[155] Kitanovski A, Tušek J, Tomc U, Plaznik U, Ožbolt M, Poredoš A. Magnetocaloric Energy Conversion: From Theory to Applications. Cham: Springer International Publishing; 2015. https://doi.org/10.1007/978-3-319-08741-2.
[156] Pecharsky VK, Gschneidner JrKA. Giant Magnetocaloric Effect in Gd5sSi2Ge2d. Phys Rev Lett 1997;78:4494–7. https://doi.org/10.1103/PhysRevLett.78.4494.
[157] Dan'kov SYu, Tishin AM, Pecharsky VK, Gschneidner KA. Magnetic phase transitions and the magnetothermal properties of gadolinium. Phys Rev B 1998;57:3478–90. https://doi.org/10.1103/PhysRevB.57.3478.
[158] Tušek J, Engelbrecht K, Millán-Solsona R, Mañosa L, Vives E, Mikkelsen LP, et al. The Elastocaloric Effect: A Way to Cool Efficiently. Adv Energy Mater 2015;5. https://doi.org/10.1002/aenm.201500361.
[159] Mischenko AS, Zhang Q, Scott JF, Whatmore RW, Mathur ND. Giant Electrocaloric Effect in Thin-Film PbZr0.95Ti0.05O3. Science 2006;311:1270–1. https://doi.org/10.1126/science.1123811.
[160] Hou H, Qian S, Takeuchi I. Materials, physics and systems for multicaloric cooling. Nat Rev Mater 2022;7:633–52. https://doi.org/10.1038/s41578-022-00428-x.
[161] Kar-Narayan S, Mathur ND. Predicted cooling powers for multilayer capacitors based on various electrocaloric and electrode materials. Appl Phys Lett 2009;95:242903. https://doi.org/10.1063/1.3275013.
[162] Nair B, Usui T, Crossley S, Kurdi S, Guzmán-Verri GG, Moya X, et al. Large electrocaloric effects in oxide multilayer capacitors over a wide temperature range. Nature 2019;575:468–72. https://doi.org/10.1038/s41586-019-1634-0.
[163] Kobayashi A. Elastocaloric Effect in Many-Valley Semiconductors. J Phys Soc Jpn 1962;17:1518–1518. https://doi.org/10.1143/JPSJ.17.1518.
[164] Miyazaki S, Otsuka K. Development of Shape Memory Alloys. ISIJ Int 1989;29:353–77. https://doi.org/10.2355/isijinternational.29.353.
[165] Mañosa L, Planes A. Materials with Giant Mechanocaloric Effects: Cooling by Strength. Adv Mater 2017;29:1603607. https://doi.org/10.1002/adma.201603607.
[166] Otsuka K, Wayman, CM, editors. Shape memory materials. 1. Cambridge: Cambridge University Press; 1999.
[167] Frenzel J, Wieczorek A, Opahle I, Maaß B, Drautz R, Eggeler G. On the effect of alloy composition on martensite start temperatures and latent heats in Ni-Ti-based shape memory alloys. Acta Mater 2015;90:213–31. https://doi.org/10.1016/j.actamat.2015.02.029.
[168] Tušek J, Engelbrecht K, Mikkelsen LP, Pryds N. Elastocaloric effect of Ni-Ti wire for application in a cooling device. J Appl Phys 2015;117:124901. https://doi.org/10.1063/1.4913878.

[169] Bom NM, Imamura W, Usuda EO, Paixão LS, Carvalho AMG. Giant Barocaloric Effects in Natural Rubber: A Relevant Step toward Solid-State Cooling. ACS Macro Lett 2018;7:31–6. https://doi.org/10.1021/acsmacrolett.7b00744.

[170] Stern-Taulats E, Gràcia-Condal A, Planes A, Lloveras P, Barrio M, Tamarit J-L, et al. Reversible adiabatic temperature changes at the magnetocaloric and barocaloric effects in Fe 49 Rh 51. Appl Phys Lett 2015;107. https://doi.org/10.1063/1.4933409.

[171] Stern-Taulats E, Lloveras P, Barrio M, Defay E, Egilmez M, Planes A, et al. Inverse barocaloric effects in ferroelectric BaTiO3 ceramics. APL Mater 2016;4:091102. https://doi.org/10.1063/1.4961598.

[172] Meng H, Li B, Ren W, Zhang Z. Coupled caloric effects in multiferroics. Phys Lett A 2013;377:567–71. https://doi.org/10.1016/j.physleta.2012.12.033.

[173] Patel S, Chauhan A, Vaish R. Multiple caloric effects in (Ba0.865Ca0.135Zr0.1089Ti0.8811Fe0.01)O3 ferroelectric ceramic. Appl Phys Lett 2015;107:042902. https://doi.org/10.1063/1.4927558.

[174] Vopson MM. Theory of giant-caloric effects in multiferroic materials. J Phys Appl Phys 2013;46. https://doi.org/10.1088/0022-3727/46/34/345304.

[175] Vopson MM. The multicaloric effect in multiferroic materials. Solid State Commun 2012;152:2067–70. https://doi.org/10.1016/j.ssc.2012.08.016.

[176] Schmidt M, Kirsch S-M, Seelecke S, Schütze A. Elastocaloric cooling: From fundamental thermodynamics to solid state air conditioning. Sci Technol Built Environ 2016;22:475–88. https://doi.org/10.1080/23744731.2016.1186423.

[177] Wang K, Engelbrecht K, Bahl CRH, Bjørk R. A 3D-printed full-soft regenerative elastocaloric cooler. Energy Convers Manag 2025;336:119811. https://doi.org/10.1016/j.enconman.2025.119811.

[178] Ludwig C, Kohl M. Bistability-enhanced elastocaloric cooling device based on a natural rubber foil. J Appl Phys 2024;136:165001. https://doi.org/10.1063/5.0231213.

[179] Mevada H, Liu B, Gao L, Hwang Y, Takeuchi I, Radermacher R. Elastocaloric cooling: A pathway towards future cooling technology. Int J Refrig 2024;162:86–98. https://doi.org/10.1016/j.ijrefrig.2024.03.014.

[180] Kirsch S-M, Welsch F, Ehl L, Michaelis N, Motzki P, Schütze A, et al. Continuous Operating Elastocaloric Heating and Cooling Device: Air Flow Investigation and Experimental Parameter Study, American Society of Mechanical Engineers Digital Collection; 2019. https://doi.org/10.1115/SMASIS2019-5633.

[181] Qian S, Catalini D, Muehlbauer J, Liu B, Mevada H, Hou H, et al. High-performance multimode elastocaloric cooling system. Science 2023;380:722–7. https://doi.org/10.1126/science.adg7043.

[182] Zhou G, Zhu Y, Yao S, Sun Q. Giant temperature span and cooling power in elastocaloric regenerator. Joule 2023;7:2003–15. https://doi.org/10.1016/j.joule.2023.07.004.

[183] Tušek J, Engelbrecht K, Eriksen D, Dall'Olio S, Tušek J, Pryds N. A regenerative elastocaloric heat pump. Nat Energy 2016;1:10. https://doi.org/10.1038/nenergy.2016.134.

[184] Dall'Olio S, Ahčin Ž, Žerovnik A, Kabirifar P, Brojan M, Tušek J. Development of a Tube-Based Elastocaloric Regenerator Loaded in Compression: A Review. Shape Mem Superelasticity 2024;10:99–118. https://doi.org/10.1007/s40830-024-00483-z.

[185] Bruederlin F, Bumke L, Quandt E, Kohl M. Kaskadiertes Elastokalorisches Kühlsystem - Cascaded Elastocaloric Cooling System, Berlin Offenbach: VDE VERLAG GMBH; 2019, p. 340.

[186] Ossmer H, Wendler F, Gueltig M, Lambrecht F, Miyazaki S, Kohl M. Energy-efficient miniature-scale heat pumping based on shape memory alloys. Smart Mater Struct 2016;25:085037. https://doi.org/10.1088/0964-1726/25/8/085037.
[187] Cui J, Wu Y, Muehlbauer J, Hwang Y, Radermacher R, Fackler S, et al. Demonstration of high efficiency elastocaloric cooling with large ΔT using NiTi wires. Appl Phys Lett 2012;101. https://doi.org/10.1063/1.4746257.
[188] Huang W. On the selection of shape memory alloys for actuators. Mater Des 2002;23:11–9. https://doi.org/10.1016/S0261-3069(01)00039-5.
[189] Stephan P. VDI-Wärmeatlas. 11th ed. Berlin, Heidelberg: Springer Vieweg; 2013.
[190] Hannoschöck. Wärmeleitung und -transport: Grundlagen der Wärmeund Stoffübertragung. Heidelberg: Springer Vieweg; 2018.
[191] Bruederlin F, Ossmer H, Wendler F, Miyazaki S, Kohl M. SMA foil-based elastocaloric cooling: from material behavior to device engineering. J Phys Appl Phys 2017;50:424003. https://doi.org/10.1088/1361-6463/aa87a2.
[192] Ossmer H, Lambrecht F, Gültig M, Chluba C, Quandt E, Kohl M. Evolution of temperature profiles in TiNi films for elastocaloric cooling. Acta Mater 2014;81:9–20. https://doi.org/10.1016/j.actamat.2014.08.006.
[193] Bruederlin F. Advanced Elastocaloric Cooling Devices Based on Shape Memory Alloy Films. Karlsruher Instituts für Technologie (KIT), 2020. https://doi.org/10.5445/IR/1000124631/v3.
[194] Sebald G, Lombardi G, Coativy G, Komiya A. Converting low-grade heat into mechanical energy using a natural rubber elastocaloric device. Joule 2025;9:102012. https://doi.org/10.1016/j.joule.2025.102012.
[195] Kirsch S-M, Welsch F, Michaelis N, Schmidt M, Wieczorek A, Frenzel J, et al. NiTi-Based Elastocaloric Cooling on the Macroscale: From Basic Concepts to Realization. Energy Technol 2018;6:1567–87. https://doi.org/10.1002/ente.201800152.
[196] Qian S, Ling J, Hwang Y, Radermacher R, Takeuchi I. Thermodynamics cycle analysis and numerical modeling of thermoelastic cooling systems. Int J Refrig 2015;56:65–80. https://doi.org/10.1016/j.ijrefrig.2015.04.001.
[197] Schmidt M, Schütze A, Seelecke S. Scientific test setup for investigation of shape memory alloy based elastocaloric cooling processes. Int J Refrig 2015;54:88–97. https://doi.org/10.1016/j.ijrefrig.2015.03.001.
[198] Yao S, Dang P, Li Y, Wang Y, Zhang X, Liu Y, et al. Efficient roller-driven elastocaloric refrigerator. Nat Commun 2024;15:7203. https://doi.org/10.1038/s41467-024-51632-y.
[199] Ossmer H, Chluba C, Kauffmann-Weiss S, Quandt E, Kohl M. TiNi-based films for elastocaloric microcooling— Fatigue life and device performance. APL Mater 2016;4:064102. https://doi.org/10.1063/1.4948271.
[200] Oßmer H. Elastocaloric Microcooling. 2017.
[201] Chluba C, Ossmer H, Zamponi C, Kohl M, Quandt E. Ultra-Low Fatigue Quaternary TiNi-Based Films for Elastocaloric Cooling. Shape Mem Superelasticity 2016;2:95–103. https://doi.org/10.1007/s40830-016-0054-3.
[202] Bumke L, Chluba C, Ossmer H, Zamponi C, Kohl M, Quandt E. Cobalt Gradient Evolution in Sputtered TiNiCuCo Films for Elastocaloric Cooling. Phys Status Solidi B 2018;255:1700299. https://doi.org/10.1002/pssb.201700299.
[203] Ludwig C. Elastokalorisches Kühlen mit Elastomeren. Master thesis. Karlsruhe Institute of Technology, 2020.

[204] Frick A, Stern C. Einführung in die Kunststoffprüfung.: Prüfmethoden und Anwendungen. München: Carl Hanser Verlag GmbH & Co. KG; 2017.
[205] Tosaka M, Ikeda Y, Toki S, Hsiao BS. Crystallization and Stress Relaxation in Highly Stretched Samples of Natural Rubber and Its Synthetic Analogue. Macromolecules 2006.
[206] Pouriayevali H, Guo YB, Shim VPW. A constitutive description of elastomer behaviour at high strain rates – A strain-dependent relaxation time approach. Int J Impact Eng 2012;47:71–8. https://doi.org/10.1016/j.ijimpeng.2012.04.001.
[207] Gotsmann B, Lantz MA. Quantized thermal transport across contacts of rough surfaces. Nat Mater 2013;12:59–65. https://doi.org/10.1038/nmat3460.

Acknowledgement

First of all, I would like to express my deepest gratitude to my supervisor, Prof. Dr. Manfred Kohl, for giving me the opportunity to explore this exciting topic and the insightful discussions throughout this research. I am also deeply thankful for his constructive feedback, continuous scientific guidance, proofreading and the time and dedication he invested in this project.

I would like to express my appreciation to our collaboration partners at the University of Freiburg for their valuable contributions. In particular, I am grateful to Prof. Dr. Jürgen Rühe for serving as my co-referee and to Jan Leutner for the fabrication of elastomer sheets.

I would like to acknowledge all members of the Smart Materials and Devices Research Group for their support and collegiality. I am especially thankful to Dr. Florian Brüderlin, who introduced me to the topic, and to Dr. Kiran Jacob, who helped me to get to know the institute's procedures. I also appreciate the fruitful technical discussions with Dr. Joel Joseph and Dr. Lena Annkathrin Seigner. I would like to thank Gowtham Arivanandhan, Dr. Ali Ghotbi Varzaneh, Maxim Wischnewski, Vincent Gottwald, Danni Li, Navid Sistanizadeh Aghdam, Dr. Zixiong Li, Dr. Xi Chen, Yi-Ting Hsiau and Athira Kattiparambil Sivaprasad for creating a motivating and enjoyable working atmosphere in the lab, enriched by good humor.

I would like to thank all administrative and technical staff at the Institute of Microstructure Technology (IMT) for their support. In particular, I would like to thank Stefan Vietmeyer, Achim Voigt, Alexandra Moritz and Nina Giraud for their assistance in facilitating administrative procedures and providing the necessary technical infrastructure.

I also want to express my sincere thanks to my friends for their continuous support and making this journey more enjoyable. I sincerely thank Raphael Kern, Dr. Johannes-Christian Schmitt and Krisztina Gáll for their time and effort in proofreading this thesis. Finally, I would like to thank my family: my dear parents, Sabine and Fritz Ludwig, and my brother Andreas. Thank you for the unwavering love, constant encouragement and possibility to choose my way and follow my interests.